STRUCTURE-FUNCTION STUDIES ON A SODIUM-COUPLED PHOSPHATE COTRANSPORTER

Dissertation
zur
Erlangung der naturwissenschaftlichen Doktorwürde
(Dr. sc. nat.)
vorgelegt der
Mathematisch-naturwissenschaftlichen Fakultät
der
Universität Zürich

von
Monica Patti
aus
Italien

Promotionskomitee
Prof. Dr. François Verrey
PD Dr. Ian Forster
Prof. Dr. Carsten Wagner
PD Dr. Stephan Kellenberger
Zürich, 2013

Article1: “Conferring electrogenicity to the electroneutral phosphate cotransporter Napi-IIc (SLC34A3) reveals an internal cation release step” Patti M, Ghezzi C, Forster IC. Pflugers Arch. (2013)

Article 2: “Structural model of the human Na+-phosphate cotransporter NaPi-II” Patti M., Fenollar-Ferrer C., Knöpfel T., Werner A., Forster I. C., Forrest L. R. *Manuscript submitted.*

Article 3: “Correlating charge movements with local conformational changes of a Na+-coupled cotransporter” Patti M. and Forster IC. *Manuscript in preparation*

Article 4: “An integrates field-effect microdevice for monitoring membrane transport in *Xenopus laevis* oocytes via lateral proton diffusion” Schaffhauser DF, Patti M, Goda T, Miyahara Y, Forster IC, Dittrich PS. PLoSOne. 7(7):e39238. (2012)

Article 5: “Mutation in SLC20A2 link familial idiopathic basal ganglia calcification with phosphate homeostasis” Wang C, Li Y, Shi L, Ren J, Patti M, Wang T, de Oliveira JR, Sobrido MJ, Quintáns B,Baquero M, Cui X, Zhang XY, Wang L, Xu H, Wang J, Yao J, Dai X, Liu J, Zhang L, Ma H, Gao Y, Ma X, Feng S, Liu M, Wang QK, Forster IC, Zhang X, Liu JY. Nature Genetics. 44, 254–256 (2012)

“E quindi uscimmo a riveder le stelle.”
Dante Alighieri

TABLE OF CONTENTS

SUMMARY

Type II sodium-phosphate cotransporters (NaPi-II), encoded by the SLC34 gene family, play an important physiological role in the homeostasis of inorganic phosphate (P_i). Three protein isoforms are found in mammals designated NaPi-IIa, NaPi-IIb and NaPi-IIc (or SLC34A1,2,3). They are integral membrane proteins that mediate uphill P_i transport driven by the electrochemical gradient of sodium. Their tissue localization determines their physiological role: whereas NaPi-IIa and NaPi-IIc are mainly expressed in the renal proximal tubule, NaPi-IIb is expressed in the small intestine and other non-renal epithelial-like cells. Disturbed phosphate homeostasis is associated with many diseases. The ability to modulate the activity of NaPi-II in controlling phosphate absorption could have a large clinical impact, particularly in end stage renal disease where the ability to excrete phosphate is compromised, leading to high plasma levels and vascular calcification. For this reason the investigation of the structure-function relationships of these transport proteins has clinical relevance for the development of specifically targeted drugs.

Three themes are covered in this thesis:

Characterization of the cotransport dynamics

Protein conformational changes occurring during the transport cycle can be investigated with voltage clamp fluorometry (VCF), whereby a thiol reactive fluorescence molecule is used as an indirect reporter of motion. This technique applied to NaPi-IIb containing substituted cysteines has revealed complementary movement of two protein domains during the transport cycle. Using VCF applied to mutant transporters that retain their basic function after labelling with the fluorophore, a more detailed "map" of the movements of different domains of the protein during the transport cycle under physiological conditions was obtained.

Moreover, by combining VCF and presteady-state analysis, we investigated the correlation of kinetics of voltage-dependent transitions (manifested as presteady-state relaxations) with the kinetics of localized microenvironment changes, reported by changes in fluorescence intensity (ΔF). A direct correlation would suggest that the fluorophore senses the interaction of ions and the charge movement attributed to the empty carrier. Our findings allow us to relate protein rearrangements with the voltage-dependent events during the transport cycle such as substrate binding and translocation and predict the location of cation binding sites.

Identification of an internal cation release step

Knowledge of the internal release and binding of substrates to NaPi-II is limited. New insight was obtained using the electroneutral NaPi-IIc isoform. Electrogenicity of NaPi-IIc was restored by

replacing of three conserved amino acids, found in all electrogenic isoforms, at corresponding sites in NaPi-IIc. The Na^+:P_i stoichiometry of this engineered electrogenic construct (AAD-IIc) increased from 2:1 to 3:1. Accompanying this fundamental functional change, AAD-IIc also showed a different behaviour from the wild-type electrogenic NaPi-IIa/b, specifically a reduced apparent P_i affinity and different presteady-state kinetics. This compromised behaviour was investigated using electrophysiology and voltage clamp fluorometry (VCF). The activation energy of AAD-IIc was considerably different from NaPi-IIc and NaPi-IIa; in particular AAD-IIc shows a higher activation energy associated with the empty carrier reorientation. These studies have shown that the AAD-IIc retains the electroneutral cooperative interaction of 2 Na^+ ions of the electroneutral NaPi-IIc and the presteady-state charge relaxations of AAD-IIc are mainly due to the empty carrier (in the absence of external P_i), and to the cytosolic release of one Na^+ ion (in the presence of P_i). Using simulations of presteady-state and steady-state behavior, it was possible to identify two critical partial reactions: the final release of Na^+ to the cytosol and external P_i binding. Moreover, using VCF with Cys-mutants of AAD-IIc we confirmed the predictions from the model simulation.

Homology model and substrate binding sites localization

The transport mechanism and structure-function relationships of sodium-dependent phosphate cotransporter (NaPi-II) have been extensively studied; however, its 3D structure is still unknown. Although the structures of some sodium-dependent cotransporters have been resolved, the classical bioinformatic approaches fail to identify a suitable template for the creation of homology model of NaPi-II. Using hydrophobicity profiles and hidden Markov Models it was possible to define a structural repeat common to all NaPi-II isoforms. Now, using the recently solved crystal structure of *Vibrio cholerae* Na^+-dicarboxylate transporter VcINDY as a template, we were able to generate a homology model of human NaPi-IIa. The predicted Na^+ and P_i coordination sites are localized in specific repeat motifs in the center of the protein and furthermore biochemical and electrophysiological investigations have confirmed the importance of key amino acids predicted to be involved in substrate coordination.

ZUSAMMENFASSUNG

Natriumphosphat-Kotransporter vom Typ II (NaPi-II), kodiert von der SLC34 Genfamilie, spielen eine wichtige physiologische Rolle in der Homöostase von anorganischem Phosphat (Pi). Bei Säugetieren findet man von ihnen drei Proteinisoformen, genannt NaPi-IIa, NaPi-IIb und NaPi-IIc (oder SLC34A1,2,3). Diese sind wesentliche Membranproteine, die den Transport von Pi gegen den Gradienten erleichtern. Der Transport wird durch den elektrochemischen Gradienten des Natriums angetrieben.

Die Lokalisierung im Gewebe bestimmt ihre physiologische Aufgabe: Während NaPi-IIa and NaPi-IIc vorwiegend in der sogenannten „renal proximal tubule“ exprimiert werden, wird NaPi-IIb im Dünndarm und anderen nicht renalen Zellen, wie Epithelzellen, in der Genexpression. Eine gestörte Phosphathomöostase wird mit vielfältigen Erkrankungen in Verbindung gebracht. Die Fähigkeit, die Aktivität von NaPi-II zu beeinflussen, indem die Phosphatabsorption kontrolliert wird, könnte großen klinischen Einfluss ausüben, besonders im Bereich von Nierenerkrankungen im Endstadium. Bei diesen ist die Fähigkeit zur Phosphatausscheidung beeinträchtigt. Dies wiederum führt zu einem hohen Plasmaspiegel und Gefäßverkalkung. Gerade aus diesem Grund hat die Erforschung der Beziehung zwischen Struktur und Funktion dieser Transportproteine große klinische Relevanz in der Entwicklung von spezialisierten Medikamenten. In der vorliegenden Dissertation werden nun drei Themen abgedeckt:

Charakterisierung der Kotransportdynamik

Treten während des Transportzyklus Veränderungen in der Proteinkonformation auf, so können diese mit Hilfe der sogenannten „voltage clamp fluorometry (VCF)“ untersucht werden. Dabei wird ein Molekül, das bei Zugabe von Thiol fluoresziert, als indirekter Nachweis von Bewegung genutzt. Die Technik wurde auf NaPi-IIb angewandt, welches substituierte Cysteine enthielt. Enthüllt wurden in Folge komplementäre Bewegungen zweier Proteindomänen, die während des Transportzyklus vorkamen. Nun wandte man VCF auf mutierte Transporter an, die mit dem Fluorophor markiert wurden, ihre grundlegende Funktion jedoch behalten hatten, und erhielt eindetaillierteres Bild der Bewegungen von verschiedenen Proteindomänen während des Transportzyklus unter physiologischen Bedingungen.

Durch die Kombination von VCF und der sogenannten „presteady-state analysis“, untersuchten wir den Zusammenhang zwischen der Kinetik von spannungsabhängigen Übergängen (welche offenbar sogenannte„presteady-state relaxations“ sind) und der Kinetik von lokalisierten Veränderungen in der Mikroumgebung. Letztere wurden durch Veränderungen in der

Fluoreszenzintensität sichtbar (ΔF). Ein direkter Zusammenhang würde nahelegen, dass das Fluorophor die Interaktion von Ionen und die Übergänge durch das unbeladene Carrier-Protein erfassen kann. Unsere Entdeckungen erlauben es uns, Neuzusammensetzungen der Proteine mit den spannungsabhängigen Vorkommnissen während des Transportzyklus, wie der Substratbindung und Translokation, in Verbindung zu bringen und die Orte der Kationbindungen vorherzusagen.

Identifizierung eines internen Schrittes der Kationabgabe

Das Wissen um die interne Abgabe und Bindung von Substraten an NaPi-II ist begrenzt. Einen neuen Einblick hat jedoch die Nutzung der elektonisch neutralen Isoform von NaPi-IIc ermöglicht. Die Elektrogenität von NaPi-IIc wurde wiederhergestellt, indem man drei konservierte Aminosäuren an korrespondierenden Orten in NaPi-IIc ersetzt hat, welche man in allen elektrogenen Isoformen findet. Die Na^+:Pi Stöchiometrie dieses speziell entwickelten elektrogenen Konstruktes (AAD-IIc) hat sich von 2:1 auf 3:1 erhöht. Zusätzlich zu dieser fundamentalen funktionellen Veränderung, hat AAD-IIc ein vom Wildtyp, dem elektrogenen NaPi-IIa/b, verschiedenes Verhalten gezeigt. Im Besonderen sind zu nennen: eine offensichtliche reduzierte Pi Affinität und eine veränderte Kinetik, welche dem Festzustand vorausgeht. Dieses beeinträchtigte Verhalten wurde durch Elektrophysiologie und „voltage clamp fluorometry (VCF)“ untersucht. Die Aktivierungsenergie von AAD-IIc unterschied sich erheblich von der des NaPi-IIc und NaPi-IIa. Insbesondere zeigt AAD-IIc in Verbindung mit der Neuorientierung des unbeladenen Carrier-Proteins eine höhere Aktivierungsenergie. Die vorliegenden Studien haben gezeigt, dass AAD-IIc die elektroneutrale, kooperative Interaktion mit 2 Na^+ Ionen des elektroneutralen NaPi-IIc aufrecht erhält. Außerdem zeigte sich, dass der Nachlass in der elektrischen Ladung des AAD-IIc vor dem Festzustand, vor allem wegen des unbeladenen Carriers (in Abwesenheit externen Phosphats und der Abgabe von Na+ Ionen (in Anwesenheit von Pi) auftritt. Durch den Gebrauch von Simulationen zum Verhalten im Prägleichgewichtszustand („presteady-state“) und Gleichgewichtszustand („steady-state“), war es möglich, zwei kritische partielle Reaktionen zu identifizieren: Die finale Abgabe von Na+ ins Cytosol und die externe Pi Bindung. Außerdem, durch die Nutzung von VCF mit Cysmutaten von AAD-IIc, konnten die Vorhersagen durch die Modellsimulationen bestätigt werden.

Homologiemodell und die Lokalisierung von Orten der Substratbindung

Der Transportmechanismus und die Struktur-Funktion-Beziehungen des natriumabhängigen Phosphatkotranspoters (NaPi-II) wurden ausführlich untersucht. Trotzdem ist seine dreidimensionale Struktur weiterhin weitgehend unbekannt. Obwohl die Strukturen verschiedenster natriumabhängiger Kotransporter entdeckt wurden, scheitern klassische Annäherungen der

Bioinformatik am Problem, ein passendes Muster für ein Homologiemodell von NaPi-II zu finden. Indem Hydrophobieprofile und Markov Modelle genutzt wurden, war es möglich, eine strukturelle Wiederholung zu definieren, welche alle NaPi-II gemein haben. Nun, durch die Nutzung der kürzlich aufgelösten kristallinen Struktur des Vibrio cholerae Na^+-dicarboxylate Transporters, VcINDY, als Modell, konnte ein Homologiemuster von humanem NaPi-IIa generiert werden. Die vorhergesagten Na^+ und Pi Koordinierungsorte wurden in speziellen, sich wiederholenden Motiven, im Zentrum des Proteins, lokalisiert. Weiterhin haben elektrophysiologische Untersuchungen die Bedeutung von Schlüssel-Aminosäuren enthüllt, welche laut Vorhersage in der Substratkoordinierung involviert sein sollen

ABBREVIATIONS

AAD-IIc: electrogenic triple mutants of NaPi-IIc (SLC34A3)
ADP: adenosine diphosphate
ATP: adenosine triphosphate
BBMV: brush border membrane vesicle
BetP: betaine transporter
cAMP: cyclic adenosine monophosphate
cGMP: cyclic guanosine monophosphate
ClC: family of Cl^- transport proteins
COVC: cut-open *Xenopus* oocyte voltage clamp
E_a: activation energy
EAAT: excitatory amino acid transporter
EPR: electron paramagnetic resonance
F: fluorescence emission intensity
FRET: fluorescence resonance energy transfer
GAT: GABA transporter
Glt_{Ph}: glutamate transporter homolog from (*Pyrococcus horikoshii*)
GLUT: glucose trasporter
LCP: lipidic cubic phases
LeuT : bacterial leucine transporter
MTS: methanethiosulfonate
MTS-TAMRA: MTS 5(6)-carboxytetramethylrhodamine
NaDC: Na^+ / Dicarboxylate transporters (SLC13)
NaPi-II: sodium dependent phosphate transporter, type II (SLC34 family)
n_H : Hill coefficient
NhaA: Na^+/H^+ antiporter
NI: not injected oocyte
PDB: Protein Data Bank
P_i: inorganic phosphate
qy : apparent quantum yield
SCAM: substituted cysteine accessibility method
SDSL: site-directed spin labeling

SERT: serotonin transporter (SLC6A4)

SGLT1: Na$^+$/glucose cotransporter (SLC5A1)

smFRET: single molecule fluorescence resonance energy transfer

TEVC : two electrode voltage clamp

TM: transmembrane segment

TMD: transmembrane domains

TMRM: tetramethylrhodamine maleimide

VCF: voltage clamp fluorometry

VcINDY: *Vibrio cholerae* Na$^+$-dicarboxylate transporter

WT: wild type

ΔF: change in fluorescence intensity

INTRODUCTION

Membrane transport proteins

The lipid bilayer establishes a barrier between the external and internal environments of cells. Transport of essential nutrients including small polar organic molecules and inorganic ions across the bilayer is mediated by specialized integral membrane proteins, which can be divided in two groups on the basis of their functional mechanism: ion channels and carriers.

Ion channels

Ion channels comprise one or more subunits capable of forming a highly permeable pathway across the membrane that allows the passage of ions down their electrochemical gradient.

Ion channels are characterized by the presence of a gate and a filter for ionic selectivity. The gate opening can be mediated by numerous factors; for example, membrane potential, ligand and divalent cation interactions, cGMP/cAMP, ADP/ATP hydrolysis, temperature or mechanical forces. The ionic selectivity depends on the size of the filter region and on the location of charged residues that define the energy profile within the pore (Hille, 2001).

The major distinction between ion channels and carriers is related to the transport mechanism and the transport rate. Channels transport ions exclusively downhill according to the electrochemical gradient for the ion. In contrast, some carriers can transport substrate uphill by coupling to the electrochemical gradient of another ion (e.g. the sodium-coupled glucose cotransporter SGLT1), whereas others act as facilitated diffusers and cannot concentrate substrate (e.g the GLUT family of glucose carriers). Moreover, ion channels are characterized by rapid transport rate and this allows their activity to be measured by electrophysiology, either at the macroscopic level (whole cell) or single channel level (patch clamp) (Hille, 2001).

Carriers

Carriers can transport many different types of small organic molecules and ions. Unlike ion channels, which are gated to allow ions to flow according to their electrochemical gradient, the carrier must selectively bind and release substrates without significant leakage between the external and internal cell environment. The transport mechanism follows a series of ordered conformational changes in which the substrate binding site is accessible either from the extracellular (outward facing conformations) or intracellular (inward facing conformations) side of the membrane. The complex sequence of conformational changes thus imposes a limit on the transport rate. The turnover rate for carriers is relatively slow compared to ion channels. Typically, carriers can transport up to 10^3 molecules per second in contrast to channels that can transport $\geq 10^7$ ions per second (Vinothkumar and Henderson, 2010). The lower transport rate of carriers means that for electrogenic transport processes, the currents at the single carrier molecule level are too small to resolve with current technology and only macroscopic measurements can be made from a large population of carrier proteins.

Due to the identification of new structures of both carriers and channels, the separation between these membrane proteins has become blurred. For example in the family of Cl^- transport proteins (the ClC family) all the members share a conserved structural architecture, however they show different functional behaviors: some members work as gated chloride channels and others as secondary-active chloride transporters coupled to proton flux. Moreover, the CLC family is characterized by the presence of fast pumps, with characteristic small gates that it can move rapidly, and by the presence of exceptionally slow ion channels, in which the ion conduction deforms the pathway slowing the ion diffusion (Dutzler, 2006; Gadsby, 2009).

Carriers can be divided in three groups:

- Uniporters, able to translocate a single substrate across the membrane along its electrochemical gradient (also known as facilitated diffusers).
- Symporters (cotransporter), able to translocate two or more substrates in the same direction.
- Antiporters, able to translocate two substrates in opposite directions.

Carriers can also be distinguished on the basis of the energetics of the transport process. For primary active transport, the source of energy derives from the hydrolysis of ATP and GTP, light or redox energy; for secondary active transport, the energy is provided by the co-substrate translocation along its electrochemical gradient that promotes the substrate translocation against its electrochemical gradient.

Alternating access model and structural characterization

According to the alternating access model originally proposed by Jardetzky (Jardetzky, 1966), a carrier protein uploads the substrates from one side of the membrane then it changes its conformation and releases the substrates to the other side such that during each transport cycle the substrates are never exposed to both sides of the membrane simultaneously. To complete the transport cycle, a carrier undergoes a series of conformational rearrangements that can be generalized as outward facing conformations in which the binding sites are exposed to the extracellular environment and inward facing conformations in which the binding sites are expose to the intracellular environment (*Figure 1).*

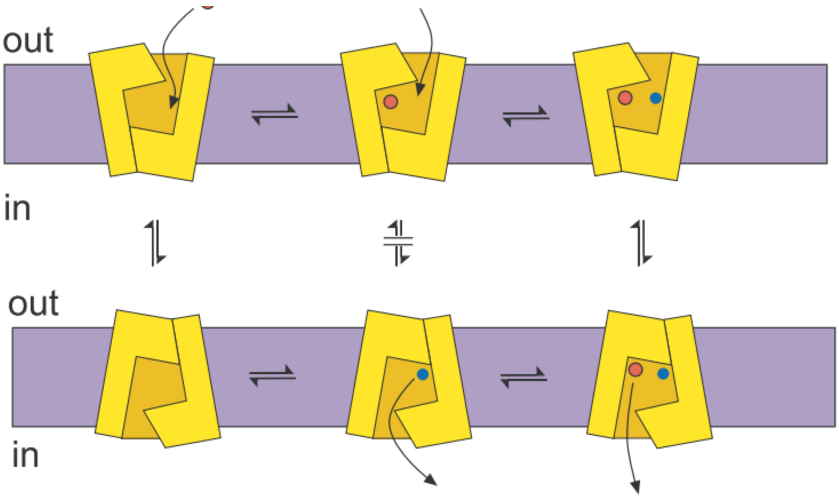

Figure 1 Alternating access mechanisms for symport. Two solutes bind from the outside to form a ternary complex (upper right) with the transporter. A conformational change closes external access and opens a path to the inside (right). Following dissociation of the solutes, the empty transporter can undergo a second conformational change to regenerate the outside-facing form. Note that interconversion of the transporter with a partially filled binding site is incompatible with efficient symport of the two solutes. From Rudnick, 2006.

The 3D structure of membrane transporters can provide information about the general architecture of the protein in the membrane and its transport mechanism. The most common technique used for the identification of the 3D structures of protein is X-ray crystallography. This technique requires high quality diffracting crystals that provide sufficient resolution to allow the identification of important feature of the transporter such as binding sites etc. The greatest obstacle to the structural resolution of membrane proteins derives from their amphiphilicity (property of having hydrophilic and hydrophobic regions), this feature causes a misfolding of these proteins in aqueous media; therefore the crystal formation represents the critical step. The first advance came in the 1980’s with the use of detergent-based micelles designed to solubilize membrane proteins; this method led to the first structure of a membrane protein (Deisenhofer et al., 1985). The second breakthrough came in 1996 with the new approach of lipidic cubic phases (LCP): Bacteriorhodopsin was the first membrane protein crystallized using LCP crystallization (Landau and Rosenbusch, 1996).

Thanks to these and other technical advances, the number of resolved and known 3D structures of transmembrane proteins has markedly increased; however, it is estimated that membrane proteins encoded in the human genome number at least 10,000 and up to now only approximately 700 of these have been structurally resolved (http://blanco.biomol.uci.edu/Membrane_Proteins_xtal).

Most of the 3D crystal structures reported for different carrier appear to be perfectly consistent with the alternating access model. *Figure 2* shows a schematic representation of the conformational changes for the bacterial leucine transporter (LeuT) (Krishnamurthy and Gouaux, 2012).

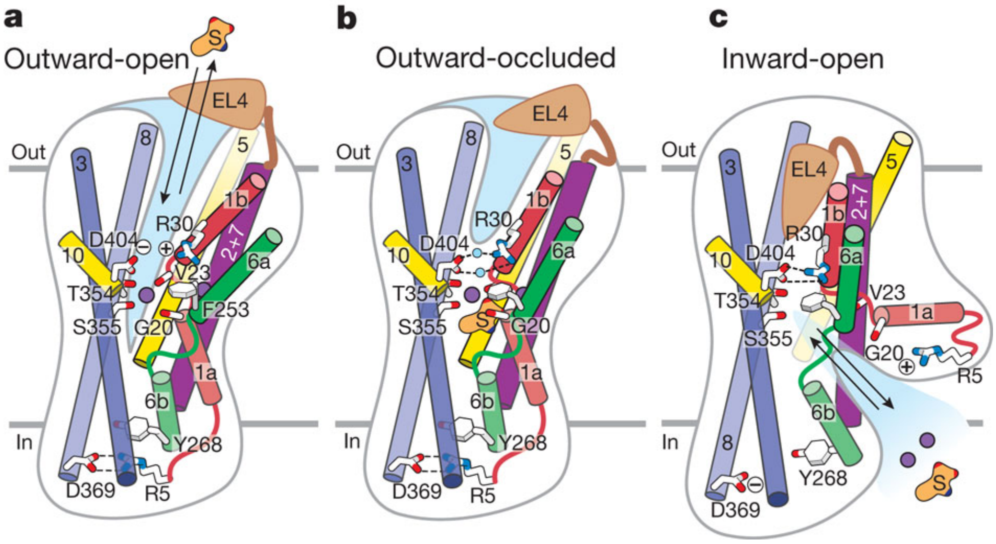

Figure 2 Schematic of transport in LeuT. a–**c**, Shown are structural elements and gating residues instrumental to conformational changes associated with the transition from the outward-open (**a**) to the outward-occluded state (**b**) and the inward-open state (**c**). At present there is no crystal structure for an inward-occluded state and thus no schematic is provided. From Krishnamurthy and Gouaux, 2012.

Secondary active transporters

Secondary active transporters are involved in a variety of important cellular functions. They are responsible for transmembrane transport of essential metabolites, ion homeostasis and synaptic function. Secondary active transporters can be divided into different families based on their primary structures (Busch and Saier, 2002), hydropathy profiles (Lolkema and Slotboom, 2003), and driving cation (mainly Na^+ and H^+).

The classification based on functional and phylogenetic properties identifies about 5000 representative transporters (Saier et al., 2009). However to detect more distant evolutionary relationships between proteins the hydropathy profile analysis is recommended. For example, with this method Lolkema included 32 families of transporter proteins in a unique structural class designated ST[3], among which are LeuT, vSGLT1, BetP. (Lolkema and Slotboom, 2003).

Moreover, the recent determination of 3D structures at atomic resolution improved the transporter classification on the base of their folding (Forrest et al., 2011).

One common characteristic of these proteins is the evidence of a gene duplication in their evolution: transmembrane segments are duplicated, moreover a duplication of helical bundles can causes a parallel or antiparallel orientation (Vinothkumar and Henderson, 2010; Forrest, 2013). Most of these transporters have structural architectures characterized by a pseudo-two-fold symmetry. Their structures can be divided in two units that have a slightly different arrangements and such differences lead to the structural asymmetry. The difference between the units allows the opening of a gate while the other is closed thereby satisfying the alternating access requirement (*Figure 3B*) (Forrest, 2013).

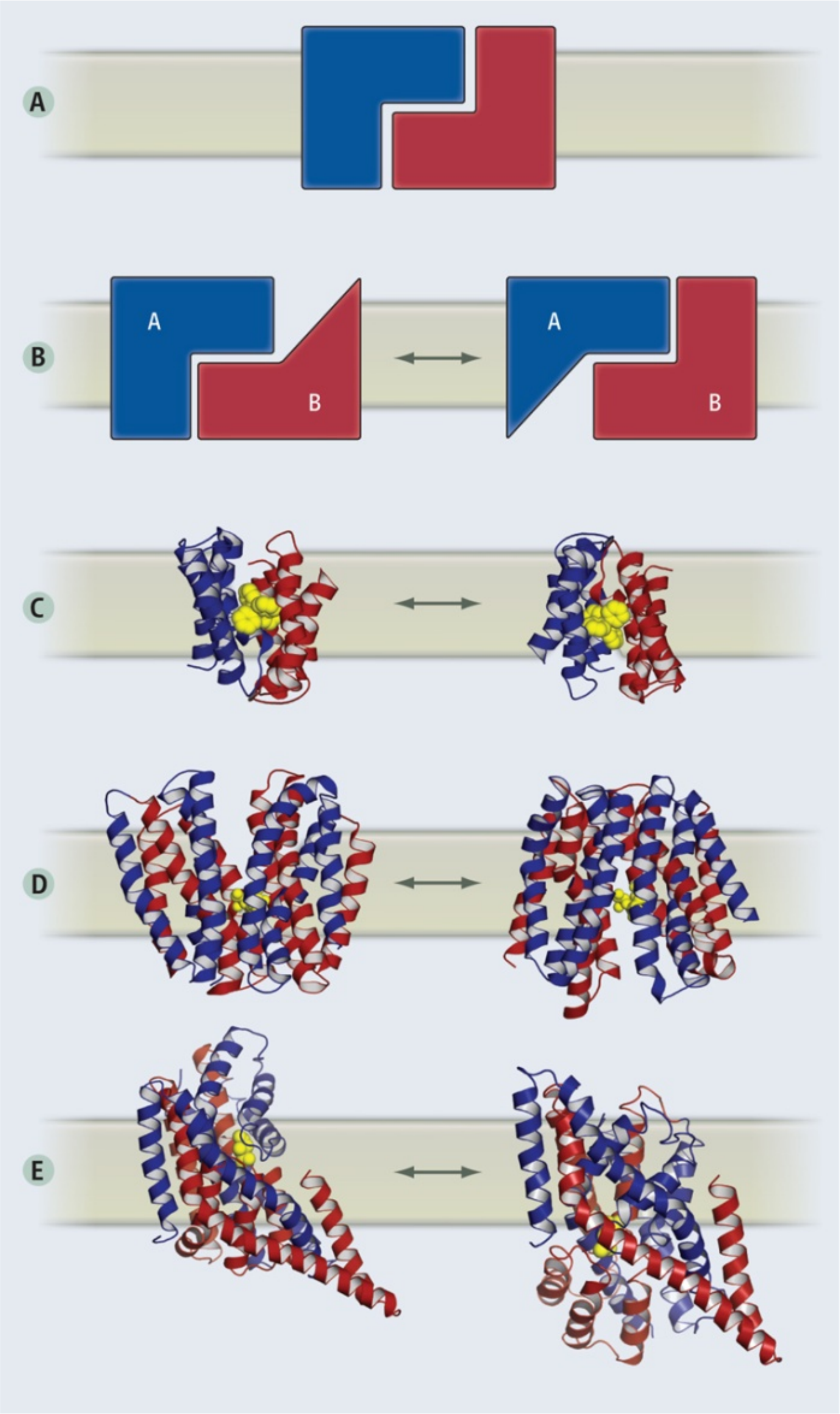

Figure 3 A) Inverted-topology repeats with similar structures can form channels through the membrane. (**B**) In transporters, the difference between the two halves creates an asymmetry in the overall protein structure, resulting in opening of the outer or inner gate. (**C**) In the antiparallel form of the dimeric transporter EmrE, the outside-open structure (left) has the same energy as the inside-open structure (right, same structure rotated 180°). (**D**) In lactose permease, the repeated elements of the protein are part of a continuous polymer chain and are intertwined. As in EmrE, the two halves appear to alternate between two distinct conformations. (**E**) Exchange between the two conformations of the aspartate transporter, Glt_{Ph}, involves a dramatic elevator-like movement of the substrate across the membrane. From Forrest, 2013.

Sodium coupled transporters

Sodium coupled transporters are secondary active transporters in which the substrate transport energy is derived from the sodium transmembrane gradient.

The first 3D structure at atomic resolution of a sodium-coupled secondary active transporter was the glutamate transporter homolog GltPh (Yernool et al., 2004), followed by the Na^+/H^+ antiporter NhaA (Hunte et al., 2005) and the bacterial leucine transporter LeuT (Yamashita et al., 2005). The core region of these transporters has a similar fold despite the difference in preferred substrates and the difference in their sequences. Their structure has revealed the inverted topology architecture as a structural means by which alternating access can be readily achieved; this common architecture defines a central substrate translocation pathway with the substrate binding sites located approximately halfway through the membrane. Through relatively simple structural rearrangements, we can easily imagine how the access from the external or internal side of the membrane can be achieved.

Unknown conformational states of secondary active transporters can be generated by homology modeling and bioinformatic approaches (Forrest et al., 2008; Crisman et al., 2009; Radestock and Forrest, 2011). The ability to recognize two homologous repeat units with a slight asymmetry has allowed two units to be swapped to obtain a different conformational state. This approach has been used for the first time on LeuT transporter (Forrest et al., 2008), subsequently new conformational states of the LacY transporter were resolved (*Figure 4*).

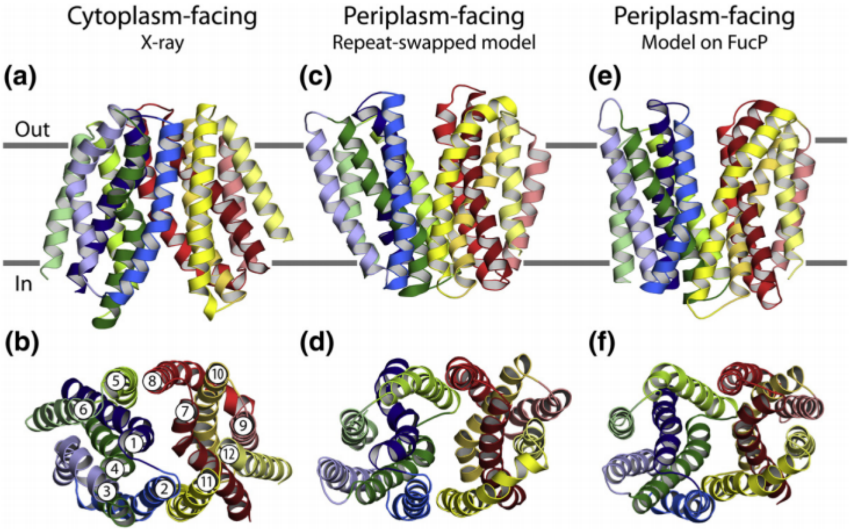

Figure 4 Models of the outward-facing conformation of LacY generated by swapping the conformations of the repeats or by using the crystal structure of FucP in an outward-facing conformation as a template. The inward-facing crystal structure (a and b) is compared to the outward-facing repeat-swapped model (c and d) and to the outward-facing model based on FucP (e and f). The transporter is viewed along the plane of the membrane (a, c, and e) or from the periplasm (b, d, and f). From Radestock and Forrest, 2011.

Substrate binding for sodium coupled transporters

Identification of the substrate binding sites represents one of the important steps toward the elucidation of the transport mechanism. For sodium-dependent cotransporters like LeuT and vSGLT, the main chain carbonyl oxygen atoms and the negatively charged side chains from Glu or Asp are involved in the binding coordination (Perez and Ziegler, 2013). In most cases, this site is localized in the discontinuous transmembrane helices. Moreover, one or more aromatic amino acids are frequently presented adjacent to the substrate-binding sites and they are involved in the formation of the occluded conformation (*Figure 2*).

For LeuT, the crystal structure estimates the presence of two sodium binding sites designated Na1 and Na2; the Na1 site is coordinated by two main-chain carbonyl oxygens (A22, T254) and three side-chain oxygens (N27, N286, T254). The Na2 site is instead coordinated by three main-chain carbonylic oxygens (G20, V23, A351) and by two side-chain hydroxylic oxygens (T354, S355). It has been hypothesized that the Na2 is important for the stabilization of the binding pocket and that it may help to facilitate the binging of the Na1 through a positive cooperation (Perez and Ziegler, 2013).

vSGLT is able to transport only one Na^+ ion per transport cycle; by structural comparison with LeuT it was possible to identify the sodium binding site at the level of Na2, which is coordinated by two hydroxy side chains (S365, S364) and by two backbone oxygen atoms from residues A361,A62 and I65 (Perez and Ziegler, 2013) (*Figure 5*).

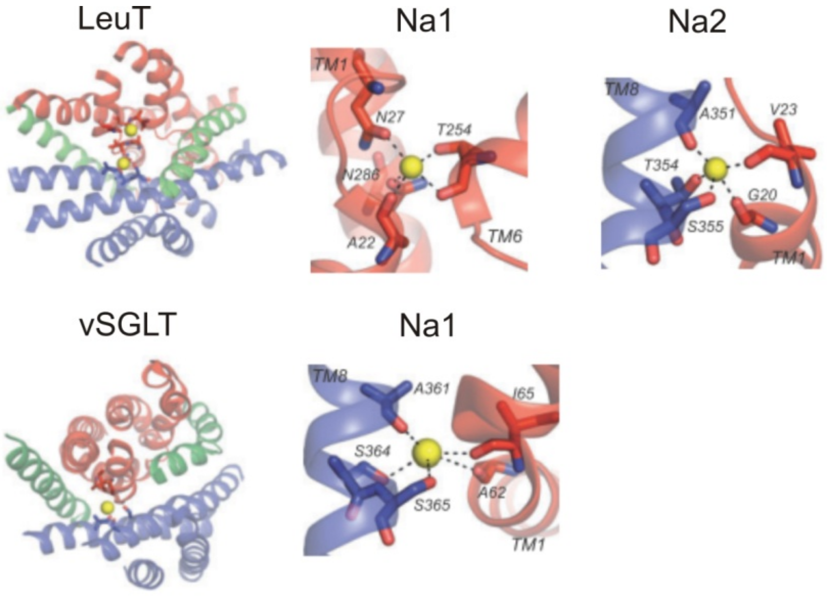

Figure 5 Sodium binding sites in LeuT and vSGLT. Sodium ions are in yellow. Modified from Perez and Ziegler, 2013

Transport kinetics of sodium coupled transporters

Before the advent of expression cloning, transport kinetics of specific transport systems were studied using native membrane preparations. For epithelial transport systems, the brush border membrane vesicle (BBMV) preparation was one of the most commonly used (Biber et al., 2007). Bacterial transporters (e.g. lactose permease), which could be purified, were studied using a liposome preparation (Garcia et al., 1983). One disadvantage of these techniques is that the transport process is assayed under non-real-time conditions (tracer uptake) and in the case of the BBMV preparation, several isoforms of transporters might mediate transport of the same substrate. Expression cloning has allowed a more detailed characterization of transport kinetics of sodium coupled transporters to be performed under conditions in which contamination from endogenous membrane proteins can be minimized and well defined driving force conditions. In this respect the *X. laevis* oocyte expression system has become the method of choice, at least for eukaryotic proteins. A variety of different assays can be performed using this system such as standard tracer influx or efflux assays even applied to single oocytes. In the case of electrogenic transporters, electrophysiological measurements on single oocytes can be made using the two electrode voltage clamp (TEVC) and patch clamp methods (Wagner et al., 2000; Bossi et al., 2007; Kvist et al., 2011). The latter technique can also be applied to cultured cells transfected to express the protein of interest. The principal advantage of voltage clamping the cell membrane is that it allows the membrane potential to be defined and transport kinetics (in terms of the transmembrane current) to be studied in real time.

Electrogenic sodium coupled transporters are generally characterized by two types of currents that depend on the voltage clamp protocol:

1. **Steady-state currents**: measured as the difference between the current in presence and in absence of substrates at a constant membrane potential. The transport currents measured at each voltage can be plotted as a function of membrane potential to obtain a current-voltage relationship (IV plot). Steady-state protocols can be used to obtain information regarding the apparent substrate affinity and the maximum transport rate.
2. **Presteady-state currents:** observed in respond to rapid changes in the membrane potential. The cell membrane acts as an electrical capacitor and a change in the membrane potential induces transient displacement currents as equal and opposite free charges move from the bulk extracellular and intracellular media to align with the lipid bilayer: the total charge moved is proportional to the change in membrane potential. For an oocyte expressing electrogenic carriers, an additional relaxing current component is superimposed on the linear endogenous

component. The charge associated with these so-called "presteady-state currents" is a non-linear function of the change in membrane potential. The charge movements are related to the rearrangement of intrinsic charge or polar amino acids of the protein (i.e. associated with the so-called empty carrier), and to the movement of charged substrates with the membrane electric field, which appears across the protein. To resolve the presteady state currents associated with the electrogenic carrier it is necessary to eliminate the oocyte endogenous capacitive charging component from the total current; this is done by fitting the transient currents with a multiple exponential function. Generally, the linear endogenous component is faster than the transporter related components and the endogenous component can be subtracted from the total current relaxations.

For a population of carriers, the macroscopic presteady-state relaxations could arise according to a deterministic model with each protein contributing the same microscopic relaxing charge movement or a stochastic type model, where the charge displacements are rapid and determined by the probability of the movement taking place (*Figure 6*).

In analogy to the stochastic mechanism of voltage gating proposed for ion channels (Bezanilla, 2005), the stochastic model is favoured. Moreover, smFRET measurements (see below) of transporter conformational changes also reveal the stochastic nature of the conformation changes (Akyuz et al., 2013).

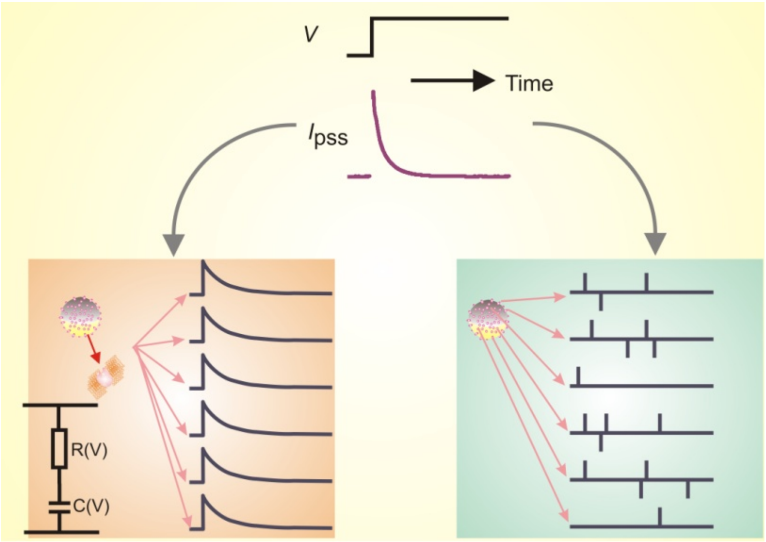

Figure 6 Schematic representation of deterministic (left) and the stochastic (right) model that could explain the macroscopic presteady-state current relaxation. In each case the same current would be measured from a population of transporters in response to a voltage step although the underlying microscopic mechanism is different. In the deterministic model, each protein can be modeled as a series R-C circuit. From Forster IC, unpublished figure.

Presteady state currents have been documented for many electrogenic sodium coupled transporters for example the hSGLT1 (Loo et al., 1993) (*Figure 7*), EAAT2 (Wadiche et al., 1995), GAT1 (Mager et al., 1993), NaDC-1 (Pajor et al., 1998) NaPi-II (Forster et al., 1998).

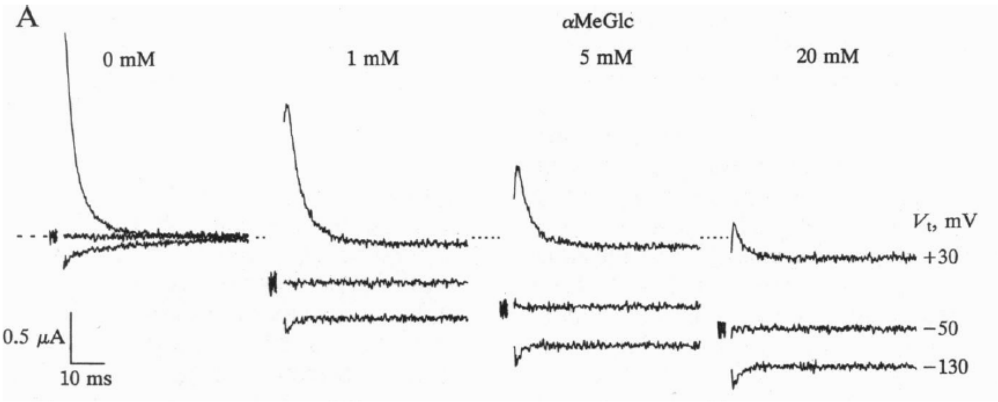

Figure 7 Transient and steady-state current. Records made in the presence of 0-20 mM aMeGlc in the Na buffer (100mM Na^+). V_h was -50mVand the membrane was stepped to +30 and -130 mV. As the substrate concentration increases, the relaxations are suppressed, indicating that in the cotransport mode, there is no net mobile charge movement within the transmembrane electrical field. From Loo et al., 1993.

Transport dynamics for sodium coupled transporters

In general the 3D structures obtained using X-ray crystallography or homology modelling give a non-physiological view of the protein because they represent a specific conformation that depends on the crystallization conditions. This limitation becomes important when considering that a complete description of the transport function requires the identification of all the possible conformational states and the probability of transitions between states to occur.

Indirect evidence of transporter dynamic processes were obtained with different techniques such as single-molecule fluorescence resonance energy transfer (smFRET) (Brunger et al., 2011), electron paramagnetic resonance (EPR) (Klare, 2013) and voltage clamp fluorometry (VCF).

Single-molecule fluorescence resonance energy transfer (smFRET)

The technique of smFRET can be used to visualize several steps in the cycle of a transporter as it translocates a substrate. This technique involves measuring the distance between fluorescent probes (donor and acceptor dyes) attached at strategic sites of a protein. In particular, the dipole-dipole interaction between donor and acceptor causes energy transfer, which leads to an increase in the acceptor emission and a decrease in the donor emission (FRET or Förster (Fluorescence) Resonance Energy Transfer). The energy transfer efficiency depends on the distance and the orientation between the two dyes. In this way it is possible to monitor the time course and magnitude of conformational changes, and moreover to determine the time spent in a particular conformation (Brunger et al., 2011) (*Figure 8*).

This technique was used to investigate the conformational changes that are associated with substrate binding and transport for LeuT transporter (Zhao et al., 2010). It was observed that the movement of specific transmembrane segment (TM1) is associated with the intracellular gating. These movements can be modulated by the presence of substrates or inhibitors and by mutations that can stabilized an inward-closed state (Zhao et al., 2010).

A disadvantage of the smFRET technique, as applied here, is that it requires purified protein. Moreover, smFRET has so far been performed on immobilized on surfaces or stabilized in liposomes that may compromise the protein folding and its activity.

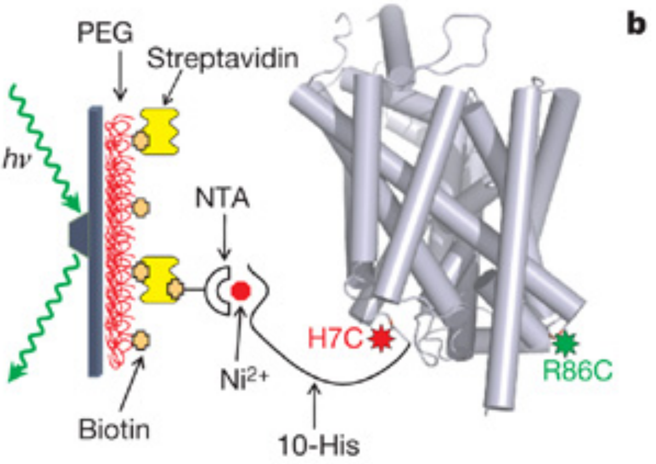

Figure 8 smFRET in LeuT. His-tagged, dye-labelled LeuT-H7C/R86C was immobilized by biotin-NTA-Ni^{2+} to the streptavidin-treated surface. From Zhao et al., 2010 .

Electron paramagnetic resonance (EPR)

Site-directed spin labeling (SDSL) in combination with electron paramagnetic resonance (EPR) spectroscopy are used to elucidate the structure and the conformational dynamics of carrier under conditions close to the physiological state. Cysteine substitution mutagenesis followed by modification of the sulfhydryl group with a nitroxide reagent is used for the introduction of spin labels (SDSL methods) (*Figure 9*). EPR spectroscopy of the spin-labeled molecules allows one to obtain information about the nitroxide side-chain such as solvent accessibility, mobility and the polarity of its immediate environment. Moreover, intramolecular or intermolecular distances between two or more nitroxides can be obtain with a resolution of ~8 to 80 Å (Klare, 2013).

Claxton and colleagues used site-directed spin labeling and electron paramagnetic resonance spectroscopy to analyze the dynamics that are associated with the substrate binding of LeuT in a specific extracellular region. They observed that the binding of inhibitors induces peculiar structural changes in LeuT, different from the ones induced by the leucine interaction (Claxton et al., 2010). EPR has similar disadvantages, as indicated above for smFRET.

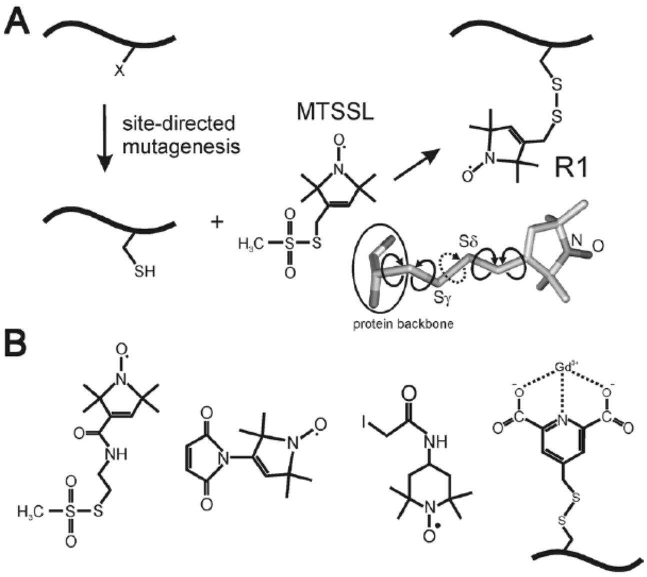

Figure 9 SDSL methods. A. After site-directed mutagenesis to replace the residue of interest by cysteine, reaction of the MTSSL with the sulfhydryl group of the cysteine yields the spin label side chain commonly abbreviated as R1. Rotatable bonds are indicated in a stick representation of the R1 side-chain structure. **B.** Selection of spin label agents for the modification cysteine side chains. Image and legend from Klare, 2013.

Voltage clamp fluorometry (VCF)

Voltage clamp fluorometry (VCF) is a real-time approach that allows the indirect visualisation of protein conformational changes under physiological conditions and is particularly applicable to the the *Xenopus* oocyte system, working with single cells.

In the VCF approach, a cysteine mutant of the protein is expressed in a model system (usually *X. laevis* oocytes) and a thiol-reactive fluorophore is covalently linked to the engineered cysteine; native cysteines are assumed to remain unlabeled. It is important to ensure that the mutagenesis and the labeling do not alter the transport kinetics.

Changes in fluorescence intensity are due to modification of the microenvironment around the fluorophore caused by the conformational rearrangement of the protein. For the interpretation of the data obtained with VCF it is necessary to consider that changes in fluorescence arise from a large population of transporters that are assumed to move independently in a stochastic manner (*Figure 10*); therefore the fluorescence changes are related to the occupancy probability of the different conformational states. The occupancy probability, in case of electrogenic cotransporters, can be modulated by voltage and by changes in substrate and cosubstrate concentration in the extracellular solution.

The physical response time of the fluorophore to these changes is approximately 10^{-8} seconds; this means that major protein conformational changes, which are expected to occur in the order of 10^{-6} seconds or slower in case of cotransporter, can be recorded in real-time.

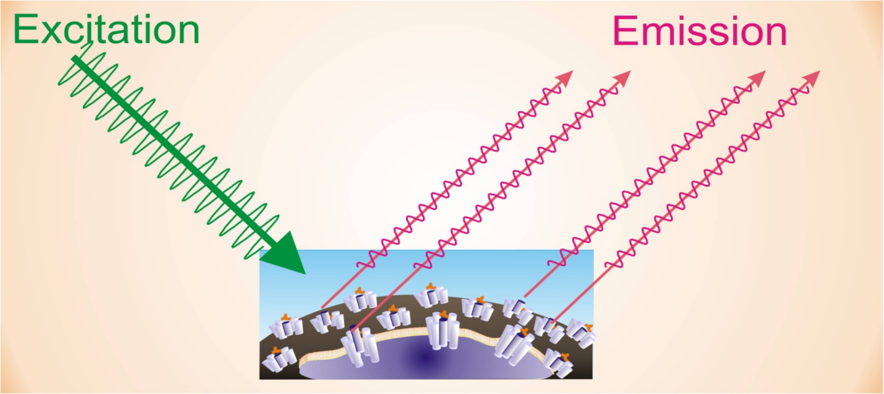

Figure 10 Cartoon illustrating a basic principle of VCF. A section of oocyte membrane is shown**.**The fluorescence changes are quantal events arising from a large population of transporters that change conformation independently. From Forster IC, unpublished figure.

The VCF technique was developed by Isacoff and colleagues with the aim of studying conformational rearrangements in the potassium channel (Shaker K^+ channel) (Mannuzzu et al., 1996) by combining electrophysiological and fluorescence measurements simultaneously. Using this technique, they were able to confirmed the presence of gating charge in the S4 segment of potassium channel and that its activation involves the movement of the amino terminal portion of S4 from a position that is buried in the membrane to a more exposed position in the extracellular environment (Mannuzzu et al., 1996).

To date, a number of laboratories have used this technique to investigate the transport dynamics in different sodium coupled transporters. The Wright group used voltage-clamp fluorometry applied to the human Na^+/glucose cotransporter (hSGLT1) to examine the partial reactions involving sugar binding and its transport. They were able to establish that the partial reaction involving sugar binding and Na^+/sugar cotransport were neither voltage-dependent nor rate limiting. Moreover they demonstrated that the presence of sugar in the external solution increased the occupancy probability of an inward-facing conformation (Loo et al., 2006).

Other insights regarding the conformation dynamic in the glutamate transporter (EAAT) were made by the Larsson group (Larsson, 2004). They demonstrated that EAAT transporter undergoes at least three major conformational changes during each transport cycle; moreover the reported results suggest that the binding of Na^+ causes an additional conformational change that precedes glutamate binding.

The VCF hardware comprises two parts: the electrophysiological and photonic components (*Figure 11*). The former comprises standard two-electrode voltage clamp (TEVC) hardware with an oocyte recording chamber fitted with a transparent base positioned above a fluorescence objective. The photonic components comprises a stable light source and shutter, an optical cube containing dichroic mirror and filters for defining the excitation and emission spectra, and a photodiode detector. The photocurrent is then converted to a voltage signal using a low noise integrating patch clamp amplifier.

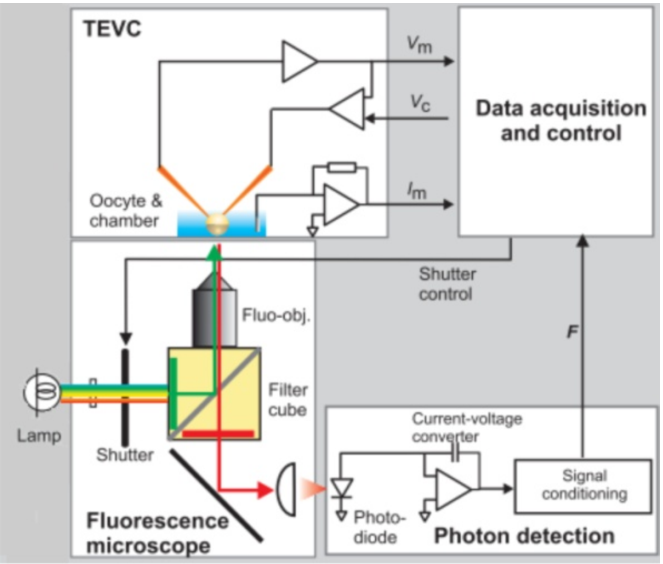

Figure 11 Voltage Clamp Fluorometry setup. VCF hardware comprises a conventional TEVC with oocyte mounted in a recording chamber with a transparent bottom. A simple fluorescent microscope allows the fluorophore excitation and the emitted light is measured using a photodiode connected to an integrating current-to-voltage converter. From Forster et al. 2012.

Although this technique has proven to be very useful in the study of protein dynamics, its potential limitation arises from the interpretation of the fluorescence changes; different mechanisms have been proposed to explain this phenomena (Cha and Bezanilla, 1998). Fluorescence changes can be postulated to arise from:

1. re-orientation of the fluorophore’s transition dipole;
2. shift in the excitation spectrum of the fluorescent label;
3. interaction with nearby protein residues that can quench the fluorophore;
4. changes in the hydrophobicity of the fluorophore’s environment.

Further insights into the underlying mechanism for the changes in fluorescence were obtained by for example fluorescence quencher or analysis of the chemical properties of the fluorophore used.

To improve the interpretation of the VCF results, the Bezanilla group (Cha and Bezanilla, 1998) have investigated if the fluorescence quenching was caused by interaction of the fluorophore with a nearby region of protein or to exposition of the fluorophore to the aqueous environment. They added iodide (I^-) to the external solution; this negatively charged anion can amplify the decrease of fluorescence intensity (collisonal quenching) if the fluorophore is located in sites accessible to the external medium. Using two mutants of Shaker potassium channel (M356C and A359C) labeled with the fluorophore tetramethylrhodamine maleimide (TMRM), they detected an increase in the fluorescence quenching in presence of I^- at two different membrane potentiasl. These results demonstrate that the accessibility of the fluorophore to the aqueous environment at these particular sites is independent of the assumed conformational states and therefore they concluded that the effect of nearby protein residues is the major cause of fluorescence quenching. (Cha and Bezanilla, 1998). Iodide was used also by Isacoff and colleagues to interpret the quenching phenomenon for other different mutants of the Shaker potassium channel; in this case, they detect an increase of fluorescence quenching caused by the presence of iodide for only one mutant (A359C) (Mannuzzu et al., 1996).

Na^+/P_i cotransporters

This thesis focuses on the structure-function relationships of the Na^+-coupled inorganic phosphate cotransporters from the SLC34 family. These proteins play an essential role in phosphate homeostasis in mammals and have been extensively studied in both the physiological context as well as the molecular level (for reviews: (Forster et al., 2012, 2013) (Biber et al., 2013)). What follows is a brief overview of their physiological role, kinetics and structure function features at the start of the research period.

Inorganic phosphate in its physiological context-the need for active transport

Phosphorus is an essential constituent of all living cells and plays key roles in protein synthesis, energy transduction, signaling, and maintaining the integrity of the genetic material. Phosphorus is present in every organism, plant and animal on Earth. The average adult human contains about 600 g of phosphorus present in the form of complex organic compounds in the blood, muscles, and nerves, and in the form of calcium phosphate in bones and teeth. Phosphorus that is not complexed or bound to protein appears as free phosphate ions in solution called inorganic phosphate (P_i); at the physiological pH (7.4) it comprises HPO_4^{2-} and $H_2PO_4^-$ ions in a 4:1 ratio. All P_i is sourced from the daily diet; the recommended intake is 1400 mg/day (Boron and Boulpaep, 2012).

Given the importance of P_i in many biological processes, its circulating plasma levels are regulated such that the plasma phosphate concentration is typically maintained in the range 0.8-1.5 mM. P_i homeostasis is controlled at three sites: kidney, small intestine and bones. Thus, serum P_i can be affected by modulation of intestinal absorption, renal re-absorption or excretion and exchange between extracellular compartments and bone storage (Penido, Maria Goretti M G and Alon, 2012). At the cellular level, the movement of P_i across the luminal membrane requires an active membrane transport process due to the anionic nature of the solute and the need for vectorial flux of P_i from the lumen to blood. The energy for the process is derived from the electrochemical gradient for sodium ions and represents one of the most common strategies utilized by solute transport systems (Vinothkumar and Henderson, 2010).

In mammals, there are two distinct families of sodium-coupled cotransporters that mediate the P_i transport: SLC20 and SLC34. The SLC20 family comprises two members SLC20A1 (PiT-1) and SLC20A2 (PiT-2), the SLC34 family comprises three members SLC34A1 (NaPi-IIa), SLC34A2 (NaPi-IIb) and SLC34A3 (NaPi-IIc). All these proteins have a high specificity for transporting anionic P_i by using the electrochemical gradient of sodium as a driving force for transport. There are two main differences between these families: tissue localization and preferred species of P_i

transported. At the RNA level, SLC34 members are highly expressed in two organs, kidney and small intestine, whereas the SLC20 members are ubiquitously expressed (*Figure 12*). At physiological pH (7.4) P_i is present as monovalent ($H_2PO_4^-$) and divalent (HPO_4^{2-}) ions (4:1); the SLC20 family preferentially transport monovalent P_i in contrast to the SLC34 family that prefer divalent P_i.

Tissue localization and physiological relevance of SLC34 proteins

The members of SLC34 are the principal responsible for the P_i homeostasis. Among the SLC34 family, the three isoforms NaPi-IIa/b/c show different tissue localization: 1) the isoforms NaPi-IIa/c are mainly expressed in the kidney and they are responsible for the re-absorption of P_i in the nephrons 2) the isoform NaPi-IIb is mainly express in the small intestine and it is responsible for the absorption of P_i from the diet (*Figure 12)*. Moreover, NaPi-IIc may also have a role in the bone mineralization (Segawa et al., 2009) as discussed below.

NaPi-IIa/b cotransporters are characterized by a Na^+: P_i stoichiometry of 3:1, in contrast to NaPi-IIc that shows a 2:1 stoichiometry. This difference results in a 100-fold increase in the P_i concentrating capacity of NaPi-IIa/b. The physiological consequences of this difference have not been fully elucidated.

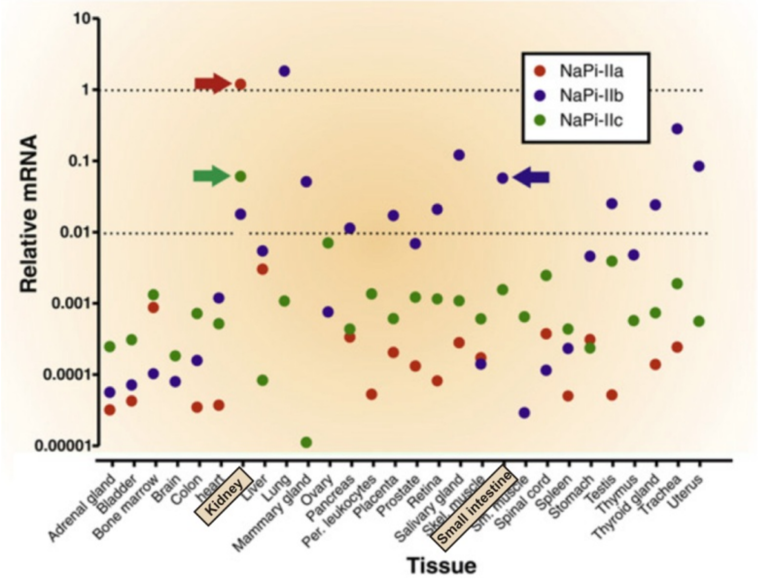

Figure 12 Tissue localization of mRNA Na/Pi-II cotransporters. the mRNAs of NaPi-IIa and II-c are mainly present in the kidney whereas expression of NaPi-IIb is mainly found in lung and small intestine and non-renal epithelia. Modified from Forster et al., 2013 .

Intestinal phosphate absorption

Dietary phosphate is absorbed mainly in the epithelium of the small intestine through the cellular and the paracellular pathways; the NaPi-IIb isoform is responsible for the cellular pathway uptake, and it is highly expressed at the luminal surface of the enterocyte (Eto et al., 2006). Inward P_i flux via NaPi-IIb results from the electrochemical gradient of the sodium maintained by the Na^+/K^+-ATPase pump at the basolateral membrane (*Figure 13*).

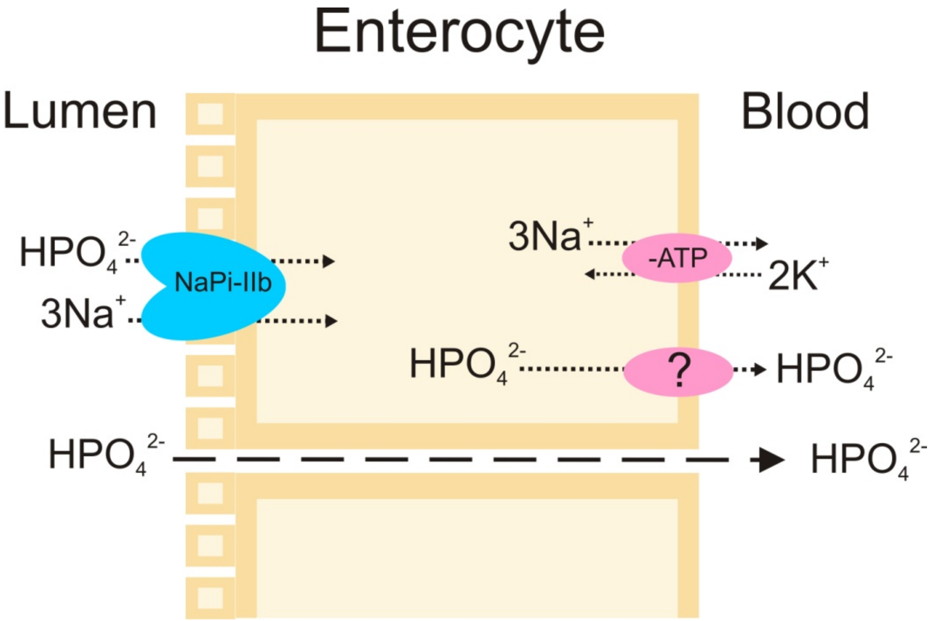

Figure 13 Phosphate transport in the intestine. NaPi-IIb is expressed at the luminal surface of the enterocyte, the electrochemical gradient of the sodium is maintained by the Na^+/K^+-ATPase pump. The basolateral pathway for P_i efflux from the cytosol is not yet identified

Renal phosphate reabsorption

The kidney is the main organ responsible for the P_i homeostasis. Under physiological conditions 80-90% of the filtered phosphorus is reabsorbed; the remainder is excreted in the urine. The reabsorption of phosphate occurs primarily in the proximal tubule: P_i enters the cell through the apical membrane by the NaPi-IIa/c and exits at the basolateral membrane by an unknown transporter. Unlike intestinal absorption, in the kidney there is no evidence of paracellular transport pathway (Ullrich and Murer, 1982). The Na^+/K^+-ATPase pump is required to maintain the sodium electrochemical gradient to drive transport the active transport (*Figure 14*).

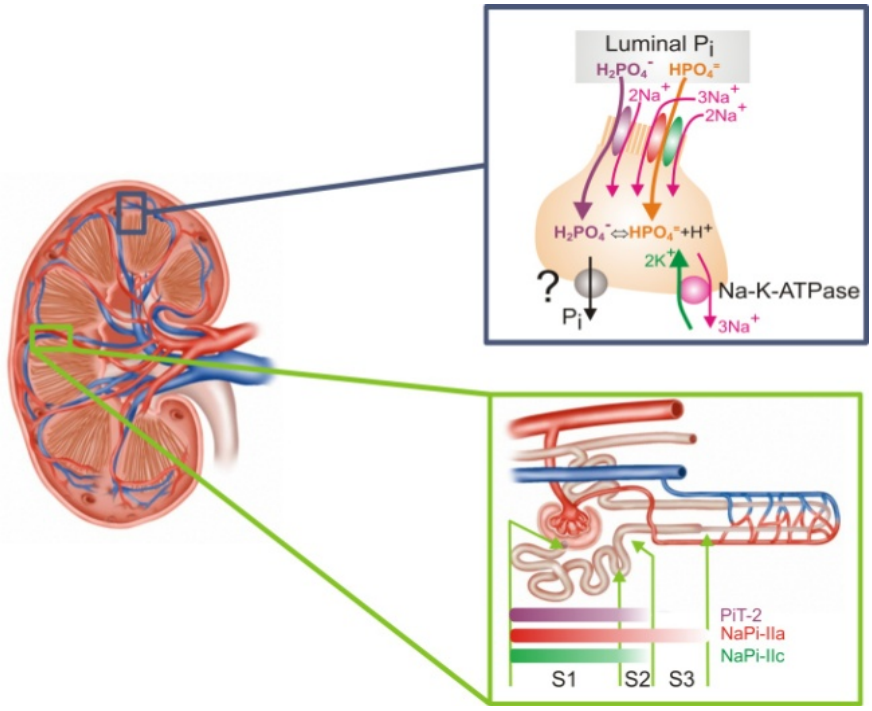

Figure 14 Localization of phosphate transport proteins in the kidney. The Pi reabsorption pathway through proximal tubule epithelia shows that NaPi-IIa and NaPi-IIc transport divalent Pi (HPO_4^{2-}), whereas PiT-2 prefers monovalent Pi ($H_2PO_4^-$), The basolateral exit pathway remains unknown. NaPi-lla, NaPi-llc and Pit-2 are localized at the brush borders membranes of epithelial in S1 and S2 segments of the proximal tubule cells, whereas NaPi-llc is absent in S3 segments. Modified from Biber et al., 2013.

Phosphate importance for the bone health

Phosphate and calcium are the basic components of the inorganic constituent of the bones (hydroxyapatite); it follows that maintaining physiological phosphate balance has a crucial biological importance for bone health. Osteoporosis is a common form of bone disease, and it is characterized by the deterioration of the bone structure and by low bone mass. Studies for the osteoporosis prevention have always been focused primarily on calcium, however, these studies are now concentrated on the importance of the balance of calcium and phosphorus in treatment for this diseases (Kuntz et al., 1986).

Dysfunction of phosphate transporters

Given the great importance of the phosphate for many biological processes, it follows that hypophosphatemia or hyperphosphatemia, which result from compromised regulation of transporter expression or specific mutations that affect targeting and function, can have adverse clinical consequences (*Figure 5*). Some diseases can be directly related to malfunctioning of specific NaPi-II isoform. In most cases, the mutations appear to affect the population of transporters expressed in the membrane rather than the transport function itself.

NaPi-IIa

Heterozygous alterations in the gene that encodes for the NaPi-IIa transporter are reported to cause urolithiasis and bone demineralization (Prié et al., 2002), moreover a heterozygous duplication in the same gene causes Fanconi renotubular syndrome 2 (Magen et al., 2010). This syndrome is characterized by severe renal phosphate wasting, renal failure and hypophosphatemic rickets with grave bone deformities, fractures, and stunted growth.

NaPi-IIb

The loss of function of NaPi-IIb transporter in the intestine can be compensated by an increase of the NaPi-IIa expression in renal proximal tubule to reduce the P_i excretion, which is the reason why the heterozygous alteration in its encoding gene is often silent. Nevertheless, pulmonary alveolar microlothiasis can manifest itself in case of autosomal recessive inheritance. NaPi-IIb is, in fact, expressed in the lungs and it is responsible for the transport the P_i from the alveolar space into the alveolar cells; alteration in its function makes the cells unable to remove phosphorus from the alveolar space causing accumulation (Kashyap and Mohapatra, 2013).

NaPi-IIc

Mutations in NaPi-IIc protein are associated with hereditary hypophosphatemic rickets with hypercalciuria, a rare autosomal recessive disorder (Bergwitz et al., 2006).

In humans, mutations in the gene encoding the type IIc sodium–dependent phosphate transporter lead to hereditary hypophophatemic rickets with hypercalciuria. Mice homozygous mutants (NaPi-IIc$^{-/-}$) exhibit hypercalcemia, hypercalciuria and elevated plasma vitamin D, but they do not develop hypophosphatemia, hyperphosphaturia, renal calcification, rickets, or osteomalacia. The Miyamoto group has suggested that NaPi-IIc is responsible for the maintaining of a normal calcium metabolism, in part achieved by modulating the vitamin D level (Segawa et al., 2009).

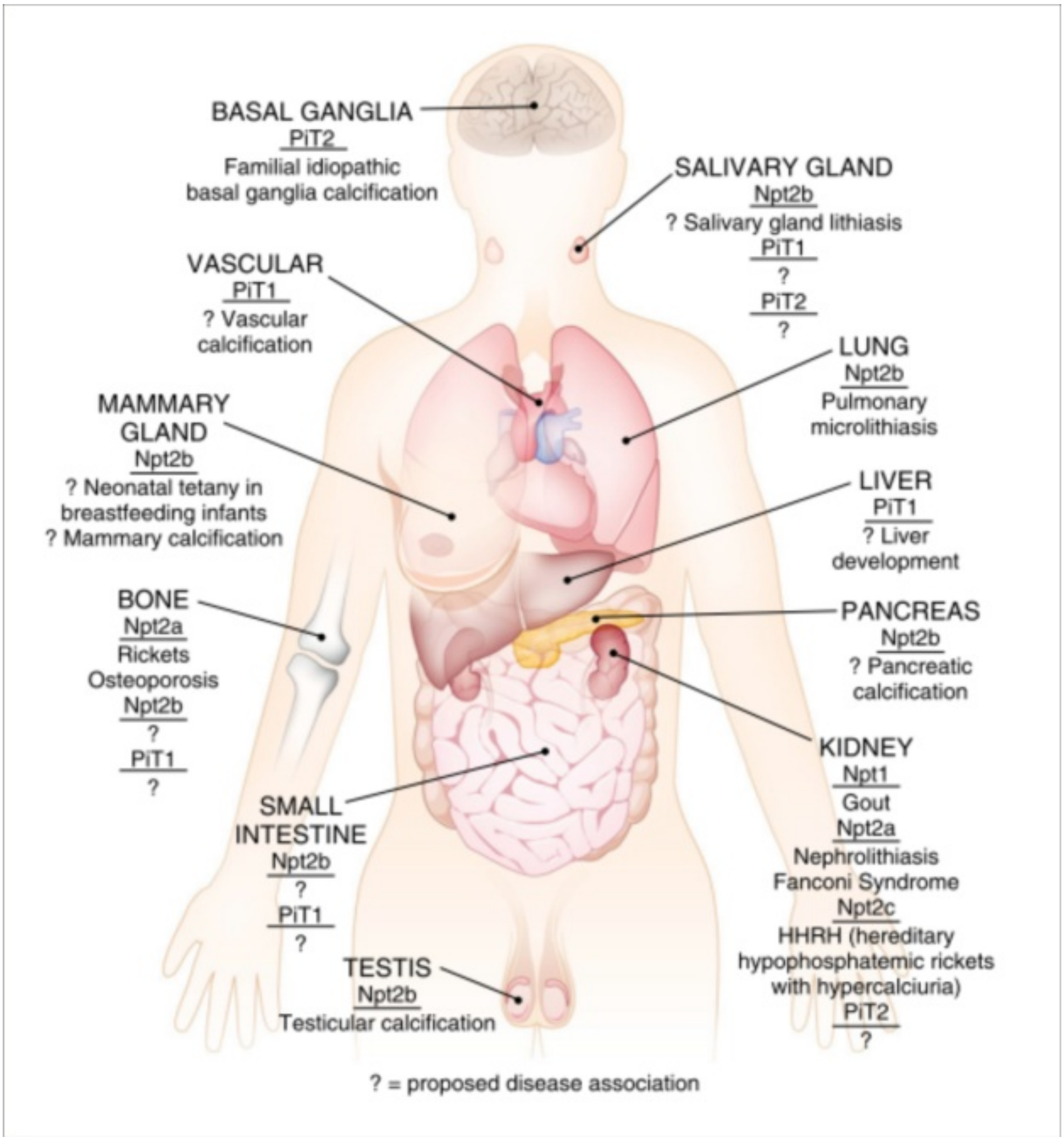

Figure 15 Diseases associated with dysregulation/dysfunction of phosphate transporters. Proposed but not identified disease associations are indicated by a question mark (?). Modified from Lederer and Miyamoto, 2012 .

Transport kinetics

Transport kinetics of the electrogenic isoforms of NaPi-II

The initial investigations on P_i transporter were done in brush-border membrane vesicles isolated from small intestine (Berner et al., 1976) and kidney (Hoffmann et al., 1976), in which it was reported that P_i transport dependended on external Na^+ ions and was therefore most likely secondary active process. These early studies were unable to clearly identify if the transport process was electrogenic or not. The first identification of a NaPi-II isoforms was reported in 1993 by expression cloning using cDNA libraries derived from rat and human kidney and by the functional expression of in *X. laevis* oocytes. (Magagnin et al., 1993).

Subsequent studies on the kinetic characterization of the different isoforms of NaPi-II were mostly done by heterologous expression in *X. laevis* oocytes, using two electrode voltage clamp (TEVC) and radioactive trace uptake ((Busch et al., 1994), for review see (Forster et al., 2012; Biber et al., 2013)

The Na:P_i transport stoichiometry of 3:1 for two electrogenic isoforms of NaPi-II was determined in 1999 (Forster et al., 1999). This was achieved by simultaneous measurements of phosphate induced inward current and uptake of radioactive $^{32}P_i$ and ^{22}Na in *X. laevis* oocytes. *Figure 16A* shows a representative electrophysiological recording of phosphate induced current for an oocyte expressing the flounder NaPi-IIb isoform and voltage clamped to -50 mV at pH 7.4. *Figure 16B* shows the relationships between the net charge transferred, obtained by integration of the P_i-induced current with time, and the corresponding P_i and Na^+ uptake. The slope of the line fitted to the Q/P_i data is close to unity, thus one net positive charge was transferred per P_i transported; the slope of the line fitted to the Q/Na data was close to 0.3, these findings were consistent with three Na^+ ions being transported per net inward charge.

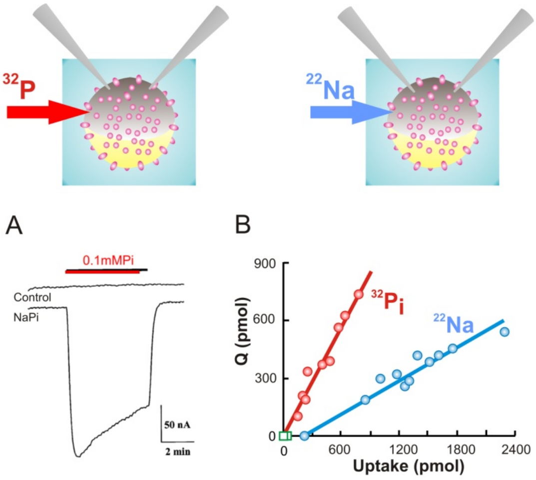

Figure 16 Cotransport stoichiometry. A. Representative electrophysiological recording of phosphate–induced current. Example recording from a control (non-injected) oocyte (upper trace) and an oocyte expressing the flounder isoform NaPi-IIb (lower trace). **B.** Relationship between the net charge transfer (Q) and Na or P_i uptake for oocytes expressing the flounder NaPi-IIb isoforms at holding potential of -50 mV and pH of 7.4. Each point represents data from a single oocyte. Modified from Forster et al., 1999.

It is now known that NaPi-II proteins possess different stoichiometries: NaPi-IIa and NaPi-IIb are electrogenic with three Na^+ ions and one HPO_4^{2-} cotransported inside the cell for a total net translocation of one positive charge and NaPi-IIc is electroneutral with a stoichiometry of two Na^+ ions and one HPO_4^{2-} (see below).

Binding order

Coransport of P_i by NaPi-II proceeds in an ordered manner and different kinetic studies established the binding order of substrate and cosubstrate. On the basis of electrophysiological assays, a kinetic model was proposed in 1998 (*Figure 17*). Each numeral represents a unique conformational state of the protein and the arrows indicate partial reactions that reflect molecular rearrangements as substrates bind and debind. This model proposed that the interaction of one sodium ion occurred before P_i binding, and at least one sodium ion was the last substrate to bind (Forster et al., 1998).

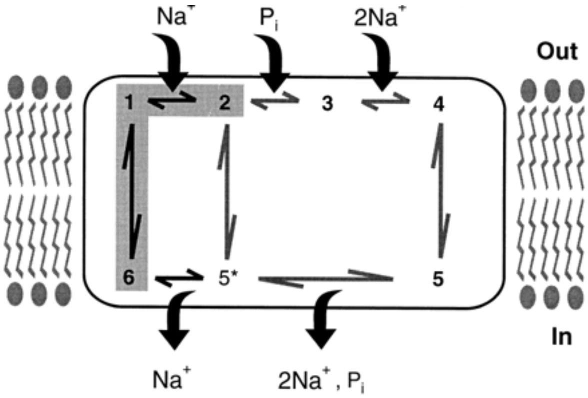

Figure 17A kinetic scheme of an ordered binding model for NaPi-II. Each number represents a unique conformational state of the protein and the double arrows represent allowed partial reactions between the states. From Forster et al., 1998.

This model was revised with the studies performed with the voltage clamp fluorometry (VCF) technique (Virkki et al., 2006b) in which it was proposed that two sodium ions bind sequentially the protein before P_i binds.

Figure 18 shows the current kinetic model proposed for the electrogenic isoform of NaPi-II. Transitions 0-1 and 5-6 are related to the translocation between the outward facing conformation and inward facing conformation; the partial reactions between states 0 and 2 are involved in charge translocation. The partial reactions that occur in the extracellular environment have been well investigated in oocytes because the external superfusion solutions could be easily changed; in contrast the conformational changes and the order of substrate release that occur in the cytosol were still unknown.

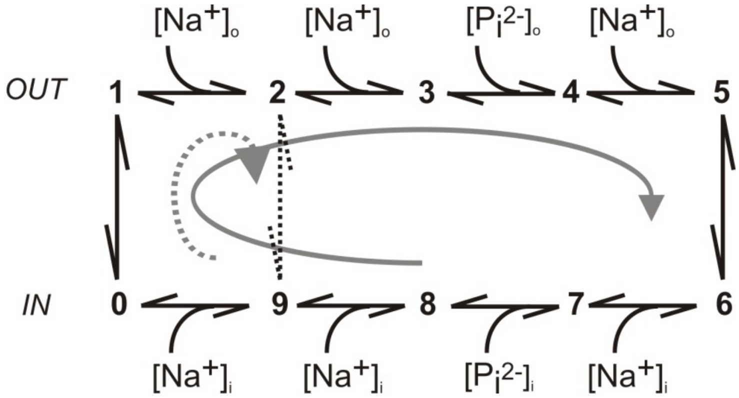

Figure 18 Kinetic scheme for electrogenic cotransport cycle. Transitions 0-1 and 5-6 represent the translocation between the outward face conformation and inward facing conformations. States 1-5 represent externally orientated conformations environment and states 0, 6-9 represent internally orientated conformations. A leak pathway operates (2-9) in the absence of external (Andrini et al., 2008).

The P_i apparent affinity ($K_{0.5}^{Pi}$) for the three NaPi-II isoforms was estimated with the TEVC, by measuring the P_i–induced current in NaPi-II expressing oocytes as a function of membrane potential (IV plot), for different P_i concentration in the extracellular solution (*Figure 19*). The transposed data were then fitted with Michaelis-Menten equation allowing the estimation of the P_i apparent affinity as ~0.1 mM (pH 7.4 and $[Na^+]$ =96 mM). The apparent affinity for Na ($K_{0.5}^{Na}$) is in the range 40-60 mM (determined with 1 mM P_i) and is comparable among the different isoforms. These apparent affinities indicate that in mammals, under physiological conditions, the NaPi-II isoforms can function close to their maximum transport velocity.

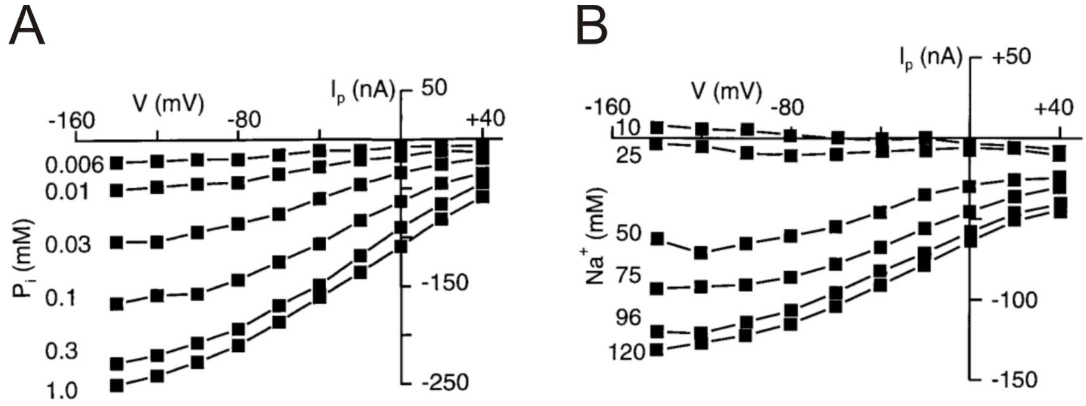

Figure 19 IV data for NaPi-IIa depicting phosphate-dependent current as a function of membrane potential A. Representative data for one oocyte superfused with 96 mM external Na^+ and different P_i concentrations in the range 0.006–1.0 mM from which the apparent P_i affinity was determined. **B.** Representative data for one oocyte with 1mM P_i and Na^+ different concentrations from which the apparent Na^+ affinity was determined. From Forster et al., 1998 .

Steady state and presteady state current

Figure 20 shows representative TEVC current recordings data from a *X. laevis* oocyte expressing flounder NaPi-IIb isoform for different steps of voltage and for two external solutions (100 mM Na^+ and 100 mM Na^+ + 1 mM P_i). From these data it is possible to distinguish the two types of currents: presteady-state currents that relax within the first 20 ms after the voltage steps and the steady state currents (page 17). Presteady-state current relaxations depend on the external Na^+ concentration and they are suppressed in presence of P_i but still visible in absence in Na^+.

.

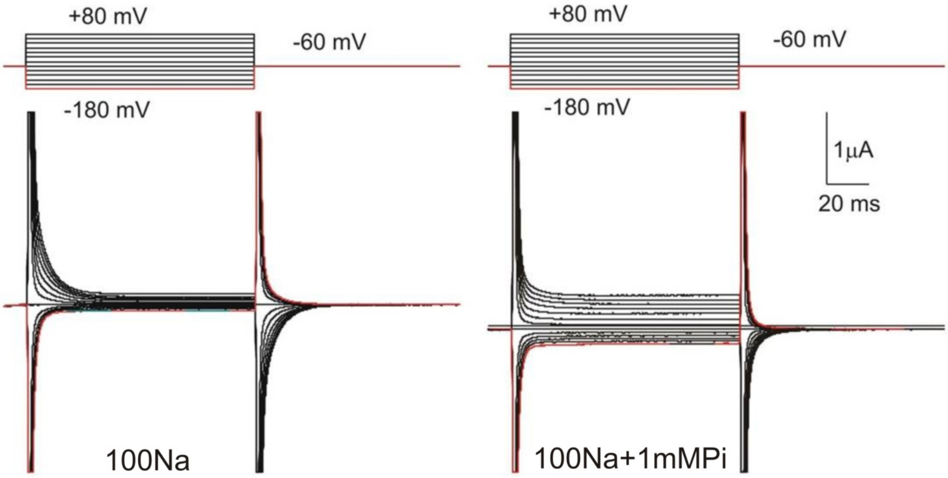

Figure 20 Representative current recorded form *X. laevis* oocyte expressing flounder NaPi-IIb. Left: currents recorded in presence of 100 mM Na^+ (100Na) , **right:** currents recorded in presence of 100Na + 1mMPi.

The time constant of the exogenous relaxation and the number of charges that are involved in the cotransport cycle (*Figure 21*) can then be quantified. Analysis of the NaPi-II presteady-state relaxations can be summarized in terms of two graphical representations: the time constant (τ) and charge (Q) plotted as a function of membrane voltage, respectively.

The τ-V plot of the *Figure 21A* shows a strong dependence of the time constant of presteady-state currents on membrane voltage. This voltage dependence arises from transitions between conformational states that involve charges sensing the membrane potential: at very positive potentials, most of the transporters occupy state 0 (*Figure 18*), while at very negative potentials, state 3 (*Figure 18*) is occupied with the higher probability.

The Q-V (*Figure 21B*) data can be fitted with a single Boltzmann function:

$$Q(V)= Q_{max}/1+exp\ (V_{0.5}-V)ze/kT)+Q_{hyp} \qquad \text{(Eq. 1 from (Forster et al., 2012)}$$

where:

Q(V) is the charge displaced for a voltage step from a given holding potential to V;

z is the slope factor indicating the apparent valence for an equivalent charged entity that moves in the membrane electric field;

Q_{max} is the total charge displaced;

Q_{hyp} is the charge at the hyperpolarizing extreme;

$V_{0.5}$ is the voltage at 50% of the total charge has been displaced;

k, e, T have their usual meaning.

The Boltzmann model applied here assumes the system can be reduced to two states with a lumped effective charge that is displaced across a fraction of the transmembrane electric field. Although this can seem like a significant over-simplification, it helps to interpret the observed behavior in terms of a simple charge displacement system.

The parameters $V_{0.5}$ and z can be used to compare the voltage-dependent behavior under different superfusion conditions and between isoforms as well as mutants.

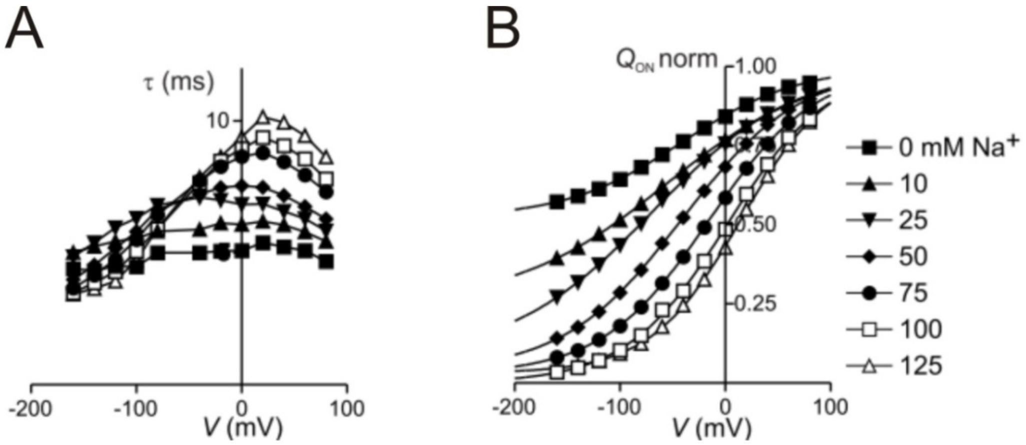

Figure 21 Time constant and charge movements obtained from analysis of presteady-state current under different superfusion conditions. A. voltage dependence of the main relaxation time constant (τ) as a function of the different Na^+ concentrations. **B.** Corresponding voltage dependence of the on-charge (Q_{on}) associated with the main relaxation component plotted for different Na^+ concentrations. Continuous lines are fits with eq. 1. From Forster et al., 2012.

Transport kinetics of NaPi-IIc

The isoform NaPi-IIc was cloned in 2002 by the Miyamoto group (Segawa et al., 2002). NaPi-IIc is the unique isoform of the NaPi-II family for it is electroneutral, with a Na:P_i stochiometry of 2:1 (Bacconi et al., 2005). Moreover, *Xenopus* oocytes expressing functional NaPi-IIc do not show presteady-state relaxations, this can be explained by the absence of voltage-dependent partial reactions that contribute to its transport cycle. The absence of presteady-state currents represent, also, a first hint of a different sodium binding phenomenon compared with the electrogenic isoforms. Uptake, efflux and voltage clamp fluorometry experiments have allowed elucidation of this difference (Ghezzi et al., 2009). Three sodium ions can interact with the electroneutral isoform NaPi-IIc but, in contrast to the electrogenic isoforms, only two sodium ions can be translocated inside the cell; the first sodium act as catalyst for the subsequent partial reactions (Figure 22). The apparent substrate affinities for NaPi-IIc are similar to NaPi-IIa/b and this suggests that all three isoforms share the same common substrate recognition elements.

At the primary structure level, the main difference between the electrogenic and electroneutral isoform appears to be the presence of a negative charged amino acid (aspartic acid) that in the electrogenic isoform would favor the first sodium interaction and promote the outward open conformation after the release of all substrate in the cytosol (*Figure 22*). Amino acid sequence analysis between the three different NaPi-II isoforms reveal an high degree of similarity, in support of the similar transport kinetics among isoforms. The study conducted by our laboratory (Bacconi et al., 2005) reported that the electrogenicity of NaPi-IIc could be restored by replacing of three conserved amino acids, found in all electrogenic isoforms, at corresponding sites in NaPi-IIc (S189A, S191A, and G195D). The Na^+:P_i stoichiometry of this engineered electrogenic construct (AAD-IIc) increased from 2:1 to 3:1 and the presteady-state current were detected. Accompanying this fundamental functional change, AAD-IIc also showed a different behaviour from the wild-type electrogenic NaPi-IIa/b, specifically a reduced apparent P_i affinity and different presteady-state kinetics (Bacconi et al., 2005).

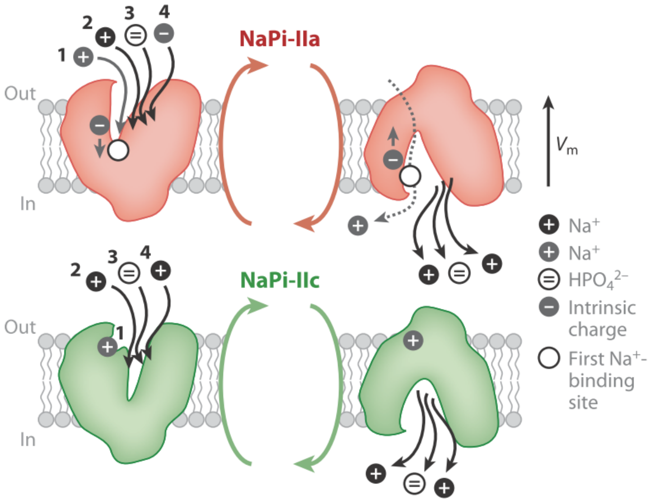

Figure 22 Cartoon of substrate interaction with the electrogenic isoform NaPi-IIa and the electroneutral isoform NaPi-IIc. For the electrogenic NaPi-IIa, an intrinsic negative charge (proposed to be an aspartic acid) confers voltage dependence to the transport cycle. This allows the binding of the first Na+ ion and his subsequent translocation together with the other substrates, giving a 3:1 Na^+: Pi stoichiometry (left and upper part). All substrates are released to the cytosol, the intrinsic charge senses the transmembrane field, leading to a voltage-dependent reorientation of the empty carrier (upper right). Electroneutral NaPi-IIc, which contains a conserved glycine at the same site, binds one Na^+ ion, like NaPi-IIa, but this ion is not translocated, giving the 2:1 Na^+: Pi transport stoichiometry. Modified from Biber et al., 2013.

Structure and binding sites

Unfortunately, the crystallized structure of homologs of NaPi-II is not yet available; however, it is reasonable to think that it should have similar structure to the other sodium-dependent transporters. Without experimental structure data available, we must rely on homology modeling to obtain a 3D view of NaPi-II; this is a multi-step process in which the first step is represented by the research of modeling template obtained usually performing a BLAST or PSI-BLAST search against the Protein Data Bank (PDB). Before 2012, an adequate template for NaPi-II was unavailable. Despite this limitation, investigating the structural properties of NaPi-II has remained an active field and different techniques have been used for that purpose. For example, the combination of molecular biology and electrophysiological assays was used to identify amino acids with structural and functional relevance. Moreover, a topological model of NaPi-II was solved by combining combination of bioinformatics methods and functional validation. Different algorithms predict 8–12 transmembrane domains (TMDs) and experimental evidence confirmed the intracellular orientation of both N- and C-termini and the presence of a large hydrophilic extracellular loop between the 5-6 TMDs (Radanovic et al., 2006) (*Figure 23*), in this loop a disulfide bridge was found that helps to stabilize the structure (Lambert et al., 2000).

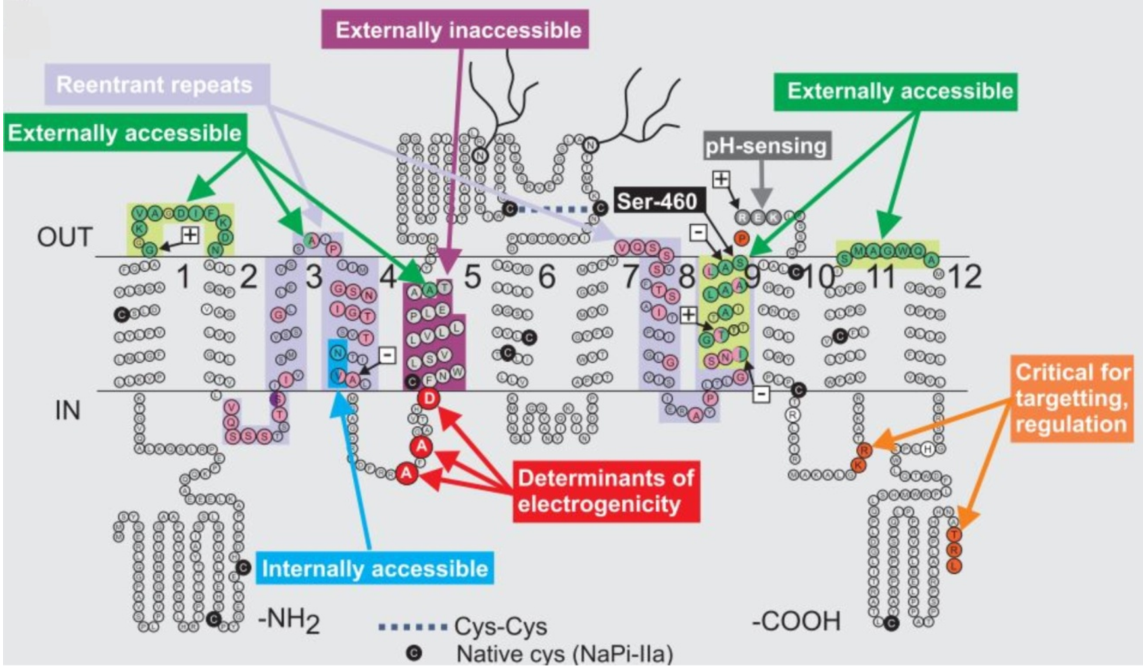

Figure 23 Topology model based on rat NaPi-IIa sequence. The model was drawn using TOPO2 software(http://www.sacs.ucsf.edu/TOPO/topo.html). Enlarged symbols indicate sites of significant structure–function importance. *Pink*: Identical residues in the re-entrant repeats; *green*: sites when mutated to a Cys that are externally accessible; *blue*: sites when mutated to a cysteine that are internally accessible; *purple*: sites externally inaccessible; *red*: sites critical for electrogenicity; *orange*: sites important for regulation and targeting; *black*: native Cys; *grey*: determinants of pH dependence. An essential disulfide bridge in the large extracellular loop is indicated (*dashed line*). From Forster et al.,2012.

The topological model was experimentally confirmed mainly using biochemical and biophysical studies. Epitope labeling revealed intracellular location for the NH_2- and COOH-termini (Lambert et al., 1999). The substituted cysteine accessibility method (SCAM) was used to estimate degree of accessibility for extracellular linkers (Lambert et al., 2001; Ehnes et al., 2004b), to identify functional important sites (Köhler et al., 2002a, 2003; Ehnes et al., 2004a) and to predict an α-helical organization for the transmembrane segment 9 (Lambert et al., 2001).

SCAM is used for mapping the intracellular and extracellular accessible sites and can also give information about the importance of specific sites for the protein function. The basic SCAM protocol requires mutating, one by one, different amino acid residues to a cysteine, then the protein is expressed in a model system and the substituted cysteine is labeled with methanethiosulfonate (MTS) functionalized compounds. The cysteine modification often causes an alteration of the functionality of the protein such as an impairment of transport activity; exposing the cotransporter to a fixed and moderate concentration of MTS reagent for different periods allows the loss of activity to be followed that reflects the number of modified proteins. By plotting the transport current against the cumulative time of exposure to the MTS reagent and fitting the line with a single decay exponential function it is possible to obtained the rate of cysteine modification (Karlin and Akabas, 1998). This procedure assumes that the reaction can be reduced to a 1st order system. By comparing the modification rates for different substitution sites, their relative accessibility to the medium can be derived.

There are two possible ways to test the function alteration of the proteins: the radioactive transport assay and the real time electrophysiological measurement. To compare the apparent reaction rate of different mutants, it is important to fix the conditions of the assay to define the state occupancy of the protein. Radioactive tracer transport assays as used, for example, in SCAM studies of the serotonin transporter (SERT) (Chen et al., 1997)) and the glutamate transporter (EAAT) (Leighton et al., 2002) have the disadvantage of not allowing straightforward control of the voltage membrane and this could lead to errors in the reaction rate estimation. In contrast, for electrogenic transporters, the reaction can be followed in real time and with controlled membrane potential. All the SCAM investigations carried on NaPi-IIa/b have used the real-time electrophysiological measurement.

Further studies using Cu-phenanthroline to induce a disulfide bridge formation have revealed two other important regions in the topology of NaPi-II comprising two reentrant repeats that share a sequence identity of more that 30%; these domains are localized between TMDs 3-4 and TMDs 8-9, they contain critical sites for the determination of voltage dependence and substrate interaction. The results of these studies support the hypothesis of a structural similarity between all members of the NaPi-II family (Ghezzi et al., 2011).

Without a crystal structure or a homology model for NaPi-II, it is difficult to localize precisely the binding site of sodium and phosphate. Based on information obtained from the same family of sodium-dependent cotransporters it is possible hypothesize the location of binding sites in the discontinuous helices. Moreover, analysis of mutagenesis has allowed validation of the importance of certain amino acids for substrate coordination and the transport function, for example, site S448 in NaPi-IIb (Virkki et al., 2006b) and the corresponding sites in NaPi-IIa (S460) (Lambert 1999) and NaPi-IIc (S437) (Ghezzi 2009).

Transport dynamics

The first study analyzing the transport dynamics of NaPi-II proteins involved the investigation of the fluorescence changes (ΔF) for the fNaPi-IIb mutant, S448C (Virkki et al., 2006b). This site was chosen based on previous cysteine mutagenesis studies on the rat NaPi-IIa isoform in which site Ser-460 was identified as being functionally important (Lambert et al., 1999). After fluorophore labeling, S448C showed a suppression of P_i-induced current, indicating an incomplete transport cycle and confirmed the previously documented phenotype (Lambert et al., 1999). However, oocytes expressing S448C gave steady-state fluorescence emissions that were dependent on membrane potential and substrate (Na^+ and P_i). These data indicated that substrates could still interact with the protein despite its inability to cotransport P_i. Moreover, the dependence of fluorescence quenching could be fitted with the Hill equation: for changes in Na^+ concentration a Hill coefficient (n_H) of 1.8 and for changes in P_i concentration n_H was close to unity. These data were interpreted as a further indication of the ability of this mutant to interact with 2 Na^+ and 1 P_i, and as an indication of the ability of the fluorophore's microenvironment to sense substrate interactions.

As previously discussed (page 17), the presteady-state charge movements provide an indirect measure of the global voltage-dependent conformational changes of the protein, in contrast, ΔF reports local conformational changes of the protein. To investigate if the kinetics of charge movements were reflected in the time course of the fluorescence signal a comparison was done for the S448C mutant by plotting parametrically one time constant against the other. A direct correlation was found between these two parameters only over a limited potential range ($V > -40$ mV) and in the presence of external Na^+ ions (*Figure 24*). These data suggest that the fluorophore can detect large transitions occurring between that inward-facing conformation (state 0, *Figure 18*) and the conformations relative to the binding of sodium (state 2 or 3, *Figure 18*) (Virkki et al., 2006b). A more detailed interpretation of the relative level of fluorescence intensity in different conformational states can be obtained using simulated fluorescence with a kinetic model (see Discussion).

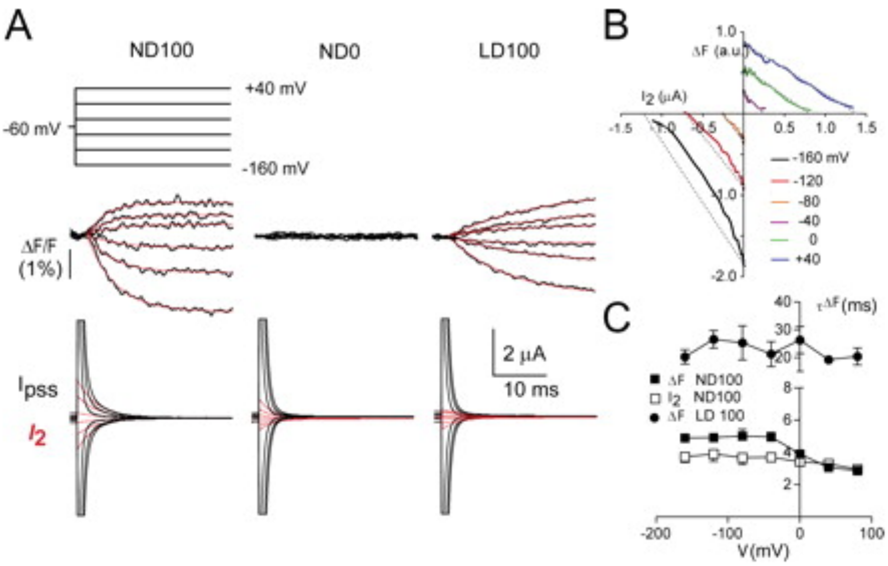

Figure 24 Presteady-state charge movements and fluorescence. (A) Simultaneous recordings of percent change in fluorescence (Δ*F/F*) for a representative oocyte in response to the voltage step protocol as shown, for superfusion in full Na^+ (ND100), choline replacement (ND0), and Li^+ replacement (LD100) and corresponding presteady-state currents (I_{pss}, black traces). For I_{pss}, the records were fit with a double decaying exponential and the main component (I_2 assumed to be S448C-related is shown superimposed, red traces). For the Δ*F/F* records, the data were fit with a single growing exponential, shown superimposed on each trace (red traces). Recording bandwidth was 500 Hz for I_{pss} and Δ*F/F*. Baseline adjustment was performed for I_{pss}. (B) Parametric plot of Δ*F/F* against I_2 as a function of time for the cell in A at the indicated test potentials. Dotted lines indicate deviations from linear behavior for hyperpolarizing potentials. (C) Voltage dependency of the time constants associated with the decay of I_2 (ND100) and time-dependent phase of Δ*F/F* (ND100, LD100). Note that the ordinate scale covers two ranges. Data pooled from *n* = 5 cells. From Virkki et al., 2006b.

Subsequently, the VCF technique was applied on NaPi-IIb mutants expressed in *X. laevis* oocytes to create a map of the conformational changes that occur in different regions of the protein during the transport cycle. The fluorescence changes of four sites (Ser-155, Ser226, Gln-319, Glu-451) of NaPi-IIb were investigated under different conditions. Fluorescence was recorded in presence of different substrates in the extracellular solution and for different membrane voltages. For mutants S155C and S226C, membrane depolarization causes an increase in the fluorescence intensity whereas for mutants Q319C and E415C it causes a decrease (*Figure* 25). These results permitted characterization of the substrate and voltage-dependent conformational changes associated with specific partial reactions, a complementary Δ*F* obtained for the different sites suggested that two parts of the protein experience complementary and opposite rearrangements for the same change in membrane voltage (Virkki et al., 2006a).

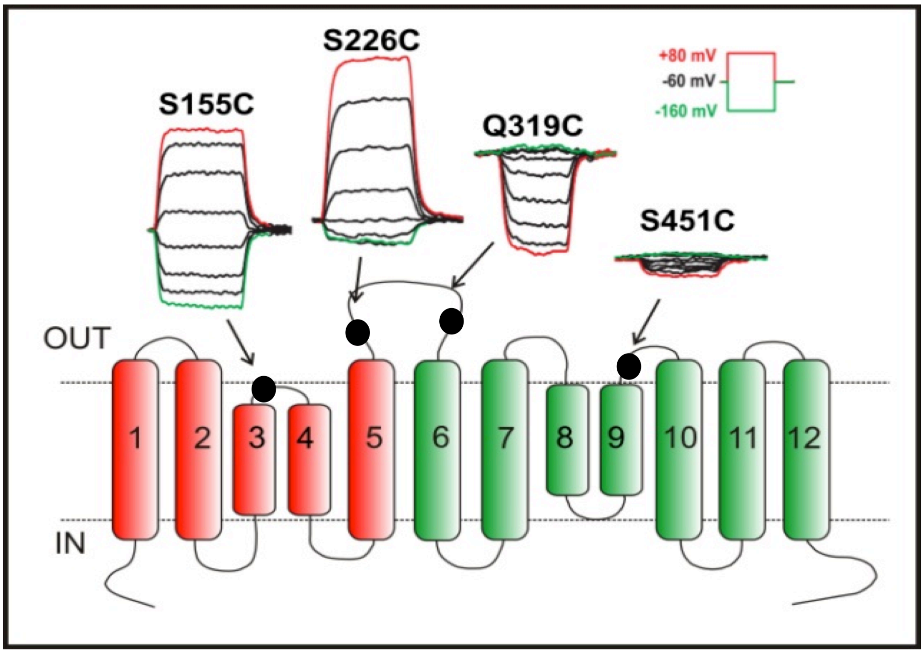

Figure 25 Complementary fluorescence changes observed in two parts of NaPi-II. Topological scheme of flNaPi-IIb isoform shows the localization of the cysteines for mutants S155C, S226C, Q319 and E451C. The original F-V recordings made for the corresponding mutant in presence of 100 mM Na^+ in the extracellular solution in response to the change in the membrane potential. From Virkki et al., 2006a.

OPEN QUESTIONS

At the start of my dissertation, a number of aspects of the structure-function relationships of NaPi-II were still unresolved and three of them were addressed during the dissertation period:

1) Investigation of the internal substrate release steps.

2) Construction of a homology model of NaPi-II

3) Characterization of the cotransport dynamics

Investigation of the internal substrate release steps

From the numerous experiments conducted using *X. laevis* oocytes expressing NaPi-II, it was possible to characterize the extracellular conformational states that allow the binding with the substrate and co-substrates. For all NaPi-II isoforms, it was established that two sodium ions bind before the P_i interaction, followed by a third sodium ion before translocation. However, knowledge about the release of the substrates and co-substrate in the intracellular environment is limited. An obvious approach would be to modulate the intracellular concentrations of substrate and co-substrate in the oocytes and to study their influence in the transport kinetic. This approach cannot be investigated with the standard two electrode voltage clamp that does not allow ready exchange of cytosolic contents. Possible methods that could be applied include the cut-open oocyte voltage clamp technique and whole cell patch clamp.

Construction of an homology model of NaPi-II

The lack of a resolved crystal structure of NaPi-II or its bacterial homologs has prevented defining the location of the sodium and phosphate binding sites or even to identify specific protein conformations. Furthermore, the low sequence and structural identity between NaPi-II and the other sodium-dependent cotransporters with resolved 3D structures has prevented pursuing homology modeling strategies with reasonable confidence.

In addition, to furthering our general knowledge of the transport mechanism, having a 3D structure could help in the design of specific inhibitors with large clinical potential in cases of compromised P_i handling such as end stage renal disease.

Characterization of the cotransport dynamics

The 3D structures obtained from crystallisation and homology modelling strategies provide a static image of one conformational state, and quite likely give a limited, non-physiological view of the protein when considering the conditions necessary to obtain diffracting crystals. NaPi-II is a cotransporter and its function is tightly connected to the conformational states that it must undergo for the transport to occur. The elucidation of its transport dynamics-how the molecule behaves under physiological conditions during the transport cycle- is then crucial to understand the transport mechanism at the molecular level.

METHODS AND RESULTS

Methods

Methods used:

- Single point mutagenesis
- Two electrode voltage clamp (TEVC)
- Radiotracer uptake
- Voltage clamp fluorometry (VCF)
- Substituted cysteine accessibility method (SCAM)

PUBLICATIONS THAT CONTRIBUTE TO THIS WORK

A. Conferring electrogenicity to the electroneutral phosphate cotransporter NaPi-IIc (SLC34A3) reveals an internal cation release step. (published (Patti et al., 2013))

B. Structural model of the human Na^+-phosphate cotransporter NaPi-II. (under review)

C. Correlating charge movements with local conformational changes of a Na^+-coupled cotransporter (ready for submission)

A. Conferring electrogenicity to the electroneutral phosphate cotransporter Napi-IIc (SLC34A3) reveals an internal cation release step.

This section contains the original research article published in the European Journal of Physiology (Pflügers Archiv) (Patti et al., 2013)

The aim of this project was to investigate partial reactions that confer the unique properties of mutant of NaPi-IIc (AAD-IIc). By studying the kinetics of an electrogenic mutant AAD-IIc we were able to identify the internal sodium release step during the transport cycle of NaPi-II. This was an unexpected finding and has led to greater insight into the cotransport cycle of NaPi-II proteins.

My contributions to this paper included performing of part of experiments involving the AAD-IIc mutants including voltage clamp fluorometry assay and performing uptake experiments using ^{32}Pi in Xenopus oocytes expressing the WT NaPi-IIc isoform at different temperature. I also performed data analysis, data interpretation and drafted the manuscript.

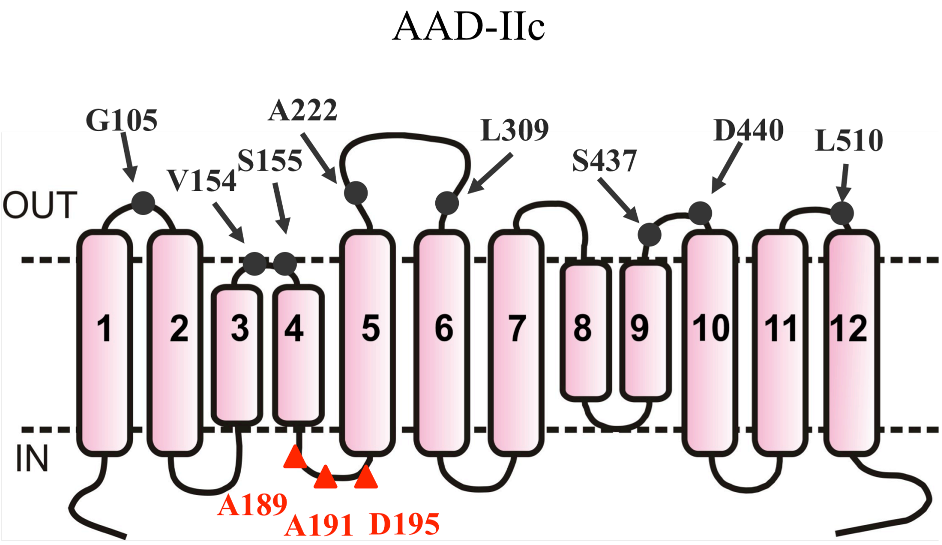

Figure 26 Secondary topology model of AAD-IIc showing the mutants investigated in this paper(black). Red triangles indicate the three critical sites for restoring electrogenicity to form the AAD-IIc construct.

Pflugers Arch - Eur J Physiol
DOI 10.1007/s00424-013-1261-9

ION CHANNELS, RECEPTORS AND TRANSPORTERS

Conferring electrogenicity to the electroneutral phosphate cotransporter NaPi-IIc (SLC34A3) reveals an internal cation release step

Monica Patti · Chiara Ghezzi · Ian C. Forster

Received: 19 December 2012 / Revised: 14 February 2013 / Accepted: 4 March 2013

Abstract The SLC34 family of Na^+-dependent inorganic phosphate cotransporters comprises two electrogenic isoforms (NaPi-IIa, NaPi-IIb) and an electroneutral isoform (NaPi-IIc). Both fulfill essential physiological roles in mammalian phosphate homeostasis. By substitution of three conserved amino acids, found in all electrogenic isoforms, at corresponding sites in NaPi-IIc, electrogenicity was re-established and the Na^+/P_i stoichiometry increased from 2:1 to 3:1. However, this engineered electrogenic construct (AAD-IIc) had a reduced apparent P_i affinity and different presteady-state kinetics from the wild-type NaPi-IIa/b. We investigated AAD-IIc using electrophysiology and voltage clamp fluorometry to elucidate the compromised behavior. The activation energy for cotransport was threefold higher than for NaPi-IIc and 1.5-fold higher than for NaPi-IIa and the temperature dependence of presteady-state charge displacements suggested that the large activation energy was associated with the empty carrier reorientation. AAD-IIc shows a weak interaction of external Na^+ ions with the electric field, and thus retains the electroneutral cooperative interaction of two Na^+ ions preceding external P_i binding of NaPi-IIc. Most of the presteady-state charge movement was accounted for by the empty carrier (in the absence of external P_i), and the cytosolic release of one Na^+ ion (in the presence of P_i). Simulations using a kinetic model recapitulated the presteady-state and steady-state behavior and allowed identification of two critical partial reactions: the final release of Na^+ to the cytosol and external P_i binding. Fluorometric recordings from AAD-IIc mutants with Cys substituted at functionally important sites established that AAD-IIc undergoes substrate- and voltage-dependent conformational changes that correlated qualitatively with its presteady-state kinetics.

Keywords Phosphate cotransport · Electrophysiology · Voltage clamp fluorometry · Presteady state · Steady state · Activation energy

Introduction

Type II sodium/phosphate cotransporters (NaPi-II) catalyze transport of inorganic phosphate (P_i) using the transmembrane Na^+ electrochemical gradient. They belong to the SLC34 family of solute carriers (www.bioparadigms.com) [15] that preferentially transport divalent P_i (HPO_4^{2-}) [17]. The family comprises three isoforms to which all currently identified members have been assigned according to their genetic pedigree, molecular features, and tissue localization: the electrogenic NaPi-IIa and electroneutral NaPi-IIc are localized exclusively in the renal proximal tubule and the electrogenic NaPi-IIb is expressed in nonrenal, epithelial-like tissues. The difference between the electrogenic and electroneutral isoforms is reflected in their Na^+–P_i cotransport stoichiometries: NaPi-IIa,b (SLC34A1, A2) have a 3:1 stoichiometry [17] and translocate one net charge per transport cycle; NaPi-IIc (SLC34A3) has a 2:1 stoichiometry with no detectable net charge translocation. The electrogenic and electroneutral cotransport mechanisms can be understood in terms of a kinetic scheme (Fig. 1a) that describes their respective transport cycles as an ordered sequence of partial reactions, some of which have been identified experimentally. For example, electrogenicity can be accounted for by assigning charge displacement to the empty carrier (0↔1) together with extra- and

---

Monica Patti and Chiara Ghezzi contributed equally to this work.

M. Patti · C. Ghezzi · I. C. Forster (✉)
Institute of Physiology and Zurich Center for Integrative Human Physiology (ZIHP), University of Zurich, Winterthurerstrasse 190, 8057 Zurich, Switzerland
e-mail: iforster@access.uzh.ch

intracellular interactions of one Na^+ ion (1↔2, 0↔9) [2, 13, 19]. This cation is postulated to account for the uncoupled leak [2]. To reconcile this model with electroneutral cotransport mediated by SLC34A3 (NaPi-IIc), the scheme was modified (*shaded area*, Fig. 1a), based on the interpretation of fluorometric assays [20]. For NaPi-IIc, 2 Na^+ ions are assumed to interact with the protein before P_i, but unlike NaPi-IIa/b, only one of these cations contributes to net transport. We postulated that the first Na^+ ion to interact with NaPi-IIc acts as a "catalytic activator" for cotransport [20] that gives rise to cooperative binding of a 2nd Na^+ ion before P_i binds (2↔3). This first Na^+ ion would remain bound during the cotransport cycle, but contributes neither to net coupled transport nor leak, which in the case of NaPi-IIc is undetectable [4]. Thus, for the electrogenic isoforms both leak and cotransport modes involve the translocation of one net positive charge between the external and internal milieus, and both involve an electroneutral intrinsic translocation of substrate (transitions 2↔9 and 5↔6, respectively).

Apart from electrogenicity and leak, other kinetic properties (apparent substrate affinities, pH dependence) are essentially the same for the electrogenic and electroneutral isoforms [13, 31, 33]. These common functional properties accord with the finding that SLC34 proteins display an overall amino acid similarity of ≈57 %. This is even greater in the predicted transmembrane domain regions [36] and therefore all isoforms most likely share a common 3-D structure. The current lack of a 3-D structure and apparent absence of homology with membrane transport proteins with resolved structures has necessitated using indirect approaches (mutagenesis, cysteine scanning, and crosslinking) to determine the structure–function relationships [16, 19, 20].

It is noteworthy that small differences in the amino acid sequence in SLC34 proteins can lead to significant functional changes in pH sensitivity [9] and electrogenicity [4]. In the latter case, we identified a trio of amino acids (Ala-218, Ala-220, Asp-224, mouse NaPi-IIa sequence numbering), located in a putative linker region between two predicted α-helical transmembrane domains (TMD4 and 5, Fig. 1b), which were shown to be critical for electrogenic behavior. A comparison of the sequences of the electrogenic isoforms from a number of species reveals that the Ala-Ala-Asp trio is conserved. In the electroneutral isoforms, these are replaced with a Ser-Ser-Gly trio (Fig. 1b, inset). If the Ala-Ala-Asp trio was substituted at the equivalent sites in the electroneutral NaPi-IIc (Ser-189, Ser-191, Gly-195) electrogenicity was re-established, as evidenced by robust P_i-induced steady-state currents, presteady-state relaxations and the predicted 3:1 stoichiometry [4], all of which are hallmarks of electrogenic SLC34 proteins. Moreover, the replacement of the critical aspartic acid in NaPi-IIa with a glycine resulted in electroneutral cotransport [32]. However, the molecular engineering of NaPi-IIc resulted in compromised cotransport kinetics. The modified protein (hereafter referred to as AAD-IIc) showed a >200-fold reduced apparent affinity for P_i: the Michaelis constant ($K_{0.5}{}^{Pi}$) was >1 mM (compared with ≈0.06 mM for NaPi-IIc), whereas for Na^+ activation (1 mM P_i), the apparent affinity constant ($K_{0.5}{}^{Na}$) ≈80 mM was only marginally affected (≈40 mM for NaPi-IIc) [19]. Furthermore, compared with other electrogenic isoforms, the presteady-state charge movements appeared to show little dependence on external [Na^+] (e.g., [2, 33]). These deviations from expected behavior suggested that other differences in the respective amino acid sequences were also important determinants of the AAD-IIc kinetic profile.

This study focuses on the identification of partial reactions in the SLC34 cotransport cycle (Fig. 1a) that confer the unique behavior of AAD-IIc. By combining presteady-state analysis and voltage clamp fluorometry (VCF) under conditions where the state occupancy of AAD-IIc can be readily defined, we could relate these partial reactions to specific voltage- and substrate-dependent conformational changes of the protein. Our findings offer new insights into how membrane voltage is transduced by cation-driven transporters and provide compelling evidence that the final step in substrate release to the cytosol involves the release of a single Na^+ ion.

Methods

Solutions and reagents

Standard extracellular solution (100Na) contained (in millimolar): 100 NaCl, 2 KCl, 1.0 $MgCl_2$, 1.8 $CaCl_2$, 10 HEPES, pH 7.4 adjusted with TRIS base. In Na^+ substitution experiments, NaCl was equimolarly replaced with choline Cl (100Ch) and solutions with intermediate [Na^+] were obtained by mixing 100Na with 100Ch in appropriate portions to maintain a constant molarity. P_i was added from a 1 M K_2HPO_4/KH_2PO_4 stock premixed to give pH 7.4. Modified Barth's solution for storing oocytes contained (in in millimolar): 88 NaCl, 1 KCl, 0.41 $CaCl_2$, 0.82 $MgSO_4$, 2.5 $NaHCO_3$, 2 $Ca(NO_3)_2$, 7.5 HEPES, pH 7.5 adjusted with Tris and supplemented with 5 mg/l doxycyclin and 5 mg/l gentamicin. All standard reagents were obtained from either Sigma-Aldrich or Fluka (Buchs, Switzerland). 2-(Trimethylammonium) ethylmethanethiosulfonate bromide (MTSET) and 2-aminoethyl methanethiosulfonate (MTSEA) were obtained from Toronto Research Chemicals or Biotium (USA); 2-((5(6)-tetramethylrhodamine)carboxylamino) ethyl methanethiosulfonate (MTS-TAMRA) was obtained from Biotium (USA).

Site-directed mutagnesis and cRNA preparation

cDNA encoding wild-type (WT) mouse NaPi-IIc (GenBank/EMBL/DDBJ accession n. AB054999) was subcloned into a plasmid (pT7T3D-Pac, a kind gift from K.-I. Miyamoto,

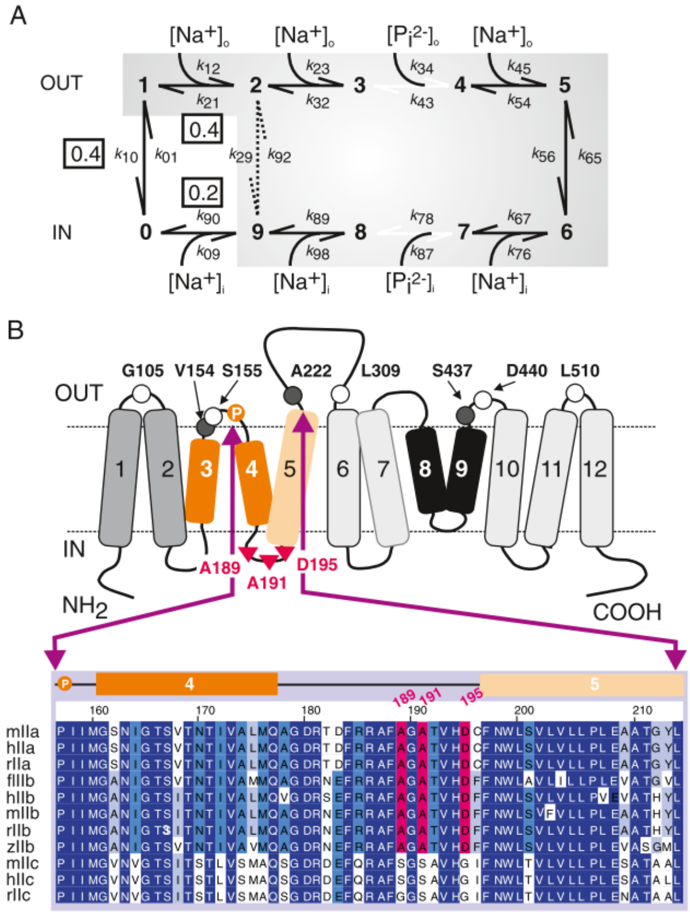

```
mIIa  PIIMGSNIGTSVTNTIVALMQAGDRTDFRRAFAGATVHDCFNWLSVLVLLPLEAATGYL
hIIa  PIIMGSNIGTSVTNTIVALMQAGDRTDFRRAFAGATVHDCFNWLSVLVLLPLEAATGYL
rIIa  PIIMGSNIGTSVTNTIVALMQAGDRTDFRRAFAGATVHDCFNWLSVLVLLPLEAATGYL
fIIIb PIIMGANIGTSVTNTIVAMMQAGDRNEFRRAFAGATVHDFFNWLAVLILLPLEVATGVL
hIIb  PIIMGANIGTSITNTIVALMQVGDRSEFRRAFAGATVHDFFNWLSVLVLLPVEVATHYL
mIIb  PIIMGANIGTSITNTIVALMQAGDRNEFRRAFAGATVHDFFNWLSVFVLLPLEAATHYL
rIIb  PIIMGANIGTSITNTIVALMQAGDRNEFRRAFAGATVHDFFNWLSVLVLLPLEAATHYL
zIIb  PIIMGANIGTSVTNTIVAVMQAGDRNEFRRAFAGATVHDFFNWLSVLVLLPLEVASGML
mIIc  PIIMGVNVGTSITSTLVSMAQSGDRDEFQRAFSGSAVHGIFNWLTVLVLLPLESATAAL
hIIc  PIIMGVNVGTSITSTLVSMAQSGDRDEFQRAFSGSAVHGIFNWLTVLVLLPLESATALL
rIIc  PIIMGVNVGTSITSTLVSMAQSGDRDEFQRAFGGSAVHGIFNWLTVLVLLPLENATAAL
```

Fig. 1 SLC34 protein structure-function background. **a** A 10-state kinetic scheme for SLC34 proteins describes the electrogenic transport cycle. *Shaded* states and associated transitions are postulated to be occur in the electroneutral NaPi-IIc transport cycle (see [20]). *Boxed values* indicate effective valence associated with three partial reactions for the electrogenic NaPi-IIa/b. Transition (2↔9) accounts for uncoupled Na^+ leak (see [1]). The empty carrier is assumed to occupy one of two states ("inward" or "outward" oriented), transitions between which involve the movement of an equivalent $0.4e^-$ across the transmembrane electric field. Hyperpolarizing potentials increase the probability of occupancy of state 1, which allows the sequential binding of two Na^+ ions to their respective binding sites within the transmembrane electric field and is equivalent to $0.4e^-$ moving across the transmembrane electric field. This is followed by binding of HPO_4^{2-} and a third Na^+ to form an electroneutral complex followed by substrate translocation. Substrate release to the cytosol is also assumed to be ordered. The final release of the third Na^+ ion is modeled as a weakly voltage dependent ($0.2e^-$ equivalent charge) transition that leaves the protein in an "inward" oriented empty carrier state (state 0) and a reorientation to state 1 occurs under the influence of the transmembrane electric field. **b** Secondary topology model showing the three sites in NaPi-IIc critical for restoring electrogenicity to form the AAD-IIc construct (*triangles*). For Cys mutagenesis of AAD-IIc, cysteines were substituted individually at sites predicted to be externally accessible (*circles*). Sites that were labeled with a fluorophore, as evidenced by resolvable voltage-dependent changes in fluorescence, are indicated (*filled circles*). Sites were selected to correspond to previous data obtained from Cys mutagenesis studies of SLC34 isoforms (see Table 1). Inset shows the sequence alignment for the indicated region to emphasize the high degree of identity in the predicted transmembrane domain regions and the lack of charge at site 195 for the electroneutral NaPi-IIc. Abbreviations for species prefixes: *f* flounder, *h* human, *m* mouse, *r* rat, *z* zebra fish. Numbering according to mouse NaPi-IIc sequence

Tokushima University, Tokushima, Japan). Novel cysteines were introduced using the Quickchange site-directed mutagenesis kit (Stratagene Inc., La Jolla, CA, USA) into the AAD-IIc protein at the following sites according to the mouse NaPi-IIc sequence numbering (new mutant name in parenthesis): Gly-105 (AAD-IIc-105), Val-154 (AAD-IIc-154), Ser-155 (AAD-IIc-155), Ala-222 (AAD-IIc-222), Leu-309 (AAD-IIc-309), Ser-437 (AAD-IIc-437), Asp-440 (AAD-IIc-440), and Leu-510 (AAD-IIc-510). The sequence was verified by sequencing (Microsynth, Switzerland), linearized with *NotI* and cRNA was synthesized in the presence of Cap analog using the T7 Message Machine kit (Ambion, Inc., Austin, TX, USA).

Expression in *Xenopus laevis* oocytes

Female *X. laevis* frogs were purchased from *Xenopus* Express (France). Portions of ovaries were surgically removed from frogs anesthetized in MS222 (tricaine methansulphonate) and cut in small pieces. Oocytes were treated for 45 min with collagenase (crude type 1A) 1 mg/ml in 100Na solution (without Ca^{2+}) in presence of 0.1 mg/ml trypsin inhibitor type III-O. Healthy stage V-VI oocytes were selected, maintained in modified Barth's solution at 16 °C, and injected with 10 ng of cRNA. Experiments were performed 4–7 days after injection. All animal procedures were conducted in accordance with the Swiss Cantonal and Federal legislation relating to animal experimentation.

Two-electrode voltage clamp

All voltage clamp experiments were performed using a two-electrode voltage clamp (TEC-10CX, NPI, Tamm, Germany). Oocytes were impaled with microelectrodes filled with 3 M KCl, with a typical resistance of <1 MΩ [13, 18]. The temperature of the recording chamber was monitored using a thermistor probe (TS-2, NPI, Tamm, Germany) placed close to the oocyte. The temperature of the recording chamber and incoming superfusate were regulated using Peltier cooling elements driven by a continuous feedback controller (TC-10, NPI Tamm, Germany). Data acquisition was performed using a 1440 Digidata (Molecular Devices Corp, USA). For recordings at constant holding potential, currents were acquired at >20 samples/s and filtered at 10 Hz. Faster sampling rates (up to 20 k samples/s) were used for voltage step recordings with filtering (digital and analog) adjusted accordingly.

Steady-state currents were obtained using a protocol in which membrane voltage steps were made from the holding potential (V_h)=−60 mV, to test voltages in the range −180 to +80 mV in 20 mV increments. The steady-state P_i-dependent current (I_{Pi}) was obtained by subtracting control traces (in 100Na solution) from the corresponding traces in the presence of P_i. The current was measured in a region where all presteady-state relaxations were completed. Data was rejected if contaminated by endogenous Cl^- currents. Steady state P_i activation was determined by varying the P_i concentration in presence of 100Na and subtracting the respective currents in 100Na from those in 100Na+P_i. I_{Pi} were fit with a form of the modified Hill equation:

$$I_{Pi} = I_{Pi}^{\max}\left([S]^{n_H} / \left([S]^{n_H} + \left(K_{0.5}^{S}\right)^{n_H}\right)\right) + K \tag{1}$$

where $[S]$ is the concentration of variable substrate (Na^+ or P_i), $I_{\mathrm{Pi}}^{\max}$ is the maximum electrogenic activity, $K_{0.5}^{S}$ is the apparent affinity constant for substrate S, n_{H} is the Hill coefficient and K is a constant that take in account of uncoupled leak effects [10]. For P_i activation, the Michaelian form of Eq. 1 was used with n_{H}=1.

Pre-steady state relaxations were recorded using a similar voltage step protocol as for the steady-state assay with steps from V_h=−60 or 0 mV, as indicated, to test voltages in the range of −180 to +80 mV in 20 mV increments. The pulse period and period after return to the holding potential was chosen to ensure that relaxations were completed within the recording time window. Signal averaging (typically fourfold) was used to reduce noise. Relaxations were quantified by fitting with one or two component exponential functions unless otherwise noted, commencing the fit approximately 5 ms after the ON or OFF step onset to ensure that endogenous charging components had reached a steady-state. The fits were back-extrapolated to a time point 2 ms after the step onset, at which approximately 90 % of the membrane was charged. The fits were numerically integrated to obtain the charge moved (Q) for a step from the holding potential to the test potential. The Q–V data were fitted with a Boltzmann function of the form given by:

$$Q = Q_{hyp} + Q_{\max}/1 + \exp(ze(V_{0.5} - V)/kT)) \tag{2}$$

where $V_{0.5}$ is the voltage at which the charge is distributed equally between two hypothetical states, z is the apparent valence of an equivalent charge that moves through the whole of the membrane field, $Q_{\max}$ is the total mobile charge available, Q_{hyp} is the charge of the hyperpolarizing limit and is a function of V_h, and e, k, and T have their usual meanings.

Determination of activation energy

The Arrhenius equation (e.g., [37]) was used for determining the temperature dependence of the transport kinetics:

$$k_r = A \exp\left(-\frac{E_a}{RT}\right) \tag{3a}$$

where k_{r} is the reaction rate (substrate-induced current or presteady-state current relaxation rate), A is a constant, R the gas constant, and E_{a} the activation energy (in kilocalorie per mole). Equation 3a can be recast in a logarithmic form:

$$\ln\ k_r = -(\mathrm{E_a/R})(1/\mathrm{T}) + \ln\ \mathrm{A} \tag{3b}$$

Linear regression analysis applied to the data plotted as ln k_{r} vs $1/T$ was used to estimate E_{a} from the slope.

^{32}P uptake

Oocytes (6–10 oocytes/group) were first allowed to equilibrate in 100Na solution without tracer. After aspiration of this solution, oocytes were incubated in 100Na solution containing 1 mM cold P_i and ^{32}P (specific activity 10 mCi/mmol P_i). Uptake proceeded for 10 min and then oocytes were washed three to four times with ice-cold 100Ch solution containing 2 mM P_i, and lysed individually in 10 % SDS for 1 h before addition of scintillation cocktail. The amount of radioactivity taken up by each oocyte was measured by scintillation counting. For temperature-dependence assays, individual oocytes were incubated in the uptake medium and held at the required temperature using a water bath cooling system.

Simultaneous voltage clamp and fluorometry

The apparatus for simultaneous VCF has been described in detail elsewhere [34, 35]. Cys mutants were labeled in 100Na in presence of MTS-TAMRA (0.4 mM) at room temperature for 4 min. Voltage-dependent changes in fluorescence intensity (ΔF) were determined using a voltage step protocol in which the membrane voltage was stepped from V_h=−60 mV to test potentials ranging between −200 and +200 mV in 40 mV increments for a duration of 100–200 ms, and averaged over 20–64 sweeps. Fluorescence signals were analog filtered (eight-pole Bessel) with a low-pass cutoff frequency chosen to optimize the signal-to-noise ratio (typically 500 Hz). ΔF was measured in 100Ch, XNa (where X represents the [Na$^+$] in millimolar, or 100Na +1P$_i$ (100 mM Na$^+$+1 mM P_i); each test substrate concentration application was bracketed with a control solution application (100Na) to allow for correction of a loss of fluorescence. After application of the superfusate, the oocyte was allowed to stabilize in the recording chamber for ~2 min and then fluorescence was recorded. Recordings were baseline corrected relative to the value at V_h=−60 mV. The data from single oocytes were corrected for photobleaching and then were normalized to the predicted maximum change in fluorescence ($\Delta F_{\max}$) recorded in 100Na and finally pooled. The ΔF–V data were described analytically by fitting with the Boltzmann equation (Eq. 2) to yield the maximum change in fluorescence intensity ($F_{\max}$), the midpoint voltage of the ΔF–V distribution ($V_{0.5}{}^{F}$) and a slope factor z^{F}.

Thiol modification by MTS reagents

MTSET (or MTSEA) was prepared from dry stock in water or DMSO to give 1 M stock solution in DMSO, which was kept at −20 °C until required and further diluted with water or DMSO to give 1,000:1 experimental stocks before and adding to 100Na solution to give a final concentration as indicated. MTSET was applied to the recording chamber with gravity feed via a 0.5-mm diameter cannula positioned near the cell. For normal labeling, the incubation time was 3 min and was followed by a 1 min washout period. For determining the apparent accessibility, the superfusion with MTSET was conducted for 1 min followed by washout. During incubation, oocytes were kept at V_h=−50 mV unless otherwise noted. After a 1 min washout, the current response to 1 mM P_i at V_h=−50 mV was again determined and the MTSET application was repeated. The fixed MTSET concentrations were chosen by pretesting to facilitate determination of the modification rate. The P_i-induced current remaining after each successive application of MTS reagent was measured and plotted as a function of the cumulative exposure time, normalized to the initial P_i-induced current. The data were fit with a single decaying exponential to determine the effective second order reaction constant using an equation of the form:

$$I_{\mathrm{Pi}}{}^{t} = \left(I_{\mathrm{Pi}}{}^{0} - \mathrm{I_{Pi}}{}^{\infty}\right)\exp\left(-\mathrm{ctk}^{*}\right) + I_{\mathrm{Pi}}{}^{\infty} \qquad (4)$$

where $I_{\mathrm{Pi}}{}^{t}$ is the P_i-induced current after a cumulative exposure time t, $I_{\mathrm{Pi}}{}^{0}$ is the initial P_i-induced current, $I_{\mathrm{Pi}}{}^{\infty}$ is the P_i-induced current at $t=\infty$, c is the concentration of MTS reagent (assumed to be in excess) and k^* is the effective second order rate constant, e.g., [22]. For some experiments as indicated, MTSEA was used instead of MTSET and gave the same results.

Software and data analysis

Simulations of a seven-state model describing electrogenic cotransport were performed using Berkeley Madonna V8.0.2a8 software (www.berkeleymadonna.com). Exponential curve fitting was performed using Clampfit software (Molecular Devices Corp) and subsequent nonlinear regression of data was performed using GraphPad Prism version 3.02/4.02 for Windows (GraphPad Software, San Diego, CA, USA; www.graphpad.com). Data points are shown as mean±SEM. Error bars are not displayed if smaller than symbol.

Results

Temperature dependence of steady-state and presteady-state kinetics

To identify partial reactions in the cotransport cycle that determine the unique behavior of AAD-IIc, we measured the temperature dependence of I_{Pi} and presteady-state relaxations. The rationale for these experiments was that if one or more partial reactions were influenced by the mutagenesis, the activation energy may differ from the WT.

At all membrane potentials (V) in the test range (−180 mV≤V≤+80 mV), I_{Pi} (100Na, 1 mM P_i) showed a strong temperature dependence, whereby it decreased by approximately

60 % for a decrease in temperature from 24 to 20 °C (Fig. 2a). For the electrogenic NaPi-IIa (human isoform), measured under the same conditions, the decrease was typically ≈40 % (data not shown). To quantify the temperature dependence, the I_{Pi}–V data were transformed and replotted as Arrhenius plots (see "Methods" section) for test potentials in the range of −180 to −20 mV (Fig. 2b). Data for $V>-20$ mV were too unreliable to fit well and were excluded from analysis. We estimated the activation energy (E_a) from the slopes reported by linear regression fitting (Eq. 3b). This showed little dependence on membrane potential and varied from 43±2 kcalmol^{-1} (−180 mV) to 47±6 kcalmol^{-1} (0 mV). In contrast, for the human WT NaPi-IIa, E_a at −180 mV was significantly smaller: (19±4 kcalmol^{-1}) and increased to 30±10 kcalmol^{-1} at −20 mV, where there was more experimental uncertainty in the data (Fig. 2c). To establish whether the high E_a for AAD-IIc was caused by the mutations or was an intrinsic property of NaPi-IIc, we performed ^{32}P uptake at different temperatures on WT NaPi-IIc expressing oocytes. For these data, the Arrhenius analysis gave E_a=13±4 kcalmol^{-1} (*data not shown*).

We next examined the temperature dependence of the presteady-state current relaxations for the AAD-IIc. In the absence of P_i and external interacting cations, voltage steps induce presteady-state currents that reflect charge movements associated with the voltage-dependent reorientation of the unloaded protein alone. In the presence of external Na$^+$ ions, additional charge movement is detected due to Na$^+$ interactions (e.g., [15]). Figure 3a shows example recordings of membrane currents induced by voltage steps recorded from the same oocyte, superfused with 100Na at two temperatures. By reducing the temperature from 26 to 22 °C, the relaxations slowed, which indicated that the underlying process was temperature dependent. We quantified this behavior by fitting the data with a single exponential decay starting 5 ms after the voltage step. For superfusion with 100Na, the ON time constant (τ_{ON}) obtained from fitting relaxations induced by voltage steps from −60 mV to the test potential showed a strong voltage dependence (Fig. 3b) that became more marked at lower temperatures. The OFF time constant (τ_{OFF}) was similarly obtained by fitting relaxations for the corresponding return step to −60 mV. As expected, τ_{OFF} was independent of the starting potential and the mean values also increased with decreasing temperature and corresponded approximately with the interpolated value at −60 mV for τ_{ON} (Fig. 3b). The increase in τ_{ON} and τ_{OFF} was fully reversible and we confirmed for measurements at 22 and 26 °C that the total charge displaced (see "Methods" section) was unchanged with temperature, as expected (*data not shown*). Resolution of the charge movements at temperatures <20 °C was difficult because of the compromised signal-to-noise ratio and contamination from endogenous currents that depended on the oocyte batch.

As for the steady-state I_{Pi} analysis, the Arrhenius plots for the relaxation rates ($\tau_{ON}{}^{-1}$ and $\tau_{OFF}{}^{-1}$) (Fig. 3c) showed a linear dependence on $1/T$. For the $\tau_{ON}{}^{-1}$ data, there was a small change in the slopes with V and a vertical shift between plots. In contrast, the plots superimposed for $\tau_{OFF}{}^{-1}$, consistent with the notion that only the target potential determines the relaxation rate, which in this case, was constant (=−60 mV). For superfusion with 100Ch, the predicted E_a obtained from linear regression fits to the Arrhenius plots was ≈40 kcalmol^{-1}. There was an upward trend with increasing V and the values were comparable with the E_a determined for I_{Pi}. For superfusion with 100Na, the predicted E_a were slightly less than that for I_{Pi} (Fig. 2c) and showed a similar upward trend with V.

Presteady-state relaxations at a fixed temperature

The above findings suggested that partial reactions preceding P_i interaction could account for the temperature dependence of AAD-IIc, We next investigated the presteady-state kinetics in more detail at a fixed temperature (≈22–23 °C) by first focusing on the interaction of Na$^+$ ions with the empty carrier.

We explored the Na$^+$-dependence quantitatively by recording relaxations for equimolar replacement of choline with different [Na$^+$]. Relaxations recorded from a representative oocyte expressing AAD-IIc were similar whether 100 mM Na$^+$ was present in the external medium (100Na) or Na$^+$ was replaced with choline (100Ch; Fig. 4a). To quantify the charge movement, we estimated the charge displacement, by fitting the relaxations with a double exponential function, commencing after completion of the endogenous charging component and integrating the total fit after backward extrapolation ("Methods" section). We found that this fitting procedure described the relaxations better than using a single exponential fit, as judged by the almost complete elimination of residuals (difference between data and fit) as reported by the fitting algorithm over the fitting window. Moreover, we found that by setting the prestep holding potential to 0 mV, we were able to resolve the relaxations over the entire test voltage range without significant contamination from endogenous Cl$^-$ currents. These were usually activated for $V>0$, when stepping from hyperpolarizing potentials and were dependent on the oocyte batch.[1]

For all test solutions, the data showed a characteristic sigmoidal shape (Fig. 4b) that could be described by a Boltzmann function (Eq. 2). The time constants for the

---

[1] Standard procedures to minimize the contamination by endogenous Ca^{2+}-dependent Cl$^-$ currents, such as preincubation of oocytes in BAPTA-AM, or replacement of external Ca^{2+} with Ba^{2+} did not fully suppress these currents.

Fig. 2 Temperature dependence of electrogenic cotransport mediated by AAD-IIc. **a** Current–voltage relationship of P_i-induced current (I_{Pi}) at different temperatures indicated. Data were normalized to I_{Pi} measured at 24 °C and −100 mV. Data pooled from eight oocytes from two donor animals. Points joined by lines for visualization. **b** Arrhenius plot of AAD-IIc I_{Pi}–V data from **a** transformed (see "Materials and methods" section) at selected potentials. Straight lines generated by linear regression analysis. **c** Activation energy (E_a) obtained from slope of linear regression fits to Arrhenius plot data for AAD-IIc (*filled squares*) and human NaPi-IIa (hIIa) (*open squares*) plotted as a function of membrane potential. *Dotted line* indicates E_a determined for the electroneutral NaPi-IIc (mouse isoform)

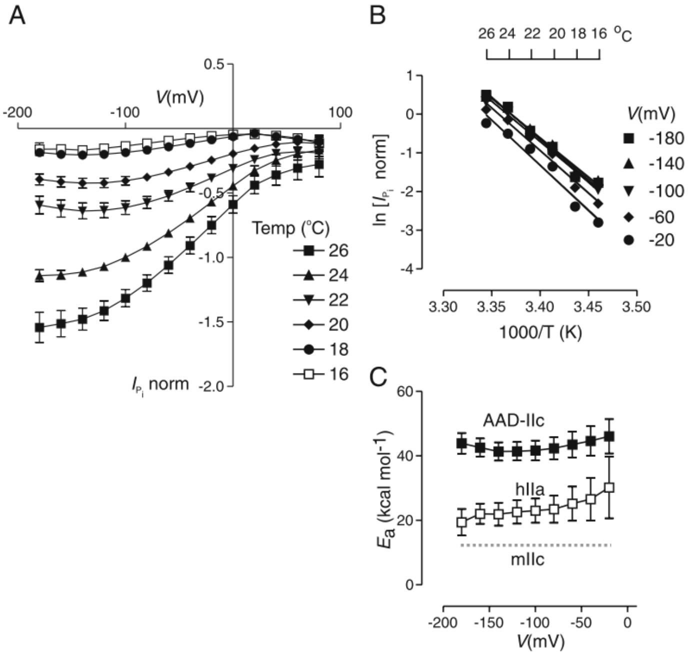

two components (τ_1 and τ_2), plotted as a function of V for different [Na$^+$] showed ≈5-fold difference (for $V<0$ mV) and the slower time constant (τ_2) showed a more obvious voltage dependence with a peak at approximately +30 mV (Fig. 4c). There was also little systematic difference in the magnitude or voltage dependence between the respective time constants in 100Ch or 100Na as well as intermediate [Na$^+$]. This suggested that changing [Na$^+$] did not significantly alter the interactions of external Na$^+$ with AAD-IIc.

The Q–V data were fitted with Eq. 2 to obtain the Boltzmann fit parameters (Q_{max}, z and $V_{0.5}$) (Fig. 4b). As expected, changing [Na$^+$] did not significantly affect Q_{max} (Fig. 4d) and z was similarly insensitive to [Na$^+$] (Fig. 4e). The mid-point potential ($V_{0.5}$) showed a small depolarizing shift with increasing [Na$^+$] of approximately 30 mV for a tenfold change in [Na$^+$] from 10 to 100 mM (Fig. 4f). For WT human NaPi-IIa and flounder NaPi-IIb, a semilogarithmic plot of $V_{0.5}$ vs [Na$^+$] typically gives a straight line for [Na$^+$]> 10 mM with a slope of 100–120 mV/tenfold [Na$^+$] [2, 33]. Compared with the corresponding data for the electrogenic human NaPi-IIa data [33], the AAD-IIc data were shifted vertically and the linear dependence of $V_{0.5}$ on log$_{10}$[Na$^+$] was not obvious for the range of [Na$^+$] used (inset, Fig. 4f).

We next investigated the effect of adding 1 mM P_i to the 100Na buffer. Under these conditions, presteady-state relaxations were still visible (Fig. 4a). This differs from the behavior that we have previously reported for WT electrogenic SLC34 proteins, whereby 1 mM P_i strongly suppresses presteady-state charge movements [13, 14, 18]. Moreover, the relaxations for hyperpolarizing steps from the holding potential, V_h=−60 mV, indicated that more charge movement was induced in the presence of P_i and this charge then returned during the corresponding OFF step (Fig. 4a, *arrowed*). When P_i was added to 100Ch in the superfusion medium, the presteady-state relaxations were unaffected (data not shown). This confirmed that the presence of Na$^+$ was a prerequisite for P_i interaction with AAD-IIc, consistent with all WT SLC34 isoforms. The results of fitting the corresponding charge movements with Eq. 2, gave $V_{0.5}$=−91±11 mV, z=0.51±0.05 and Q_{max} decreased by 18±6 % relative to 100Ch (n=5). The main effect of P_i was therefore a hyperpolarizing shift of the equilibrium distribution of mobile charge. We characterized this by determining the dependence of the shift in $V_{0.5}$ on external [P_i] (Fig. 5). Figure 5a shows pooled, normalized Q–V data (n=4) obtained for the ON transition for different [P_i] indicated. Increasing [P_i] caused a systematic shift of the charge distribution towards hyperpolarizing potentials. As above, the data were fitted with a single Boltzmann function (Eq. 2). For these data, the uncertainties in the Boltzmann fit parameters (z, $V_{0.5}$) were reduced by constraining Q_{max} to the value obtained with 0 mM P_i. Whereas the predicted z remained reasonably insensitive to changes in [P_i] (Fig. 5b), the hyperpolarizing shift of $V_{0.5}$ plotted as a function of [P_i] could be well described by fitting with a modified form of Eq. 1 (n_H=1; Fig. 5c). This yielded a Michaelis constant ($K_{0.5}{}^{Pi}$)= 1.5±0.5 mM.

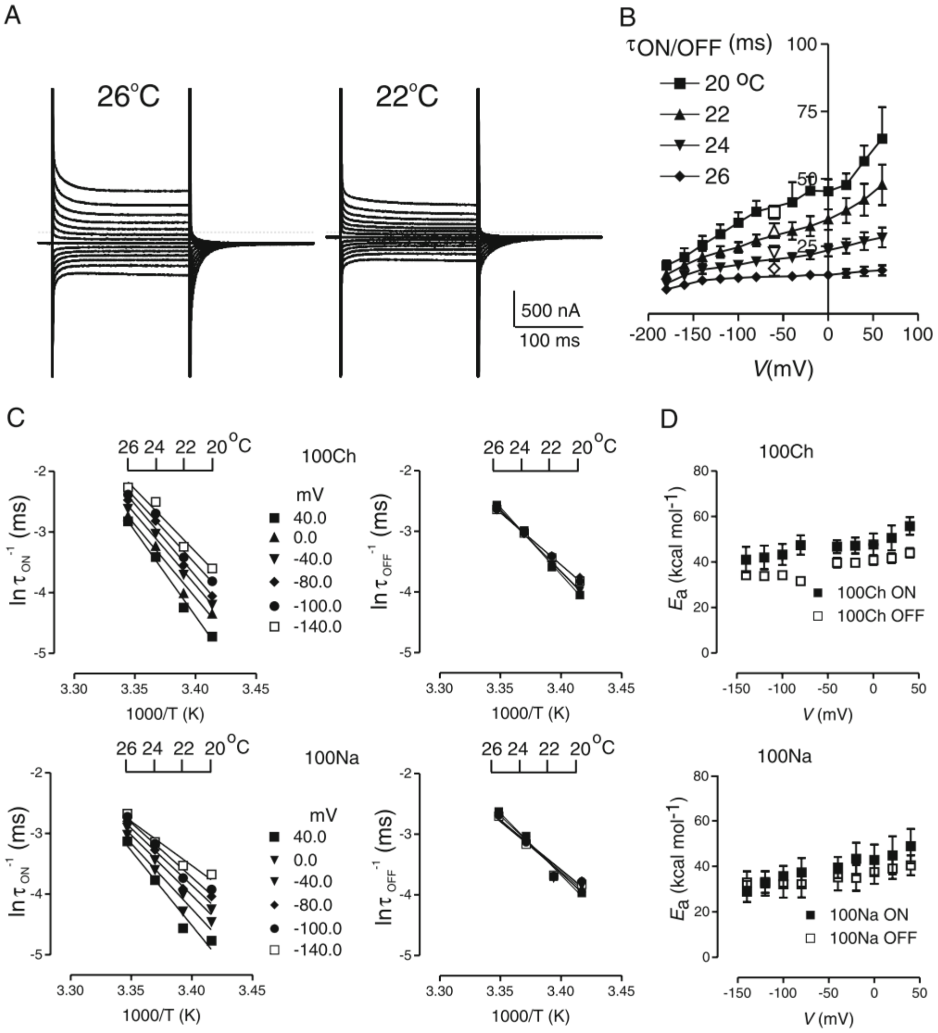

Fig. 3 Temperature dependence of AAD-IIc presteady-state relaxations. **a** Representative current relaxations recorded from an oocyte expressing AAD-IIc at 26 and 22 °C, superfused in 100Na. Voltage steps shown are from the holding potential of −60 mV to potentials in the range −180 to +80 mV. **b** Relaxation time constant for ON (τ_{ON}, *filled symbols*) and OFF (τ_{OFF}, *open symbols*) steps measured as a function of the test membrane potential for the temperatures indicated (n=4). For the OFF relaxations, the data points indicate the mean±SEM of τ_{OFF} determined from the pooled data at each step. Data points joined for visualization. **c** Arrhenius plots for presteady-state relaxation rate (τ_{ON}^{-1} and τ_{OFF}^{-1}) for superfusion with 100Ch and 100Na for steps to selected test potentials. Data shown for ON step (from −60 mV holding potential to test potential indicated; *left panels*) and OFF step (from test potential to holding potential; *right panels*). Straight lines are linear regression fits. Data pooled from four oocytes. **d** Activation energies (E_a) for the presteady-state relaxation time constants, obtained from slope of linear regression fits to Arrhenius plot data for ON steps (*filled squares*) OFF steps (*open squares*) plotted as a function of membrane potential for the superfusion condition indicated

Cysteine substitutions in AAD-IIc

Cysteine mutagenesis has proven a useful technique to identify functionally important sites of SLC34 proteins (e.g., [15]. We made Cys substitutions in AAD-IIc and investigated the constructs by means of conventional steady-state kinetics and VCF [7, 19, 20, 34, 35]. We chose sites in AAD-IIc that corresponded to those previously characterized in other SLC34 isoforms (Fig. 6, Table 1). Our rationale was that substitutions at these conserved sites may show similar deviations from WT behavior as found for the AAD-IIc kinetics, and thereby allow us to predict structure-function relationships.

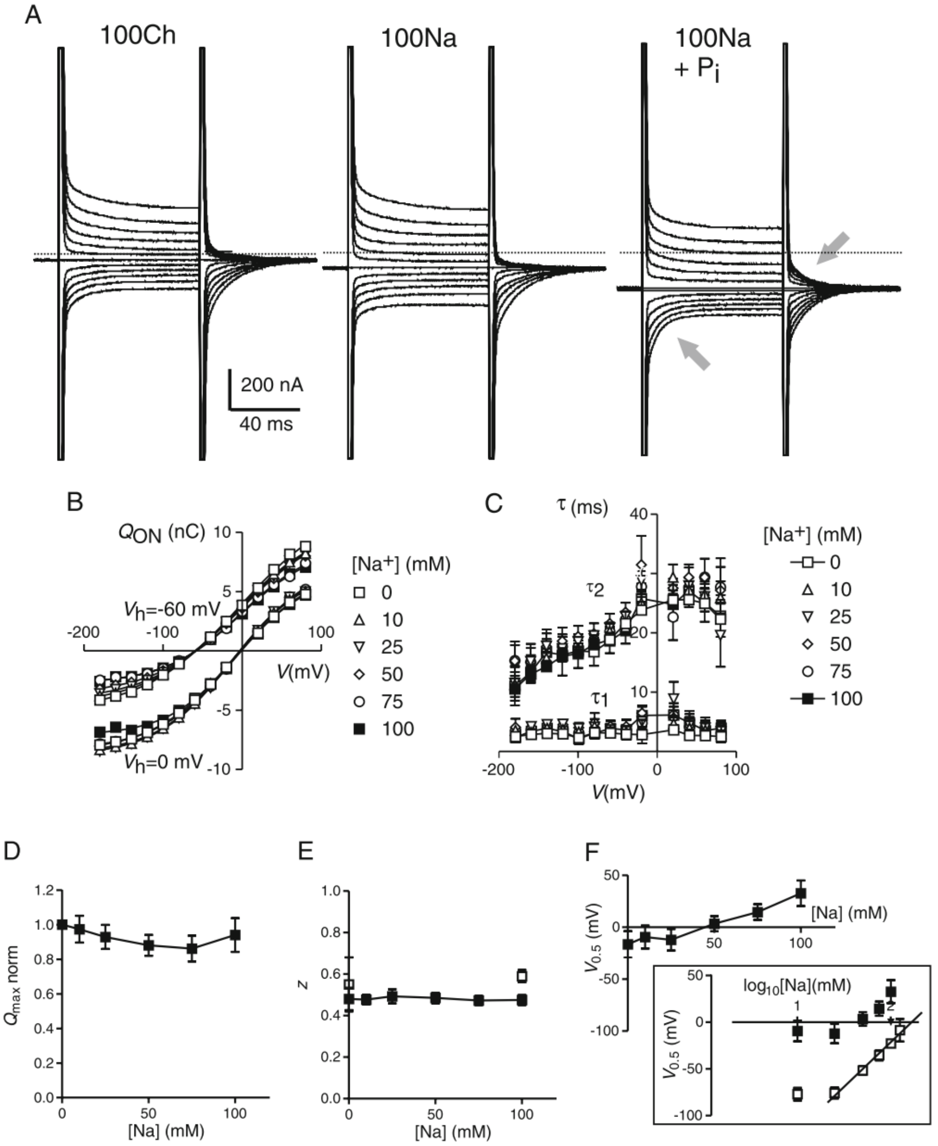

Fig. 4 Dependence of AAD-IIc presteady-state relaxations on external [Na$^+$]. **a** Presteady-state relaxations recorded in response to voltage steps from a V_h=−60 mV to test potentials in the range −160 to +60 mV for three superfusion conditions indicated. *Dotted lines* indicate zero holding current level. For superfusion with 100Na+1P$_i$, the presteady-state relaxations were altered such that more charge movement was induced for steps to and from hyperpolarizing potentials (*arrows*). **b** Typical *Q–V* data from a representative oocyte superfused with different [Na$^+$] as indicated, for steps from two holding potentials (V_h=0, −60 mV). Data are shown for the ON steps. *Continuous lines* are fits with Eq. 2. **c** Voltage dependence of the two fitted time constants (τ_1, τ_2) for the same superfusion conditions as in **b**. Data pooled from four oocytes. Lines join points corresponding to superfusion with 100Ch and 100Na. **d** Total charge (Q_{max}) displaced obtained from Boltzmann fits to data from individual oocytes using Eq. 2 plotted a function of [Na$^+$]. Data were normalized to Q_{max} from 100Ch data set. Data pooled from five cells. **e** Effective valence (*z*) obtained from Boltzmann fits to data from individual oocytes using Eq. 2 plotted as a function of [Na$^+$]. Data pooled from five cells. Open squares are data at 0 and 100 mM Na$^+$ for the human NaPi-IIa from [33]. **f** Midpoint voltage ($V_{0.5}$) from Boltzmann fits to data from individual oocytes using Eq. 2 plotted as a function of [Na$^+$] obtained (*left panel*). Data were replotted on a log$_{10}$[Na$^+$] scale (*inset*, *filled symbols*). Equivalent data for the human NaPi-IIa are shown (*open symbols*) for comparison (data replotted from [33])

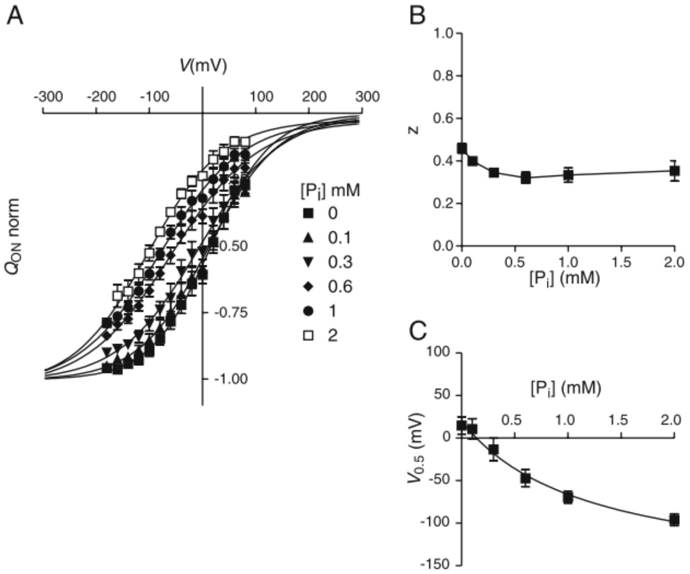

Fig. 5 Dependence of AAD-IIc presteady-state relaxations on external [P_i]. **a** Typical *Q-V* data from a representative oocyte superfused with different [P_i] as indicated, for steps from two holding potentials (V_h=0, −60 mV). Data are shown for the ON steps. *Continuous lines* are fits with Eq. 2. **b** Effective valence (*z*) obtained from Boltzmann fits to data from individual oocytes, using a modified form of Eq. 1 (n_H=1) plotted as a function of [P_i]. Data pooled from four cells. **c** Midpoint voltage ($V_{0.5}$) from Boltzmann fits to data from individual oocytes using a modified form of Eq. 1 (n_H=1) plotted as a function of [P_i] obtained

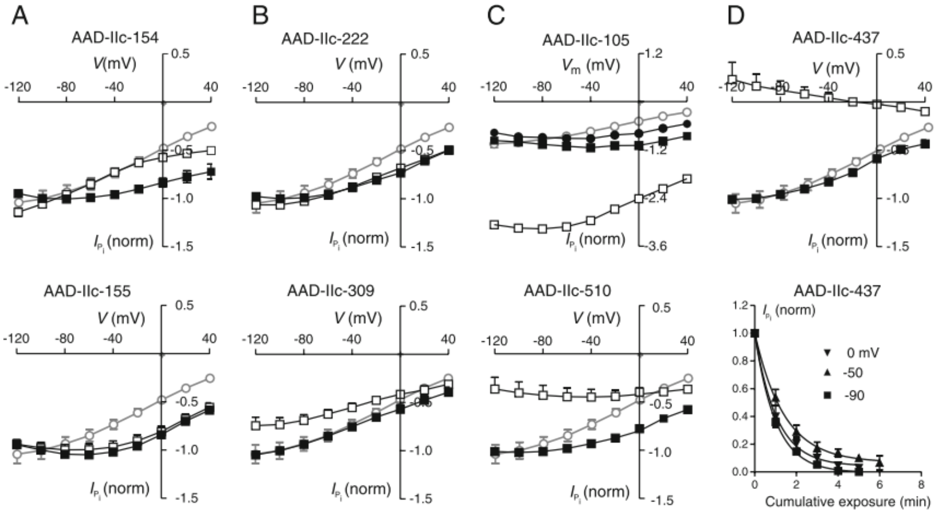

Fig. 6 Cysteine mutagenesis in the AAD-IIc constructs-dependence of P_i-dependent current (I_{Pi}) on voltage before and after MTS incubation. After determination of the control I_{Pi} vs V relationship (*filled squares*), oocytes were incubated in 1 mM MTSET for 5 min (*open squares*) and the assay repeated. Data shown normalized to I_{Pi} at −100 mV control condition. Mean±SEM for ≥3 oocytes. *Error bars* smaller than symbol size not shown. Normalized data (n=4) for the AAD-IIc are superimposed on each plot for comparison (*gray-filled circles*). **a** For two mutants with adjacent Cys substitutions in the linker between predicted TMD-4 and TMD-5 (Fig. 1b) AAD-IIc-154 (*upper*) showed a hyperpolarizing shift in the voltage dependence of I_{Pi}, whereas AAD-IIIc-155 (*lower*) showed no change after MTS incubation. **b** I_{Pi} vs V data for two mutants with Cys substitutions at each end of the large extracellular loop (Fig. 1b), AAD-IIc-222 (*upper*) and AAD-IIc-309 (*lower*). Only AAD-IIc-309 showed a significant change after MTS incubation. **c** I_{Pi} vs V data for Cys mutants AAD-IIc-105 (*upper*) and AAD-IIc-510 (*lower*) that showed reciprocal changes of I_{Pi} after MTS incubation. After MTS modification, one representative AAD-IIc-105 expressing oocyte was exposed to DTT (10 mM, 30 min), which caused a reversion to the initial response (*filled circles*). **d** *Upper* mutant AAD-IIc-437 showed complete suppression of cotransport behavior after MTS incubation with an outward I_{Pi} for hyperpolarizing potentials. *Lower* loss of cotransport activity for mutant AAD-IIc-437 following modification of Cys 437. Normalized response plotted as a function of cumulative exposure time for MTSET (10 μM) exposure with the individual oocytes voltage clamped during incubation to the potential indicated. *Continuous lines* are fits with Eq. 4. See text for more details

Table 1 Comparison of selected Cys substitution sites among SLC34 isoforms [see Fig. 6]

	Site of Cys substitution							
mAAD-IIc	G105	V154	S155	A222	L309	S437	D440	L510
rNaPi-IIa	G134 [10, 11]		S183 [30]			S460 [24, 25]	E463 [25]	M533 [10, 11]
fNaPi-IIb		S155 [19, 35]		S226 [34]	Q319 [34]	S448 [19, 35]		
mNaPi-IIc						S437 [20]		

Blank entry indicates constructs that have not been synthesized or investigated in our laboratory. Equivalent sites indicated according to a multiple sequence alignment for the isoforms and species indicated

f flounder, *m* mouse, *r* rat

Before proceeding with the mutagenesis, we first determined if exposure of oocytes expressing AAD-IIc to MTS reagents (MTSET, 1 mM) altered their electrogenic behavior. That no change was observed confirmed that the triple mutation itself had not exposed any previously inaccessible native cysteines that might involved in conformational changes associated with transport function (data not shown). All Cys mutants gave robust I_{Pi}, with typical magnitudes of >50 nA at −100 mV. With the exception of AAD-IIc-309, all showed a weak apparent affinity for P_i that is characteristic for AAD-IIc (Table 2). The smaller P_i affinity constant ($K_{0.5}^{\mathrm{Pi}}$) for AAD-IIc-309 indicated that this site may be critically associated with P_i interactions. For the other constructs, the $K_{0.5}^{\mathrm{Pi}}$ values similar to AAD-IIc and indicated that the Cys substitution had not significantly affected the substrate interactions. In general, the large variation in $K_{0.5}^{\mathrm{P}}$ arose from uncertainties in fitting the weakly saturating dose dependence data with Eq. 1. For five of the mutants (AAD-IIc-105, -154,-155,-222, and -510) the Cys substitution weakened the voltage dependence of I_{Pi} compared with AAD-IIc alone, whereas for AAD-IIc-309 and -437 we observed no change in the electrogenic response (Fig. 6).

The effect on I_{Pi} of exposure of oocytes expressing each mutant to MTSET (1 mM for 5 min) depended critically on the site of Cys substitution (Fig. 1b). Mutants fell into two groups: those in which there was no change in the magnitude and voltage dependence of I_{Pi}, like AAD-IIc itself, and those that resulted in a marked alteration (Fig. 6, Table 2). We concluded that for the former group the sites of mutagenesis (Ser-155, A-222, and D-440) were either not functionally critical in AAD-IIc, or were not accessible from the external medium. The importance of the site is illustrated in the case of mutations in the predicted re-entrant loop (TMD3,4, Fig. 1b): modification of the Cys substituted at Val-154 caused a significant hyperpolarizing shift in the voltage dependence of I_{Pi} (Fig. 6a, upper panel), whereas the construct AAD-IIc-155 with a Cys substituted at the adjacent Ser showed no detectable change in I_{Pi} after incubation (Fig. 6a, lower panel). Oocytes expressing AAD-IIc with Cys substitution at Ala-222 at one end of the predicted large extracellular loop showed no change in I_{Pi}, whereas at the other end (Leu-309) we found a modest ~25 % inhibition in I_{Pi} but with no change voltage dependence (Fig. 6b, lower panel).

Thiol modification of Cys at sites in the two predicted outer linkers (G105 and L510) showed complementary changes in I_{Pi} (Fig. 6c), consistent with previous findings for Cys substituted at the equivalent sites in NaPi-IIa [10]. The voltage dependence of AAD-IIc-105 was weak and after modification I_{Pi} increased fourfold (V=−100 mV) to give a voltage dependence that resembled that of AAD-IIc. To verify that this was a direct result of the modification of Cys 105, we exposed oocytes expressing AAD-IIc-105 and prelabeled with MTSEA to the reducing agent DTT. This resulted in a reversion of the electrogenic response close to the original *I*–*V* relation (Fig. 6c, upper panel). In contrast, AAD-IIc-510 showed the opposite behavior, whereby I_{Pi} was inhibited by ~50 % and after thiol modification, its voltage dependence was similar to AAD-IIc-105 before MTS exposure (Fig. 6c, lower panel).

Table 2 Summary of properties of Cys mutations in AAD-IIc (see Fig. 6)

Property	AAD-IIc	+G105C	+V154C	+S155C	+A222C	+L309C	+S437C	+D440C	L510C
$K_{0.5}^{\mathrm{Pi}}$–60 mV (mM)	6.5±4.8 (4)	n.d.	1.1±0.4	2.9±0.8	1.5±0.4	0.6±0.1	1.6±0.4	2.0±.8	1.5±0.3
$I_{\mathrm{Pi}}^{+\mathrm{MTS}}/I_{\mathrm{Pi}}^{-\mathrm{MTS}}$	↔	↑	↓	↔	↔	↓	↓	↔	↓
ΔF	No	No	Yes	No	Yes	No	Yes	No	No

↔ indicates that ratio $I_{\mathrm{Pi}}^{+\mathrm{MTS}}/I_{\mathrm{Pi}}^{-\mathrm{MTS}}$ remains unchanged, ↑ ratio $I_{\mathrm{Pi}}^{+\mathrm{MTS}}/I_{\mathrm{Pi}}^{-\mathrm{MTS}}$ increased, ↓ indicates that ratio $I_{\mathrm{Pi}}^{+\mathrm{MTS}}/I_{\mathrm{Pi}}^{-\mathrm{MTS}}$ decreased, *n.d.* not determined

Finally, two mutants involving Cys substitutions at nearby locations in the predicted linker between TMD9 and TMD10 also displayed contrasting behavior. Whereas mutant AAD-IIc-440 showed no resolvable change after incubation (*data not shown*), exposure of oocytes that expressed AAD-IIc-437 to MTS reagents resulted in a significant suppression of I_{Pi} (Fig. 6d, upper panel). For this construct, the typical *I*–*V* response to 1 mM P_i reversed at −30 mV and displayed a negative slope. This behavior has been previously interpreted to represent full inhibition of cotransport function and recapitulates the behavior of other electrogenic SLC34 isoforms with a Cys at the equivalent site (Table 1, see "Discussion" section) [25, 35]. To quantitate the Cys modification reaction for AAD-IIc-437 and investigate if membrane potential could influence the accessibility of the Cys, we applied MTSET (10 µM) for 1 min intervals at a defined holding potential and measured I_{Pi} at −50 mV after each exposure. The data were fitted with a single decaying exponential function (Eq. 4) to yield the effective pseudo first order rate constants (see "Methods" section): 1.57±0.1 $\mathrm{mM^{-1}s^{-1}}$ (0 mV), 1.18±0.03 $\mathrm{mM^{-1}s^{-1}}$ (−50 mV), 1.63±0.05 $\mathrm{mM^{-1}s^{-1}}$ (−90 mV) (n=4; Fig. 6d, lower panel).

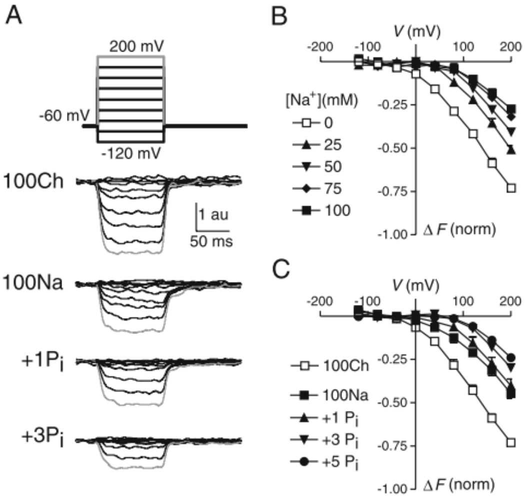

Fig. 7 VCF recordings from oocytes expressing AAD-IIc-437 and labeled with the fluorophore MTS-TAMRA. **a** Representative VCF recordings from the same oocyte expressing AAD-IIc-437 for the voltage step protocol shown and for the different superfusion conditions indicated. Data traces offset-adjusted to the steady-state fluorescence level at V_h=−60 mV. **b** Change in fluorescence (Δ*F*) plotted as a function of *V* for oocytes expressing AAD-IIc-437 with external [Na$^+$] varied as indicated. Data for individual oocytes were corrected from photobleaching and loss of fluorescence during the experiment (see "Methods" section) and pooled (n=5) by first normalizing to $F_{\max}$ predicted from a fit to the 100Ch data using Eq. 2. **c** Change in fluorescence (Δ*F*) plotted as a function of *V* oocytes expressing AAD-IIc-437 with external [P_i] varied as indicated in the presence of 100 mM Na$^+$. Data from individual oocytes were corrected for photobleaching and loss of fluorescence during the experiment (see "Methods" section) and pooled (n=5) by first normalizing to $F_{\max}$ predicted from a fit to the 100Ch, 0 mM P_i data using Eq. 2

Labeling with MTS-TAMRA and changes in emitted fluorescence intensity

For VCF measurements, we incubated oocytes expressing each of the Cys mutants in a medium containing the fluorophore MTS-TAMRA and tested them for voltage-induced changes in emitted fluorescence intensity under different substrate superfusion conditions (100Na, 100Ch, and 100Na+1P$_i$). Three of the constructs (AAD-IIc-154C, AAD-IIc-222, and AAD-IIc-437) gave measurable Δ*F* and were characterized in detail.

AAD-IIc-437 After labeling with MTS-TAMRA, oocytes expressing AAD-II-437 showed the expected suppressed electrogenic response to 1 mM P_i, consistent with the behavior of this mutant when labeled with MTSET (Fig. 6d). We first examined if the steady-state fluorescence was dependent on the superfusate, as we reported for the labeled mutant S437C in NaPi-IIc [20]. Indeed oocytes expressing AAD-IIc-437 and voltage clamped at −60 mV showed up to 3 % reversible quench of *F* (data not shown), when switching the superfusate from 100Ch to 100Na. All other experiments were performed using a voltage step protocol (see "Methods" section). Representative voltage-induced Δ*F* recordings are shown in Fig. 7a. For *V*<0, little or no Δ*F* was detected whereas for strongly depolarizing signals Δ*F* was quenched in a voltage- and substrate-dependent manner. The quenching was the strongest in the absence of external Na$^+$ (Fig 7b) and at a given *V*, addition of Na$^+$ to the external medium reduced the amount of quenching in a dose-dependent manner. Saturation of the Δ*F*–*V* data was not observed at the depolarizing extreme and we were unable to reliably voltage clamp oocytes for *V*>200mV. In the presence of 100 mM Na$^+$, addition of P_i to the external medium reduced the amount of quenching further in a dose-dependent manner (Fig 7a, c).

AAD-IIc-154 Based on a previous study on the flounder NaPi-IIb isoform [34], we had expected that labeling a Cys substituted at the equivalent site (S155) in AAD-IIc would result in voltage-induced Δ*F*. Surprisingly, we could not resolve Δ*F* from oocytes expressing the construct AAD-IIc-155 (data not shown). However, Cys substitution at the neighboring site (V154) gave a functional construct that exhibited robust Δ*F* (Fig. 8a). The voltage step induced Δ*F* was similar for superfusion in 100Ch and 100Na; however, the addition of P_i suppressed Δ*F* for depolarizing steps and increased Δ*F* for hyperpolarizing steps. The Δ*F*–*V* data were fit with a single Boltzmann function (Eq. 2, see "Methods" section) to yield

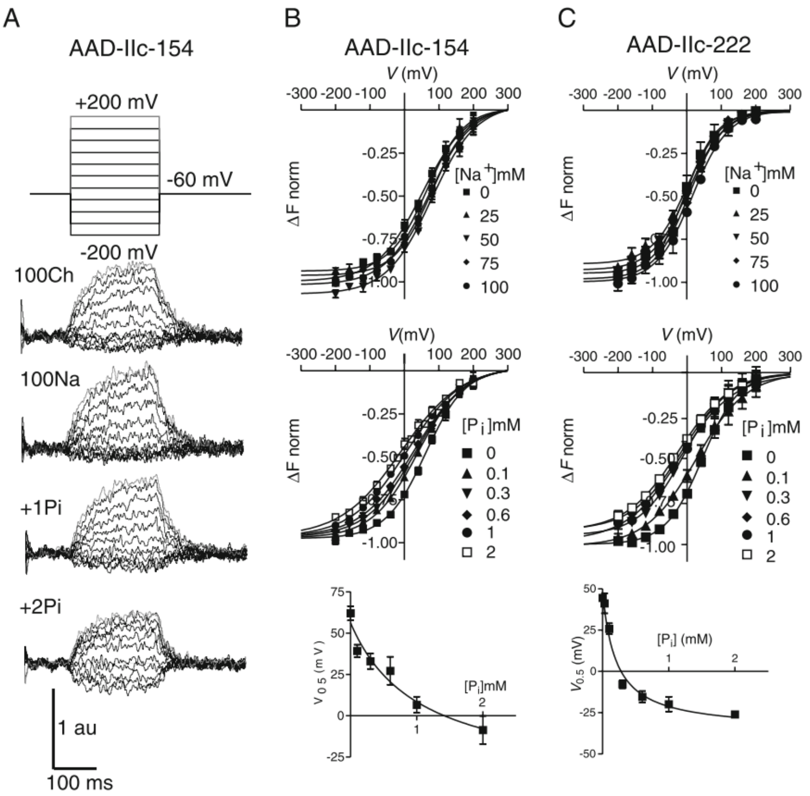

Fig. 8 VCF recordings from oocytes expressing AAD-IIc-154 and AAD-IIc-222, labeled with the fluorophore MTS-TAMRA. **a** Representative VCF recordings from the same oocyte expressing AAD-IIc-154 for the voltage step protocol shown and the superfusion conditions indicated. All data traces were baseline-adjusted to the steady-state fluorescence level at V_h=−60 mV. **b** AAD-IIc-154; *upper* Δ*F*–*V* data for different external [Na$^+$]. Data were offset to Δ*F* at the depolarizing limit predicted from a fit with Eq. 2 and normalized to $F_{\max}$ determined for 100 mM Na$^+$. *Continuous lines* are refits to the adjusted data using Eq. 2. Data pooled from four oocytes. *Center* Δ*F*–*V* data for different [P_i] in the presence of 100 mM Na$^+$. Data were offset to Δ*F* at the depolarizing limit predicted from a fit with Eq. 2 and normalized to $F_{\max}$ determined for 0 mM P_i. *Continuous lines* are refits to the adjusted data using Eq. 2. Data pooled from four oocytes. *Lower* midpoint voltage ($V_{0.5}$) plotted as a function of [P_i] derived from Boltzmann fit. *Continuous line* is fit using a modified form of Eq. 1 (n_H=1). **c** AAD-IIc-222; *upper* Δ*F*–*V* data for different external [Na$^+$]. Data were offset to Δ*F* at the depolarizing limit predicted from a fit with Eq. 2 and normalized to $F_{\max}$ determined for 100 mM Na$^+$. *Continuous lines* are refits to the adjusted data using Eq. 2. Data pooled from four oocytes. *Center* Δ*F*–*V* data for different [P_i] in the presence of 100 mM Na$^+$. Data were offset to Δ*F* at the depolarizing limit predicted from a fit with Eq. 2 and normalized to $F_{\max}$ determined for 0 mM P_i. *Continuous lines* are refits to the adjusted data using Eq. 2. Data pooled from four oocytes. *Lower* midpoint voltage ($V_{0.5}$) plotted as a function of [P_i] derived from Boltzmann fit. *Continuous line* is fit using a modified form of Eq. 1 (n_H=1)

estimates for the midpoint voltage ($V_{0.5}^F$) and slope factor (z^F). Unconstrained fits confirmed that $F_{\max}$ was largely insensitive to manipulations of the external [Na$^+$] (Fig. 8b, upper). The predicted $V_{0.5}^F$ showed a modest increase from +51±9 mV (100Ch) to +71±11 mV (100Na) whereas z^F remained unchanged (0.39±0.06 (100Na) and 0.38±0.05 (100Ch)). We then quantitated the effect of progressively increasing external [P_i] (in 100Na; Fig. 8b, center). This resulted in a systematic hyperpolarizing shift in $V_{0.5}^F$ (Fig. 8b, lower) together with a reduction in the slope factor z^F from 0.43±0.02 (0 mM P_i) to 0.29±0.01 (2 mM P_i) (n=4). The dependence of $V_{0.5}^F$ on [P_i] could be described analytically with a modified form of the Michaelis function (Eq. 1 (n_H=1) to give an apparent $K_{0.5}^{Pi}$=1.04±0.7 mM (Fig. 8b, lower).

AAD-IIc-222 Oocytes expressing this mutant showed no significant change in electrogenic activity after labeling (Fig. 6b, upper), yet robust Δ*F*–*V* was resolved. Like AAD-IIc-154, there was little change in Δ*F* when replacing choline with Na$^+$ in the superfusate; however, when P_i (1 or 2 mM) was added to the superfusate (100Na), Δ*F* increased for hyperpolarizing voltage steps and decreased for depolarizing steps relative to the holding potential, like AAD-IIc-154. The ΔF–V data with variable [Na$^+$] were fit with the Boltzmann function (Eq. 2) (Fig. 8c, upper) and the Boltzmann analysis revealed a small depolarizing shift $V_{0.5}^F$ as [Na$^+$] increased : with 100Ch, $V_{0.5}^F=-2.2\pm5.2$ mV and at 100Na, $V_{0.5}^F=+16.0\pm4.9$ mV. In constrast, F_{max} was relatively insensitive to this manipulation and z^F decreased from 0.57±0.06 (100Ch) to 0.48±0.05 (100Na). We also investigated the effect of adding P_i to the 100Na medium (Fig. 8c, center). This caused a hyperpolarizing shift of $V_{0.5}^F$, without significantly affecting F_{max}. For this mutant, $V_{0.5}^F$ also showed evidence of saturation at high [P_i] and the dependence of $V_{0.5}^F$ on [P_i] could be described analytically in terms of a modified form of the Michaelis fit (Eq. 1, $n_H=1$) to give $K_{0.5}^{Pi}=0.22\pm0.1$mM (Fig. 8c, lower).

Discussion

For many Na$^+$-coupled solute carriers, transmembrane electrical potential is a source of free energy to drive coupled transport, in addition to the chemical energy imparted by the Na$^+$ concentration gradient. The effect of membrane potential is manifested as the voltage dependence of transport rates (substrate-induced currents) assayed under voltage clamp conditions. Hyperpolarizing membrane potentials increase the inwardly directed transport-associated membrane current and this current correlates directly with solute flux (e.g., [2, 17, 27–29]). Voltage dependence of transport rate implies that there must be one or more partial reactions in the transport cycle whose rate constants are membrane potential dependent. Furthermore, these partial reactions must involve charge displacements that could be either intrinsic to the protein, or arise from the driving cations moving within transmembrane electric field. Such charge displacements are thought to accompany protein conformational changes. It is also possible that the overall transport cycle is electroneutral and one or more partial reactions are voltage dependent and become rate limiting [26], although this not been demonstrated experimentally in the case of SLC34.

For AAD-IIc, which displays three hallmarks of electrogenic SLC34 cotransport (net charge translocation, 3:1 Na$^+$/HPO$_4^{2-}$ stoichiometry and presteady-state charge displacement), we have proposed that its electrogenicity is a direct result of the re-establishment of the cotranslocation of the Na$^+$ ion associated with transition 1↔2 during the cotransport cycle , as proposed for the WT electrogenic isoforms [4]. Thus, according to our kinetic scheme (Fig. 1a), the salient difference between the electrogenic and electroneutral SLC34 proteins concerns partial reactions between states 0, 1, 2, and 9. This is also supported by the presence of a leak mode for electrogenic SLC34 proteins, that we have hypothesized to involve the translocation of a single Na$^+$ ion per cycle, in the absence of P_i and which can be described kinetically by transitions between these four states [1].[2] In this study, we used AAD-IIc together with mutant constructs involving Cys substitutions at sites previously identified in studies on the electrogenic (NaPi-IIa/b) and electroneutral (NaPi-IIc) to gain new insights into the mechanism of electrogenic cotransport.

Electrogenicity of the empty carrier imposes an energetic cost to AAD-IIc

Although AAD-IIc displays the qualitative features expected for an electrogenic SLC34 protein, its kinetic characteristics depart significantly from that of the WT electrogenic isoforms, which implied that the mutagenesis altered the kinetics of one or more partial reactions in the cotransport cycle. To identify these reactions, we first examined the temperature dependence of the kinetics of cotransport and cation interactions. Solute coupled carrier proteins generally exhibit a high-temperature dependence that differs significantly from that of ion channels and can be used to distinguish between diffusional processes and those involving conformational changes [3, 5, 6, 21]. With respect to steady-state cotransport rate (I_{Pi}), we estimated that E_a for the electrogenic human NaPi-IIa and AAD-IIc was respectively ≈2- and ≈3-fold larger than for the corresponding P_i uptake rate of the electroneutral NaPi-IIc (Fig. 2c). This was clear evidence that cotransporting an additional Na$^+$ ion by the electrogenic isoforms invoked a larger energetic cost. Moreover, our finding that E_a for AAD-IIc was significantly greater than for NaPi-IIa indicated that the mutagenesis in NaPi-IIc had resulted in a less efficient transporter. Given that the cotransport cycle involves a number of partial reactions, one or more of which might be responsible for the overall high E_a, we limited the number of possible states the proteins could populate and focused on the temperature dependence of presteady-state relaxations in the absence of P_i. In the absence of external Na$^+$ (100Ch) E_a was essentially unchanged (Fig. 3d), we therefore propose that the high E_a of AAD-IIc results from partial reactions that involve neither external Na$^+$ ions nor P_i, with the empty carrier (0↔1, Fig. 9a) being the most likely candidate. We cannot explicitly discount the contribution of partial reactions between "inward facing" states, however with low activity of substrates in the cytosol, the probability of occupancy of these states is expected to be concomitantly low. It is therefore most likely that the introduction of the charged Asp-196 into NaPi-IIc has resulted in an electrogenic transition that represents a conformational change between states 0 and 1. This transition is energetically

---

[2] We also previously reported evidence of a leak mode for AAD-IIc based on the electrogenic response to application of the blocker phosphonoformic acid (PFA) [4]. A detailed characterisation of this mode was not undertaken in the present study due to the low apparent affinity of AAD-IIc for P_i and PFA that would result incomplete suppression of the leak current with the substrate concentrations used.

unfavorable compared to the same transition in the WT electrogenic isoforms [3] and would be expected to involve a concomitantly larger conformational change.

A seven-state model accounts for the kinetic properties of AAD-IIc

We obtained further insight into the AAD-IIc kinetics, by performing numerical simulations using a set of differential equations that described the rate of change of state occupancy of a reduced form of the 10-state scheme (Fig. 9a). This seven-state scheme allowed us to investigate the steady-state and presteady-state behavior of AAD-IIc with a workable number of free parameters and compare its behavior with corresponding experimental data. We lumped the interactions of P_i and the final Na^+ ion before translocation together, but took account of two Na^+ ions interacting sequentially before P_i binding and we further simplified the ordered sequence of substrate interactions at the cytoplasmic face by assuming that rapid equilibrium conditions applied to the transitions between states 7 and 9 (Fig. 1a). The simulations successfully predicted the main features of the presteady-state current relaxations (Fig. 9b), namely the weak influence of external Na^+ on charge movement and the presence of a significant charge movement in the presence of external P_i. For comparison, selected traces from representative data (Fig. 4a) are also shown.

Based on the presteady-state data obtained for AAD-IIc in the absence of external Na^+ (100Ch), the effective charge displacement of the empty carrier was the same as in the original model ($0.4e^-$); however, the assignment of voltage dependence to the partial reactions 1↔2 and 9↔0 differed in two respects. First, it was necessary to assign a weaker interaction of the first Na^+ ion (1↔2) with the transmembrane electric field (effective valence$=0.1e^-$) to account for: (1) the absence of a strong effect of external $[Na^+]$ on the presteady-state charge distribution and the total detectable charge displacement (Figs. 4b and 9c) and (2) the weak hyperpolarizing shift in the midpoint voltage ($V_{0.5}$) of the Q–V distribution (Figs. 4f and 9c, lower panel). Second, we increased the effective valence of the partial reaction that accounts for the release of the third Na^+ ion on the cytosolic side (9↔0) to $0.5e^-$. Together with a slow backward rate (Na^+ release; $k_{09}=7\ s^{-1}$) and a highly asymmetrical barrier for the transition 0↔9, we could also account for: (1) the increased charge movement for hyperpolarizing steps in the presence of P_i (Figs. 4a and 9b, right panel) and (2) the hyperpolarizing shift in $V_{0.5}$ with increasing $[P_i]$ (Figs. 5c and 9d). Moreover, this showed Michaelian behavior (Fig. 9d, lower panel) in accord with the analysis of the experimental data (Fig. 5c) .In the absence of external P_i and the low internal $[Na^+]$, the state occupancy is distributed between states 0, 1, and 2. When external P_i is present, state 9 can accumulate after ordered release of 2 Na^+ ions and P_i to the cytosol (6→9). The completion of the cotransport cycle only occurs after release of the third Na^+ ion, which gives rise to the presteady-state charge movement induced by hyperpolarizing voltage steps (Fig. 9b, right panel) and to a net inward cotransport current in the steady-state.

The most important functional characteristic of AAD-IIc that differed from the WT transporters is the apparent affinity constant for P_i ($K_{0.5}{}^{Pi}$) that we originally reported to be >100-fold higher than that of either the electrogenic or electroneutral isoforms [4]. This suggested that the triple mutation of NaPi-IIc had specifically affected P_i interactions with the protein. In general, although $K_{0.5}{}^{Pi}$ can be influenced by all rate constants (forward and backward) associated with partial reactions of the transport cycle, likely candidates could also include those associated with Na^+ ion interactions that precede external P_i binding. As expected, our simulations confirmed that $K_{0.5}{}^{Pi}$ was dependent on the ratio of forward to backward rate constants associated with transitions 1↔2, 2↔3 and 3↔5. However, given the constraints on the model parameters imposed by having good agreement with all the experimental data, we found that partial reaction 3↔5 was indeed the most critical determinant of $K_{0.5}{}^{Pi}$. Specifically, the ratio $k^0{}_{12}/k^0{}_{21}$ was constrained by the dependence of $V_{0.5}$ on external $[Na^+]$ [2] and was fixed ≈5 in the simulations to give reasonable agreement with measurement. Furthermore, although altering $k^0{}_{23}/k^0{}_{32}$ had little influence on the simulated presteady-state behavior in 0 mM P_i, this ratio was also found to be a critical determinant of the apparent affinity constant for Na^+ at a given $[P_i]$, ($K_{0.5}{}^{Na)}$, and the cooperativity of Na activation of I_{Pi} [4]. Thus, for AAD-IIc, the low apparent affinity for P_i compared to the electrogenic and electroneutral isoforms most likely results from the effect of the mutagenesis on the P_i binding partial reaction (3↔6) and is largely unaffected by the preceding Na^+ interactions. The final set of parameters that gave good agreement with the steady-state data [4] were consistent with a cooperative interaction of two Na^+ ions preceding P_i binding ($k^0{}_{12}/k^0{}_{21}<k^0{}_{23}/k^0{}_{32}$) and with $k^0{}_{35}/k^0{}_{53}$ adjusted to give $K_{0.5}{}^{Pi}\approx 1$ mM and $K_{0.5}{}^{Na}\approx 110$ mM (at −60 mV; Fig. 9e), similar to previously reported values [4].

In summary, the simulations helped to identify two critical partial reactions that contribute to the AAD-IIc kinetics: (1) the cytosolic release of one Na^+ ion from the protein that establishes a rate limiting step in the transport cycle to define the maximum transport rate, and (2) the external P_i interaction which defines the apparent affinity for P_i.

Fluorometric assays complement presteady-state relaxation analysis

The altered kinetic behavior of AAD-IIc compared to the WT proteins indicated that mutagenesis had modified the voltage- and substrate-dependence of the conformational changes during the transport cycle. To relate these kinetic findings to dynamic changes in the molecular structure, we substituted Cys at sites that previous studies had suggested were involved in unique conformational changes determined by membrane potential and substrate availability [10, 11, 20, 23, 25, 34]. Cys substitution itself was well-tolerated and similar phenotypes were observed after thiol modification, exemplified by mutants AAD-IIc-437, AAD-IIc-105, and AAD-IIc-510.

Exposure of oocytes expressing AAD-IIc-437 to MTS reagents resulted in suppression of cotransport activity, as we have previously reported for the equivalent mutation in other SLC34 isoforms [20, 24, 25, 35] (Fig. 6d). Moreover, the pseudo first-order rate constant for the Cys modification reaction was similar to values we previously reported for modification of a Cys at the equivalent site in rat NaPi-IIa (S460C) [25] and the flounder NaPi-IIb (S448C) [35]. This indicated that external accessibility of this critical site was not changed and moreover, the accessibility was also insensitive to membrane potential ($V \leq 0$ mV). The voltage dependence of mutants AAD-IIc-105 and AAD-IIc-510 (Fig. 6c) also showed qualitatively similar behavior as previously reported for the equivalent Cys substitutions in the rat NaPi-IIa [11] whereby Cys modification resulted in a complementary change in the voltage dependence. These findings not only confirmed that AAD-IIc has a similar topology to NaPi-IIa at these critical sites, but that the functional consequences of Cys modification at these sites were comparable.

The substituted Cys were labeled with fluorophores to act as reporters of local conformational changes [19, 20, 34, 35]. The behavior of labeled oocytes expressing AAD-IIc-437 in response to changing the superfusate from 100Na to 100Ch was qualitatively the same as we previously reported for the NaPi-IIc mutant S437C [20]: in the steady-state ($V_h=-60$ mV), addition of Na^+ quenched the fluorescence. However, the response of AAD-IIc-437 to voltage steps differed from the electrogenic NaPi-IIb mutant S448C [35], whereby under all superfusion conditions there was resolvable voltage-induced change in fluorescence intensity (ΔF) *only* for depolarizing voltage steps (Fig. 7). Superfusion with 100Ch gave the largest quench of ΔF at a given positive test potential and this diminished in a concentration-dependent manner with the addition of more external Na^+ as well as with the addition of external P_i. In contrast, for the electrogenic S448C mutant in flounder NaPi-IIb [35], no resolvable ΔF was reported for voltage steps from −60 mV to test potentials >0 mV, and increasing external $[Na^+]$ quenched ΔF for hyperpolarizing potentials. Similarly, for S437C mutant made in the mouse NaPi-IIc we reported that the addition of external Na^+ caused a quenching of the steady-state fluorescence [20] as we also observed for the steady-state F reported by AAD-IIc-437.

One interpretation of the behavior of AAD-IIc-437 is that the microenvironment of the fluorophore at site 437 reports Na^+ interactions from *either* side of the membrane, depending on the membrane potential and availability of Na^+ ions. This would be consistent with the alternating access mechanism for cation driven transport (e.g., [12]). Thus, for strongly depolarizing voltage steps, and *no* external Na^+, cytosolic Na^+ ions would be driven to their binding site (partial reaction 0→9), thus giving rise to ΔF when superfusing with external 100Ch (Fig. 6b). As fluorescent quenching is thought to result from exposure of the fluorophore to a hydrophilic environment (e.g., [8]), this behavior would suggest that this site becomes more exposed to the cytosol as *internal* Na^+ ions bind to the protein. By

Fig. 9 Simulations using a reduced seven-state model recapitulate AAD-IIc kinetic behavior. **a** Reduced seven-state model used for AAD-IIc simulations. *Boxed values* indicate effective valence associated with partial reactions representing empty carrier and Na^+ interactions and should be compared with the equivalent for the WT electrogenic transport cycle (Fig. 1a). Transition (2↔9) accounts for uncoupled Na^+-leak (see [1]). The voltage dependence of these partial reactions was modeled by applying Eyring transition state theory to describe the dependence of transition rate constants on membrane potential. The voltage-dependent partial reactions involve the movement of the equivalent lumped charges that result in a conformational state change by crossing a sharp energy barrier. We assumed symmetrical barriers, except for transition 9↔0 where an asymmetry factor (asf=0.15) was used to improve agreement with experimental data. The rate constants (in per second) were as follows: $-k_{10}=40\exp(-Vz_{10}\mu/2)$, $k_{01}=40\exp(Vz_{10}\mu/2)$; $k_{12}=[\mathrm{Na}]_0\,5{,}000\exp(-Vz_{12}\,\mu/2)$, $k_{21}=1{,}200\exp(Vz_{12}\,\mu/2)$, $k_{23}=[\mathrm{Na}]_0\,5{,}000$, $k_{32}=400$, $k_{35}=[\mathrm{Na}]_0\,[P_i]_0 2{,}000$, $k_{53}=100$, $k_{56}=k_{65}=10$, $k_{69}=10^4$, $k_{29}=1$, $?k_{09}=[\mathrm{Na}]_i 200\exp(Vz_{09}\,\mu\times\mathrm{asf})$, $k_{90}=7\exp(-Vz_{09}\,\mu(1-\mathrm{asf}))$ and $\mu=e/kT\approx 40\ \mathrm{V}^{-1}$ at 20 °C, $z_{10}=0.4$, $z_{12}=0.1$,$z_{09}=0.5$. The rates constants k_{96}, k_{92} were defined independently in terms of the other rate constants under conditions of zero driving force to satisfy the detailed balance for the leak and cotransport cycles. We assumed the following substrate concentrations on the cytosolic side: $[\mathrm{Na}]_i=10$ mM and $[P_i]_i=1$ μM. **b** Simulations of presteady-state currents in response to voltage steps from −60 mV to test potentials as indicated for three superfusion conditions. In each case, baseline correction has been made. To obtain the true relaxation current magnitude (in **b**), traces should be scaled by $N_t e$, where N_t is the number of transporters and e=the electronic charge. For each case, the corresponding traces from the representative oocyte (Fig. 4a) are shown (*boxed*) for test potentials to −180 and +80 mV with the endogenous oocyte charging transients removed by curve fitting. The measured data were scaled vertically to give a reasonable match to the simulated data. **c** *Upper* normalized Q–V data for Na^+ interaction with external $P_i=0$. *Continuous lines* are fits to data using Eq. 2 with all parameters unconstrained. Q–V data were normalized to Q_{max} obtained from fit to the data set for 100 mM Na^+. *Lower* dependence $V_{0.5}$ on $[Na^+]$. This should be compared with Fig. 4f. **d** *Upper* normalized Q–V data for P_i interaction with external $[Na^+]=100$ mM. *Continuous lines* are fits to data using Eq. 2 with all parameters unconstrained. Q–V data were normalized to Q_{max} obtained from fit to 0 mM P_i data set. *Lower* Dependence of $V_{0.5}$) on $[P_i]$. This should be compared with Fig. 5c. *Continuous line* is a fit using a modified form of Eq. 1 ($n_H=1$), giving $K_{0.5}{}^{Pi}=1$ mM. **e** Simulated steady-state P_i activation (−60 mV, 100 mM Na^+; *filled symbols*) and Na^+ activation (−60 mV, 1 mM P_i; *open symbols*) using data set in **b**. The apparent affinity constants under these conditions were $K_{0.5}{}^{Pi}=1.05$ mM and $K_{0.5}{}^{Na}=102$ mM and the Hill coeff $(n_H)=2.4$, for Na^+ activation found by fitting simulated data points with Eq. 1. Data should be scaled by $N_t e$ to obtain the P_i-induced current ▶

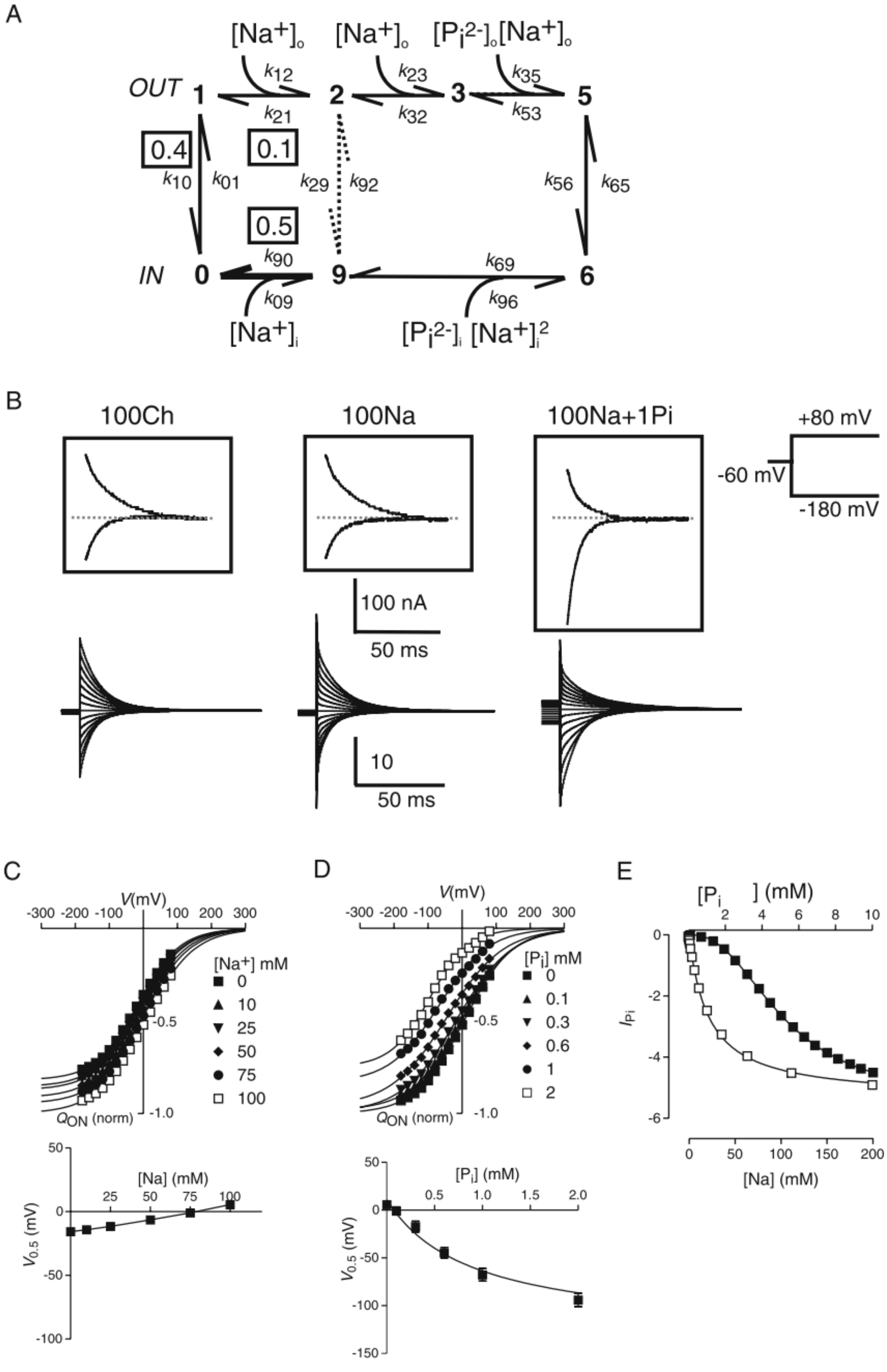
A
[Na+]o
[Na+]o
[Pi2-]o[Na+]o
OUT
1
2
3
5
k12
k21
k23
k32
k35
k53
0.4
0.1
0.5
k10
k01
k29
k92
k56
k65
k90
k09
k69
k96
IN
0
9
6
[Na+]i
[Pi2-]i [Na+]i2
B
100Ch
100Na
100Na+1Pi
+80 mV
-60 mV
-180 mV
100 nA
50 ms
10
50 ms
C
V(mV)
-300 -200 -100 100 200 300
[Na+] mM
■ 0
▲ 10
▼ 25
◆ 50
● 75
□ 100
-0.5
-1.0
QON (norm)
[Na] (mM)
25 50 75 100
V0.5 (mV)
50
0
-50
-100
D
V(mV)
-300 -200 -100 100 200 300
[Pi] mM
■ 0
▲ 0.1
▼ 0.3
◆ 0.6
● 1
□ 2
-0.5
-1.0
QON (norm)
[Pi] (mM)
0.5 1.0 1.5 2.0
V0.5 (mV)
50
0
-50
-100
-150
E
[Pi] (mM)
2 4 6 8 10
IPi
0
-2
-4
-6
0 50 100 150 200
[Na] (mM)

increasing *external* [Na$^+$], the state distribution of AAD-IIc would be altered to favor states 1 and 2 (external binding of Na$^+$) with little voltage-dependent conformational change when external Na$^+$ binds, consistent with our presteady-state relaxation findings. Under these conditions, site 437 would become exposed to the external medium and thereby account for the quenching of steady-state fluorescence in the presence of external Na$^+$. The addition of external P_i (in the presence of external Na$^+$) would further diminish the effect of the cytosolic Na$^+$ interaction on ΔF, as the transport cycle proceeds in the forward (clockwise direction, Fig. 9a). That we did not observe ΔF for depolarizing voltage steps with the S448C flounder NaPi-IIb mutant [35] suggests that for the WT electrogenic isoforms, the conformational changes associated with the binding and release of the last Na$^+$ ion to the cytosol (9↔0) are small compared to AAD-IIc. This is also supported by the model prediction, whereby this Na$^+$ ion would move through a smaller fraction of the transmembrane electric field (Fig. 9a).

The other two AAD-IIc Cys mutants from which we could detect fluorescence changes (AAD-IIc-154, AAD-IIc-222) showed behavior consistent with the altered kinetics of AAD-IIc. The ΔF reported by a fluorophore linked to the Cys −154 (AAD-IIc-154) can be compared with that for the equivalent mutant in flounder NaPi-IIb (S155C) [34]. This mutant shows strong dependence of ΔF on external [Na$^+$] (slope of $V_{0.5}$ vs log [Na$^+$]=140 mV/decade), unlike the weak dependence we report here for AAD-IIc-154 (Fig. 8a, b). Moreover, for S155C when external [P_i] is changed in the presence of 100 mM Na$^+$, we observe strong quenching, but no obvious shift in $V_{0.5}{}^{F}$, whereas AAD-IIc-154 showed a hyperpolarizing shift (Fig. 8b) that was qualitatively similar to the shift found for presteady-state relaxations with variable [P_i] (Fig. 5c) and comparable to the transport $K_{0.5}{}^{Pi}$ (Table 1). The insensitivity to changes in external [Na$^+$] for AAD-IIc-154 indeed suggested that the microenvironment of the fluorophore at Cys −154 reports similar conformational changes to those that give rise to the presteady-state charge movement: reorientation of the empty carrier, including the release of the final Na$^+$ ion to the cytosol during cotransport. Qualitatively similar behavior was found for the ΔF–V data obtained by labeling mutant AAD-IIc-222. Taken together, these findings suggest that the local environments of these sites undergo voltage-dependent conformational changes associated with the empty carrier and cytosolic Na$^+$ release.

Conclusions

Electrogenicity can be conferred to the electroneutral Na$^+$-coupled P_i cotransporter (NaPi-IIc) by the substitution of three amino acids, one of which is negatively charged (D195). We hypothesize that the movement of this charge (evidenced by presteady-state relaxations), results in a conformational change of the empty carrier between inward and outward facing orientations (evidenced by fluorometric recordings), that allows a single Na$^+$ ion to bind from either side of the membrane, subsequently translocate and dissociate, driven by the electrochemical gradient for Na$^+$. Whether or not this charge itself is part of the cation coordination or indirectly exposes a binding site cannot be determined without 3-D structural information. Certainly, for this charged residue to fulfill the role as the empty carrier “voltage sensor”, the current secondary topology model of SLC34 proteins [15], which places D195 close to the cytosolic end of TMD5 and effectively outside the transmembrane electric field (Fig. 1b), would require reassessment.

Although AAD-IIc can be considered an “imperfect” transporter, with a significantly greater E_a than the WT electroneutral and electrogenic isoforms, its deviation from WT behavior has revealed an important partial reaction in the physiologically relevant transport cycle, namely the cytosolic release of a Na$^+$ ion prior to reorientation of the empty carrier. For AAD-IIc, the kinetics of this transition impose a rate-limiting step on the transport cycle, consistent with this ion being more tightly bound to AAD-IIc than for the electrogenic WT isoforms. Identification of this partial reaction in the electrogenic WT would otherwise be difficult to achieve experimentally using the intact oocyte system. The cytosolic dissociation of this Na$^+$ ion, revealed through mutagenesis, means that AAD-IIc provides a unique tool to investigate cation interactions at the internal protein interface for SLC34 proteins.

We originally identified three critical regions in the SLC34 sequences that differed significantly between electrogenic and electroneutral isoforms [4]. Although one of these regions contains D195 (or its equivalent) found in the electrogenic isoforms, the roles played by other dissimilar polar and nonpolar residues in the other regions in establishing a voltage-dependent interaction of external Na$^+$ ions, together with the high apparent affinity for P_i, remain to be elucidated.

Acknowledgments We gratefully acknowledge Eva Hänsenberger for oocyte preparation. Special thanks to Dr Anne-Kristine Meinild (UZH) and Dr Donald D.F. Loo (UCLA) for their insightful comments. This work was supported by the Swiss National Science Foundation grant to ICF and Hartmann Müller-Stiftung grant to CG.

References

1. Andrini O, Ghezzi C, Murer H, Forster IC (2008) The leak mode of type II Na(+)-P(i) cotransporters. Channels (Austin) 2:346–357
2. Andrini O, Meinild AK, Ghezzi C, Murer H, Forster IC (2012) Lithium interactions with Na$^+$-coupled inorganic phosphate cotransporters: insights into the mechanism of sequential cation binding. Am J Physiol Cell Physiol 302:C539–554

3. Bacconi A, Ravera S, Virkki LV, Murer H, Forster IC (2007) Temperature-dependency of steady-state and presteady-state kinetics of a type IIb Na^+/P_i cotransporter. J Mem Bio 215(2–3):81–92
4. Bacconi A, Virkki LV, Biber J, Murer H, Forster IC (2005) Renouncing electrogenicity is not free of charge: switching on electrogenicity in a Na^+-coupled phosphate cotransporter. Proc Natl Acad Sci U S A 102:12606–12611
5. Binda F, Bossi E, Giovannardi S, Forlani G, Peres A (2002) Temperature effects on the presteady-state and transport-associated currents of GABA cotransporter rGAT1. FEBS Lett 512:303–307
6. Bossi E, Cherubino F, Margheritis E, Oyadeyi AS, Vollero A, Peres A (2012) Temperature effects on the kinetic properties of the rabbit intestinal oligopeptide cotransporter PepT1. Pflugers Arch 464:183–191
7. Breusegem SY, Takahashi H, Giral-Arnal H, Wang X, Jiang T, Verlander JW, Wilson P, Miyazaki-Anzai S, Sutherland E, Caldas Y, Blaine JT, Segawa H, Miyamoto K, Barry NP, Levi M (2009) Differential regulation of the renal sodium-phosphate cotransporters NaPi-IIa, NaPi-IIc, and PiT-2 in dietary potassium deficiency. Am J Physiol Renal Physiol 297:F350–361
8. Cha A, Bezanilla F (1998) Structural implications of fluorescence quenching in the Shaker K^+ channel. J Gen Physiol 112:391–408
9. de la Horra C, Hernando N, Lambert G, Forster I, Biber J, Murer H (2000) Molecular determinants of pH sensitivity of the type IIa Na/P(i) cotransporter. J Biol Chem 275:6284–6287
10. Ehnes C, Forster IC, Bacconi A, Kohler K, Biber J, Murer H (2004) Structure-function relations of the first and fourth extracellular linkers of the type IIa Na^+/P_i cotransporter: II Substrate interaction and voltage dependency of two functionally important sites. J Gen Physiol 124:489–503
11. Ehnes C, Forster IC, Kohler K, Bacconi A, Stange G, Biber J, Murer H (2004) Structure-function relations of the first and fourth predicted extracellular linkers of the type IIa Na^+/Pi cotransporter: I Cysteine scanning mutagenesis. J Gen Physiol 124:475–488
12. Forrest LR, Kramer R, Ziegler C (2011) The structural basis of secondary active transport mechanisms. Biochim Biophys Acta 1807:167–188
13. Forster I, Hernando N, Biber J, Murer H (1998) The voltage dependence of a cloned mammalian renal type II Na^+/P_i cotransporter (NaPi-2). J Gen Physiol 112:1–18
14. Forster IC, Biber J, Murer H (2000) Proton-sensitive transitions of renal type II Na^+-coupled phosphate cotransporter kinetics. Biophys J 79:215–230
15. Forster IC, Hernando N, Biber J, Murer H (2012) Phosphate transport kinetics and structure–function relationships of SLC34 and SLC20 proteins. Curr Top Membr 70:313–356
16. Forster IC, Kohler K, Biber J, Murer H (2002) Forging the link between structure and function of electrogenic cotransporters: the renal type IIa Na^+/P_i cotransporter as a case study. Prog Biophys Mol Biol 80:69–108
17. Forster IC, Loo DD, Eskandari S (1999) Stoichiometry and Na^+ binding cooperativity of rat and flounder renal type II Na^+-P_i cotransporters. Am J Physiol 276:F644–649
18. Forster IC, Wagner CA, Busch AE, Lang F, Biber J, Hernando N, Murer H, Werner A (1997) Electrophysiological characterization of the flounder type II Na^+/P_i cotransporter (NaPi-5) expressed in *Xenopus laevis* oocytes. J Membr Biol 160:9–25
19. Ghezzi C, Meinild AK, Murer H, Forster IC (2011) Voltage- and substrate-dependent interactions between sites in putative re-entrant domains of a Na(+)-coupled phosphate cotransporter. Pflugers Arch 461:645–663
20. Ghezzi C, Murer H, Forster IC (2009) Substrate interactions of the electroneutral Na^+-coupled inorganic phosphate cotransporter (NaPi-IIc). J Physiol 587:4293–4307
21. Hazama A, Loo DD, Wright EM (1997) Presteady-state currents of the rabbit Na+/glucose cotransporter (SGLT1). J Membr Biol 155:175–186
22. Karlin A, Akabas MH (1998) Substituted-cysteine accessibility method. Methods Enzymol 293:123–145
23. Lambert G, Forster IC, Biber J, Murer H (2000) Cysteine residues and the structure of the rat renal proximal tubular type II sodium phosphate cotransporter (rat NaPi IIa). J Membr Biol 176:133–141
24. Lambert G, Forster IC, Stange G, Biber J, Murer H (1999) Properties of the mutant Ser-460-Cys implicate this site in a functionally important region of the type IIa Na^+/P_i cotransporter protein. J Gen Physiol 114:637–652
25. Lambert G, Forster IC, Stange G, Kohler K, Biber J, Murer H (2001) Cysteine mutagenesis reveals novel structure-function features within the predicted third extracellular loop of the type IIa Na^+/P_i cotransporter. J Gen Physiol 117:533–546
26. Lester HA, Mager S, Quick MW, Corey JL (1994) Permeation properties of neurotransmitter transporters. Annu Rev Pharmacol Toxicol 34:219–249
27. Mackenzie B, Loo DD, Wright EM (1998) Relationships between Na+/glucose cotransporter (SGLT1) currents and fluxes. J Membr Biol 162:101–106
28. Matthews E Jr, Rahnama-Vaghef A, Eskandari S (2009) Inhibitors of the gamma-aminobutyric acid transporter 1 (GAT1) do not reveal a channel mode of conduction. Neurochem Int 55:732–740
29. Meinild AK, Forster IC (2012) Using lithium to probe sequential cation interactions with GAT1. Am J Physiol Cell Physiol 302: C1661–1675
30. Radanovic T, Gisler SM, Biber J, Murer H (2006) Topology of the type IIa Na+/P(i) cotransporter. J Membr Biol 212:41–49
31. Segawa H, Kaneko I, Takahashi A, Kuwahata M, Ito M, Ohkido I, Tatsumi S, Miyamoto K (2002) Growth-related renal type II Na/Pi cotransporter. J Biol Chem 277:19665–19672
32. Virkki LV, Forster IC, Bacconi A, Biber J, Murer H (2005) Functionally important residues in the predicted 3rd transmembrane domain of the type IIa sodium-phosphate co-transporter (NaPi-IIa). J Membr Biol 206:227–238
33. Virkki LV, Forster IC, Biber J, Murer H (2005) Substrate interactions in the human type IIa sodium-phosphate cotransporter (NaPi-IIa). Am J Physiol 288:F969–F981
34. Virkki LV, Murer H, Forster IC (2006) Mapping conformational changes of the type IIb Na^+/P_i cotransporter by voltage clamp fluorometry. J Biol Chem 281:28837–28849
35. Virkki LV, Murer H, Forster IC (2006) Voltage clamp fluorometric measurements on a type II Na^+-coupled P_i cotransporter: shedding light on substrate binding order. J Gen Physiol 127:539–555
36. Werner A, Kinne RK (2001) Evolution of the Na-P_i cotransport systems. Am J Physiol 280:R301–312
37. Winzor DJ, Jackson CM (2006) Interpretation of the temperature dependence of equilibrium and rate constants. J Mol Recognit 19:389–407

B. Structural model of the human Na$^+$-phosphate cotransporter NaPi-II.

This section contains an original research article as submitted to PNAS. It is currently under revision.

This work is the result of a collaboration between the University of Zurich, the Computational Biology Group at the MPI-Biophysics, Frankfurt (Head, L R Forrest), Dr A. Werner, Newcastle University.

Our attempts to find a suitable template for the construction of a structural homology model for NaPi-II started in 2011 with my visit in the laboratory of Dr Forrest, however at that time no suitable template was found. As a result of further work in Frankfurt, a model was developed based on the bacterial dicarboxylate cotransporter, VcINDY.

My contribution to this paper included the design of mutants, molecular biology, transport assays on mutants to validate the predicted binding sites. I also participated in the data analysis, data interpretation and in the drafting of the manuscript including figures.

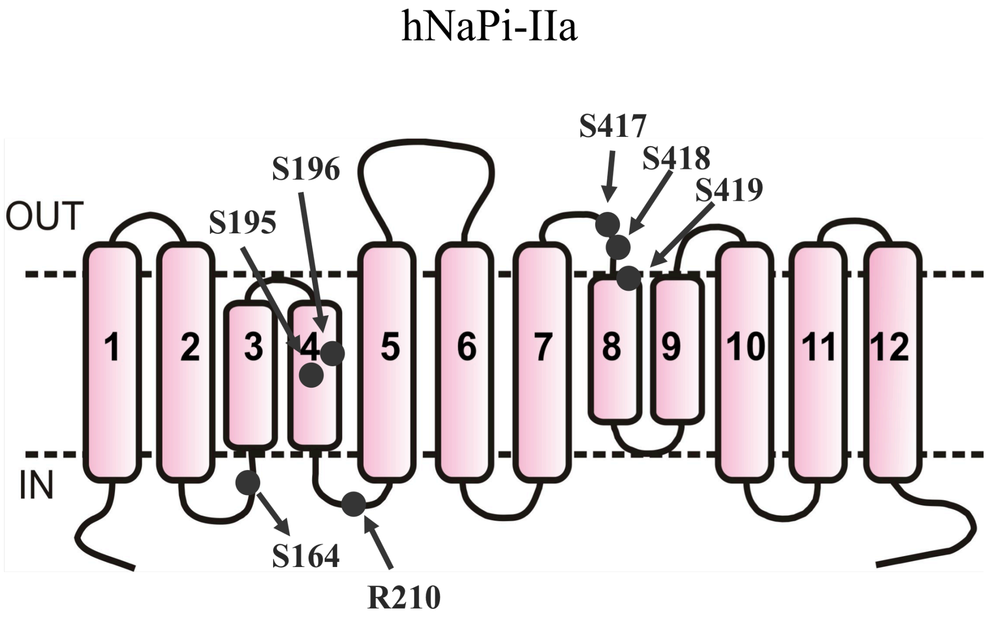

Figure 27 Secondary topology model of hNaPi-IIa showing the mutants investigated in this paper(filled circles).

Structural model of the human Na^+-phosphate cotransporter NaPi-II

Cristina Fenollar-Ferrer[1], Monica Patti[2], Thomas Knöpfel[2], Andreas Werner[3], Ian C. Forster[2] and Lucy R. Forrest[1]

[1]Computational Structural Biology Group, Max Planck Institute of Biophysics, Max-von-Laue-Straße 3, D-60438 Frankfurt am Main, Germany [2]Institute of Physiology and Zurich Center for Integrative Human Physiology, University of Zurich, Winterthurerstrasse 190, CH-8057 Zürich Switzerland [3]Institute for Cell and Molecular Biosciences. Medical School, University of Newcastle upon Tyne, Newcastle upon Tyne, NE2 4HH, United Kingdom

Submitted to Proceedings of the National Academy of Sciences of the United States of America

Homeostasis of inorganic phosphate (P_i) in vertebrates is maintained by control of intestinal absorption, storage and release in bones, and renal excretion. These processes depend on tightly regulated expression of Na^+-coupled P_i transporters of the SLC34 solute carrier family (NaPi-II). Their crucial role in P_i homeostasis is underscored by pathologies resulting from naturally occurring SLC34 mutations and SLC34 knock-out animals. SLC34 isoforms have been extensively studied with respect to transport mechanism and structure-function relationships; however, the 3-dimensional structure is unknown. All SLC34 transporters share a duplicated motif comprising a glutamine followed by a stretch of threonine or serine residues, suggesting the presence of structural repeats as found in other transporter families. Nevertheless, standard bioinformatic approaches fail to clearly identify a suitable template for molecular modeling. Here, we used hydrophobicity profiles and hidden Markov Models to first define a structural repeat common to all SLC34 isoforms. Similar approaches identify a relationship with the core regions in a crystal structure of *Vibrio cholerae* Na^+-dicarboxylate transporter VcINDY, from which we generated a homology model of human NaPi-IIa. The aforementioned SLC34 motifs in each repeat localize to the center of the model, and were predicted to form Na^+ and P_i coordination sites. Functional relevance of key amino acids was confirmed by biochemical and electrophysiological analysis of expressed, mutated transporters. Moreover, the validity of the predicted architecture is corroborated by extensive published structure-function studies. The NaPi-IIa model provides a firm foundation for a molecular understanding of Na^+-coupled P_i uptake by SLC34 transporters.

secondary-active carrier | homology modelling | inverted repeat topology | phosphate transport | membrane protein

Introduction

Cells depend on inorganic phosphate (P_i) to ensure growth and structural integrity, maintain energy balance and communicate with their environment. In mammals, P_i transport across the cell membrane is mediated by secondary-active transporter proteins that use the free energy from the Na^+ gradient and transmembrane electrical potential to catalyse uphill P_i transport. Multicellular organisms, especially vertebrates, face a particular challenge in maintaining whole body P_i homeostasis: the solubility of P_i is limited in the presence of divalent cations, especially calcium, and excess of P_i in bodily fluids promotes Ca-P_i precipitation. This is of particular concern in patients with chronic kidney disease who tend to retain excessive levels of P_i (hyperphosphatemia) that leads to vascular calcification (1).

A family of Na^+-coupled P_i transporters belonging to the solute carrier family SLC34 (NaPi-II), is central to maintaining whole body P_i homeostasis (2). All vertebrates express up to three isoforms of NaPi-II in organs that contribute to maintaining P_i balance. Mammals express NaPi-IIa (SLC34A1) and NaPi-IIc (SLC34A3) in the renal proximal tubule and NaPi-IIb (SLC34A2) in intestine, where they mediate intestinal absorption and renal excretion of P_i, respectively (2-4). The central role of NaPi-II proteins emerged when hormones and metabolic factors known to influence body P_i levels, such as parathyroid hormone, calcitonin, growth hormones or P_i availability, were found to regulate NaPi-II membrane expression (reviewed in (5, 6)). Their homeostatic role was further corroborated when NaPi-II knockout mice displayed organ specific perturbations of P_i handling (7). Importantly, in humans, dysfunction in renal P_i handling can be attributed to naturally occurring mutations in NaPi-IIa (8, 9); NaPi-IIc (10) and to P_i-related pathologies for NaPi-IIb in lung and testes (11), further underscoring the importance of these proteins.

A detailed characterization of all three isoforms (NaPi-IIa/b/c) has emerged from functional analyses of wild type and mutant transporters expressed in *Xenopus laevis* oocytes. NaPi-II proteins transport one divalent P_i ion with an apparent affinity ($K_{0.5}^{Pi}$) of 10-70 μM, together with two (NaPi-IIc) or three Na^+ ions (NaPi-IIa and NaPi-IIb) with an apparent affinity ($K_{0.5}^{Na}$) of 25-50mM (reviewed in (12)). The experimental evidence supports the notion that NaPi-II proteins mediate transport according to the canonical alternating access mechanism (e.g. (13-15)). In the normal transport cycle (Fig. 1A), substrate binding at the external side is ordered, with 2 Na^+ ions binding before P_i. These cation interactions, together with mobile charges associated with the empty carrier reorientation, determine the voltage dependence of the NaPi-IIa/b transport cycle (12). In contrast, the electroneutral NaPi-IIc cycle lacks sensitivity to membrane voltage and only one of the Na^+ ions preceding P_i binding is translocated. For all 3

Significance

Phosphate plays a multitude of essential biological roles and its plasma level requires tight control to avoid bone loss (insufficiency) or vascular calcification (excess). Intestinal absorption and renal reabsorption of phosphate are mediated by the SLC34 family of sodium-coupled transporters. Consequently they are potentially important pharmaceutical targets for controlling phosphate levels. However, the design of SLC34-specific inhibitors is hampered by the lack of 3-dimensional protein structure. We report the results of a novel strategy to predict the structure of a human SLC34 isoform, involving hydropathy analysis of its inverted repeat architecture and homology modeling using the crystallized dicarboxylate transporter VcINDY as a template. The model provides key information to elucidate the transport mechanism and identify potential sites for drug action.

Reserved for Publication Footnotes

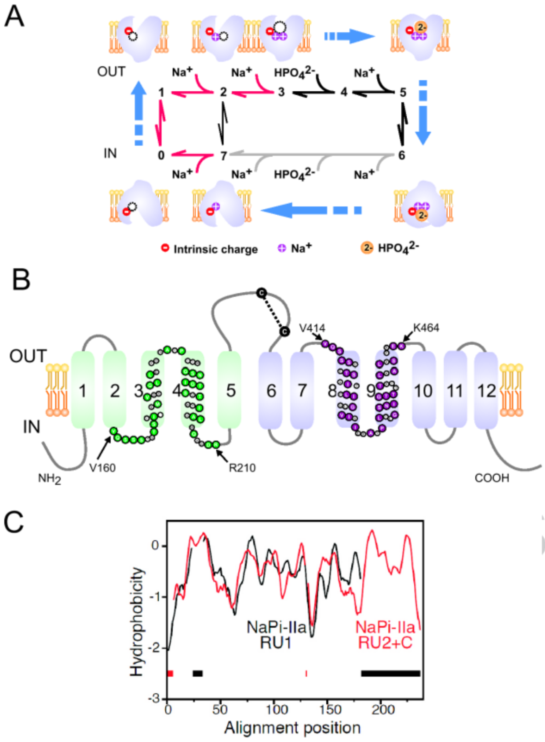

Fig. 1. Kinetic and structural features of NaPi-IIa. **A** The transport cycle is depicted as a sequence of partial reactions between conformational states, numbered 0-7 (reviewed in (12)). Cartoons illustrate the ordered nature of protein-substrate interaction based on experimental evidence. Partial reactions on the cytosolic side have not been explicitly identified except the last Na$^+$ release (step 7→0) (56). Red arrows: electrogenic partial reactions (involving charge movement); black arrows: electroneutral partial reactions. In the absence of external P$_i$, Na$^+$ ions can also translocate via a leak transition (2↔7) (37). For the electroneutral cycle (of NaPi-IIc), all transitions are electroneutral and the first Na$^+$ ion to bind (step 1↔2) is hypothesized not to translocate (17). **B** Secondary topology of NaPi-IIa based on previous experimental evidence and bioinformatic predictions (12). The assumed boundaries of repeat regions (rat sequence) are indicated (31); colored symbols indicate identical or conserved residues in each repeat. A disulfide bridge links the two halves of the protein in the large extracellular loop. **C** Hydropathy plots of the regions predicted to contain the structural repeats in NaPi-II, averaged over a set of sequence homologues and aligned using AlignMe. Region 1, containing residues 86-256 of the human NaPi-IIa (RU1, *black*) is aligned to region 2 plus C-terminus consisting of residues 335-564 (RU2+C, *red*). Gaps in the alignment are indicated by dashes along the base of the plot.

isoforms, binding of the last Na$^+$ is a rate-determining partial reaction (Fig. 1A, step 4↔5) (16, 17).

All vertebrate NaPi-II homologs identified and studied to date appear to share an identical transmembrane (TM) topology (12, 18) (Fig. 1B). Specifically, the protein contains two sets of TM helices, each containing a copy of a conserved sequence motif, separated by a large extracellular loop. Epitope tagging and cysteine scanning mutagenesis experiments suggest that these repeated units have inverted transmembrane topologies and that both termini are in the cytosol (12, 18). However, a three-dimensional structural model of NaPi-II proteins that integrates these functional and structural data is still lacking, preventing further understanding and limiting experimental design.

The recognition that NaPi-II proteins possess an inverted-topology repeat architecture, which represents the key signature in a number of secondary active transporters (e.g. (13, 19)), prompted us to search for a suitable template among the crystal structures of solute transporters reported to date, from which a homology model could be generated.

Results *Identifying the repeated elements and peripheral transmembrane helices in NaPi-IIa*

Modeling the structure of a protein is aided by knowledge of the conserved and repeated structural elements within its fold. Although it was clear from earlier studies, and from the presence of a repeated conserved motif (Fig. S1), that NaPi-II transporters contain a structural repeat with inverted topology, it was not clear where the boundaries of the repeat units lay, nor whether their overall fold had an equivalent already reported. Aligning family-averaged hydropathy profiles of different fragments of the sequence clearly shows that the structure comprises the two repeat units (RU1, RU2) plus a C-terminal extension of two additional TM helices (Fig. 1C). These segments correspond to TMs 1-5, TMs 6-10 and TMs 11-12, respectively, of the published topology (Fig. 1B).

A similar result was obtained by aligning HHalign hidden Markov models (HMMs) of region 1 with region2 or with region2+C (see Methods; Figs. S1, S2), which confirmed that regions 1 and 2 have similar secondary structure and further indicated that they have ∼27% identical residues. We concluded that RU1 and RU2 in NaPi-II comprised residues 86-256 and 335-489, respectively, and residues 504-564 form peripheral TM helices that are not part of the core fold.

Identifying a structural homolog of NaPi-IIa

To identify a putative template structure for NaPi-IIa, several approaches were attempted (see Methods), of which only HHpred produced hits. The E-values of the top ten hits were large (>2.4×10^2), indicating that the confidence levels were low, and three water-soluble proteins had to be excluded. The remaining seven hits included three aquaporins, a GlpG protease, a KQT potassium channel and a disulphide reductase, DsbD, none of which are involved in cation-coupled cotransport. However, the fifth-place hit was a Na$^+$-coupled dicarboxylate transporter from *Vibrio cholerae,* called VcINDY (20).

Alignments of NaPi-IIa with four of the five highest-scoring membrane proteins (aquaporin-4, GlpG protease, AQY1 aquaporin and VcINDY) using AlignMe in PS mode, indicated that, despite its lower ranking, the template with the greatest fold similarity is indeed VcINDY, with 62% sequence coverage and 7% identical residues, compared to ≤40% coverage and ≤4% identity for the other four proteins. (The other hit in the top five, the KQT potassium channel, was excluded because the matched region obtained by HHpred comprised unconserved residues.) Like NaPi-II, VcINDY also contains an inverted-repeat topology, and the aligned fragment matches the conserved QSSS NaPi-II motif to the SNT motif that contributes to Na$^+$ and dicarboxylate binding in VcINDY (Fig. S3A), suggesting that the binding site regions are somewhat conserved.

To identify all of the corresponding helices in the VcINDY and NaPi-II repeats, we aligned hydropathy profiles of RU1 or RU2 from the two proteins (Fig. 2A), as well as HMMs of these repeat units (Fig. S3B and S3C). Alignments from both methods, as well as from AlignMe (in PST mode), indicated that the first two TMs of each of the repeats of VcINDY have no equivalent in NaPi-IIa (Fig. S4A). These additional helices (TMs 2, 3, 7 and 8) are located at the periphery of the VcINDY structure (Fig. S4B), and therefore could be omitted from the model of NaPi-IIa without affecting the core transport unit. Moreover, according to HHalign and AlignMePST, the proposed Na$^+$ and substrate binding site residues of both RU1 and RU2 of VcINDY were aligned to the most conserved regions of NaPi-IIa (Figs. 2B, S3B

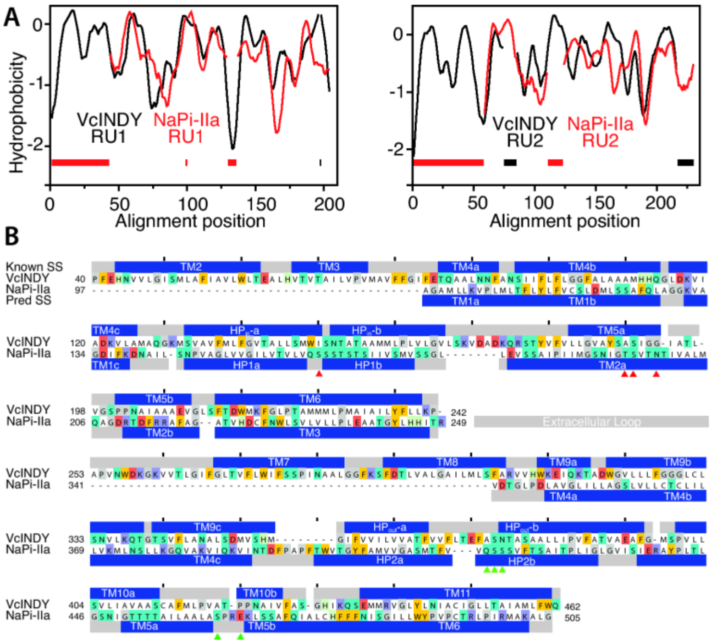

Fig. 2. Figure 2. Comparison of repeat units in NaPi-II and the sodium-carboxylate transporter VcINDY suggests that they share a common fold. **A)** Hydrophobicity profiles of the two repeat units in NaPi-II (*red line*) and VcINDY (*black line*). Hydropathy plots averaged over a set of sequence homologs of human NaPi-IIa or of VcINDY were aligned using AlignMe for repeat unit 1 (*left*) and repeat unit 2 (*right*). **B** Sequence alignment between VcINDY and the core region of human NaPi-IIa used for modeling. The helices assigned from the structure of VcINDY ("Known SS") and the PSIPRED predictions for helices in NaPi-IIa ("Pred SS") are shown as blue bars above and below the sequences, respectively. Residues whose side chains contribute to site Na2 (*red triangles*) or Na3 (*green triangles*) are indicated.

and S3C). Together these results strongly support the choice of VcINDY as a template for NaPi-II transporters, in spite of the low confidence of the identification by HHpred.

Accordingly, the core structure of NaPi-IIa constitutes an inverted-topology repeat of 3TM+hairpin (HP, Fig. 3), which was modeled using the two inverted repeats of VcINDY and excluding the first two TMs of each repeat as a template (Fig. S4A).

An atomistic structural model of human NaPi-IIa

A model of human NaPi-IIa comprising residues 97-249 (RU1) and 341-505 (RU2) was constructed (Fig. 4A-C), whose topology (Fig. 3) differs slightly from earlier proposals (Fig. 1B), due to the presence of helical hairpins that do not fully span the membrane, and due to long non-helical elements within TMs 2 and 5. Nevertheless, the new topology agrees well with results from studies on various SLC34 isoforms expressed in *Xenopus* oocytes using cysteine scanning mutagenesis and accessibility measurements (SCAM, e.g. (21-27)), cross-linking (28), and *in vitro* glycosylation techniques (29). These studies together predicted a number of topological features consistent with our model (Fig. 3B).

First, SCAM applied to the linker between TM1 and TM2 of RU1 (see Fig. 3B) established that this region is accessible to the external medium (27), consistent with its position at the exposed external surface of our model (helix 1c, Fig. 4C).

Second, in RU2, an externally accessible region was found by cysteine scanning in loop L5ab between TM5a and TM5b (Fig. 3B) (24). In our model (Fig. 4C), this linker is localized deeper in the protein than in our earlier prediction (Fig. 1B), as deep as the proposed substrate coordination sites (see below). Nevertheless, it would be accessible to cysteine modifiers via the same aqueous pathway as the substrates.

Third, when S183 in NaPi-IIa or the equivalent site in flounder NaPi-IIb (S155) at the top of helix 2a in RU1 (Fig. 3B) is substituted by Cys, thiol modification from the external medium is possible, albeit with minimal functional consequences (28-30). These findings are consistent with the relatively exposed position of this site in our model (Fig. 4C).

Fourth, according to SCAM, there are four sites that are accessible only from the cytosol: N199 at the end of TM2a, as well as V202, A203 and M205 from L2ab (22) (Fig. 3B). The model suggests that these sites are buried in the modeled outward-facing state of the transporter, but are likely to be accessible from the internal medium in a cytosolic-facing state.

Fifth, according to our model, TM3 acts as a buried "scaffold" (Fig. 3C). Indeed, Cys-mutagenesis of human NaPi-IIa indicated that this region was inaccessible from the external medium, with the exception of A240 at its extracellular end (25) (Fig. 3B).

We note that the NaPi-IIa model has the opposite TM topology compared to the core of VcINDY, with the first helix of RU1 in NaPi-II originating in the cytoplasm (Fig. S4). This may reflect the additional N-terminal TM helix in VcINDY (Fig. S4), which may cause inversion of the subsequent helices. As a consequence, the model of NaPi-IIa corresponds to an extracellular-facing state, even though the template structure reflects a cytoplasm-facing orientation.

In summary, given the excellent agreement of the model with the published topological data, we then proceeded to use this model to predict the binding sites for Na$^+$ and P$_i$ in NaPi-IIa.

Proposed Na2 binding site

As noted above, the Na$^+$ and citrate coordinating residues located in the loops of the hairpins (HP$_{in}$ and HP$_{out}$) in VcINDY have conserved polar counterparts in the NaPi-IIa hairpins HP1 and HP2 (Fig. 2B, 4C). In addition, after comparing the structures, we observed that the side chain of N199 from TM2a of NaPi-IIa (Fig. 4D) occupies an equivalent position spatially to the Na$^+$-binding residue N151 of VcINDY (20) even though they come from different helices. Interestingly, Cys substitution of N199 in rat NaPi-IIa reduces the apparent Na$^+$ affinity for transport by 40-fold (22). After modeling an ion into this region, designated the Na2 site (see Discussion), three other highly con-

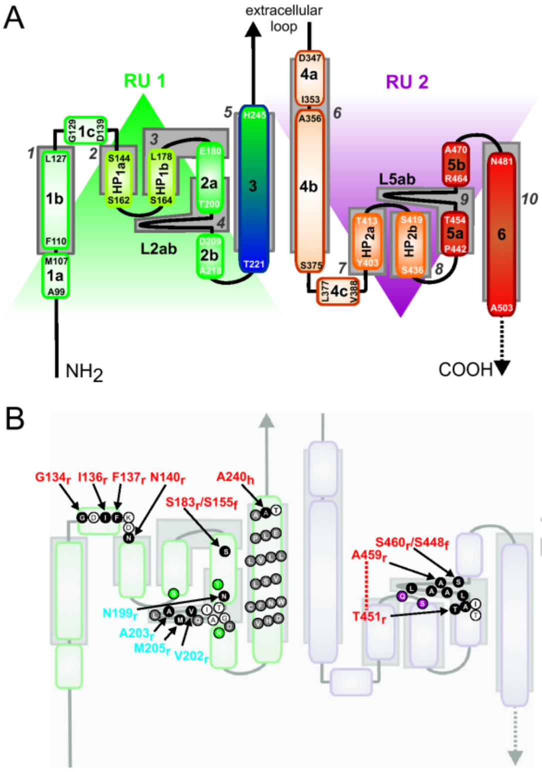

Fig. 3. Schematics of new topology of NaPi-IIa. **A** Topological elements are colored shades of green for RU1 and shades of red for RU2, and the structural repeats (RU1, RU2) are indicated (*shaded triangles*). Approximate positions of helical domains according to earlier topology (*gray boxes*) are numbered according to the scheme in Fig 1B for the human NaPi-IIa sequence. **B** Comparison with published experimental data. The position of key residues is indicated. Residues that are accessible based on cysteine scanning (SCAM) studies (*black filled circles*); residues that are inaccessible based on SCAM (*grey filled circles*) are highlighted. Sites accessible from the external milieu (*red*) or accessible only from internal milieu (*blue*) are labeled according to the organism: flounder NaPi-IIb (f), human (h) or rat (r) NaPi-IIa. Positions on topology for residues mutated in this study are also shown (*green and violet filled circles for RU1 and RU2, respectively*).

served hydroxyl-containing residues lay within the coordination shell of the ion, namely S164 from HP1b, and T195 and S196 from TM2a (Fig. 4D).

Proposed P_i binding site

Assuming direct coupling between substrate and Na^+, as in VcINDY (Fig. S4A), a P_i ion was placed at a position equivalent to that of the bound citrate (Fig. 4D), and located at the axis of the two-fold pseudo-symmetry between the structural repeats, as is common for transporter binding sites (13). We imposed coordination of the P_i by S164 and N199, such that they each coordinate one Na^+ and the P_i. Interestingly, the residue at the position of N199 was shown to be a critical determinant of the mode of transport: whereas both small polar and non-polar residues are tolerated at this site such that normal cotransport mode occurs, substitution of large polar and acidic or basic residues at this position results in exclusively uncoupled leak (transition 2↔7, Fig 1A) (31). Such an important role in coupling is consistent with the predicted direct coordination of both substrates (Fig. 4D).

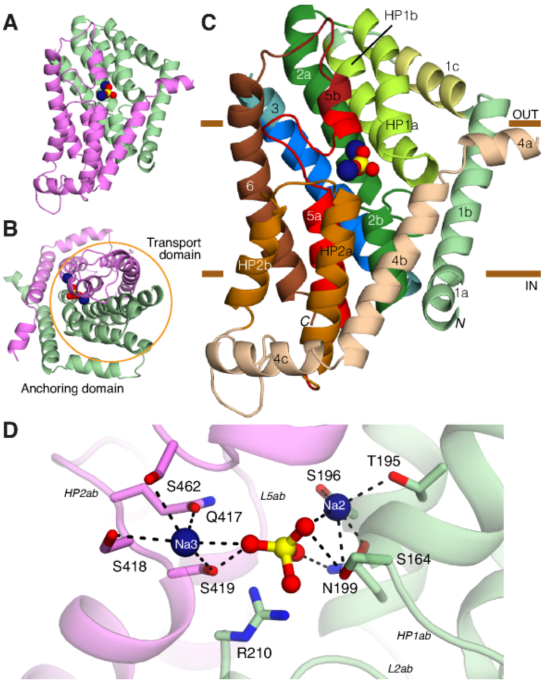

Fig. 4. Structural model of human NaPi-IIa in atomic detail. **(A,B,C)** Overview of the fold of the NaPi-IIa model represented by cartoon helices. Two sodium ions (*blue*) and P_i (*yellow, red*) are shown as spheres. The model is viewed **(A,C)** from within the plane of the membrane, or **(B)** from the extracellular side. **(A,B)** Location of the structural repeats RU1 (*green*) and RU2 (*pink*). The transport domain is highlighted by an orange circle, in **A**. **C** Individual helices are colored according to Fig. 3A. Regions for which experimental data relating to the topology are highlighted: residues accessible to the extracellular side (*yellow*) or buried (*blue*) in helix 1c and 3, respectively; and residues expected to be helical in TM5a, TM5b and the 5ab loop (*red*). The approximate extents of the membrane are indicated by brown bars. **D** Close-up of the predicted substrate binding sites in NaPi-IIa, using the same orientation as in **A**. Residues close to the binding site are highlighted (*sticks*), as are bound P_i (*ball and stick*), and sodium ions (*spheres*). Residues S164, N199 and S462 have previously been implicated in substrate binding. Residues T195, S196, N199, R210, Q417, S418, S419 are investigated in the present study.

In the model, S164 (at the start of HP1b) has a symmetry-equivalent position S419 at the start of HP2b, and so we propose that S419 also coordinates P_i. Finally, R210 from TM2b was also close to this P_i binding site in this model and therefore has been considered here as a putative P_i coordinating residue.

Proposed Na3 binding site

From our model, a second Na^+ site was identifiable, based on the pseudo-symmetry of position S419, which also involves direct coordination by the substrate P_i. S462 lay within the coordination sphere of that site at the start of TM5b, whose mutation to Cys in flounder NaPi-IIb (S448) and at the equivalent position in NaPi-IIc (S437), when modified by a thiol reagent, abolishes transport (17, 23) (32). Under these conditions, Na^+ and P_i can still bind (partial reactions 1↔2, 2↔3 and 3↔4, Fig. 1A) (17, 23, 28, 32), but either the final Na^+ binding step or the translocation step has been compromised, consistent with the notion that S462 contributes to the third Na^+ binding site, hereafter designated Na3.

Table 1. Functional properties of mutants

Construct	^{32}P uptake	Presteady-state		Activation index	
		100Na	100Na +P$_i$	P$_i$[1]	Na[1]
WT	+	+	↓	0.61	0.63
S164A	-	+	↓	n.a.	n.a.
S164C	-	+	↓	n.a.	n.a.
T195C	-	+	↓	n.a.	n.a.
S196C	-	-	-	n.a.	n.a.
N199C[2]	+	n.d.	n.d.	0.20	0.10
R210C	+	+	↓	0.60	0.65
Q417C	+	+	↓	0.46	0.39
S418C	-	-	-	n.a.	n.a.
S419A	-	+	↔	n.a.	n.a.
S419C	-	-	-	n.a.	n.a.

1. Activation indices were defined as ratio of P$_i$-induced current at -50 mV for 0.1 mM P$_i$ and 1 mM P$_i$ in 100 mM Na$^+$ (P$_i$ index) and for 50 mM Na$^+$ and 100 mM Na$^+$ for 1 mM P$_i$ (Na index). These ratios give an approximate indication of shifts in the apparent substrate affinity for screening purposes (e.g. 27).
2. Data taken from (22) for mouse NaPi-IIa isoform.
3. n.a.: not applicable; n.d.: not determined; -: not detected; +: detected.
4. Presteady-state relaxations suppressed (↓) or left unchanged (↔) by 1 mM P$_i$.
5. Bold entries indicate constructs used for immunohistological confirmation of membrane expression (Fig S5).

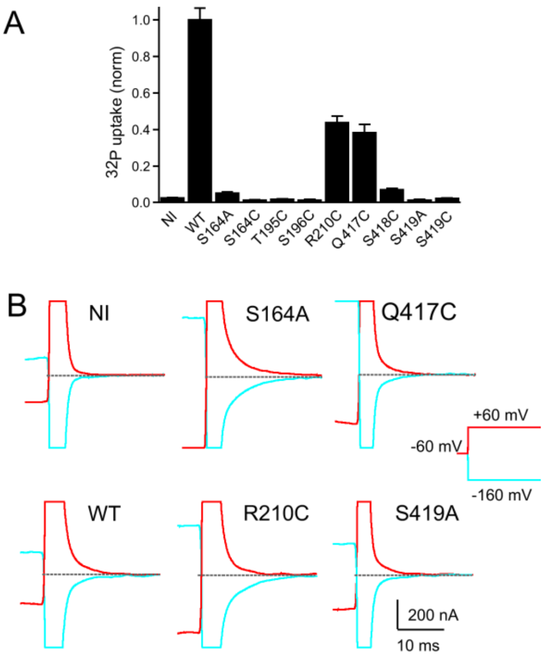

Fig. 5. Effect of site-specific mutations on transport and substrate interactions in human NaPi-IIa. **A** Tracer uptake (^{32}P) data normalized to WT for the mutants and non-injected (NI) oocytes as control. Each data set is the mean±SEM of data from two batches of oocytes (4-5 oocytes per batch). **B** Representative presteady-state relaxations measured from selected constructs as indicated, representing mutations in each repeat together with WT and NI as controls. Currents shown in response to voltage steps as indicated, from a holding potential = –60 mV to two test potentials: –160 (*blue*) and +60 mV (*red*). Data were baseline corrected (*dashed line*) and are shown within a ±500 nA range only.

Two other sites located in L5ab, corresponding to A455 and L457 have been mutated to Cys and subjected to thiol modification. Not only was cotransport function compromised, but the uncoupled leak activity (transition 2↔7, Fig. 1A) significantly increased (24), providing further confirmation of the importance of this loop in substrate translocation.

Finally, according to their proximity in the model, we propose that residues Q417 and S418 coordinate this ion in addition to S419 and S462.

Confirmation of predictions by functional studies of NaPi-IIa mutants

To examine the possible involvement of these sites for substrate coordination in NaPi-IIa, we mutated S164, T195, S196, R210, Q417, S418 and S419 to Ala or Cys, expressed the mutant constructs in *Xenopus* oocytes and performed standard radiotracer and electrophysiological assays to compare their functional behavior with that of WT NaPi-IIa (Table 1 and Fig. 5). Expression of the mutated, potentially non-functional transporters in the oocyte membrane was confirmed by immunohistochemistry and pre-steady state relaxation measurements (Figs. 5 and S5, Table 1). The latter reflect intramolecular rearrangements induced by rapid changes in the membrane potential associated with the empty carrier reorientation and Na$^+$ binding (Fig. 1A) (12).

Two constructs (R210C and Q417C) gave significant ^{32}P uptake (Fig. 5A) as well as P$_i$-induced currents under voltage clamp (Table 1). The activation indices, which indicate whether significant changes in apparent affinities for Na$^+$ and P$_i$ have occurred (e.g. (27)) were close to the WT values for R210C, whereas Q417C showed significantly reduced activation indices (Table 1). These findings indicate that transport and binding were unaffected by the R210C mutation, but that the Gln-Cys substitution in the predicted Na3 site (Fig. 4D) reduced the apparent substrate affinities.

Three constructs (S196C, S418C, S419C) showed neither functional transport nor resolvable presteady-state relaxations (Table 1), which suggested that the native Ser are critical for Na$^+$ coordination in both the predicted Na2 and Na3 sites (Fig. 4D).

Four constructs (S164A, S164C, T195C and S419A) gave resolvable presteady-state relaxations in the presence of 100 mM Na$^+$, but insignificant ^{32}P uptake and no P$_i$-induced current under voltage clamp (Table 1). The detection of presteady-state relaxations superimposed on the linear capacitive charge current of the oocyte membrane (Fig. 5B) provided strong experimental evidence that one or more Na$^+$ ions could still interact with these four mutant proteins in the absence of P$_i$, in agreement with our kinetic scheme for the WT (Fig. 1A). However, subsequent partial reactions required for cotransport were compromised by these mutations. For three of these constructs with mutations located in RU1 (S164A/C and T195C), we also observed that P$_i$ inhibited the presteady-state relaxations in the presence of 100 mM Na$^+$ (Table 1), as previously reported for the WT (16, 33). This behaviour was taken as evidence that P$_i$ could still interact with the protein, but that the conservative mutations at positions 164 and 195 prevented completion of the normal cotransport cycle. At position 419, the Ser to Cys substitution abolished transport, but relaxations were observed in the Ser to Ala mutant: interestingly, it was found that P$_i$ did not suppress those relaxations (Table 1), suggesting that the P$_i$ coordination had been compromised, in agreement with the predicted involvement of S419 in coordinating both Na3 and P$_i$ (Fig 4).

Taken together, the experimental data are consistent with our predictions that S164 coordinates Na2 and/or P$_i$; that T195 and S196 contribute to the Na2 binding site; and that Q417, S418 and S419 coordinate Na3, with the latter also likely to contribute to P$_i$ coordination. However, based on the WT-like behavior for

R210C, it is likely that R210 does not contribute to substrate coordination.

Discussion

Here we propose a structural model for the human NaPi-II cotransporter (SLC34A1) consistent with the inverted repeat architecture common to all members of this family of Na$^+$-coupled cotransporters. The crystal structure of the bacterial Na$^+$-dicarboxylate transporter (VcINDY) (20) was used as a template for a homology modeling approach.

The structural repeat has emerged as a common architectural *leitmotif* in a number of the transporters with solved 3-D structures (e.g. (13, 34)), of which a large proportion contains an inverted transmembrane topology. In NaPi-IIa the repeated sequence of the QSSS motif is particularly prominent, and biochemical studies suggested that these were indeed accessible from opposite sides of the membrane, consistent with them exhibiting inverted topologies (22, 24). Attempts to compare the NaPi-II hydropathy profiles with those of published transporter structures containing inverted repeats failed to reveal any significant profile similarities, in terms of peak heights, widths and number, until the structure of VcINDY was reported (20). We followed up the qualitative indications from the hydropathy analysis with more statistical approaches such as COMA and HHalign, although only the latter identified VcINDY as a putative relative, and even then with a low confidence and ranking. Careful sequence comparisons of the structurally repeated regions and identification of unrelated peripheral helices was required to obtain greater confidence in their relationship. Hydropathy-profile alignments, which can detect remote relationships (e.g. (35)), were essential to identify the equivalent elements. However, this approach is rather imprecise and statistically poorly defined, so the final sequence comparisons were made with quantitative techniques using detailed sequence profiles to represent each region. The two strategies converged in their matching of transmembrane segments, and placed conserved residues from NaPi-II at the binding region of VcINDY.

To our knowledge, the strategy used to identify equivalent regions in the template by separating out the structural repeats is novel and may be applied to model other transporters of as yet unknown architecture.

The QSSS repeats are hallmarks of all NaPi-II isoforms from bacteria to human (36) and, according to our model, help coordinate P$_i$, Na2 and Na3. When we mutated residues that contribute to the predicted coordination sites (S164, T195, S196, Q417, S418 and S419), even with very conservative substitutions, transport was either markedly affected or abolished completely. These data, combined with previous evidence for N199 and S462, provide very strong support for our model.

Currently, there is insufficient evidence to locate the binding site of the first Na$^+$ ion, designated Na1, (partial reaction $1 \leftrightarrow 2$, Fig. 1A). In the electroneutral isoform this ion is hypothesized to allosterically interact with NaPi-IIc and contribute to the overall cooperativity of Na$^+$ activation, but not be translocated (17). In contrast, for the electrogenic isoforms (NaPi-IIa and NaPi-IIb) the binding of a Na$^+$ ion to Na1 to the outward facing conformation (state 1) is critical for conferring electrogenicity to the transport cycle; moreover, in the absence of P$_i$, this ion is assumed to contribute to the uncoupled leak (37). The model proposes that P$_i$ is tightly coordinated with 2 Na$^+$ ions (at sites Na2 and Na3), and so together these would constitute the translocated, and effectively electroneutral, complex for both electroneutral and electrogenic isoforms.

In addition to the functional importance that we demonstrate, the phylogentic conservation of the QSSS signature also indicates that the reported model is representative of all NaPi-II isoforms. Recently, the structure of a fungal proton-dependent P$_i$ transporter has been reported (38). This protein is homologous to the yeast high affinity P$_i$ transporter PHO84 and, to a lesser extent, similar to the mammalian solute transporters SLC22 and SLC2, and is therefore a member of the major facilitator superfamily (MFS) of transporters, with its characteristic fold of two lobes, each containing 6 TM helices. Thus, the new structure is unrelated to the SLC34 family of epithelial P$_i$ transporters.

To conclude, this work reports the first structural insights into a human, epithelial Na$^+$-coupled phosphate transport protein. Since the proposed model is relevant for all members of the SLC34 family it will impact on strategies to inhibit or enhance P$_i$ transport. This is of particular importance for the treatment of end stage renal disease (ESRD), which is prominently associated with hyperphosphataemia. Disturbed P$_i$ homeostasis promotes atherosclerosis, a major cause of morbidity and mortality for patients suffering from ESRD (39). Phosphate binders to reduce the P$_i$ load in these patients have severe side effects (40) so structure-based design of inhibitors of NaPi-II to reduce intestinal P$_i$ uptake has significant clinical potential.

Methods

Sequence analysis of NaPi-IIa

To identify conserved structural regions in NaPi-II transporters, sequence homologs of NaPi-IIa were collected with a 3-iteration HMMER search using the sequence of mouse NaPi-IIa (accession NP_035522) on the HHMER server (41). Note that the mouse and human NaPi-IIa sequences share 91% identical residues overall, and 97% in core regions; for ease of comparison we use the human residue numbering throughout. The NaPi-IIa sequence was scanned against the NCBI nr database dated 20.02.13 and the homologs obtained were clustered using UCLUST (42)with a similarity cutoff of 50%. Representative sequences <400 residues in length were excluded so that every sequence in the final alignment covered >70% of the query sequence. The resultant 300 sequences were multiply aligned using MSAProbs (43). Blocks of conserved residues in the resultant multiple-sequence alignment (see subset in Fig. S1) were identified as belonging to repeated regions in NaPi-IIa (see Results), and given preliminary assignments of region 1 (residues 86-256), and region 2 (residues 335-489). These residue definitions were made as inclusive as possible, so as not to truncate any helices. However, it was not clear whether an additional conserved segment at the C-terminal end of region 2 (region C, residues 504-564) is part of the structural repeat.

To refine the boundaries of the structural repeats, we analyzed hydropathy profiles of the three regions. From the MSAprobs multiple-sequence alignment, three segments were extracted, namely region 1, region 2, and a longer version of the latter including region C, called region 2+C. Hydropathy profiles for these segments, averaged over all sequences in each multiple-sequence alignment, were constructed and aligned using the AlignMe (44) web server (http://www.bioinfo.mpg.de/AlignMe), using the Hessa et al. (45) hydrophobicity scale and a 13-residue long triangular window for smoothing.

To identify more precisely the equivalent residues in the identified structural repeats of NaPi-II at the sequence level, we used hidden Markov Models (HMMs) as descriptors of a given sequence region. First, an HHalign HMM based on NaPi-II sequences was obtained by using the HHblits web server to scan the mouse NaPi-IIa sequence against the NCBI nr20 database dated 22.02.13 (46). From these results, the best 50 sequence hits were selected, short sequences that covered only one of the two repeats were excluded, and from the remaining sequences the final HMM for NaPi-II was constructed. From this full-length profile, shorter HMMs were extracted that corresponded to the different regions mentioned above. Subsequently, the region 1 HMM was aligned with either the region 2 HMM, or the region2+C HMM, using the HHalign server (47) (Fig. S2).

These approaches led to a definition of repeat unit 1 (RU1) as residues 86-256, and repeat unit 2 (RU2) as residues 335-489 (see Results).

Identification of VcINDY as a suitable template

Putative templates were searched for using PSI-BLAST (48), Phyre2 (49) and COMA (50). We also used the full-length HHalign HMM of NaPi-IIa to scan the pdb70 database (from 4.4.13) using the HHpred server (47). Hits from the HHpred search were compared with NaPi-II by full-length pair-wise alignments using the Profile+Secondary-Structure (AlignMePS) mode on the AlignMe server (http://www.bioinfo.mpg.de/AlignMe).

Sequence homologs of a putative template, VcINDY (see Results) were identified as above for NaPi-IIa. Sequences too short to cover an entire structural repeat of VcINDY (<300 residues) were excluded. The resultant HHalign HMM of full-length VcINDY contained 729 sequences. From this, fragment HMMs were extracted for RU1 and RU2 of VcINDY, i.e., residues 40-242 covering TMs 2-6, and residues 253-462 covering TMs 7-11, respectively.

Structural Modelling of NaPi-IIa

For a given template, the sequence alignment to the target protein (here, human NaPi-IIa) is the most critical determinant of model accuracy.

However, attempts to align full-length NaPi-IIa with full-length VcINDY using several approaches, such as HHalign, produced unsuitable alignments replete with gaps, particularly in the C-terminal half. Thus, we aligned the repeat units independently. First, to obtain an overview of the equivalent TM helices, AlignMe was used to align family-averaged hydropathy profiles of a given repeat unit of the template and target proteins. A more precise alignment of each repeat unit for VcINDY and NaPi-IIa was then obtained using the AlignMe by providing the server with a position-specific substitution matrix (generated for the HHalign homologues) for each repeat unit using the Profile+Secondary-Structure+Transmembrane (AlignMePST) mode. These alignments of RU1 and RU2 were combined into a single alignment of the core of the two proteins.

The alignment of the core was used to build a preliminary model of human NaPi-IIa with Modeller 9v5 (51), using the X-ray structure of VcINDY (PDB identifier 4F35) as a template, in particular TMs 4-6 (residues 83-242) and TMs 9-11 (residues 310-462) for RU1 and RU2, respectively (see Fig S4). Following an iterative procedure, the alignment was refined in order to: a) remove gaps within secondary structure elements; b) orient less conserved residues towards the protein surface; c) ensure that more conserved residues participate in the packing of the protein or in the binding site and; d) be as consistent as possible with a local (fragment) alignment obtained by HHalign for each repeat (Figs. S2B and S2C). Optimization of the position of conserved and variable residues was aided by conservation scores for human NaPi-IIa obtained using the ConSurf server (52).

The final alignment (Fig. 2B) was used to model the NaPi-IIa core domain, which included residues 97-249 of RU1 and 341-505 of RU2, i.e., those residues for which a template was present. In a final modeling stage, two Na^+ ions and a phosphate substrate were included. Harmonic upper bound distance restraints of 3.3 Å were imposed between: the Na^+ ion at Na2 and side chain O atoms of residues S164, T195, S196, N199 and substrate P_i; the Na^+ ion at Na3 and side chain O atoms of residues Q417, S419; and P_i and side chain O atom of residue S164, or side chain N atom of N199. The final model was that with the lowest Modeller probability distribution function score out of a set of 2000 models. The ProQM score (53) of this model was 0.545 (improved from 0.465 for the preliminary model) compared to a ProQM score of 0.675 for the template; and only four residues were found in disallowed regions of the Ramachandran plot according to PROCHECK (54), all of which are located in loops.

Functional expression in oocytes and transport assays

Reagents and solutions

Standard reagents were obtained from either Sigma-Aldrich or Fluka (Buchs, Switzerland. Oocytes were incubated in Modified Barth's solution that contained (in mM): 88 NaCl, 1 KCl, 0.41 $CaCl_2$, 0.82 $MgSO_4$, 2.5 $NaHCO_3$, 2 $Ca(NO_3)_2$, 7.5 HEPES, adjusted to pH 7.5 with TRIS and supplemented with antibiotics doxycyclin and gentamicin (5 mg/l). The solution compositions were as follows: Control superfusate (100Na) (in mM): 100 NaCl, 2 KCl, 1.8 $CaCl_2$, 1 $MgCl_2$, 10 HEPES, adjusted to pH 7.4 using TRIS. Choline solution (100Ch): as for 100Na with isosmotic substitution of 100 mM choline chloride. P_i was added to the required substrate concentration from 1 M K_2HPO_4 and KH_2PO_4 stocks premixed to give the required pH (7.4).

Molecular Biology and single point mutations

cDNA encoding wild-type (WT) human NaPi-IIa was subcloned into a vector containing the 5' and 3' UTRs from *Xenopus* β-globin to improve its expression in oocytes. Novel cysteines were introduced using the Quickchange site-directed mutagenesis kit (Stratagene Inc.). The sequence was verified by sequencing (Microsynth, Switzerland), linearized with XbaI and cRNA was synthesized in presence of Cap analog using the T3 Message Machine kit (Ambion).

Functional expression and transport assays

Xenopus laevis frogs were purchased from Xenopus Express (France). Ovarian lobes were surgically removed and the oocytes isolated following standard protocols (e.g.Patti et al 2012). Injected oocytes (50 nl of cRNA (0.2 µg/µl)) were incubated for 3-5 days in modified Barth's solution. All animal procedures were performed according to Swiss Cantonal and Federal legislation relating to animal experimentation. For radioisotope uptake assays, groups of oocytes (7–10 oocytes/group) were first allowed to equilibrate in uptake solution without tracer. After aspiration of this solution we added 100 µl uptake solution containing radiotracer (^{32}P) (Perkin Elmer, Switzerland). The uptake proceeded for 10 min and was stopped by washing the oocytes 4 times with 4 ml ice-cold 100Ch solution containing 2 mM cold P_i. Uptake of $^{32}P_i$ alone was done using 100Na solution and 1 mM cold P_i, to which $^{32}P_i$ (specific activity 10 mCi/ mmol P_i) was added. After washing, oocytes were placed individually in a scintillation vial and lysed in 100 µl 10% SDS. $^{32}P_i$ activities of individual oocytes were counted using a Packard Tri-Carb 2900TR scintillation counter.

Standard two-electrode voltage clamp hardware was used for electrophysiology (GeneClamp, Model 500, Molecular Devices). The voltage clamp hardware was controlled, and data were acquired, using pClamp 8-9 software (Molecular Devices Post-acquisition analysis was performed using Clampfit (Molecular Devices).

Immunostaining

After three days of expression oocytes were washed with phosphate buffered saline (PBS: H_2KPO_4 1.76mM, Na_2HPO_4 10mM, KCl 27mM, NaCl 137mM, pH 7.4) and incubated in 3% paraformaldehyde/PBS for 4 hours at 4°C followed by overnight incubation in 30% sucrose/PBS at 4°C. Before freezing, oocytes were kept for 15 min in PBS and 4 to 6 oocytes were placed in a cryomold (Cryomold Biopsy, Tissue-Tek) containing embedding medium (O.C.T. embedding Matrix, Cell Path) and frozen in liquid propane. Frozen oocytes were cut into 7µm slices with a cryotome (Leica CM1850), mounted on slides (Superfrost Plus, Thermo Scientific) and rehydrated in PBS for 30 min. Sections were blocked in 1% BSA/PBS for 15 min at room temperature. NaPi-IIa antibody raised against a COOH-terminal peptide (55) diluted 1/400 in 0.02% Na-azide/PBS and incubated on the slides overnight at 4°C. Sections were washed twice with hypertonic PBS (PBS with additional 18g NaCl/L) and once in PBS for 5 min. Sections were incubated with secondary Donkey anti-rabbit Alexa-488 antibody (Invitrogen) diluted 1/1000 in 0.02% Na-azide/PBS for 1 hour. Slides were washed again and mounted. Fluorescence was detected using a fluorescence microscope (Leica CTR600).

Acknowledgements.

Financial support was given by The Dunhill Medical Trust (AW) and Swiss National Science Foundation (ICF). We thank Eva Hänsenberger for oocyte preparation.

1. Shroff R, Long DA, & Shanahan C (2013) Mechanistic insights into vascular calcification in CKD. *J. Am. Soc. Nephrol.* 24(2):179-189.
2. Biber J, Hernando N, & Forster I (2013) Phosphate transporters and their function. *Annu. Rev. Physiol.* 75:535-550.
3. Forster IC, Hernando N, Biber J, & Murer H (2013) Phosphate transporters of the SLC20 and SLC34 families. *Mol. Aspects Med.* 34(2-3):386-395.
4. Sabbagh Y, Giral H, Caldas Y, Levi M, & Schiavi SC (2011) Intestinal phosphate transport. *Adv Chronic Kidney Dis* 18(2):85-90.
5. Biber J, Hernando N, Forster I, & Murer H (2009) Regulation of phosphate transport in proximal tubules. *Pflugers Arch.* 458(1):39-52.
6. Forster I, Hernando N, Sorribas V, & Werner A (2011) Phosphate transporters in renal, gastrointestinal, and other tissues. *Adv Chronic Kidney Dis* 18(2):63-76.
7. Beck L, *et al.* (1998) Targeted inactivation of Npt2 in mice leads to severe renal phosphate wasting, hypercalciuria, and skeletal abnormalities. *Proc. Natl. Acad. Sci. U. S. A.* 95(9):5372-5377.
8. Kenny J, *et al.* (2011) Sotos syndrome, infantile hypercalcemia, and nephrocalcinosis: a contiguous gene syndrome. *Pediatr. Nephrol.* 26(8):1331-1334.
9. Magen D, *et al.* (2010) A loss-of-function mutation in NaPi-IIa and renal Fanconi's syndrome. *N. Engl. J. Med.* 362(12):1102-1109.
10. Bergwitz C, *et al.* (2006) SLC34A3 Mutations in Patients with Hereditary Hypophosphatemic Rickets with Hypercalciuria Predict a Key Role for the Sodium-Phosphate Cotransporter NaPi-IIc in Maintaining Phosphate Homeostasis. *Am. J. Hum. Genet.* 78(2):179-192.
11. Corut A, *et al.* (2006) Mutations in SLC34A2 cause pulmonary alveolar microlithiasis and are possibly associated with testicular microlithiasis. *Am. J. Hum. Genet.* 79(4):650-656.
12. Forster IC, Hernando N, Biber J, & Murer H (2012) Phosphate transport kinetics and structure-function relationships of SLC34 and SLC20 proteins. *Curr Top Membr* 70:313-356.
13. Forrest LR, Kramer R, & Ziegler C (2011) The structural basis of secondary active transport mechanisms. *Biochim. Biophys. Acta* 1807(2):167-188.
14. Forrest LR, *et al.* (2008) Mechanism for alternating access in neurotransmitter transporters. *Proc. Natl. Acad. Sci. U. S. A.* 105(30):10338-10343.
15. Jardetzky O (1966) Simple allosteric model for membrane pumps. *Nature* 211(5052):969-970.
16. Forster I, Hernando N, Biber J, & Murer H (1998) The voltage dependence of a cloned mammalian renal type II Na^+/P_i cotransporter (NaPi-2). *J. Gen. Physiol.* 112(1):1-18.
17. Ghezzi C, Murer H, & Forster IC (2009) Substrate interactions of the electroneutral Na+-coupled inorganic phosphate cotransporter (NaPi-IIc). *J Physiol* 587(Pt 17):4293-4307.
18. Forster IC, Kohler K, Biber J, & Murer H (2002) Forging the link between structure and function of electrogenic cotransporters: the renal type IIa Na^+/P_i cotransporter as a case study. *Prog. Biophys. Mol. Biol.* 80(3):69-108.
19. Abramson J & Wright EM (2009) Structure and function of Na(+)-symporters with inverted repeats. *Curr. Opin. Struct. Biol.* 19(4):425-432.
20. Mancusso R, Gregorio GG, Liu Q, & Wang DN (2012) Structure and mechanism of a bacterial sodium-dependent dicarboxylate transporter. *Nature* 491(7425):622-626.
21. Karlin A & Akabas MH (1998) Substituted-cysteine accessibility method. *Methods Enzymol.* 293:123-145.
22. Kohler K, Forster IC, Stange G, Biber J, & Murer H (2002) Identification of functionally important sites in the first intracellular loop of the NaPi-IIa cotransporter. *Am. J. Physiol.* 282(4):F687-696.
23. Lambert G, Forster IC, Stange G, Biber J, & Murer H (1999) Properties of the mutant Ser-460-Cys implicate this site in a functionally important region of the type IIa Na^+/P_i cotransporter protein. *J. Gen. Physiol.* 114(5):637-652.
24. Lambert G, *et al.* (2001) Cysteine mutagenesis reveals novel structure-function features within the predicted third extracellular loop of the type IIa Na^+/P_i cotransporter. *J. Gen. Physiol.* 117(6):533-546.
25. Virkki LV, Forster IC, Bacconi A, Biber J, & Murer H (2005) Functionally important residues in the predicted 3rd transmembrane domain of the type IIa sodium-phosphate co-transporter (NaPi-IIa). *J. Membr. Biol.* 206(3):227-238.
26. Ehnes C, *et al.* (2004) Structure-function relations of the first and fourth extracellular linkers of the type IIa Na^+/P_i cotransporter: II. Substrate interaction and voltage dependency of two functionally important sites. *J. Gen. Physiol.* 124:489-503.
27. Ehnes C, *et al.* (2004) Structure-function relations of the first and fourth predicted extracel-

lular linkers of the type IIa Na^+/Pi cotransporter: I. Cysteine scanning mutagenesis. *J. Gen. Physiol.* 124(5):475-488.
28. Ghezzi C, Meinild AK, Murer H, & Forster IC (2011) Voltage- and substrate-dependent interactions between sites in putative re-entrant domains of a Na(+)-coupled phosphate cotransporter. *Pflugers Arch.* 461(6):645-663.
29. Radanovic T, Gisler SM, Biber J, & Murer H (2006) Topology of the type IIa Na+/P(i) cotransporter. *J. Membr. Biol.* 212(1):41-49.
30. Virkki LV, Murer H, & Forster IC (2006) Mapping conformational changes of the type IIb Na^+/P_i cotransporter by voltage clamp fluorometry. *J. Biol. Chem.* 281:28837-28849.
31. Kohler K, Forster IC, Stange G, Biber J, & Murer H (2002) Transport function of the renal type IIa Na^+/P_i cotransporter is codetermined by residues in two opposing linker regions. *J. Gen. Physiol.* 120:693-703.
32. Virkki LV, Murer H, & Forster IC (2006) Voltage clamp fluorometric measurements on a type II Na^+-coupled P_i cotransporter: shedding light on substrate binding order. *J. Gen. Physiol.* 127:539-555.
33. Forster IC, *et al.* (1997) Electrophysiological characterization of the flounder type II Na^+/P_i cotransporter (NaPi-5) expressed in Xenopus laevis oocytes. *J. Membr. Biol.* 160(1):9-25.
34. Forrest LR & Rudnick G (2009) The rocking bundle: a mechanism for ion-coupled solute flux by symmetrical transporters. *Physiology (Bethesda)* 24:377-386.
35. Lolkema JS & Slotboom DJ (2003) Classification of 29 families of secondary transport proteins into a single structural class using hydropathy profile analysis. *J. Mol. Biol.* 327(5):901-909.
36. Werner A & Kinne RK (2001) Evolution of the Na-P_i cotransport systems. *Am. J. Physiol.* 280(2):R301-312.
37. Andrini O, Ghezzi C, Murer H, & Forster IC (2008) The leak mode of type II Na(+)-P(i) cotransporters. *Channels (Austin)* 2(5):346-357.
38. Pedersen BP, *et al.* (2013) Crystal structure of a eukaryotic phosphate transporter. *Nature* 496(7446):533-536.
39. Gonzalez-Parra E, Tunon J, Egido J, & Ortiz A (2012) Phosphate: a stealthier killer than previously thought? *Cardiovasc Pathol* 21(5):372-381.
40. Salusky IB (2006) A new era in phosphate binder therapy: what are the options? *Kidney Int. Suppl.* (105):S10-15.
41. Finn RD, Clements J, & Eddy SR (2011) HMMER web server: interactive sequence similarity searching. *Nucleic Acids Res.* 39(Web Server):W29-W37.
42. Edgar RC (2010) Search and clustering orders of magnitude faster than BLAST. *Bioinformatics* 26(19):2460-2461.
43. Liu Y, Schmidt B, & Maskell DL (2010) MSAProbs: multiple sequence alignment based on pair hidden Markov models and partition function posterior probabilities. *Bioinformatics* 26(16):1958-1964.
44. Stamm M, Staritzbichler R, Khafizov K, & Forrest LR (2013) Alignment of helical membrane protein sequences using AlignMe. *PLoS ONE* 8(3):e57731.
45. Hessa T, *et al.* (2005) Recognition of transmembrane helices by the endoplasmic reticulum translocon. *Nature* 433(7024):377-381.
46. Remmert M, Biegert A, Hauser A, & Soding J (2011) HHblits: lightning-fast iterative protein sequence searching by HMM-HMM alignment. *Nat Methods*.
47. Söding J (2005) Protein homology detection by HMM-HMM comparison. *Bioinformatics* 21(7):951-960.
48. Altschul SF, *et al.* (1997) Gapped BLAST and PSI-BLAST: a new generation of protein database search programs. *Nucleic Acids Res.* 25(17):3389-3402.
49. Kelley LA & Sternberg MJ (2009) Protein structure prediction on the Web: a case study using the Phyre server. *Nat Protoc* 4(3):363-371.
50. Margelevicius M, Laganeckas M, & Venclovas C (2010) COMA server for protein distant homology search. *Bioinformatics* 26(15):1905-1906.
51. Šali A & Blundell TL (1993) Comparative protein modelling by satisfaction of spatial restraints. *J. Mol. Biol.* 234:779-815.
52. Ashkenazy H, Erez E, Martz E, Pupko T, & Ben-Tal N (2010) ConSurf 2010: calculating evolutionary conservation in sequence and structure of proteins and nucleic acids. *Nucleic Acids Res* 38(Web Server issue):W529-533.
53. Ray A, Lindahl E, & Wallner B (2010) Model quality assessment for membrane proteins. *Bioinformatics* 26(24):3067-3074.
54. Laskowski RA, Macarthur MW, Moss DS, & Thornton JM (1993) PROCHECK - A program to check the stereochemical quality of protein structures. *J. Appl. Crystall.* 26:283-291.
55. Custer M, Lotscher M, Biber J, Murer H, & Kaissling B (1994) Expression of Na-P(i) cotransport in rat kidney: localization by RT-PCR and immunohistochemistry. *Am. J. Physiol.* 266(5 Pt 2):F767-774.
56. Patti M, Ghezzi C, & Forster IC (2013) Conferring electrogenicity to the electroneutral phosphate cotransporter NaPi-IIc (SLC34A3) reveals an internal cation release step. *Pflugers Arch.* DOI 10.1007/s00424-013-1261-9

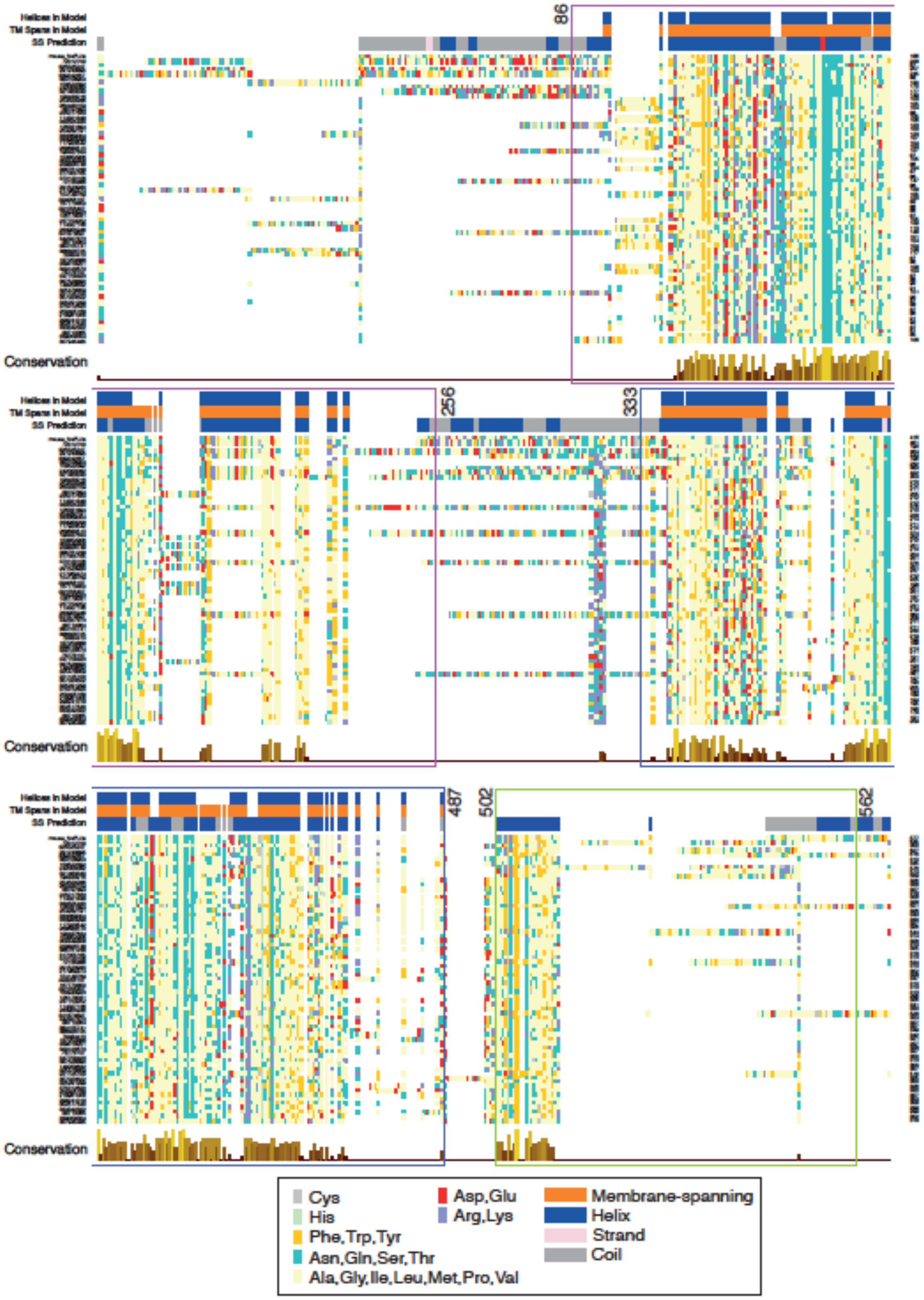
Helices in Model
TM Spans in Model
SS Prediction
Conservation
86
256
333
487
502
562
Cys
His
Phe,Trp,Tyr
Asn,Gln,Ser,Thr
Ala,Gly,Ile,Leu,Met,Pro,Val
Asp,Glu
Arg,Lys
Membrane-spanning
Helix
Strand
Coil

Fig S1 - Multiple sequence alignment of NaPi-II homologs indicating the conserved region 1 (*purple box*, residues 86-256), region 2 (human residues 335-489, *blue box*) and region C (*green box*, human residues 504-564). The top sequence line corresponds to mouse NaPi-IIa. Only homologues that cover 90% of the sequence of mouse NaPi-II are shown. For clarity, the sequences of the cytosolic C-terminal domain are not shown, and residues are represented as squares colored by residue type and not as letters (see legend). The fraction conservation of each column is also indicated. The predicted secondary structure ("SS prediction") is shown above the alignment, along with the TM spanning residues (orange, "TM spans in model") and SS elements ("Helices in model") in the final model. Helical (*dark blue*), coiled (*gray*) and stranded (*pink*) SS elements are indicated.

Fig S2 - HHalign sequence alignment of human NaPi-IIa repeats to each other. Region 1 containing residues 86-256 was aligned to region 2+C consisting of residues 335-564, resulting in a local (i.e., not full-length) alignment that indicates the locations of the conserved repeated elements. The predicted secondary structure for each residue is indicated above and below the respective sequences, with helices in blue, coil in gray and strand in pink.

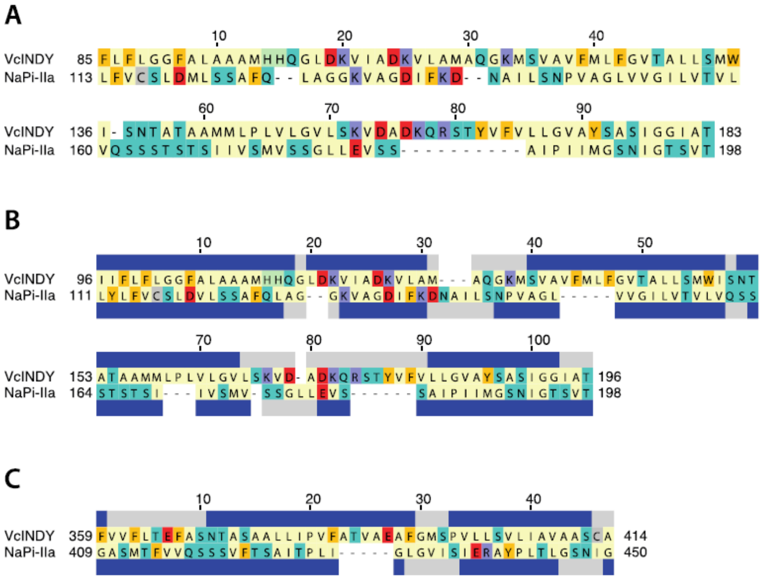

Fig S3 – Sequence comparison of core structural regions of human NaPi-IIa with those of VcINDY, a putative structural homologue. **A** Local alignment output from HHpred template search, showing that the first repeat units of each protein can be aligned. (**B, C**) HHalign sequence alignments of VcINDY and human NaPi-IIa RU1 (**B**) and RU2 (**C**). Note that even though in each case only a fragment (local) alignment is output by HHalign, the QSSS motif of the NaPi-II sequence is matched to the region of a conserved xSNT motif in VcINDY in both repeats.

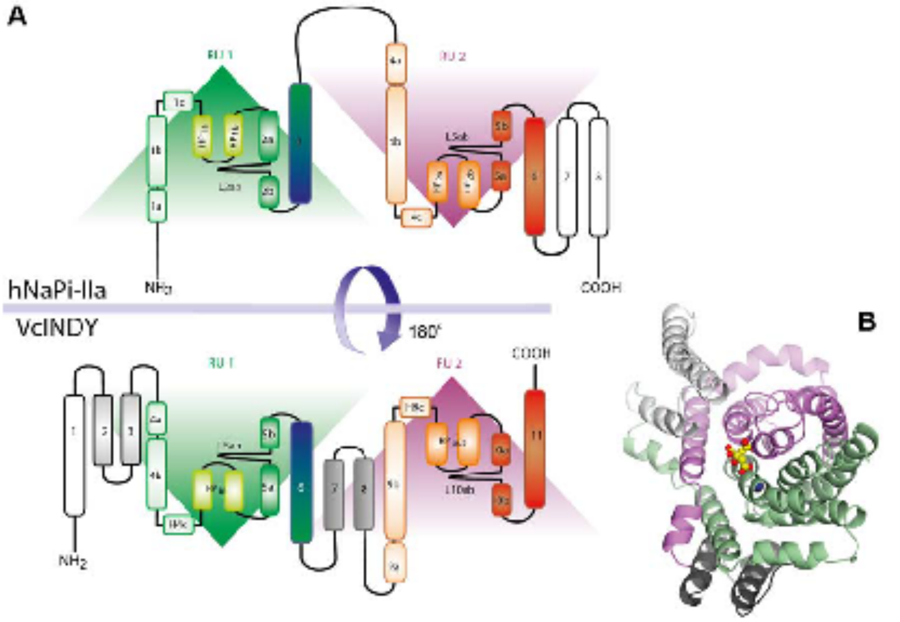

Fig S4 – Overview of the topology and fold of the template VcINDY X-ray structure (PDB identifier 4F35) compared to the predicted topology of NaPi-II. **A** Schematics of the transmembrane topologies of hNaPi-IIa (*top*) and VcINDY (*bottom*), indicating: the locations of repeat unit 1 (*green triangle*) and repeat unit 2 (*purple triangle*); the two peripheral transmembrane helices in hNaPi-IIa that have no template in VcINDY, namely TMs 7-8 (*white*); and the five peripheral transmembrane helices in VcINDY that have no equivalent in NaPi-II, namely TMs 1-3 (*white/light gray*) and TMs 7-8 (*gray*). **B** Fold of VcINDY viewed from the periplasm shown as cartoon helices, and colored to highlight the repeats (*green and purple*), and the peripheral helices (*white and gray*). Citrate (*yellow and red*) and one sodium (*blue*) observable in the structure are shown as spheres.

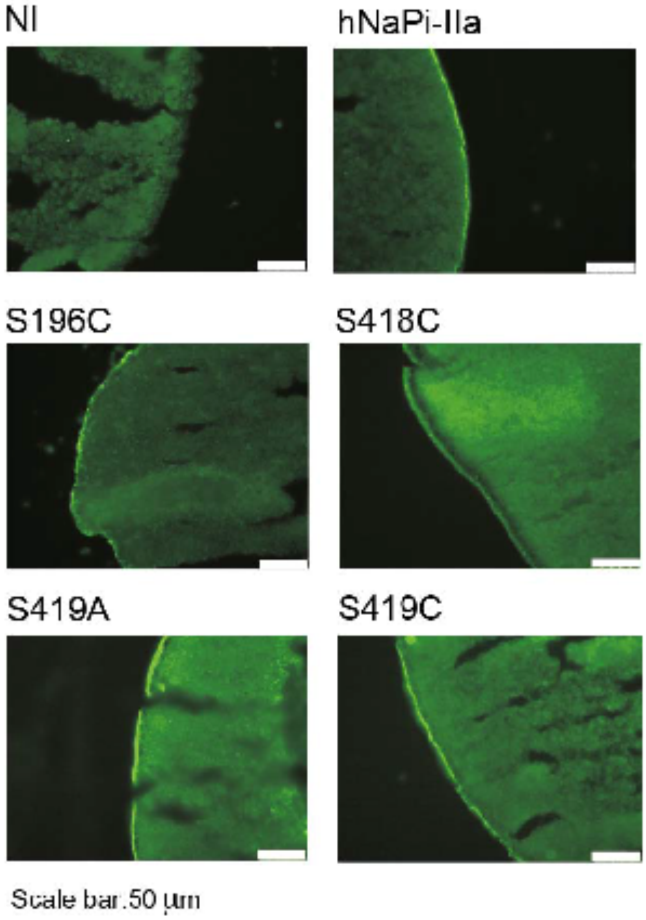

Fig S5 – Immunostaining of *Xenopus* oocytes confirms the surface localization of wild-type (WT) NaPi-IIa and selected mutants (S196C, S418C and S419C) that showed no functional behavior. NI: non-injected control oocyte.

C. Correlating charge movements with local conformational changes of a Na^+-coupled cotransporter

This section contains a manuscript ready for submission.

The general aim of this study was to gain insight in the transport dynamics of NaPi-IIb by making simultaneous presteady-state charge measurements and fluorescence intensity measurements from the same oocyte. It extends a previous fluorometry mapping (Virkki et al., 2006a) study and introduces a method to allow the fluorescence properties of different mutants to be compared by assigning an apparent quantum yield according to the conformational state occupied.

My contribution to this paper included study design, mutagenesis, experiments (electrophysiology, fluorometry), data analysis and interpretation and writing the first draft of the manuscript including preparation of figures.

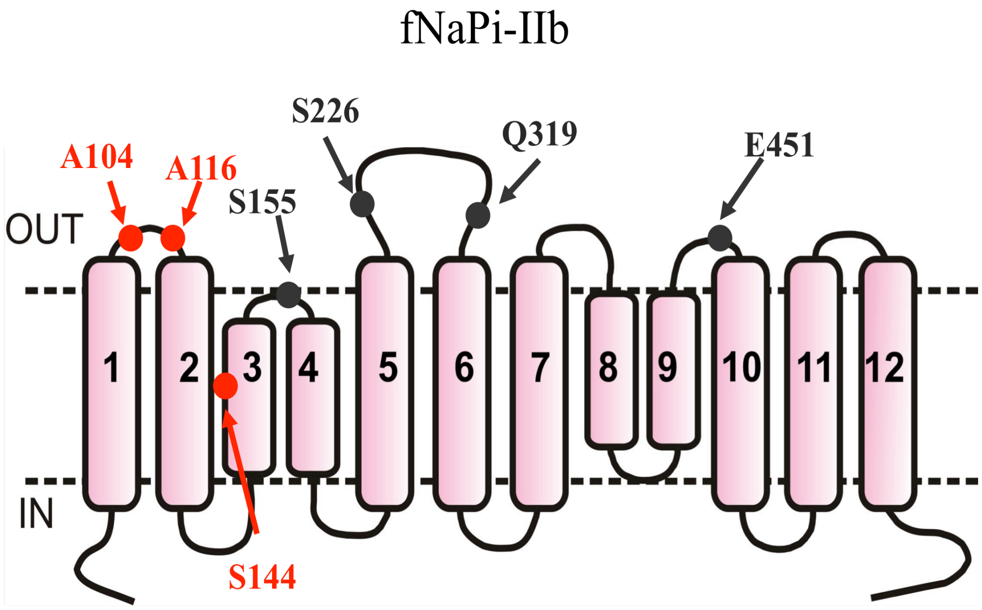

Figure 28 Secondary topology model of fNaPi-IIb showing the mutants investigated in this paper. New mutation sites are highlighted in red, sites previously investigate by Virkki et al., 2006 (Virkki et al., 2006a) are highlighted in black.

Correlating charge movements with local conformational changes of a Na^+-coupled cotransporter

Monica Patti and Ian C. Forster

Institute of Physiology and Zurich Center for Integrative Human Physiology, University of Zurich, Zurich, Switzerland

Correspondence: Ian C. Forster, PhD
Institute of Physiology
University of Zurich
Winterthurerstrasse 190
CH-8057 Zurich, Switzerland.
FAX: +41 (0) 44 635 6814
TEL: +41 (0) 44 635 5059
EMAIL: iforster@access.uzh.ch

Abstract

To gain insight into the steady-state and dynamic characteristics of structural rearrangements of an electrogenic secondary-active cotransporter during its transport cycle, two measures of conformational change (presteady-state current relaxations and intensity of fluorescence emitted from reporter fluorophores) were investigated as a function of membrane potential and external substrate. Cysteines were substituted at sites in the type IIb Na^+-coupled inorganic cotransporter (SLC34A2 flounder isoform) predicted to be involved in conformational changes. Labeling at one site resulted in complete suppression of transport activity, whereas for the other sites, function remained comparable to the wild type. For these 6 mutants, the properties of the presteady-state charge relaxations were similar for each mutant whereas fluorescence intensity changes differed significantly. Fluorescence changes could be accounted for by simulations using a 5 state model with a unique set of apparent quantum yields assigned to each state. Fluorescence from one site was associated with inward and outward conformations, whereas for the other sites, emissions were associated principally with one or the other orientation. In response to step changes in voltage, the presteady-state current relaxation and the time course of change in fluorescence intensity were described by single exponentials. For one mutant the time constants matched well with and without external Na^+, providing direct evidence that this label reports conformational changes accompanying intrinsic charge movement and cation interactions. For other mutants, correlations were found only in the presence of Na^+ and $V>0$.

Key words: phosphate transport, electrophysiology, voltage clamp fluorometry, presteady-state, conformational change, voltage dependence

Introduction

There is compelling evidence from the resolved crystal structures of secondary-active transporters that these membrane proteins adopt unique conformational changes during the transport cycle as substrates bind, translocate and are released to the opposite side of the membrane (e.g. (1)). However, the identified conformations provide only limited snapshots of the transport process without giving insight into the kinetics of the transitions between states. Indirect experimental evidence for the dynamic processes occurring comes from functional studies using techniques such as smFRET (2-4), electron parametric resonance (5) and time-resolved fluorometry (6-8). Moreover, these techniques allow observation of the protein behavior under more physiologically relevant conditions than those used for crystallography.

Electrogenic cotransporters offer a unique opportunity to study transport dynamics because one of the driving forces for transport, membrane potential, can be readily manipulated in real time by means of the voltage clamp technique. For electrogenic members of the SLC34 family of sodium-coupled phosphate cotransporters (NaPi-IIa, NaPi-IIb), the functional property of electrogenicity manifests itself as steady-state P_i-induced currents at a fixed membrane potential and presteady-state current relaxations evoked by rapid changes in membrane potential, as commonly observed in many electrogenic solute carriers (for review, see (9)). Analysis of presteady-state relaxations led to the identification of voltage-dependent partial reactions in the transport cycle (Fig 1A), namely the empty carrier transition ($0 \leftrightarrow 1$) and Na^+ interactions ($1 \leftrightarrow 2$, $2 \leftrightarrow 3$ and $7 \leftrightarrow 0$) (9, 10). Moreover, the presence of mobile charge movements that are resolvable in real-time on a macroscopic scale provides strong evidence for voltage-dependent conformational changes. Thus, in the absence of external driving cations, charge movements largely reflect transitions between inward and outward facing conformations of the protein itself; the interaction of cations contributes further to the total charge movement as these ions purportedly move within the transmembrane electric field to and from their binding sites. However, from presteady-state current relaxation analysis alone it may be difficult to identify and localize conformational changes to specific regions of the protein because of the “global” nature of the assay. In summary, the link between charge movement- reported as an equivalent lumped charge moving through a fraction of the transmembrane electric field- and protein conformational change is at best indirect, especially if the charge movement arises from a concerted redistribution of many charges.

More recently, we have applied voltage clamp fluorometry (VCF) (10-14) that yields information on local conformational changes in specific regions of the protein. Time-resolved measurement of fluorometric emissions (voltage clamp fluorometry, VCF) offers a complementary tool to observe, indirectly, voltage- (and substrate-) dependent conformational changes (e.g. (15)). By labeling each substituted cysteine of a population of proteins with thiol reactive fluorophores, changes in their microevironment caused by local conformational changes will be reported as changes in the macroscopic fluorescence intensity resulting, for example, from collisional quenching of individual fluorophores (15). As these measurements are made in real time, we can consider the fluorophore as a motion reporter at the chosen location. We have previously used this technique to identify multiple cation interactions in the flounder NaPi-IIb (13) and mouse NaPi-IIc (12), complementary movement of two re-entrant domains during the transport cycle of flounder NaPi-IIb (14) and the putative release of cations at the cytosolic face of the protein (10).

Here, we investigate possible correlations between presteady-state charge movements and simultaneously measured changes in fluorescence intensity emitted from fluorophores covalently bound to selected sites in the flounder NaPi-IIb protein. A direct correlation between the mobile charge movement and fluorescence would suggest that the fluorophore senses the same motion event as reported by the charge movement. We have previously reported that such a correlation exists over a limited range of membrane potentials for one labeled site in NaPi-IIb (13). This approach has been applied to other cation-coupled symporters (e.g. SGLT1 (7, 8, 16) and GAT1 (8, 17)) to elucidate structure-function correlates during voltage-driven conformational changes. By restricting which conformational states the protein can occupy, for example, by defining the substrate availability and membrane voltage, we aimed to identify parts of the protein involved in empty carrier reorientation, cation interactions and substrate translocation under physiological conditions. The choice of site should reflect its proximity to functionally important regions that undergo conformational changes in response to membrane potential changes and, ideally, satisfy our requirement that neither the Cys-substitution nor the thiol labeling should significantly alter the transport behavior. Four sites that fulfill these criteria were identified in a previous study (14), however, correlations between charge and fluorescence were not explored. Here, we introduce three new sites to augment our functional mapping of local conformational changes in response to a globally induced state change by an externally applied step in membrane voltage (Fig 1B).

Materials and Methods

Solutions and reagents

Oocytes were incubated in Modified Barth's solution that contained (in mM): 88 NaCl, 1 KCl, 0.41 $CaCl_2$, 0.82 $MgSO_4$, 2.5 $NaHCO_3$, 2 $Ca(NO_3)_2$, 7.5 HEPES, adjusted to pH 7.5 with TRIS and supplemented with antibiotics doxycyclin and gentamicin (5 mg/l). The superfusing solutions contained (in mM)): 100Na: 100 NaCl, 2 KCl, 1.8 $CaCl_2$, 1 $MgCl_2$, 10 HEPES, pH 7.4 adjusted with TRIS; 100Ch: same as for 100Na solution with equimolar replacement of NaCl with choline Cl. For intermediate Na^+ concentrations, 100Na and 100Ch were appropriately mixed to maintain the same osmolarity. Inorganic phosphate (P_i) was added to the superfusate from 1 M K_2HPO_4 and KH_2PO_4 stocks that were mixed to give pH 7.4. All standard reagents were obtained from either Sigma-Aldrich or Fluka (Buchs, Switzerland). 2-(trimethylammonium) ethylmethanethiosulfonate bromide (MTSET) and 2-((5(6)-tetramethylrhodamine)carboxylamino) ethyl methanethiosulfonate (MTS-TAMRA) were obtained from Biotium (USA).

Site-directed mutagnesis and cRNA preparation

cDNA encoding wild-type (WT) flounder NaPi-IIb (GenBank/EMBL/DDBJ accession n. AAB16821) was subcloned into a vector containing the 5' and 3' UTRs from *Xenopus* β-globin to improve its expression in oocytes. Novel cysteines were introduced using the Quickchange site-directed mutagenesis kit (Agilent Technologies Inc.). The sequence was verified by sequencing (Microsynth, Switzerland), linearized with XbaI and cRNA was synthesized in presence of Cap analog using the T3 Message Machine kit (Ambion).

Expression in Xenopus laevis oocytes

Animal procedures and preparation of oocytes was according to standard procedures (e.g.(10, 18)) and in accordance with the Swiss Cantonal and Federal legislation relating to animal experimentation. Stage V-VI oocytes were selected, maintained in modified Barth's solution at 16°C and injected with injected with 50 nl of cRNA (200 ng/μl), and experiments were performed 4-5 days after injection.

^{32}P uptake

Control oocytes (NI) and oocyte expressing fNaPi-IIb WT and cysteine mutants (10-15 oocytes/group) were first allowed to equilibrate in 100Na without tracer. After aspiration of this solution, oocytes were incubated in 100Na containing 1mM cold P_i and ^{32}P (specific activity 10 mCi $mmol^{-1}$). Uptake proceeded for 10 min and then oocytes were washed 4 times with ice-cold 100Ch containing 2 mM P_i, and lysed individually in 2% SDS for 10 min before addition of scintillation cocktail. The amount of radioactivity in each oocyte was measured by scintillation counting.

Two electrode voltage clamp

Standard two-electrode voltage clamp hardware was used (GeneClamp, Model 500, Molecular Devices, USA or TEC-10X, NPI, Tamm, Germany). Clamp control, data acquisition and perfusion valve switching was done using pClamp 8-9 software (Molecular Devices, USA).

Determination of apparent P_i affinity

To determine the apparent affinity constant for P_i ($K_{0.5}^{P_i}$) the electrogenic response to different P_i concentrations added to the 100Na control solution was measured at a defined membrane potential. Oocytes were voltage-clamped to V_h = -60 mV and voltage steps were applied in the range -160 to +60 mV for typically 100 ms. To measure P_i-induced currents (I_{P_i}), the superfusate was switched from the control (100Na) solution to one containing a given concentration of P_i and when the holding current had reached a steady-state, the voltage steps were repeated. The control data set was subtracted from the data set obtained in the presence of P_i to give I_{P_i} for each [P_i] and test voltage. Estimates of $K_{0.5}^{P_i}$ were obtained by fitting data with a form of the Michaelis-Menten equation given by:

$$I_{P_i} = I_{P_i}^{max}\,[P_i]/([P_i] + K_{0.5}^{P_i}) + I_{OFF} \qquad (1)$$

where $I_{P_i}^{max}$ is the maximum current attainable, I_{OFF} is a variable offset to account for uncoupled leak effects (19). To take account of the differences in expression levels between individual oocytes, data obtained from each oocyte were normalized to I_{P_i} recorded at -100 mV with 100Na and 1 mM P_i before pooling and fitting the data with Eqn. 1.

Thiol modification by MTSET

MTSET were prepared from dry stock in water to give 1 M stock solution, which was kept at -20°C until required and diluted as required before adding to 100Na to give the working concentration. This was chosen to allow determination of the reaction rate. MTSET was applied to the chamber with gravity feed via a 0.5-mm-diameter cannula positioned near the cell. During superfusion with MTSET, oocytes were kept at V_h= -50 mV. After washout, the P_i-induced current was remeasured. The effective 2nd order reaction rates were determined by fitting a single decaying exponential to the peak P_i-dependent current after a cumulative exposure time *t*, (I^t_{Pi}) determined following each successive MTS exposure:

$$I^t_{P_i} = (I^0_{P_i} - I^\infty_{P_i})\exp(-ctk*) + I^\infty_{P_i} \qquad (2)$$

Where I^0_{Pi} is the P_i response at $t = 0$, I^∞_{Pi} is the response at $t = \infty$, *c* is the concentration of MTS reagent (assumed to be in excess), and $k*$ is the effective 2nd order rate constant (20).

Voltage clamp fluorometry

The voltage clamp fluorometry apparatus comprised a two-electrode voltage clamp (TEC-10CX, NPI, Tamm, Germany) and a laboratory-built fluorescence microscope as previously described (13), with the following changes: for some experiments we used an XF32 cube set (535DF35 excitation filter, 570DRLP dichroic mirror and 596DF35 emission filter) (Omega Optical Inc). The fluorophore was excited by a green LED light source (Luxeon, LXHL-PM02) driven by stabilized current source. For labeling, oocytes were incubated in 0.4 mM MTS-TAMRA in 100Na and kept in the dark at 20°C for 5 min.

Voltage step protocols and presteady-state analysis

The protocol for recording presteady-state current and simultaneous fluorescence comprised an average between 20-40 runs filtered at 500 Hz using voltage steps from V_h=-60 mV to voltages in the range of -200 mV to +100 mV. Presteady-state current relaxations were fitted with a double exponential function. The faster component that represents the linear capacitive charging of the oocyte membrane, was subtracted from the total relaxation to obtain the slower NaPi-II dependent component. This was numerically integrated to obtain the charge moved (Q) for a step from the holding potential to the test potential. The Q-V data were fitted with a Boltzmann function of the form given by Eqn 3:

$$Q = Q_{hyp} + Q_{\max} / \left(1 + \exp(z^Q e(V_{0.5}{}^Q - V) / kT)\right) \tag{3}$$

where $V_{0.5}{}^{Q}$ is the voltage at which the charge is distributed equally between two hypothetical states, z^Q is the apparent valency of an equivalent charge that moves through the whole of the membrane field, $Q_{\max}$ is the total mobile charge available, Q_{hyp} is the charge of the hyperpolarizing limit and is a function of V_h, and e, k and T have their usual meanings.

Each fluorescence recording was baseline corrected relative to the value at V_h= -60 mV. After correction for photobleaching, data from single oocytes were normalized to the predicted maximum change in fluorescence ($\Delta F_{\max}$) obtained in the solution that gave the highest ΔF and then pooled. $\Delta F_{\max}$ was obtained from the ΔF-V data were fitted with the Boltzmann equation (Eqn 3, where Q was substituted with ΔF and the corresponding fit parameters are $\Delta F_{\max}$, z^F and $V_{0.5}{}^F$). Fluorescence data were corrected for fluorescence rundown as described previously (13). The time course of the ΔF data was described by fitting a single growing exponential function.

Data analysis and simulations.

Curve fitting was performed using GraphPad Prism version 4 for Windows, (GraphPad Software, San Diego California USA, www.graphpad.com). Data points are shown as mean±sem. Error bars are not displayed if smaller than the graphical symbol. Kinetic simulations were performed using Berkeley Madonna V8.0.2a8 software (www.berkeleymadonna.com).

Results

Functional characterization of Cys mutants in flounder NaPi-IIb before and after thiol labeling.

Three new sites in the flounder NaPi-IIb protein (Ala-104 Ala-116 and Ser-144) were chosen for cysteine substitution (Fig 1B) based on a previous structure-function study using the rat NaPi-IIa isoform (21), which suggested that this region of the protein might undergo unique conformation changes. When expressed in *X. laevis* oocytes, the mutants showed Na^+-dependent ^{32}P uptake and P_i-induced currents (I_{P_i}) in the presence of external Na^+ (100Na solution) under voltage clamp that were comparable with wild-type (WT) levels (with P_i= 1mM, typical magnitude for $I_{P_i} \geq 100$ nA at -50 mV) (*data not shown*). These assays confirmed that the substitutions were well tolerated. Furthermore, to establish if mutagenesis had altered the basic cotransport kinetics, we determined the apparent affinity constant for P_i in 100Na ($K_{0.5}^{Pi}$) (see Materials and Methods) for each mutant. At -100 mV the $K_{0.5}^{Pi}$ values were (in mM): 0.07±0.02 (A104C), 0.04±0.02 (A116C) and 0.02±0.01 (S144C), which were comparable with reported data for the WT(0.03 ± 0.01 mM) and previously described mutants (e.g.(14)). We concluded that the Cys-mutagenesis had left the electrogenic transport mechanism intact.

In addition to tolerating the Cys substitution, we required that the substituted Cys be accessible for labeling and that this not should cause a significant deviation from WT behavior, as we previously reported for substitution at Ser-155, Ser-226, Gln-319C and Glu-451 (14). We therefore examined the electrogenic behavior of the new mutants before and after exposure to MTSET or the thiol-reactive fluorophore MTS-TAMRA. One mutant (S144C) displayed a significant reduction in I_{P_i} after exposure to these MTS reagents (1 mM, 5 min) (see Fig S1A). We characterized the loss of electrogenic transport function by exposing test oocytes expressing S144C to the MTS reagent for successive 1 min intervals and measuring I_{P_i} after each exposure (Materials and methods). The rate of decrease in I_{P_i} was dependent on the incubation medium. For incubation using 100Ch, the effective 2nd order reaction rate (k^*) = 0.746 $s^{-1}M^{-1}$, whereas for incubation in 100Na, k^*= 129 $s^{-1}M^{-1}$, which was comparable to values we have previously reported e.g. (13) (Fig S1B). The slow rate of modification in 100Ch indicated that this site was significantly less accessible from the external medium in 100Ch. As S144C did not satisfy our experimental criterion, we did not investigate its properties further.

For mutants A104C and A116C, we next investigated whether incubation with MTS-TAMRA altered the characteristics of the presteady-state charge movements. Current relaxations were measured for each mutant in response to voltage steps with varying $[Na^+]_o$

from 0 mM to 100 mM. Analysis yielded the steady-state mobile charge distribution as a function of membrane potential (see Materials and methods). The parameters obtained from Boltzmann fits that describe the main features of the charge-voltage (Q-V) relations were generally close to those previously reported for the WT (14, 18), however there were small shifts in the absolute values of the midpoint voltage of the Q-V data ($V_{0.5}^{Q}$) (Table 1) after labeling. Despite these changes, we found that the dependence of $V_{0.5}^{Q}$ on the concentration of external Na^+ ions ($[Na^+]_o$) gave similar limiting slopes when plotted against $\log_{10}[Na^+]_o$ and was close to the expected value (≈116 mV/decade) (18) (Table 1). This finding confirmed that for A104C or A116C, neither the Cys substitution nor exposure to thiol reactive reagents had significantly altered the external cation interactions.

Changes in fluorescence intensity reported by cysteine mutants after labeling with MTS-TAMRA

When voltage steps were applied to either non–injected oocytes or WT NaPi-IIb, voltage-dependent changes in the emitted fluorescence intensity (ΔF) were not detected. However, for the labelled Cys mutants, ΔF was resolved whose magnitude and polarity depended on the composition of the superfusion medium and the labeling site. For oocytes expressing A116C (Fig 2A), in the absence of external Na^+ (100Ch), equal and opposite 120 mV steps from the -60mV holding potential induced ΔF of similar magnitude, with quenching of fluorescence occurring for the depolarizing step relative to the baseline value at -60 mV. The addition of 100 mM Na^+ (100Na) resulted in a larger ΔF for the depolarizing step and reduced ΔF for the hyperpolarizing step, thus resulting in a shift of the ΔF-V distribution along the voltage axis (Fig 2B). In contrast, the addition of 1 mM P_i had marginal effect on ΔF for depolarizing potentials compared with 100Ch, but further reduced the magnitude of ΔF for the hyperpolarizing step. Mutant A104C (Fig 2A, *upper*) also showed ΔF with all 3 superfusing conditions, however unlike A116C, the direction of ΔF did not change monotonically with membrane potential. Furthermore, for superfusion in 100Na, the OFF transition (return to the holding potential) evoked a rapid fluorescence quench followed by a transient “tail” relaxation that was superimposed on a relatively small steady-state ΔF during the voltage pulse. Qualitatively similar behavior was found when 1 mM P_i was also present in the superfusate although the rapid quench transient was absent.

Normalised ΔF–V data for A104C and A116C are shown using the three superfusion conditions (100Ch, 100Na and 100Na+P_i) in Fig 2B. Unlike A116C and the 4 mutants in our previous study (14), which all showed sigmoidal ΔF-V relationships that either monotonically increased or decreased with V, A104C showed a distinct minimum for each superfusion condition within the test potential range. According to our standard analysis procedure, the ΔF-

V data for A116C were characterised by fitting with the Boltzmann equation (Eqn 3). After normalisation to account for different expression levels, the data were adjusted such that the respective fits superimposed at the depolarizing limit, where we assumed that all proteins were forced to occupy an inward facing conformation, independent of the external substrate. For A104C, we found that the data for each superfusion condition superimposed at the depolarizing limit.

To test for correlations between the charge displacement (Q) and ΔF in the steady-state, we plotted ΔF against Q parametrically for both mutants (Fig 2C). A linear relationship would indicate directly that both signals reflect the same underlying voltage-dependent process. Data sets were normalised to the respective Q_{max} and ΔF_{max} in 100Na. For superfusion in 100Ch, A116C showed an obvious linear relationship that passed through the origin, whereas the corresponding 100Na data deviated particularly at hyperpolarizing potentials such that for a given charge displacement, the measured ΔF exceeded the value expected if there were a strict 1:1 correlation. Mutant A104C also showed a linear relationship between ΔF and Q for 100Na at hyperpolaring potentials that was offset from the origin, however, for 100Ch superfusion there was no clear linear correlation.

We also obtained ΔF–V data at intermediate $[\mathrm{Na}^+]_o$ (25 mM, 50 mM and 75 mM (0 mM $\mathrm{P_i}$) (Fig 3). By fitting these data with a single Boltzmann function (Eqn 3) we obtained the midpoint voltage for fluorescence ($V_{0.5}{}^{\mathrm{F}}$) and compared its dependence on $[\mathrm{Na}^+]_o$ with the corresponding presteady-state relaxation data (Table 1). Like the presteady-state $V_{0.5}{}^{\mathrm{Q}}$ dependence on $\log_{10}[\mathrm{Na}^+]_o$, we also observed a linear relationship between $V_{0.5}{}^{\mathrm{F}}$ and $\log_{10}[\mathrm{Na}^+]_o$ for A104C and A116C with slopes comparable to the corresponding presteady-state data (Fig 3B, Table 1). These data points lay between data previously reported for labeling at Ser-155, Ser-226, Gln-319 and E451C (Fig 1B) (14).

Comparing the time course of presteady-state relaxations and fluorescence

In addition to the steady-state changes in ΔF that resulted from changing the membrane potential and superfusate (Fig 4), we also observed that the time course of ΔF in response to voltage steps depended on the target membrane potential as well as the superfusing conditions. To compare the time course of ΔF and the presteady-state charge relaxations, we recorded current relaxations and fluorescence simultaneously from the same oocyte with the same recording bandwidth for each signal. During the presteady-state period, the signals, were satisfactorily described by single time constants, designated τ^{Q} (presteady-state charge displacement) and τ^{F} (fluorescence intensity) respectively, as shown for a representative oocyte expressing A116C (Fig 4A). For these experiments, we again focussed on the previously indentified voltage-dependent partial reactions and recorded data in 100Ch, assumed to allow only transitions associated with the empty carrier (0↔1) and internal Na^+ binding (7↔0) and 100Na, assumed include both the empty carrier and Na^+ interactions (transitions 7↔0↔1↔2↔3) (Fig 1A). Fig 4B shows plots of τ^Q and τ^F vs V under the two superfusing conditions (100Ch and 100Na). Both τ^Q and τ^F showed "bell-shaped" dependences on membrane potential. For τ^Q the peak value shifted to the right in 100Na relative to 100Ch as for the WT (e.g. (9)). Mutant S155C showed excellent agreement between the τ's over the whole voltage range for both superfusion conditions. There was similar agreement between τ's for A116C when superfusing with 100Na, but they deviated when superfusing with 100Ch for $V<0$, with τ^F being significantly faster than τ^Q. In contrast, mutants A104C and S226C showed τ^F values that were significantly slower than the corresponding τ^Q for both superfusion conditions.

Discussion

Here we compare presteady-state charge relaxations and changes in fluorometric intensity to investigate possible structure-function correlates between inferred local conformational changes and charge movement in response to changes in membrane potential. We also combine data from previously identified sites (Ser-155, Ser-226, Gln-319 and Glu-451) (14) with data for three new sites characterized in this study. For such a comparison to be useful, it is desirable for the mutagenesis and subsequent labeling to have minimal effect on the transport function so that as close to WT behavior can be observed. Indeed, labeling all sites except Cys-144 left the basic transport behavior unchanged. The behavior of S144C was similar to that of a previously characterized S448C mutant (13) and reaffirms the functional importance of the two reentrant regions of the protein in which these sites are located (Fig 1B). Moreover, accessibility to Cys-144 from the external medium was strongly dependent on the presence of Na^+, which suggested that it became more exposed with Na^+ ions bound, thus implying that a significant conformational change occurred with cation binding.

Comparison between Q and ΔF in the steady-state.

Na^+-dependence: A104C and A116C as well as the previously described mutants (S155C, S226C, Q319C and E451C (14)), gave resolvable ΔF in response to voltage steps in the absence of external Na^+. This indicated that in response to changes in membrane potential they sensed conformational changes associated with the empty carrier reorientation and internal Na^+ binding/debinding (Fig 1A). The addition of Na^+ ions to the external medium modified the voltage-dependence of the presteady-state charge movements in a qualitatively similar fashion to that found for the WT (e.g.(9)) and we assumed that the electrogenic characteristics were influenced neither by the mutagenesis nor labeling. The fluorescence signals were also altered markedly by external Na^+ ions, which depended on the labeling site.

To characterize the Na^+-dependence, we compared the variation of the respective mid-point voltages for charge ($V_{0.5}{}^{Q}$) and fluorescence ($V_{0.5}{}^{F}$) as $[Na^+]_o$ was varied. In the former case, this parameter represents an equilibrium potential for the voltage-dependent redistribution of mobile charges between extreme hyperpolarizing or depolarizing potentials. A feature of the presteady-state behavior of electrogenic SLC34 proteins is the linear relationship between $V_{0.5}{}^{Q}$ and $[Na^+]_o$ for large $[Na^+]_o$ and this appears to be a common kinetic feature for a number of electrogenic cation-coupled transporters (22-25). For NaPi-IIb we have previously shown that a 4-state kinetic model can account for this characteristic, whereby both the empty carrier and sequential binding of 2 Na^+ ions from the external medium before P_i contribute to the overall voltage dependence (18). Simulations show that for 2 Na^+ ions binding sequentially, the limiting slope at high $[Na^+]_o$ approaches ≈120 mV/decade $[Na^+]_o$ at room temperature (18). As shown in

Table 1, there was reasonable agreement between the limiting slopes for charge and fluorescence for A104C, A116C, E451C and S155C. The similarity of the limiting slopes for charge and fluorescence indicated that the microenvironments of fluorophores at these sites "experienced" conformational changes directly related to the binding (and debinding) of multiple Na^+ ions. In contrast, two previously described mutants (S226C and Q319C (14)) showed markedly reduced slopes for the $V_{0.5}^F$ *vs* $\log_{10}[Na^+]_o$ plots, which initially suggested that these sites reported conformational changes possibly associated with a single Na^+ ion interaction (Fig 3B).

A 5-state kinetic scheme accounts for the fluorescence emissions

To explore the underlying mechanism for the fluorescence behavior with respect to Na^+ interactions in the absence of external P_i, we performed kinetic simulations with a 5-state model that included a recently identified single Na^+ interaction at the cytosolic interface (10) (Fig 5A). Rate constants describing the forward and backward transitions between the states were chosen based on previous kinetic simulations (e.g. (11, 18)) to give reasonable agreement between the measured Q-V data and simulation (Fig 5B, C). To simulate the voltage-induced changes in fluorescence, we expressed the total F from a fixed population of transporters (N_t) as: $F = N_t \sum X_n qy_n$, where X_n is the probability of occupancy of state n and qy_n is an apparent quantum yield associated with that state (7, 26). This is the simplest model that might reasonably account for the changes in fluorescence intensity and but makes no assumption about the underlying mechanism for quenching. With this caveat in mind, for each labeling site, we can assign a set of apparent qy's according to the state occupancy. For a given state, if the fluorophore's microenvironment is different for each labeling site, the set of qy's will be unique for that mutant. By appropriate choice of the apparent quantum yield associated with each state, we could account for the general features of voltage dependent properties of the fluorescence data, including the unique non-monotonic characteristic of A104C, as well as previously published data for labeling at Ser-155, Ser-226, Gln-319 and E451C (14) (see Fig S2).

We first categorized the ΔF-V behavior according to whether apparent quenching occurred for *depolarizing* voltage steps (A116C and the previously described Q319C and E451C (14)) or *hyperpolarizing* voltage steps (S155C, S226C (14)). Mutant A104C showed a mixture of both modes (see below). For example, we could recapitulate the measured data for A116C by assigning finite quantum yield factors to states 1, 2 and 3. To reduce the number of unknowns, we set $qy_2 = qy_3$ and found that the ratio $qy_1/qy_{2,3}$ was a critical determinant in defining the $V_{0.5}^F$ vs $\log_{10}[Na^+]_o$ slope (Fig 3B). For a given hyperpolarizing voltage, more transporters will occupy state 3 (both Na^+ ions bound) as $[Na^+]_o$ is increased, which is also reflected in the increased charge displacement from the depolarizing limit (Fig 5B). If the occupancy of state 3 is associated with a greater relative apparent quantum yield, then there will be a corresponding increase in ΔF for the same experimental conditions, as seen by comparing the example simulations with $qy_1/qy_{2,3}$=0.67 and 1, respectively (Fig 5D). For our model parameter set (see legend, Fig 5), the simulations predict that the occupancy of state 2 was relatively unlikely (*data not shown*) when partial reaction 2↔3 was very cooperative (18).

For mutants that showed apparent fluorescent quenching for *hyperpolarizing* voltage steps (S155C, S226C) (see also (14)), we obtained close agreement between measurement and simulations if non-zero apparent quantum yields were assigned to the inward facing states (0, 1 and 7) (Table 2). For example, our simulations indicated that mutant S226C, which shows a relatively weak dependence of V_{05}^{F} on $[Na^+]_o$ (Table 2) would give the highest fluorescence signal when occupying state 7 (internal Na^+ bound) with a depolarized membrane. For a hyperpolarizing voltage step, and increasing $[Na^+]_o$, the state occupancies will redistribute and movement out of states 7 and 0 will be accompanied by a decrease in emitted fluorescence. For mutant S155C, it was necessary to assign some fluorescence to state 1 to account for (i) the reduced fluorescence quenching in the absence of external Na^+ and (ii) increased the slope of $V_{0.5}^{F}$ vs $\log_{10}[Na^+]_o$, as observed experimentally.

Finally, to reproduce the biphasic characteristic of the ΔF-V data for A104C (Fig 3A), we assigned finite quantum yields to all 5 states of the kinetic scheme (see Table 2). The simulations with these parameters predicted the voltage dependence of ΔF in the steady-state (Fig 5F) and the shift in $V_{0.5}^{F}$ for hyperpolarizing potentials as $[Na^+]_o$ decreased (compare Fig 5G with Fig 3B). For this mutant, the fluorescence emitted by the fluorophore at Cys-104 reflects both inward and outward state occupancies as the imposed membrane potential is varied from strong depolarization to strong hyperpolarization, respectively. For A104C, the simulations could also successfully recapitulate the unique time-dependent relaxations observed when making a return voltage step from the depolarizing limit (Fig 5H and compare with Fig 2A). At +160 mV all transporters occupy state 7 and a depolarizing change in membrane potential results in transporters leaving this state and redistributing between the other states. The initial rapid quenching represents movement to state 0, which has a very low assigned quantum yield, and the slower relaxing increase in fluorescence represents the reorientation of the empty carrier to state 1 and eventual occupancy of state 3 (with 2 Na^+ ions bound).

The steady-state fluorescence behavior for all 6 mutants was summarized by generating a set of apparent quantum yields for each that gave a good match to the experimental data (Table 2). For a given mutant, the table entries indicate a relative measure of the change in the microenvironment of the respective fluorophore when the protein occupies each of the 5 states. Thus, fluorophores at Cys-104 report larger fluorescence emission when the protein is inward facing with Na^+ bound or outward facing with and without Na^+ bound. Fluorophores at Cys-116, Cys-319 and Cys-451 report occupancy of outward facing states and also the inward facing empty carrier (for Cys-319 and Cys-451). For the labelled Cys-116 we cannot distinguish between external Na^+ bound or unbound. In contrast, fluorophores at Cys-155 and Cys-226 show complementary behavior to Cys-116, 319, 451 and report fluorescence for the inward facing states. In addition, the fluorophore at Cys-155 also reports the change of orientation of the empty carrier in the absence of external Na^+. We note that the simulations for each mutant are based on a model in which the electrogenic properties and rates for the partial reactions are fixed and do not take account of variations in voltage dependence between mutants that result from the mutagenesis and labeling (Table 1).

Phosphate dependence

All mutants gave resolvable voltage-dependent ΔF when saturating P_i (1 mM) was superfused with 100 mM external Na^+. For the new mutants A104C and A116C, fluorescence was quenched for hyperpolarizing potentials relative to the emission level in100Na. This established that in the cotransport mode, the fluorophores at these sites reported a different change in their microenvironment from when only Na^+ was present. For strong membrane depolarization, the fluorophore at Cys-104 reported the same ΔF, independent of the superfusing condition (Fig 2B). Based on the above simulations, this suggested that only inward conformations associated with states 0 and 7 were reported under these conditions. Despite quenching of ΔF in the presence of P_i, the voltage dependence of ΔF was qualitatively similar for both A104C and A116C and showed the same sigmoidal dependence on V. Thus the quenching behavior of fluorophores at Cys-104 and Cys-116 for hyperpolarizing potentials suggests that the relative changes in the fluorophore's microenvironment remain unchanged and largely reflect voltage dependent conformational changes associated with the external cation interactions. However, for a given membrane potential, occupancy of states 4 through 6 (Fig 1A), for which the apparent quantum yields are predicted to be small, is now favoured and therefore the relative fluorescence emission is proportionally reduced. The P_i-dependence ΔF-V could in principle be quantified by extending the 5-state scheme to include the complete cotransport cycle, however with such a large number of free parameters and unknown internal rate constants, it would be difficult to determine a unique set of quantum yields with confidence.

Comparison of the time resolved charge movement and ΔF

We reasoned that if the conformational changes purportedly reported by the fluorophore were directly related to those associated with the charge movement, a correlation between τ^Q and τ^F should also exist. Only one mutant S155C fulfilled this criterion for both superfusion conditions and over a wide potential range, which suggested that the conformational changes reported by the fluorophore at Cys-155 do indeed reflect those accompanying the charge movement associated both with the empty carrier itself and cation interactions. Mutant A116C showed reasonable agreement between τ^Q and τ^F for 100Na and this result is consistent with having finite quantum yield for states 1,2 and 3. There was also good agreement between τ^Q and τ^F for superfusion in 100Ch for V>0, however the time constants deviated significantly for V<0. As the time constant is a function of all the associated rate constants for the state transitions involved, this deviation suggests that the fluorophore at this site does not report all the electrogenic conformational changes that occur in the protein as a whole. Deviations between τ^Q and τ^F were also clearly evident for A104C and S226C. In the latter case the voltage dependence was similar, however τ^F was approximately 1.5 ms slower over the test potential range. This discrepancy may also reflect a limitation of our application of single exponential curve fitting to describe the kinetics as it is only formally applicable to a two state system. For example, a hypothetical 3 state system in which a fast electrogenic transition is followed by a slower transition that leads to the final state reported by the fluorophore is formally described by two eigenvalues, however the fluorophore only reports occupancy of the final state that would be mostly determined by the slower transition.

Conclusions

We present evidence that the labeled sites in flounder NaPi-IIb are involved in specific molecular rearrangements that reflect the influence of membrane potential and availability of external Na^+ ions. In the absence of external P_i, a 5-state kinetic scheme can account for the behavior in terms of charge movement and changes in fluorescence intensity. By assigning a fractional apparent quantum yield to each state, we can interpret the steady-state fluorescence signal in terms of the state-dependent molecular rearrangements unique to the labeling site. Our findings also provide indirect evidence in support of an alternating access mechanism, whereby the probability of the cation binding sites being exposed to the external or internal media is governed by the imposed membrane potential. Furthermore, by comparing the time course of fluorescence changes and charge movement, we can identify those parts of the protein that move in response to changes in membrane potential. This approach of combining charge kinetics and fluorescence data should find application for other electrogenic cotransporters to elucidate their struction-function relationships under physiological conditions, particularly if 3-D structural data is available.

Acknowledgements

We thank Eva Hänsenberger for oocyte preparation and Drs Don Loo and Edune Gorraitz (UCLA) for critical comments on the manuscript. Financial support was provided by the Swiss National Science Foundation (to ICF).

Table 1 Comparison of properties of mid-point voltages $V_{0.5}^{Q}$ and $V_{0.5}^{F}$

Parameter	**WT**	**A104C**	**A116C**	**S155C[1]**	**S226C[1]**	**Q319C[1]**	**E451C[1]**
$V_{0.5}^{Q}$ (mV)[3]	-11±7	XX±Y	XX±Y	6±3	-9±4	-5±4	-3±5
$V_{0.5}^{Q}$ (mV)[3]	n.d.	19±19	-13±6	-8±5	2±3	-5±5	6± 3
$V_{0.5}^{F}$ (mV)[3]	n.a.	-25± 2	-16± 3	-23± 8	-11± 1	35±2	-12± 7
$V_{0.5}^{Q}$ /log[Na^{+}]$_{o}$ (mV/decade)	122 ± 18	XX±YY	XX±Y	104±12	91±7	105±8	129± 5
$V_{0.5}^{Q}$ /log[Na^{+}]$_{o}$ (mV/decade)	n.d	121 ± 7	118 ± 3	101±14	102±9	109±8	131± 4
$V_{0.5}^{F}$/log[Na^{+}]$_{o}$ (mV/decade)	n.a	121± 7[2]	94 ± 1	140±5	58±8	55±3	99± 2

Each entry is the mean SEM for $n \geq 4$ for each construct.

n.a.: not applicable; n.d.: not determined.

Grey shaded rows: fit parameters obtained after labeling with MTS-TAMRA.

[1] Data reported in (14).

[2] Boltzmann fit performed from minimum of Δ*F*-*V* data to hyperpolarizing extreme (see text).

[3] Superfusion with 100 mM Na^{+} (100Na)

Table 2 Comparison of fractional apparent quantum yields for mutants

	State				
Mutant	**7**	**0**	**1**	**2**	**3**
A104C	0.49	0.02	0.18	0.09	0.22
A116C	0	0	0.33	0.33	0.33
S155C	0.40	0.40	0.20	0	0
S226C	0.77	0.23	0	0	0
Q319C	0	0.16	0.32	0.26	0.26
E451C	0	0.07	0.13	0.27	0.53

For each mutant and a given state, the fractional quantum yield was calculated from the ratio of apparent quantum yield for that state, divided by the sum of the apparent quantum yields for each state. The apparent quantum yield was determined by trial and error to yield a best visual match between the experimental data and simulations using the kinetic scheme (Fig 5A).The same kinetic parameter set was assumed for each mutant (see legend, Fig 5).

Figure legends

Fig. 1 Kinetic scheme of NaPi-IIb transport cycle and sites of cysteine substitution.

A) An 8 state kinetic scheme describes the cotransport cycle. Under physiological conditions this proceeds in the direction shown (*dashed arrow*). The empty carrier transition (0↔9), Na^+ binding partial reactions (1↔2) and cytosolic Na^+ interaction (0↔7) are assumed to be electrogenic (*black arrows*). In this study, three experimental conditions define the occupied states and interconverting partial reactions: 100 mM choline Cl (100Ch) (*white*); 100 mM NaCl (100Na) (*grey*) and 100 mM NaCl+1 mM P_i (100Na+1P_i) (*dark grey*). For each condition, the relative occupancy of any state depends on the membrane potential.

B) Secondary topology model (e.g. (9)), showing the relative location of the Cys substitution sites considered in this study: previously described sites (*green*) (14) and black (13) and new sites in this study (*red*).

Fig. 2 Voltage and substrate-dependent changes in steady-state fluorescence intensity.

A) Recordings of changes in emitted fluorescence intensity for mutant A104C (*upper traces*) and S116C (*lower traces*) in response to voltage steps indicated for three superfusion conditions. Colors of traces correspond to same color for voltage pulses. Note that different holding potentials were used.

B) Voltage dependence of ΔF for A104C and A116C with three superfusion conditions (100Ch: *open circles;* 100Na *filled circles*; 100Na+1P_i: *filled squares*). For A116C, data for individual oocytes were fit with Eqn 3 to obtain $\Delta F_{\max}$ for 100Na and then normalized and offset so that they superimpose at the depolarizing extreme. For A104C, data were fit from the hyperpolarizing limit to the minimum and normalized to $\Delta F_{\max}$ before pooling ($n \geq 5$).

C) Parametric plots of ΔF against charge displaced, Q from pooled, normalized data as in B), to indicate potential correlations between the corresponding data sets for superfusion in 100Na (*filled squares*); 100Ch (*open squares*). For A104C (100Na, V>0)) and A116C (100Ch) linear relationships are evident (*dashed lines*). For A116C the 100Na data deviate from the theoretical relationship with 100% correlation (*continuous line*). Arrows indicate membrane potential corresponding to data point.

Fig. 3 External Na^+ shifts the ΔF-V relationship for A104C and A116C

A) Normalized ΔF-V data for A104C (*upper*) and A116C (*lower*) shown for different $[Na^+]_o$ indicated. Continuous lines are fits using Eqn 3. Note that for A104C, fits were only performed between the hyperpolarizing limit and the minimum. Normalized, pooled data were adjusted to superimpose at the depolarizing limit.

B) Relationship between mid-point voltage predicted from Boltzmann fit ($V_{0.5}^{F}$) and $\log_{10}[Na^+]_o$ for two new mutants in this study (*filled symbols*) and previously characterized mutants (*open symbols*)-data redrawn from (14). Straight lines are result of linear regression applied to data points (see Table 1 for slopes).

Fig. 4 Comparison of time constants for current and Δ*F*.

A) Representative data from the same oocyte expressing A116C and labeled with MTS-TAMRA, in response to the voltage steps shown. Presteady-state current relaxation (*center panel*) and corresponding ΔF traces (*right panel*) show single exponential fits from which the time constants τ^{Q} and τ^{F} were obtained. Note that for the same voltage step, the fluorescence and charge changes are opposite for this mutant. The recording bandwidth for both signals was 500Hz.

B) Plots of τ^{F} (*red*) and τ^{Q} (*black*) against V, for 4 mutants and superfusion in 100Ch (*open squares*) or 100Na (*filled squares*). Error bars are values reported from fits to pooled data (n>3). Data points are joined for visualization.

Fig. 5 Simulations confirm fluorescent behavior

A) Five-state kinetic scheme used simulate presteady-state and fluorescence behavior. Boxed values indicate apparent valence of the corresponding partial reaction. The voltage dependence of these partial reactions was modelled by applying Eyring Transition State Theory to describe analytically the dependence of transition rate constants on membrane potential. Voltage-dependent partial reactions account for the movement of equivalent lumped charges that change conformational state by crossing a sharp, symmetrical energy barrier. The rate constants (in s^{-1}) were as follows: $k_{10}=300\exp(-Vz_{10}\mu/2)$, $k_{01}=100\exp(Vz_{10}\mu/2)$; $k_{12}=[Na^+]_o 2000\exp(-Vz_{12}\,\mu/2)$, $k_{21}=500\exp(Vz_{12}\,\mu/2)$, $k_{23}=[Na^+]_o 8300$, $k_{32}=100$, $k_{27}=1$, $k_{07}=[Na^+]_i 2000\exp(Vz_{07}\,\mu)$, $k_{70}=500\exp(-Vz_{07}\,\mu)$ and $\mu=e/kT\approx 40\ V^{-1}$ at 20 °C, $z_{10}=0.4$, $z_{12}=0.4$, $z_{07}=0.2$. The rates constant k_{72} was defined independently in terms of the other rate constants under conditions of zero driving force to satisfy the detailed balance for the leak cycle. We assumed that $[Na^+]_i=0.02$ M.

B) Simulated Q-V data using the model parameter set given in A) for the $[Na^+]_o$ indicated. Continuous lines are fits with Eqn 3.

C) Relationship between $V_{0.5}^{Q}$ and $\log_{10}[Na^+]_o$ for the simulated data in B). A linear regression fit to these data yielded a slope of 115 ± 4 mV/decade.

D) Simulated ΔF-V data using the model in A) with two sets of quantum yield factors: qy_0= 0, qy_1= 0.2, qy_2=0.3, qy_3= 0.3, qy_7= 0 (*left panel*); qy_0= 0, qy_1= 0.2, qy_2=0.2, qy_3= 0.2, = 0, (*right panel*) and indicated $[Na^+]_o$. Continuous lines are fits with Eqn 3.

E) The mid-point voltage for simulated ΔF ($V_{0.5}^F$) shows a linear dependence on $[Na^+]_o$ with slopes that depend on the relative quantum yield between state 1 and states 2/3 as indicated. Slopes vary from 135±1 mV/decade ($qy_1/qy_{2,3}$= 0.5) to 65±4 mV ($qy_1/qy_{2,3}$=2.0).

F) Simulations recapitulate the behavior of A104C (compare with Fig 3A). Continuous lines are fits with Eqn 3 from hyperpolarizing limit to minimum for each data set. The set of quantum yields for the 5 states was as follows: qy_0=0.02, qy_1=0.2, qy_2=0.1, qy_3=0.25, qy_7=0.55.

G) The mid-point voltage of the A104C simulation ($V_{0.5}^F$) shows a linear dependence on $[Na^+]_o$ with slope: 101±5 mV/decade.

H) Simulations of A104C fluorescence behavior recapitulate the transient behavior as seen in representative data (Fig 2A). The same colors are used for the voltage step and simulated fluorescence.

Supplementary Information

Fig. S1

Cotransport activity of mutant S144C is suppressed by exposure to thiol-reactive reagents from external medium.

A) Phosphate induced current (I_{P_i}) plotted as a function of membrane potential before and after exposure for 3 min to 1 mM MTS-TAMRA. Data pooled from 4 oocytes. Data normalized to response under control conditions at -100 mV. Oocytes were incubated in 100Na at -50 mV during exposure to MTSET.

B) Time course of loss of electrogenic cotransport activity shown for incubation with fixed concentrations of MTSET in 100Na (50 μM) and 100Ch (75 μM) (at -50 mV). Continuous lines are fits to the data points using Eqn 2. Data points were normalized to the response at t=0.

Fig. S2

Simulations of ΔF-V for two mutants introduced in this study and four previously investigated (14). For each simulation, the same rate constants and other kinetic parameters were used (see legend, Fig 6) and only the apparent quantum yields were varied to obtain qualitative agreement with data.

References

1. Forrest, L. R., R. Kramer, and C. Ziegler. 2011. The structural basis of secondary active transport mechanisms. Biochimica et Biophysica Acta 1807:167-188.
2. Zhao, Y., D. S. Terry, L. Shi, M. Quick, H. Weinstein, S. C. Blanchard, and J. A. Javitch. 2011. Substrate-modulated gating dynamics in a Na+-coupled neurotransmitter transporter homologue. Nature 474:109-113.
3. Koch, H. P., and H. P. Larsson. 2005. Small-scale molecular motions accomplish glutamate uptake in human glutamate transporters. Journal of Neuroscience 25:1730-1736.
4. Akyuz, N., R. B. Altman, S. C. Blanchard, and O. Boudker. 2013. Transport dynamics in a glutamate transporter homologue. Nature.
5. Claxton, D. P., M. Quick, L. Shi, F. D. de Carvalho, H. Weinstein, J. A. Javitch, and H. S. McHaourab. 2010. Ion/substrate-dependent conformational dynamics of a bacterial homolog of neurotransmitter:sodium symporters. Nat Struct Mol Biol 17:822-829.
6. Loo, D. D., B. A. Hirayama, E. M. Gallardo, J. T. Lam, E. Turk, and E. M. Wright. 1998. Conformational changes couple Na+ and glucose transport. Proceedings of the National Academy of Sciences of the United States of America 95:7789-7794.
7. Loo, D. D., B. A. Hirayama, M. H. Karakossian, A. K. Meinild, and E. M. Wright. 2006. Conformational dynamics of hSGLT1 during Na+/glucose cotransport. Journal of General Physiology 128:701-720.
8. Meinild, A. K., B. A. Hirayama, E. M. Wright, and D. D. Loo. 2002. Fluorescence studies of ligand-induced conformational changes of the Na^+/glucose cotransporter. Biochemistry 41:1250-1258.
9. Forster, I. C., N. Hernando, J. Biber, and H. Murer. 2012. Phosphate transport kinetics and structure-function relationships of SLC34 and SLC20 proteins. Curr Top Membr 70:313-356.
10. Patti, M., C. Ghezzi, and I. C. Forster. 2013. Conferring electrogenicity to the electroneutral phosphate cotransporter NaPi-IIc (SLC34A3) reveals an internal cation release step. Pflugers Archiv. European Journal of Physiology.
11. Ghezzi, C., A. K. Meinild, H. Murer, and I. C. Forster. 2011. Voltage- and substrate-dependent interactions between sites in putative re-entrant domains of a Na(+)-coupled phosphate cotransporter. Pflugers Archiv. European Journal of Physiology 461:645-663.
12. Ghezzi, C., H. Murer, and I. C. Forster. 2009. Substrate interactions of the electroneutral Na+-coupled inorganic phosphate cotransporter (NaPi-IIc). J Physiol 587:4293-4307.
13. Virkki, L. V., H. Murer, and I. C. Forster. 2006. Voltage clamp fluorometric measurements on a type II Na^+-coupled P_i cotransporter: shedding light on substrate binding order. Journal of General Physiology 127:539-555.
14. Virkki, L. V., H. Murer, and I. C. Forster. 2006. Mapping conformational changes of the type IIb Na^+/P_i cotransporter by voltage clamp fluorometry. Journal of Biological Chemistry 281:28837-28849.
15. Cha, A., N. Zerangue, M. Kavanaugh, and F. Bezanilla. 1998. Fluorescence techniques for studying cloned channels and transporters expressed in Xenopus oocytes. Methods in Enzymology 296:566-578.
16. Loo, D. D., B. A. Hirayama, A. Cha, F. Bezanilla, and E. M. Wright. 2005. Perturbation analysis of the voltage-sensitive conformational changes of the Na+/glucose cotransporter. Journal of General Physiology 125:13-36.
17. Meinild, A. K., D. D. Loo, S. Skovstrup, U. Gether, and N. MacAulay. 2009. Elucidating conformational changes in the gamma-aminobutyric acid transporter-1. J Biol Chem 284:16226-16235.

18. Andrini, O., A. K. Meinild, C. Ghezzi, H. Murer, and I. C. Forster. 2012. Lithium interactions with Na+-coupled inorganic phosphate cotransporters: insights into the mechanism of sequential cation binding. Am J Physiol Cell Physiol 302:C539-554.
19. Ehnes, C., I. C. Forster, A. Bacconi, K. Kohler, J. Biber, and H. Murer. 2004. Structure-function relations of the first and fourth extracellular linkers of the type IIa Na^+/P_i cotransporter: II. Substrate interaction and voltage dependency of two functionally important sites. Journal of General Physiology 124:489-503.
20. Karlin, A., and M. H. Akabas. 1998. Substituted-cysteine accessibility method. Methods in Enzymology 293:123-145.
21. Ehnes, C., I. C. Forster, K. Kohler, A. Bacconi, G. Stange, J. Biber, and H. Murer. 2004. Structure-function relations of the first and fourth predicted extracellular linkers of the type IIa Na^+/Pi cotransporter: I. Cysteine scanning mutagenesis. Journal of General Physiology 124:475-488.
22. Meinild, A. K., and I. C. Forster. 2012. Using lithium to probe sequential cation interactions with GAT1. Am J Physiol Cell Physiol 302:C1661-1675.
23. Hazama, A., D. D. Loo, and E. M. Wright. 1997. Presteady-state currents of the rabbit Na+/glucose cotransporter (SGLT1). J Membr Biol 155:175-186.
24. Mager, S., Y. Cao, and H. A. Lester. 1998. Measurement of transient currents from neurotransmitter transporters expressed in Xenopus oocytes. Methods Enzymol 296:551-566.
25. Mackenzie, B., D. D. Loo, Y. Fei, W. J. Liu, V. Ganapathy, F. H. Leibach, and E. M. Wright. 1996. Mechanisms of the human intestinal H+-coupled oligopeptide transporter hPEPT1. J Biol Chem 271:5430-5437.
26. Larsson, H. P., A. V. Tzingounis, H. P. Koch, and M. P. Kavanaugh. 2004. Fluorometric measurements of conformational changes in glutamate transporters. Proceedings of the National Academy of Sciences of the United States of America 101:3951-3956.

Figure 1

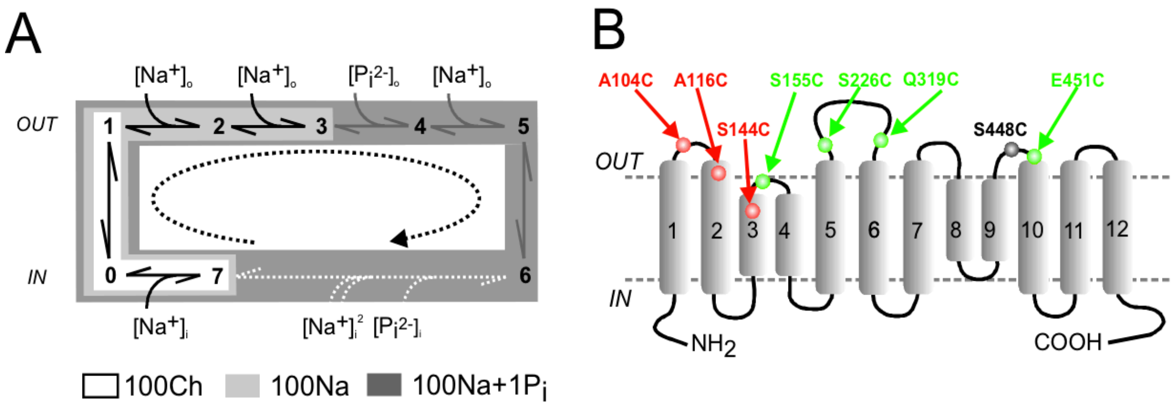
A
[Na+]o
[Na+]o
[Pi2-]o
[Na+]o
OUT
1
2
3
4
5
IN
0
7
6
[Na+]i
[Na+]i2 [Pi2-]i
100Ch
100Na
100Na+1Pi
B
A104C
A116C
S144C
S155C
S226C
Q319C
S448C
E451C
OUT
IN
1
2
3
4
5
6
7
8
9
10
11
12
NH2
COOH

Figure 2

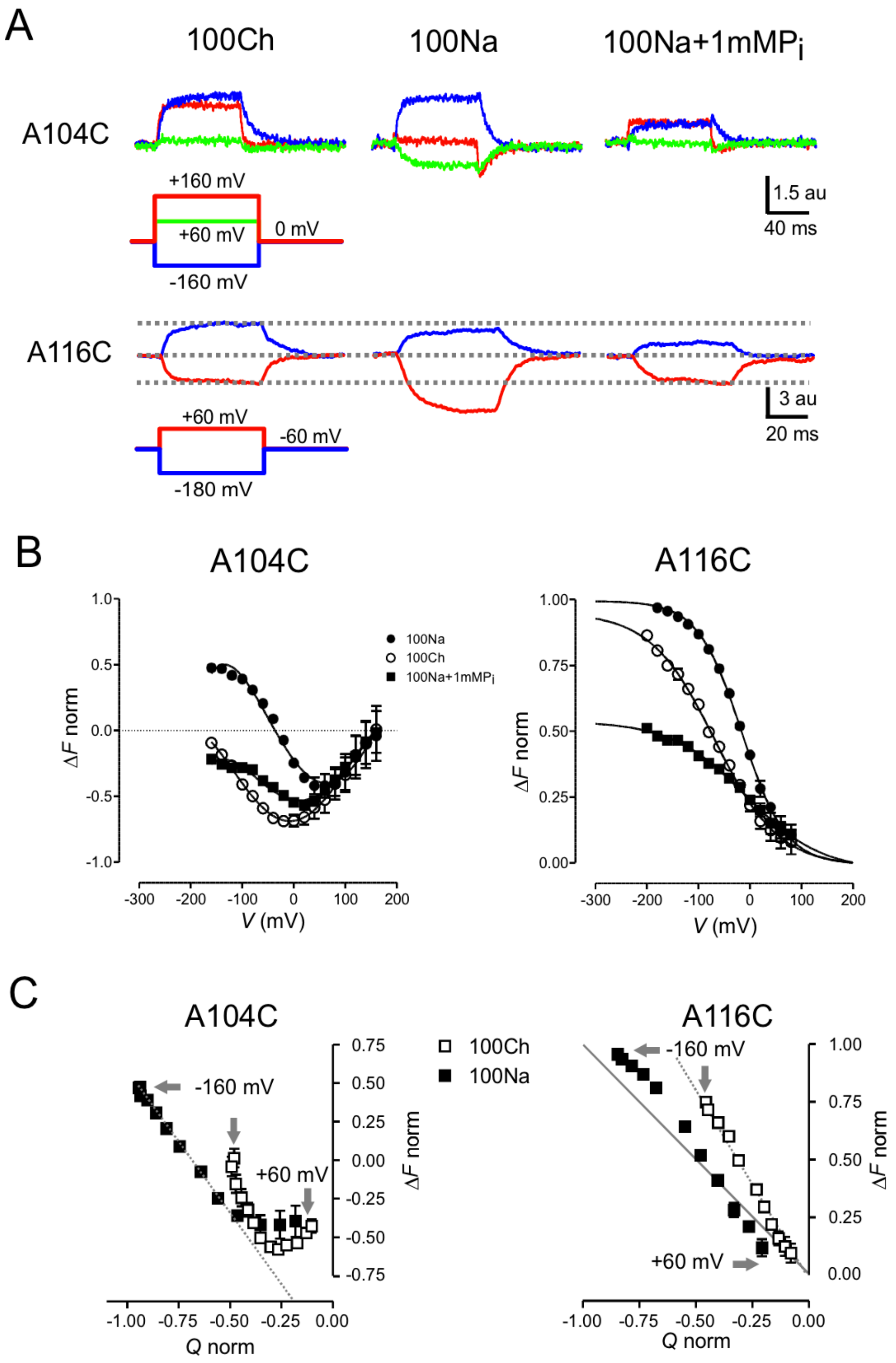
A
100Ch
100Na
100Na+1mMP$_i$
A104C
+160 mV
+60 mV
0 mV
-160 mV
1.5 au
40 ms
A116C
+60 mV
-60 mV
-180 mV
3 au
20 ms
B
A104C
A116C
ΔF norm
V (mV)
● 100Na
○ 100Ch
■ 100Na+1mMP$_i$
1.0
0.5
0.0
-0.5
-1.0
1.00
0.75
0.50
0.25
0.00
-300
-200
-100
0
100
200
C
A104C
A116C
□ 100Ch
■ 100Na
-160 mV
+60 mV
ΔF norm
Q norm
-1.00
-0.75
-0.50
-0.25
0.00
0.75
0.50
0.25
0.00
-0.25
-0.50
-0.75
1.00

Figure 3

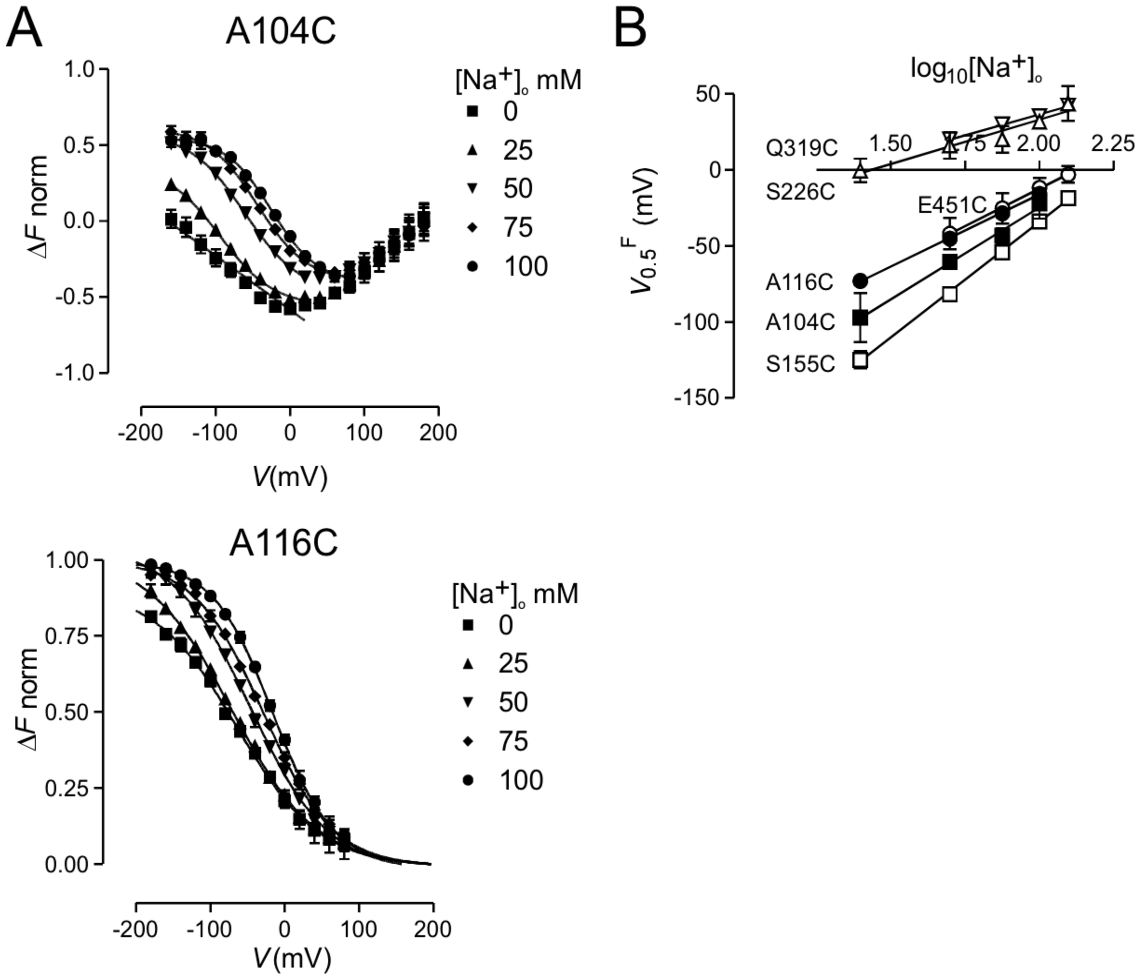
A
A104C
1.0
0.5
0.0
-0.5
-1.0
ΔF norm
-200
-100
0
100
200
V(mV)
[Na+]o mM
■ 0
▲ 25
▼ 50
◆ 75
● 100
A116C
1.00
0.75
0.50
0.25
0.00
ΔF norm
-200
-100
0
100
200
V(mV)
[Na+]o mM
■ 0
▲ 25
▼ 50
◆ 75
● 100
B
log10[Na+]o
50
0
-50
-100
-150
1.50
1.75
2.00
2.25
V0.5F (mV)
Q319C
S226C
E451C
A116C
A104C
S155C

Figure 4

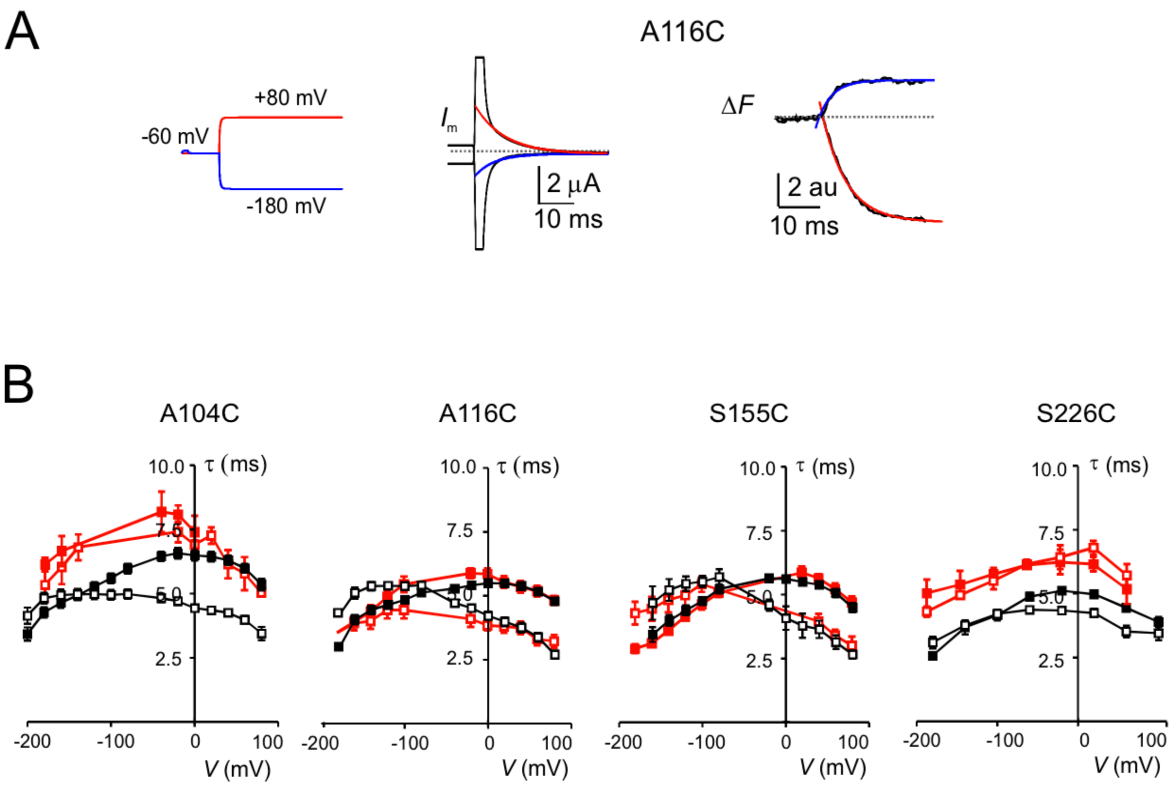
A
A116C
+80 mV
-60 mV
-180 mV
I_m
2 μA
10 ms
ΔF
2 au
10 ms
B
A104C
A116C
S155C
S226C
τ (ms)
10.0
7.5
5.0
2.5
-200
-100
0
100
V (mV)

Figure 5

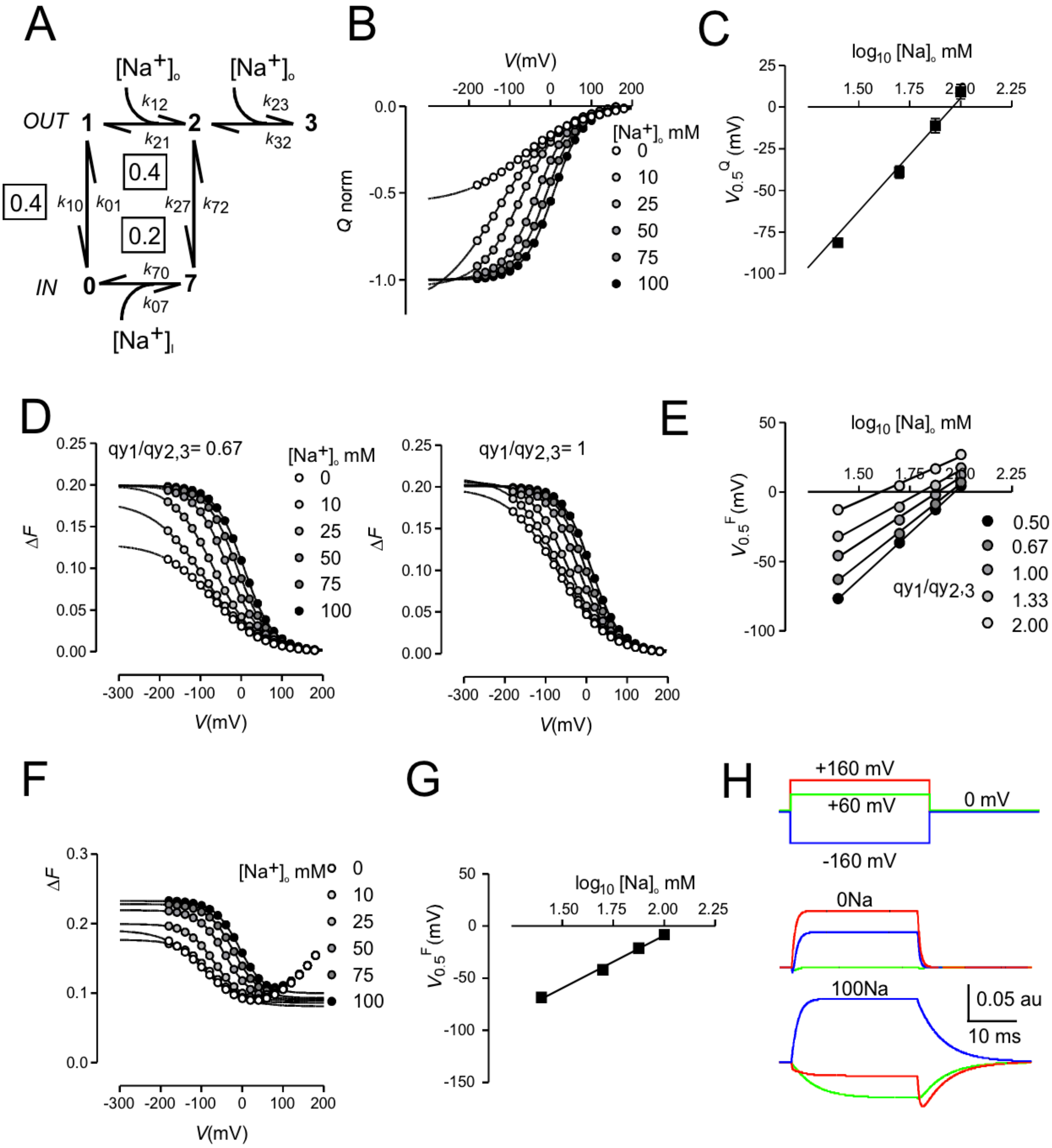
A
[Na+]o
[Na+]o
k12
k23
OUT
1
2
3
k21
k32
0.4
0.4
k10
k01
k27
k72
0.2
k70
IN
0
7
k07
[Na+]i
B
V(mV)
-200
-100
0
100
200
0.0
-0.5
-1.0
Q norm
[Na+]o mM
0
10
25
50
75
100
C
log10 [Na]o mM
1.50
1.75
2.00
2.25
25
0
-25
-50
-75
-100
V0.5 Q (mV)
D
qy1/qy2,3= 0.67
[Na+]o mM
0
10
25
50
75
100
0.25
0.20
0.15
0.10
0.05
0.00
ΔF
-300
-200
-100
0
100
200
V(mV)
qy1/qy2,3= 1
0.25
0.20
0.15
0.10
0.05
0.00
ΔF
-300
-200
-100
0
100
200
V(mV)
E
log10 [Na]o mM
50
0
-50
-100
1.50
1.75
2.00
2.25
V0.5 F (mV)
0.50
0.67
1.00
1.33
2.00
qy1/qy2,3
F
0.3
0.2
0.1
0.0
ΔF
[Na+]o mM
0
10
25
50
75
100
-300
-200
-100
0
100
200
V(mV)
G
50
0
-50
-100
-150
log10 [Na]o mM
1.50
1.75
2.00
2.25
V0.5 F (mV)
H
+160 mV
+60 mV
0 mV
-160 mV
0Na
100Na
0.05 au
10 ms

Figure S1

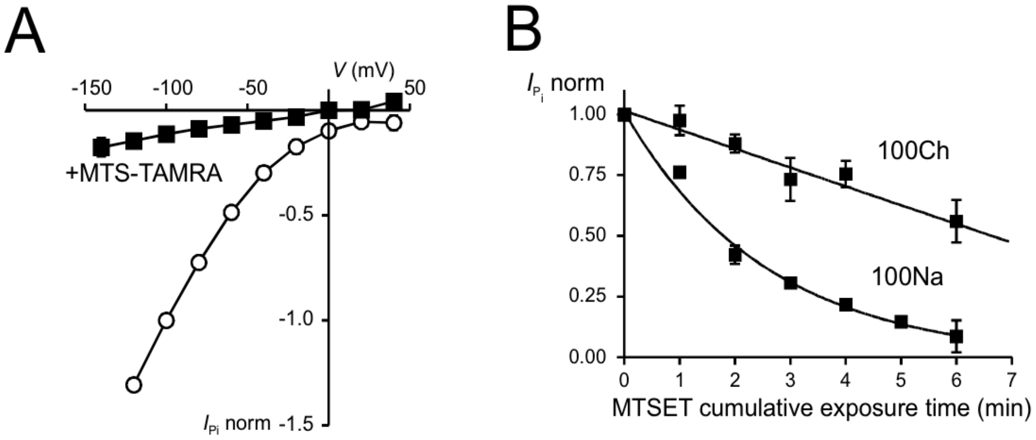
A
V (mV)
-150
-100
-50
50
+MTS-TAMRA
-0.5
-1.0
I_{Pi} norm -1.5
B
I_{P_i} norm
1.00
0.75
0.50
0.25
0.00
100Ch
100Na
0
1
2
3
4
5
6
7
MTSET cumulative exposure time (min)

Figure S2

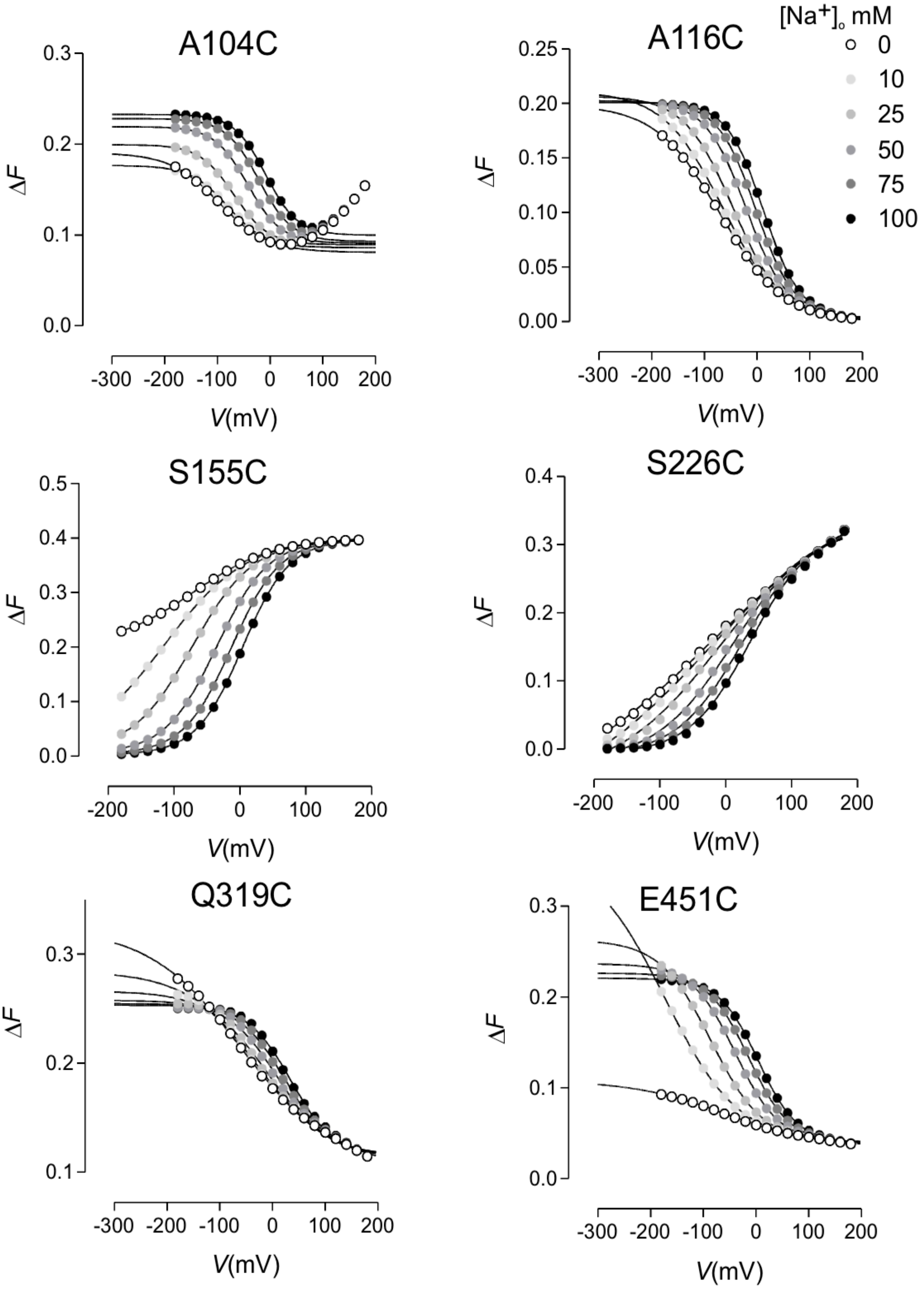
A104C
A116C
[Na+]o mM
○ 0
● 10
● 25
● 50
● 75
● 100
S155C
S226C
Q319C
E451C
ΔF
V(mV)
0.0
0.1
0.2
0.3
0.00
0.05
0.10
0.15
0.20
0.25
0.4
0.5
-300
-200
-100
0
100
200

DISCUSSION

Investigation of internal substrate release steps

Sequence comparison of the electrogenic isoforms NaPi-IIa/b with the electroneutral isoform NaPi-IIc identified specific amino acids that were critical for the electrogenic behavior (Bacconi et al., 2005). Electrogenicity was conferred to NaPi-IIc by substitution of three conserved amino acids, found in all electrogenic isoforms at corresponding sites in NaPi-IIc and the increase in Na^+:P_i stoichiometry from 2:1 to 3:1 was confirmed. Nevertheless, this construct (AAD-IIc), showed significantly altered transport kinetics compared with the WT electrogenic isoforms. Specifically AAD-IIc had a reduced apparent P_i affinity and voltage steps evoked presteady-state currents that were not suppressed by external Pi unlike WT NaPi-IIa/b. Moreover, there was little change in charge transferred with or without external Na^+ ions (Bacconi et al., 2005). The unique behavior of AAD-IIc construct could be understood in terms of alterations to specific partial reactions in the transport cycle. For a multi-state system, all the rate constants contribute to the overall phenomenological transport parameters (apparent affinity, transport velocity) and therefore it is difficult to readily identify whether the mutagenesis had affected one or more partial reactions. We were able to overcome this difficulty and identify these transitions thanks to three experimental strategies conducted using in the TEVC applied to *X. laevis* oocytes. In these experiments we restricted the number of possible states the transporter could occupy and thereby limited the number of possible partial reactions that had to be considered:

1. Activation energy (E_a) measurement of AAD-IIc and of WT NaPi-IIa/b in presence and absence of co-substrates.

   The rationale for these experiments was that the candidate partial reactions might be identified if their activation energy was different from the WT. In these experiments, the temperature dependence of the steady-state and presteady-state kinetics was determined and two main findings emerged. First, by determining the activation energies for cotransport mediated by AAD-IIC, NaPi-IIa and NaPi-IIc, we found that for the electrogenic constructs, E_a was significantly larger than for the electroneutral NaPi-IIc. This is indeed what might be expected as an electrogenic transport cycle would most likely involve more conformational changes (empty carrier charge reorientation and Na^+ ion interaction within the transmembrane electric field). The E_a for AAD-IIc was double that of NaPi-IIa. This established that the mutagenesis had in some way imposed a greater energy cost on the AAD-IIc transport cycle. Second, we found that for AAD-IIc, the temperature dependence of cotransport was very similar to that obtained for the relaxation time constant for the presteady-state assays in the absence of external Na^+. Therefore we initially assumed that the mutagenesis had most likely altered the kinetics of the empty carrier. (*Figure 30*, steps 1-9). This partial reaction represents a potential rate determining step in the transport cycle.

2. Analysis of the presteady-state current of the AAD-IIc for different superfusion conditions.

We then focused our attention on the kinetics of the presteady-state relaxations as these allow specific partial reactions and the associated rate constants to be quantified. Two important observations were made. First, analysis of the presteady-state relaxations showed that unlike the WT NaPi-IIa or NaPi-IIb, there was little change in total charge movement whether external Na^+ was present or not. For the electrogenic WT transporters, addition of external Na^+ causes an approximate 60% increase in total mobile charge (Bacconi et al., 2005; Forster et al., 2012; Patti et al., 2013). For AAD-IIc this indicated that external Na^+ ions do not interact with the transmembrane electric field and this was consistent with the fact that NaPi-IIc alone does not show presteady-state relaxations. Second, when we applied external P_i together with Na^+, the charge distribution changed dramatically, but it was not suppressed, as we would expect for the WT transporters. Instead the equilibrium potential of the voltage dependence of charge vs. voltage data was shifted. This finding meant that in the cotransport mode, instead of the protein simply shuttling between the fully loaded carrier states (5 and 6, *Figure 30*), which we assume is an electroneutral transition (Ehnes et al., 2004a), there was an additional slower electrogenic transition in the cotransport cycle.

To relate this behavior to our kinetic model, we performed simulations using Berkeley Madonna software (http://www.berkeleymadonna.com/). We began with the standard model (Ghezzi et al., 2011, 2011, 2011; Andrini et al., 2012, 2012; Meinild and Forster, 2012) and assigned most of the mobile charge to the empty carrier and internal Na^+ binding. To ensure that the kinetic model of AAD-II would be consistent with the real data, it was necessary to assign a weak interaction of the first sodium (*Figure 30*, steps 1-2, 0.1 e^- instead of 0.4 e^- in the corresponding electrogenic partial reaction for NaPi-IIa/b). By increasing the effective valence of the partial reaction for the last intracellular sodium binding/release step (*Figure 30*, transition 1-9) and setting the release (backward) rate slower than in the standard model, we could successfully recapitulate the presteady-state relaxations in the presence of external P_i.

3. Analysis of fluorescence changes (ΔF) in labeled AAD-IIc Cys mutant.

We expected that the difference in kinetics between AAD-IIc and NaPi-IIa/b should also be reflected in differences in conformational changes at the equivalent site or sites in the protein. Although we were limited by the number of sites that have been identified so far that report conformational changes during the transport cycle, we nevertheless investigated the effect of labeling cysteines substituted at 3 equivalent sites previously investigated in NaPi-IIb and NaPi-IIc (Virkki et al., 2006b, 2006a; Ghezzi et al., 2009). Only mutant AAD-IIc-437 showed a different ΔF after fluorophore labeling compared with the corresponding mutant in NaPi-IIb (S448C). The difference in ΔF was more evident in the absence of external sodium, whereby the AAD-IIc-437 shows a strong quenching of fluorescence intensity at positive membrane voltages. Previously it was shown that for the equivalent mutant (S448C) in the flounder, quenching of fluorescence occurs for membrane hyperpolarization (*Figure 29*) (Virkki et al., 2006a). For S448C we can interpret the quenching with hyperpolarization to result from the protein moving more to outward facing states with Na^+ bound that have low quantum yields, whereas for depolarizing potentials, the protein would be inward facing and give the highest quantum yield. For S437C, it appeared that the opposite was the case: states giving the highest quantum yield are outward facing. If we assume that quenching results from exposure of the fluorophore to a polar (e.g. aqueous/ionic) environment, we might propose that for depolarizing potentials, the fluorophore will be exposed to the cytosol and consequently quenched. For hyperpolarizing potentials, there is little fluorescence quenching which indicates that the fluorophore's microenvironment is hydrophobic. This is consistent with the lack of external Na^+ ion movement (presteady-state charge) observed. In summary, site 437 (or 448) allows us to view the reorientation of the empty carrier depending on membrane potential. This would also accord with an alternating access transport mechanism that allows access to binding sites either on the outside or inside, but not both simultaneously. The AAD-IIc retains the electroneutral external Na^+ interactions as for NaPi-IIc, and the mutations created an electrogenic Na^+ interaction from the cytosolic side.

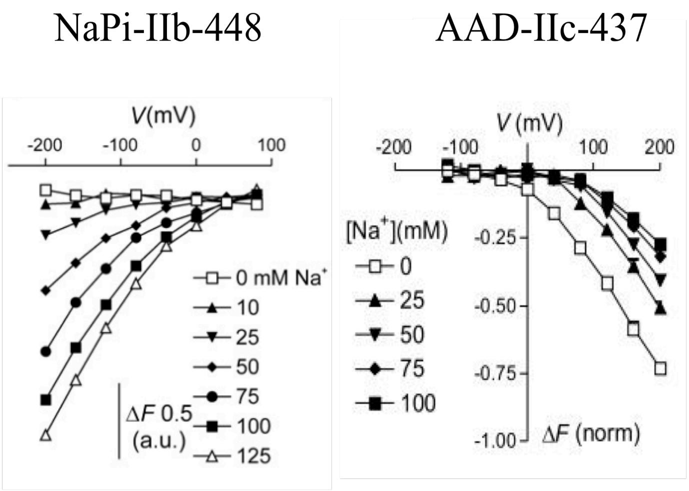

Figure 29 Na^+ dependence of the voltage-dependent fluorescence (ΔF) for mutant S448C in NaPi-IIb and the mutant S437C in AAD-IIc. Steady-state fluorescence at different membrane potentials was acquired for each Na^+ concentration indicated on the figure. Data points are joined for visualization only. Image related to NaPi-IIb-448 from Virkki et al., 2006b.

Although the above findings could explain the altered presteady-state kinetics, they were still unable to account for the reduced apparent affinity for P_i. Here, we returned to the modeling approach and found that by altering the rate constants associated with partial reaction 3-5. We could obtain an apparent P_i affinity that agreed with the experimental findings. Thus, we proposed that the mutagenesis had (i) imposed a rate limiting step-the release of one Na^+ ion to the cytosol and (ii) reduced the apparent affinity of P_i by changing the dissociation constant of the P_i binding reaction.

Figure 30 shows the new kinetic model for the AAD-IIc construct. The pink arrows indicate the two partial reactions that are altered compared to the WT electrogenic isoform; the step 0-9 relates to the intracellular sodium release and the steps 3-5 relate to the P_i and final Na^+ binding.

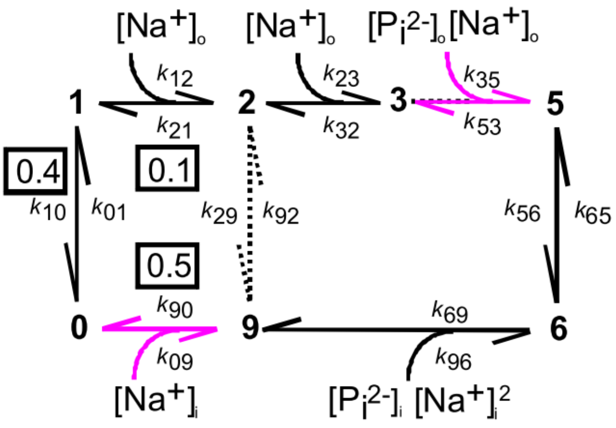

Figure 30 Kinetic model for the AAD-IIc. Boxed values indicate the effective valence associated with the relative partial reaction. Pink arrows emphasize the partial reactions that are compromise in this mutant. Modified from Patti et al., 2013.

The validity of our kinetic model for the AAD-IIc and our assumption on the rate limiting Na^+ release step is supported by the behavior of another sodium-dependent cotransporter (SGLT1). Wright and colleagues have pointed out the importance of the sodium release step in the Na^+/glucose cotransporter (SGLT), in which the rate limiting step, at extreme negative potentials is equal to the internal sodium ions dissociation rate constant (Parent et al., 1992; Wright et al., 2011). All our experiments were performed using the intact oocyte preparation. To investigate further the AAD-IIc kinetics, we would need controlled access to the cytosol, for example using the cut-open oocyte voltage clamp technique or whole cell patch clamp. Furthermore, it was noted in the original work by Bacconi (Bacconi et al., 2005) that three regions were identified as being potentially important for conferring electrogenicity. One these regions (*Figure 31*) originally termed cluster II most likely also contains residues that are critical for defining both the substrate affinities and overall electrogenic properties and should be addressed in future studies. This region has been identified in our homology model to include important residues for sodium and P_i coordination (Q417 S418, S419) (see *Figure 4D* in paper A).

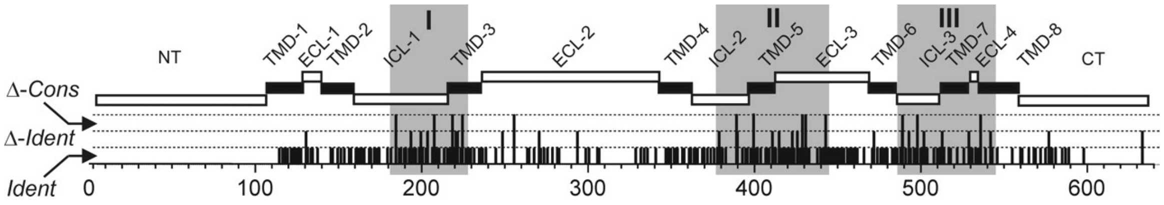

Figure 31 Sequence comparison of NaPi-IIa/c. Multiple sequence alignment indicates position of residues that are 100% identical in all 21 candidate sequences *(Ident)*, changed between putative electrogenic and electroneutral sequences with 100% identity at the respective site (Δ-*Ident*) or changed with conservative substitutions in either or both groups (Δ-*Cons*). Shaded areas (I, II, and III) indicate clusters of changed residues. Residue numbering is according to mouse NaPi-IIa sequence. Topological designation shows position and relative lengths of TMDs and linker stretches as predicted by hydrophobicity analysis. NT, N-terminal; CT, C-terminal. From Bacconi et al., 2005.

Development of a homology model of NaPi-II

The rationale for the development of a homology model for NaPi-II proteins was twofold. First, further advancement of structure-function studies is severely hampered without a 3-D structure. This would lead to a more specific choice of mutagenesis sites and areas of the protein to investigate. Second, the synthesis of inhibitors acting with high specificity on NaPi-II proteins would have a significant impact in the treatment of diseases related to disorders of P_i homeostasis and for this purpose having a 3D structure could accelerate drug design (Gu and Bourne, 2009).

Although the structures of a number of sodium-dependent cotransporters have been resolved e.g. (Yamashita et al., 2005; Faham et al., 2008; Ressl et al., 2009)), the standard bioinformatic approaches had failed to identify a suitable template for the creation of homology model of NaPi-II. Using hydrophobicity profiles and hidden Markov Models (Yoon, 2009) it was possible to define a structural repeat common to all NaPi-II isoforms. Then, using the recently solved crystal structure of *Vibrio cholerae* Na^+-dicarboxylate transporter VcINDY (Mancusso et al., 2012), we were able to generate a homology model of human NaPi-IIa. Structural information from previous studies has allowed us to validate the homology model. For example, using the substituted cysteine accessibility method (SCAM (Karlin and Akabas, 1998)) in *Xenopus* oocytes expressing NaPi-II, two regions were identified as accessible to the external medium (Lambert et al., 2001; Ehnes et al., 2004b); these regions are also externally accessibly in the homology model proposed, corresponding to the linker between TM1 and TM2 and to the loop L5ab between TM5a and TM5 (*Figure 32*, orange regions). Moreover further studies using SCAM indicated that TM3 region is inaccessible from the external medium like in our model (Virkki et al., 2005), we now hypothesize that this region acts as a buried “scaffold” of the entire structure (*Figure 32*, blue regions).

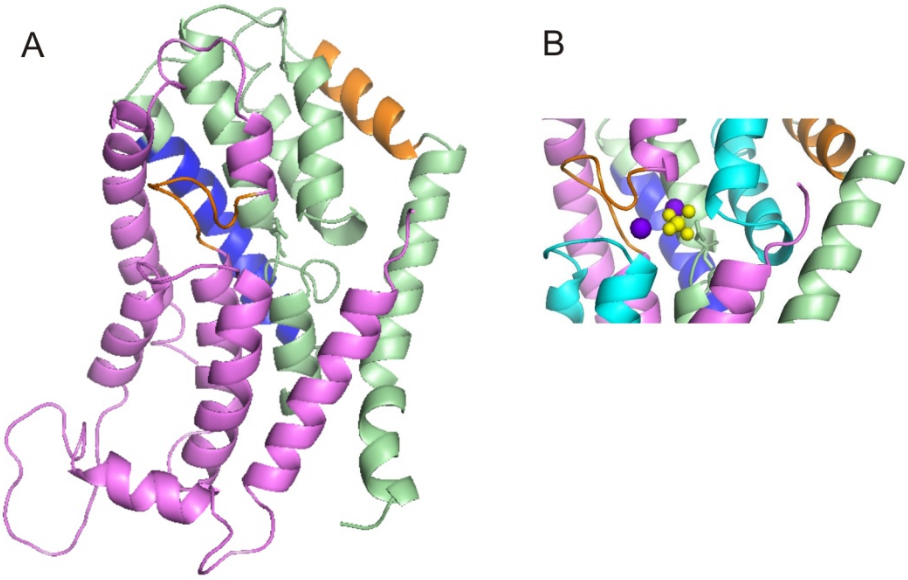

Figure 32 Structural model of human NaPi-IIa. A. Location of the structural first repeat unit (green) and second repeat unit (pink). Residues accessible to the extracellular side (orange) or buried (blue). **B.** Close-up of the predicted substrate binding sites in NaPi-IIa.

Previous sequence comparisons (Werner and Kinne, 2001) and biochemistry-based studies (Lambert et al., 1999) underscored the importance of the QSSS motif found in the N- and C-terminal halves of the protein and which is conserved down to bacterial isoforms. Two structure-function studies have focused on potential interactions between the reentrant loops during the transport cycle (Köhler et al., 2002b; Ghezzi et al., 2011). These reentrant loops overlap with the hairpin loops highlighted in the homology model, in which at the corresponding regions in VcINDY the binding sites for Na^+ and citrate are localized. We therefore propose the localization of the Na^+ and P_i interaction sites in NaPi-II based on the symmetry and pseudo-symmetry with VcINDY.

It was particularly important to obtain functional data to support the proposed model. To this end we mutated the candidate sites in the hairpin loops; their expression in the oocyte membrane was determined by immunohistochemistry and their functionality was investigated by tracer uptake and electrophysiology (steady-state and presteady-state). Nine mutants of the human NaPi-IIa isoform, were tested by uptake assay with ^{32}P for sodium-dependent transport. Transport was confirmed for two mutants (R210C and Q417C) and was statistically indistinguishable from the non-injected cells for S164A/C, T195C, S196C, S418C, S419A/C. This finding alone allowed us to conclude that the sites of mutagenesis were in a region critical for transport function. By performing presteady-state assays, we were further able to confirm that for 4 sites modified in the first repeat and two sites modified in the second repeat, Na^+ interactions could still take place. A complete kinetic analysis of the mutants was not feasible because of the low functional expression for most constructs. Nevertheless for two mutants (R210C and Q417C) we could perform a limited steady-state kinetic analysis to show that for the former, the apparent substrate activation was indistinguishable from the WT, whereas for the latter mutant the apparent substrate affinities were reduced (see Table in manuscript B). This result confirmed that the residue at site 417 was critical for substrate coordination.

The proposed 3-D model does not make any prediction about the location of the first Na^+ ion: for the electrogenic isoforms this would possibly interact with charged or polar residues and be located deep in the protein to account for presteady-state charge movements. The other two Na^+ ions together with divalent P_i would thus form an electroneutral complex in the middle of the protein. It is this complex that would be translocated for both electroneutral and electrogenic isoforms.

In conclusion, we have generated a homology model for NaPi-IIa in which we hypothesize the location of the substrate biding sites. Validation of this model will require further mutagenesis studies and these might best be performed using the well established flounder NaPi-IIb isoform that gives greater functional expression even after mutagenesis compared with the mammalian isoforms. In particular, the proposed key amino acids, should be replaced with residues with difference size and charge and the kinetic properties of the mutants investigated, similar to a previous study that focused on site N199 (Köhler et al., 2002a).

Characterization of the cotransport dynamics

Here we focussed on how different parts of the NaPi-II protein respond to changes in membrane potential and changes in the external substrate. We used presteady-state charge relaxations and fluorophore labelled mutants. An important experimental criterion was that the necessary cysteine substitution and subsequent labelling with the fluorophore did not significantly alter the transport kinetics. If this criterion is satisfied, we could assume that the fluorescence is an indirect measure of local molecular rearrangements of the protein as it moves between states in the transport cycle as for the WT. In practice, cysteine substitution at one site did not satisfy our criterion (mutant S144C) because labelling caused a significant loss of transport activity (see Supporting *Figure 1* in paper B). Nevertheless, this result indicated that this site was most likely in a functionally critical position.

To simplify the data interpretation, we focussed mainly on the behaviour of the protein without external P_i. For data interpretation we referred to a 5-state kinetic scheme *Figure 33A* that can account for the expected states previously identified from kinetic studies on presteady-state relaxations (Ghezzi et al., 2011, 2011, 2011; Andrini et al., 2012, 2012; Meinild and Forster, 2012). Based on this model we can solve the differential equations that describe the probability of occupancy for each state using modelling software (Berkeley Madonna, (http://www.berkeleymadonna.com/, e.g. (Ghezzi et al., 2011, 2011, 2011; Andrini et al., 2012, 2012; Meinild and Forster, 2012)).

Figure 33B shows the probability of the transporter to be in one of these states as a function of membrane potential for the case of zero and 100 mM Na^+ (external). At extreme positive voltages in absence of external Na^+ (0Na) the majority of the transporters will assume an inward-open conformation, whereas at extreme negative voltages they will assume an outward-open conformation (*Figure 33B* upper panel); this is partly due to a negative intrinsic charge that senses the change in voltage and promote specific protein transitions. For superfusion with 100 mM Na^+ (100Na) at extreme negative voltages the majority of the transporters will assume an outward-open conformation in which two Na^+ ions are bound (state 3) (*Figure 33B* lower panel).

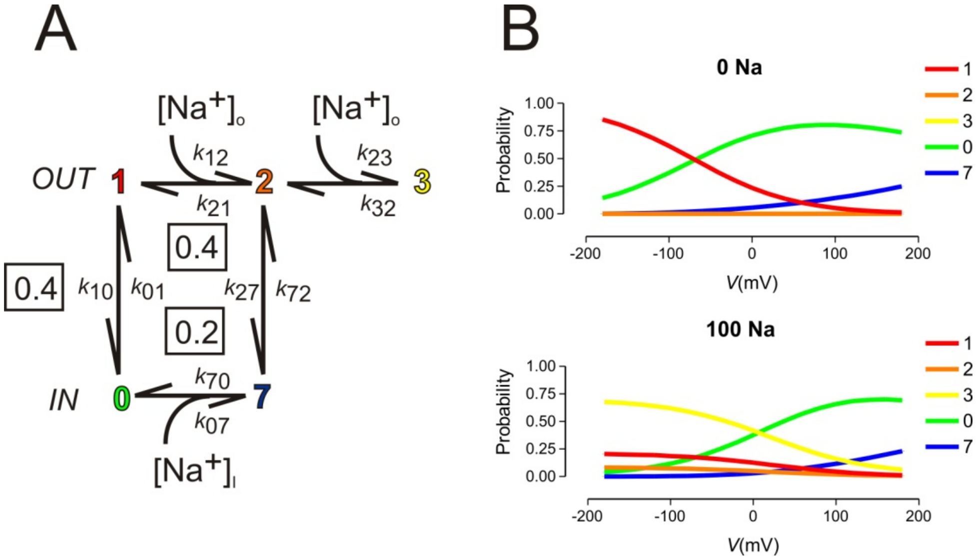

Figure 33 Five state kinetic scheme and probability of occupancy of the states. **A.** Five state kinetic scheme used simulate presteady-state and fluorescence behavior. Boxed values indicate apparent valence of the corresponding partial reaction. The voltage dependence of these partial reactions was modelled by applying Eyring Transition State Theory to describe analytically the dependence of transition rate constants on membrane potential. Voltage-dependent partial reactions account for the movement of equivalent lumped charges that change conformational state by crossing a sharp, symmetrical energy barrier. **B**. Number and color of the states are relative to the transitions show in panel A. The state occupancy was obtained from simulations of the 5 state model using the following parameters: The rate constants (in s^{-1}) were as follows: $k_{10}=300\exp(-Vz_{10}\mu/2)$, $k_{01}=100\exp(Vz_{10}/2)$; $k_{12}=[Na^+]_o 2000\exp(-Vz_{12}\ \mu/2)$, $k_{21}=500\exp(Vz_{12}\ \mu/2)$, $k_{23}=[Na^+]_o 8300$, $k_{32}=100$, $k_{27}=1$, $k_{07}=[Na^+]_i 2000\exp(Vz_{07}\ \mu)$, $k_{70}=500\exp(-Vz_{07}\ \mu)$ and $\mu=e/kT\approx 40\ V^{-1}$ at 20 °C, $z_{10}=0.4$, $z_{12}=0.4$, $z_{07}=0.2$. The rates constant k_{72} was defined independently in terms of the other rate constants under conditions of zero driving force to satisfy the detailed balance for the leak cycle. We assumed $[Na^+]_i=0.02$ M.

In the first part of this study, we focussed on the steady-state fluorescence and how this varied with membrane potential and whether or not Na^+ was present. We also combined data from a previous study (Virkki et al., 2006b, 2006a). To better understand the relationship between changes in fluorescence intensity and the conformational movements for all the mutants, we have assigned to each conformational state a value of fluorescence (F) that depends on the probability of occupancy of state (identical value for each mutant) and on the apparent quantum yield associated with the different states (these will be different for each mutant);

$F = \sum X_n \, qy_n$,

where:

X_n is the probability of occupancy of state n

qy_n is an apparent quantum yield associated with that state

We then used the 5-state kinetic model and assigned an apparent quantum yield value (qy) to each conformational state. We also assumed that the voltage-dependent kinetics were the same for all mutants. The effective quantum yield values were determined by trial and error to obtain the best visual match between the experimental data and the simulated fluorescence signal. We then tabulated the quantum yields by expressing them as a value that defines the fraction of fluorescence intensity for each conformational state and for each mutant (*Table 1*)

	State				
Mutant	**5**	**4**	**1**	**2**	**3**
A104C	0.49	0.02	0.18	0.09	0.22
A116C	0	0	0.33	0.33	0.33
S155C	0.4	0.4	0.2	0	0
S226C	0.77	0.23	0	0	0
Q319C	0	0.16	0.32	0.26	0.26
E451C	0	0.07	0.13	0.27	0.53

Table 1: Comparison of fractional apparent quantum yields for mutants. Each entry was calculated from the ratio of apparent quantum yield for that state divided by the sum of the quantum yields for the particular construct. The apparent quantum yield was determined by trial and error to yield a best visual match between the experimental data and simulations using the kinetic scheme. The same kinetic parameter was assumed for each mutant

With these data, we can now easily identify the conformational states that are reported by the fluorophore at the different labeling sites and how its environment changes from polar (low fractional apparent quantum yield) to non-polar (high fractional apparent quantum yield). By integrating these data with the location of the mutation sites in the 3-D homology model of NaPi-II, it is possible to gain new insights on the conformational changes that occur during the transport cycle. For example, the fluorophore placed in position 104 is located in short α-helical segment separate from the main core region and emits fluorescence when the protein is in anyone of the 5 conformational states, but with different fractional quantum yields (see *Table 1*). We hypothesized that it senses all the state changes occurring in the adjacent core region. The core region movements would cause the fluorophore to be exposed to less polar environments at each potential extreme causing the high quantum yields for both inward and outward orientated states.

In the second part of this study, we combined VCF and presteady-state analysis to investigate the correlation of kinetics of voltage-dependent transitions (manifested as presteady-state relaxations) with the kinetics of localized microenvironment changes, reported by changes in fluorescence intensity (ΔF). Both measurements were made simultaneously on the same oocyte and same recording bandwidth. Our working hypothesis was that if there was a direct correlation between the two signals, then the conformational changes reported by the fluorescence and the movement of charges must arise from the same underlying mechanism.

Only the mutant S155C showed this correlation in absence and in presence of sodium and over a wide potential range, which suggested that the conformational changes reported by the fluorophore at Cys-155 reflect those accompanying the charge movement associated with both the empty carrier itself and cation interactions. Mutant A116C showed this correlation only in presence of sodium, this result was consistent with the detection of finite quantum yield in states 1,2 and 3 (*Table 1*).

These findings allow us to relate protein rearrangements with the voltage-dependent events during the transport cycle such as substrate binding and translocation and help us to define the protein regions with the major functional relevance.

Two points should be noted in relation to this study. First, we assume that the mutants have exactly the same kinetic behavior as the WT. Despite their similarity in phosphate affinity, in fact small differences were observed in voltage dependence and in the time constants of presteady state current relaxations (mutant S226C in Fig. 4B in paper C). These differences were not included in the kinetic model to determine the apparent quantum yields and therefore further refinement of the model would be required.

Second, we assume that the decreased fluorescence emission arises from simple collisional quenching. Collisional quenching occurs when the excited fluorophore make contact with an atom or molecule that can facilitate the transitions to the ground state in a non-radiative manner. For example, water itself can act as collisional quencher (Lakowicz, op. 2006). In accord with this assumption, a reduced fluorescence emission may indicated exposure of fluorophore to a more aqueous environment.

However, other mechanisms have been proposed to cause the quenching phenomenon such as:

i. changes in the rotational freedom of the fluorophore (anisotropy),

ii. interactions with a nearby region of protein ,

iii. shifts in the absorption spectrum mainly due to the interaction of nearby fluorophores,

iii. changes of polarity of the environment (Levshin and Nizamov, 1966; Mannuzzu et al., 1996).

All these possibilities were investigated in detail for a rhodamine fluorophore (TMRM) used to label a heterologously expressed potassium channel (Cha and Bezanilla, 1998).

We also decide to investigate further the chemical properties of our fluorophore (MTS-TAMRA) to improve our interpretation of the fluorescence changes. We focussed on two factors that could potentially affect the fluorophore characteristics: i. effect of polar medium; ii. effect of iodide in external solution.

To investigate if the quenching phenomenon for MTS-TAMRA was correlated with the polarity of the medium, we tested the emission spectrum in solvents with different polarity (*Figure 34*). No direct correlation between polarity and fluorescence intensity was observed.

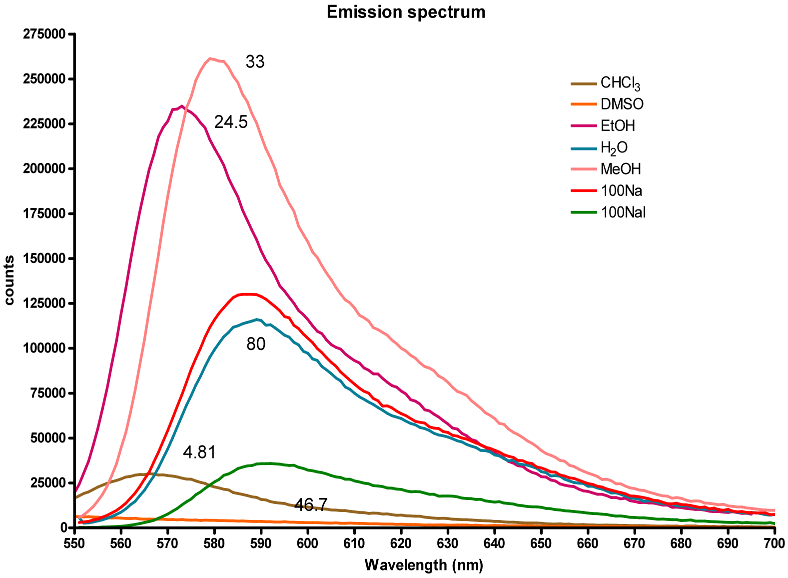

Figure 34 Emission spectrum of MTS-TAMRA in presence of solvents with different polarity. Dielectric constants for DMSO:46.7,EtOH:24,5, MeOH:33, H_2O: 80, $CHCl_3$:4.81. Measurement obtained with the spectrometer Edinburgh instruments FLS920 with an excitation light in the range of 538-550 nm. The concentration of MTS-TAMRA was 0.05mM for all the solvent tested. (M. Patti, unpublished data)

To investigate if quenching for labeled oocytes expressing different mutants of NaPi-IIb was caused by the exposure of the fluorophore to more aqueous environment, we added I^- (iodide) to the external solution; this ion is known to be a strong quencher that should amplify the decrease of fluorescence intensity (Cha and Bezanilla, 1998). Initially, we investigate the steady state fluorescence intensity in presence and in absence of I^- for labeled, not injected (NI) oocytes and for labeled oocytes expressing different NaPi-II mutants (*Figure 35*). The resulting data showed a stronger quenching phenomenon in presence of I^-, nevertheless there was no difference among the data relative to the NI oocytes and the injected ones. The variation of fluorescence for repeated measurements most likely results from incomplete washing of excess fluorophore, prevented resolution of the fluorescence changes exclusively due to fluorophores covalently bound to the transporters. In all subsequent experiments, we focused on the change in fluorescence in response to different voltage steps and considered only the changes relative to the different conformations of NaPi-II (see *Figure 5* in the paper C).

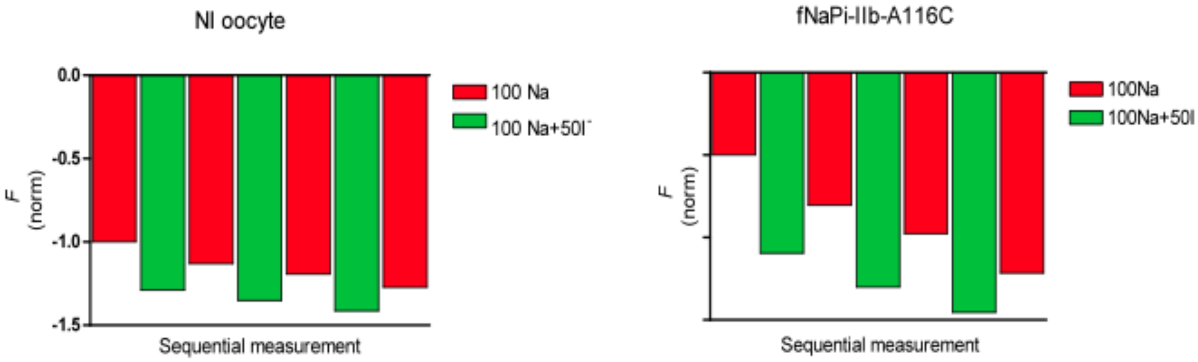

Figure 35 Steady state fluorescence changes in presence and in absence of I$^-$ The concentration of Na$^+$ and I$^-$ are express in mM. These data establish that I$^-$ also quenches the background fluorescence (NI oocyte). (M. Patti, unpublished data)

FUTURE PERSPECTIVES

Investigation of the internal substrate release steps

Based on the AAD-IIc study (paper A) we identified a cation release step in the transport cycle of NaPi-II. However, our knowledge of the substrate release order and the transition rates of the inward face conformations of NaPi-II is still limited. The effect of internal substrates on the transport kinetics has been investigated in several studies on other cotransporters. For example, for the human serotonin transporter (hSERT), changes in the internal concentration of substrate affected the presteady-state and steady-state currents using the cut-open oocyte technique (Adams and DeFelice, 2003) and for SGLT1, two studies using patch clamp of oocytes (Sauer et al., 2000; Eskandari et al., 2005) estimated apparent affinities for internal substrate interactions. In contrast, for the GABA transporter (GAT1) changes in the internal concentration of sodium and chloride in intact oocytes were found not to cause any significant changes in the presteady-state currents (Cherubino et al., 2012). Further investigations on NaPi-II transport kinetics would profit from using cut-open *Xenopus* oocyte voltage clamp (COVC) technique (Stefani and Bezanilla, 1998). With this system it is possible to have simultaneous access to the internal and external faces of the transporter to allow investigation of the interactions between substrates in the internal and in the external medium.

Refining the NaPi-II homology model

Since the homology model of hNaPi-II represents only the outward facing conformation, much of the data on the transport dynamics of NaPi-II, obtained by voltage clamp fluorometry (Virkki et al., 2006b, 2006a; Ghezzi et al., 2011) cannot be completely integrated into this static structural model. A homology model of the inward facing conformation will be necessary to hypothesize the movements of α-helices during transport and to have a complete understanding of the cotransport dynamics. Based on the strategy adopted for LeuT (Forrest and Rudnick, 2009), it may be possible to predict an inward facing conformation for our NaPi-II model. This achievement would have further impact on the generation of NaPi-II inhibitors using structure-based drug design (Greer et al., 1994).

Single molecule FRET (Zhao et al., 2011; Akyuz et al., 2013) could be used to further validate the homology model of NaPi-II in different conformational rearrangements. Using the approaches cited, a purified protein would be required, however it might be possible to perform experiments using the self-quenching properties of rhodamine applied to the oocyte expression system. Two rhodamine fluorophores such as MTS-TAMRA can stack to form dimeric complex if constrained close together or at high concentration. The dimer shows a decrease of the fluorescence intensity and it is characterized by a bathochromic shift in the emission spectrum compared with the monomer (*Figure 36*) (Chambers et al., 1974). This so called self-quenching phenomena occur when the two molecules are in a short distant of ~1nm (Okoh et al., 2006; Zhou et al., 2011). Using this unique feature of rhodamine fluorophore it might be possible to detect intramolecular conformational changes in transporters.

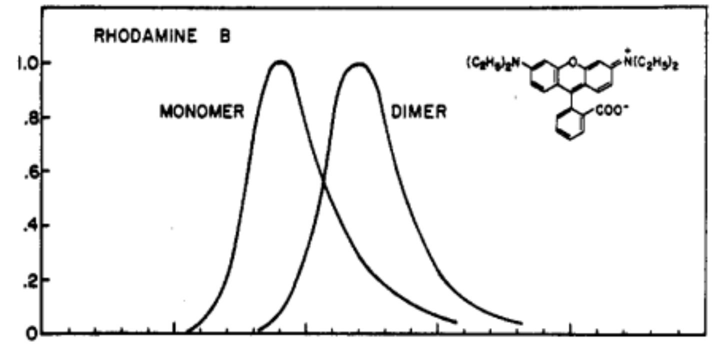

Figure 36 Emission spectrum of rhodamine in a monomeric and dimeric complex. From Chambers and Kajiwara, 1974.

Thus, two rhodamine molecules covalently attached to cysteine in a double cysteine NaPi-II mutant can act as “fluorescent rulers” to detect the distance between the two residues.

Moreover the distance between two cysteine residues could change during the transport cycle as a result of conformational rearrangement due to for example of substrate interaction or voltage membrane changes (Cha and Bezanilla, 1998). These methods will give new insights in the structure of NaPi-II at a higher resolution that can be integrated with the homology model.

SUPPLEMENTARY PROJECTS

During the dissertation period, the author was also directly involved in the experimental design, data acquisition and analysis associated with projects that resulted in the following publications and therefore appears as co-author.

1. Development of an ISFET sensor system for non-invasive transport assays on Xenopus oocytes (Schaffhauser et al., 2012).
2. Investigation of the effects of naturally occurring mutations in PiT-2 (SLC20A2) related to basal ganglia calcification (Wang et al., 2012).

OPEN ACCESS Freely available online
PLoS one

An Integrated Field-Effect Microdevice for Monitoring Membrane Transport in *Xenopus laevis* Oocytes via Lateral Proton Diffusion

Daniel Felix Schaffhauser[1], Monica Patti[2], Tatsuro Goda[3], Yuji Miyahara[3]*, Ian Cameron Forster[2]*, Petra Stephanie Dittrich[3]*

1 Department of Chemistry and Applied Biosciences, ETH Zurich, Zurich, Switzerland, **2** Institute for Physiology, University of Zurich, Zurich, Switzerland, **3** Institute of Biomaterials and Bioengineering, Tokyo Medical and Dental University, Tokyo, Japan

Abstract

An integrated microdevice for measuring proton-dependent membrane activity at the surface of *Xenopus laevis* oocytes is presented. By establishing a stable contact between the oocyte vitelline membrane and an ion-sensitive field-effect (ISFET) sensor inside a microperfusion channel, changes in surface pH that are hypothesized to result from facilitated proton lateral diffusion along the membrane were detected. The solute diffusion barrier created between the sensor and the active membrane area allowed detection of surface proton concentration free from interference of solutes in bulk solution. The proposed sensor mechanism was verified by heterologously expressing membrane transport proteins and recording changes in surface pH during application of the specific substrates. Experiments conducted on two families of phosphate-sodium cotransporters (SLC20 & SLC34) demonstrated that it is possible to detect phosphate transport for both electrogenic and electroneutral isoforms and distinguish between transport of different phosphate species. Furthermore, the transport activity of the proton/amino acid cotransporter PAT1 assayed using conventional whole cell electrophysiology correlated well with changes in surface pH, confirming the ability of the system to detect activity proportional to expression level.

Citation: Schaffhauser DF, Patti M, Goda T, Miyahara Y, Forster IC, et al. (2012) An Integrated Field-Effect Microdevice for Monitoring Membrane Transport in *Xenopus laevis* Oocytes via Lateral Proton Diffusion. PLoS ONE 7(7): e39238. doi:10.1371/journal.pone.0039238

Editor: Steven Barnes, Dalhousie University, Canada

Received February 21, 2012; **Accepted** May 17, 2012; **Published** July 5, 2012

Funding: Main funding: European Research Council (ERC Starting Grant, nμ-LIPIDS, No. 203428); National Institute for Materials Science (NIMS, Tsukuba, JPN): Research visit grant; JST-CREST (JPN): Partial financial support of materials. The funders had no role in study design, data collection and analysis, decision to publish, or preparation of the manuscript. No additional external funding received for this study.

Competing Interests: The authors have declared that no competing interests exist.

* E-mail: dittrich@org.chem.eth.ch (PSD); iforster@access.uzh.ch (ICF); miyahara.bsr@tmd.ac.jp (YM)

Introduction

For many decades, electrophysiological methods have been at the forefront of investigations of membrane conduction and excitation in living cells. [1] To measure membrane conductance, control of either the transmembrane voltage or current is required. Therefore, a key experimental challenge is to establish adequate electrical access to the cytosol. For example, in the commonly used two electrode voltage clamp (TEVC) applied to large cells such as *Xenopus laevis* oocytes, two microelectrodes impale the oocyte to sense and control the membrane potential. This procedure requires delicate glass microelectrodes and a high degree of micromanipulation, either by a human operator or precision robotics. [2,3]. In the whole cell patch clamp, electrical access to the cytosol is gained by sealing the tip of a glass microelectrode to the membrane and applying suction to eventually rupture the cell membrane within the electrode. [4] Recently, several non-invasive voltage clamp techniques for *Xenopus laevis* oocytes have been developed that leave the membrane intact. These methods rely on the physical compartmentalization of the membrane into two areas and measurement of trans-cellular currents across the entire oocyte. In the transoocyte voltage clamp (TOVC) an AC voltage is applied across symmetrically distributed membrane impedances. [5] Asymmetric variants of the TOVC have been realized to better define the transmembrane potential across a smaller region of membrane [6,7] and are akin to the loose macropatch. [8].

Even though voltage clamping has established itself as a reliable tool for performing electrophysiological experiments, its application in large-scale industrial screening has not been fully realized. Apart from the aforementioned cell manipulation requirements, parallelization of the voltage clamp requires duplication of many hardware components - including the electrodes, voltage clamp electronics and the fluidic pathways. Electronic detection methods based on field-effect devices, on the other hand, are attractive alternatives for large-scale integration. As the sensors detect local surface charge accumulation or depletion as opposed to passing current, from the cell medium, liquid domains can be shared without significant crosstalk occurring between channels. Furthermore, as the sensing field is limited by the shielding properties of ionic solutions, this would allow the realization of high density sensor arrays. The detection distance can be calculated using Debye's relation for low electrolyte concentrations. [9] Recent work on the theory of electrostatic fields in ionic solutions allows for more accurate predictions on high electrolyte concentrations, as present in physiological solutions. [10] The most appropriate field-effect sensor for use in ionic solutions, the ion-sensitive field-effect transistor (ISFET), has first been described by Bergveld. [11] The ISFET, which is derived from the metal-oxide field-effect transistor (MOSFET), replaces the metal gate electrode on the insulator with the bulk solution, the potential of which is defined using a reference electrode. Charge separation at the insulator-liquid interface then results in a detectable potential difference due to the double-layer capacitance between the reference electrode and the semiconducting channel. ISFETs have mostly been used to measure local changes in pH, such as acidification in cell cultures. [12,13] There has also been interest in using ISFETs for studying membrane transport. The first successful transport assays were reported on the human anionic transporting peptide C (OATP-C) heterologously expressed in *Xenopus laevis* oocytes. [14] In these experiments, the uptake of estrone-3-sulfate and estradiol 17β-D-glucuronide was detected with good sensitivity, and differences in uptake rates between the wild-type and mutant of the OATP-C transporter were resolved.

Xenopus laevis oocytes, like other cells, are believed to have endogenous proton-regulating mechanisms at the cell membrane that are responsible for a pH gradient across the cell membrane. In particular, there is evidence of the existence of a Na^+/H^+ exchanger that is at least partially responsible for the proton countertransport across the cell membrane. [15,16] Furthermore, overexpression of proton-dependent membrane proteins modulates local proton binding affinity upon transport activation. Transport activity mediated by heterologously expressed transport systems by pH detection using a glass microelectrode placed in close proximity to the membrane has been demonstrated. [17,18] Considering the extremely fast bulk diffusion rate of protons in water, [19,20] it may at first seem surprising that pH values different from the bulk solution can be detected at all. However, proton sinks and sources at the cell membrane change the local association/dissociation rate constants that results in lateral diffusion rates different from the bulk diffusion rate. Recently, a mathematical model for lateral diffusion kinetics at the cell membrane for protons was described, [21] which provides numerical solutions for the dwell time of a proton in buffered solutions commonly used in physiology. The results support previously conducted experiments that show that a proton can migrate laterally hundreds of micrometers along the cell membrane before diffusing back into the bulk solution. [22].

Based on the lateral diffusion model, we have developed a method for sensing proton-dependent membrane transport in *Xenopus laevis* oocytes by utilizing a novel arrangement of ISFET technology. We establish a proton-selective diffusion barrier that is created by direct contact of part of the membrane with the sensor. The membrane is stabilized against the sensor surface using our previously reported immobilization technology. [6] Due to the much higher lateral diffusion rate of the protons compared to other solutes, the detected potential change at the sensor is exclusively proton-dependent (Fig. 1). Once equilibrated, the proton concentration at the detection site $[H^+]_D$ is equal to the proton concentration at the membrane surface $[H^+]_S$, assuming ideal coupling between the sensor surface and the membrane surface. The surface potential of the sensor then reflects the surface pH for steady state membrane transport. We predict that in contrast to protons, substrate molecules *S* that interact with transport proteins at the cell membrane exposed to the bulk solution, will diffuse poorly across the diffusion barrier for two reasons. First, their lateral mobility relative to the protons is greatly reduced and second, they are effectively removed from the local medium by the transport proteins themselves before reaching the detection surface. As a consequence, modulation of substrate concentration in proximity to the detection surface will be minimal for large migration distances, as present in our system.

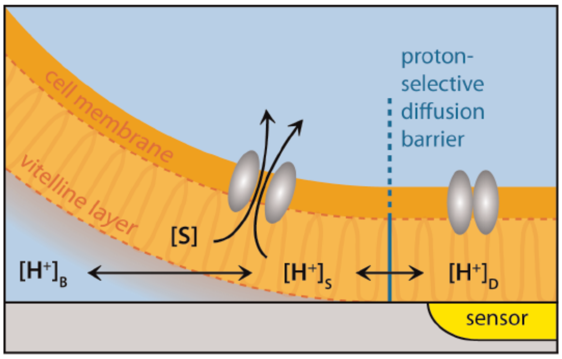

Figure 1. Lateral proton diffusion model. Simplified cartoon of the proton-selective lateral diffusion model where the oocyte interfaces to the sensor element (not to scale). The vitelline layer of the (defolliculated) oocyte comprises a network of fibrous filaments that surround the cytoplasmic membrane, which itself is not smooth due to numerous microvilli protrusions (not shown). The total thickness of the vitelline layer is estimated to be 2–3 µm for stage VI oocytes. [39] ([S]: concentration of substrate interacting with the membrane transport proteins. $[H^+]_D$, $[H^+]_S$, $[H^+]_B$: Proton concentration at the detection site, membrane surface and in buffer, respectively.) We assume the diffusion barrier is narrow compared with the sensor area so that "edge effects" can be neglected and transporters within the sensor region do not "see" the substrate S.
doi:10.1371/journal.pone.0039238.g001

To verify the validity of the proposed method, we conducted experiments on oocytes overexpressing the electrogenic sodium/phosphate cotransporters PiT-2 (SLC20A2) and NaPi-IIb (SLC34A2), the electroneutral isoform NaPi-IIc (SLC34A3) and the proton/amino acid cotransporter PAT1 (SLC36A1). The goal of this work is to demonstrate that our arrangement allows for non-invasive assays of transport processes, which result in local pH changes under physiological conditions.

Materials and Mehods

System Description

The device comprises a sensing element, a microperfusion system and a circular orifice for immobilization of the oocyte and alignment with the sensing surface (Fig. 2). The sensor is an n-channel field-effect transistor (FET) without metal gate and with a 40 nm thick layer of tantalum pentoxide (Ta_2O_5) as the insulator material (ISFETCOM Co. Ltd., Saitama, Japan). Ta_2O_5 exhibits superior proton buffering capacity compared to other metal oxides while providing a good diffusion barrier. [23] The sensor was inserted into the cavity of a precisely machined support made of aluminum, creating a flush fit. A rectangular (5 mm×10 mm) piece of perfluoroethylene (PTFE) with a thickness of 0.2 mm was then placed over the sensor to serve as a gasket and spacer for forming the microperfusion channel. A CNC-machined block made from poly(methyl methacrylate) (PMMA) was screwed onto the aluminum support. It integrated 6 liquid inlet channels and 1 outlet channel as well as the immobilization orifice. A hole (1.6 mm dia.) intersecting with the outlet channel was drilled for insertion of the reference electrode. Due to the low dimensional tolerances of all parts involved, the oocyte orifice is self-aligned with the sensor surface upon assembly of the device.

The FET was driven with a source-drain follower circuit that fixed the source-drain voltage and drain current to constant values. For all experiments, the source-drain voltage and current

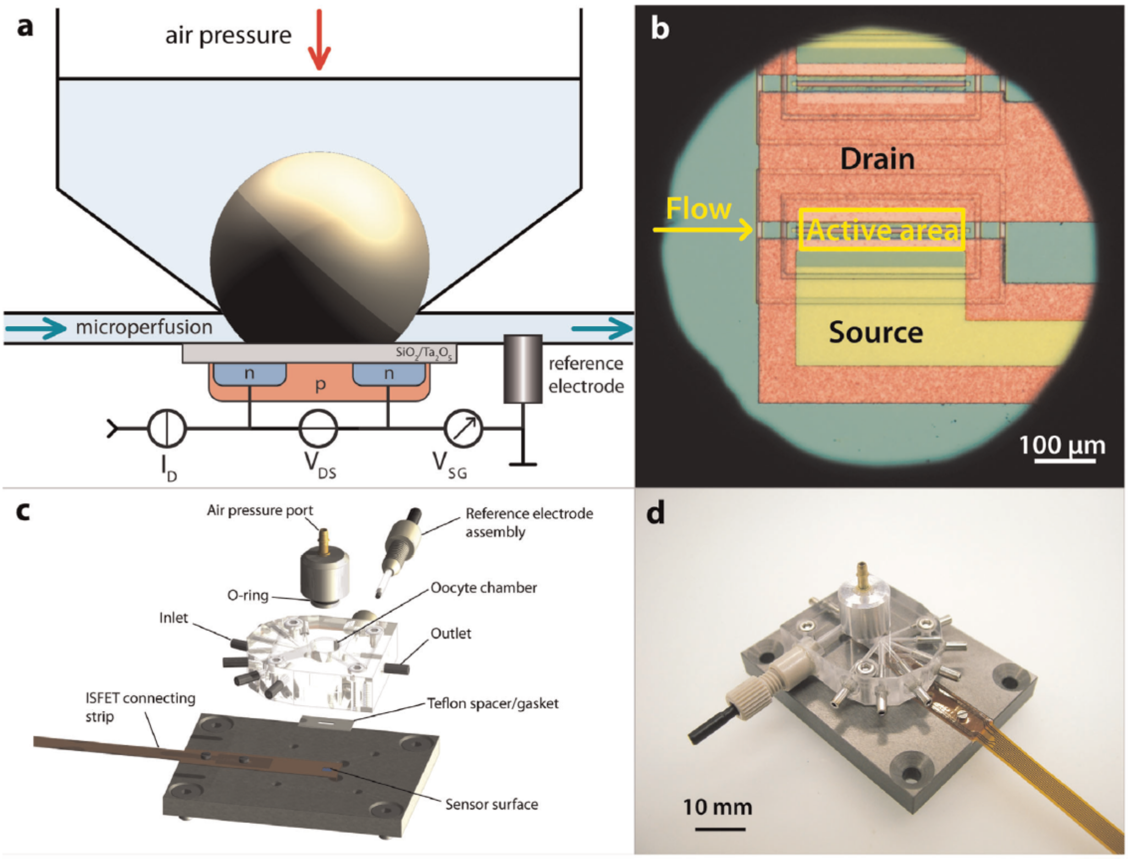

Figure 2. Design of the microdevice. a) Schematic view of the cross-section of the device (not drawn to scale). The height of the microperfusion channel is around 200 µm. A typical Xenopus oocyte would be 1000–1200 µm in diameter. b) Micrograph of the sensor as seen through the hole (ca. 800 µm in diameter) of the oocyte immobilization compartment. The oocyte membrane completely covers the active area of the sensor due to its deformability. c) Exploded view of the device using the original 3D CAD engineering data. d) Photograph of the assembled, but unconnected device.
doi:10.1371/journal.pone.0039238.g002

were set to 500 mV and 500 µA, respectively. The reference electrode was connected to the circuit's signal ground which defined the reference potential, against which the output signal V_{SG} was measured at the source connection. In this configuration, changes in V_{SG} are directly proportional to changes in the Nernst potential. The technical implementation of the drain-source follower was realized using constant current drivers. [24] Acquisition of the gate-source voltage was achieved using a high-resolution data acquisition and control (DAQ) unit (LabJack U6-Pro, LabJack Corp./USA). The DAQ unit also served as a controller for the air pressure system used for cell immobilization and solution exchange. User control of all systems was provided by our proprietary PC-based graphical user interface (GUI), which employs the Windows.NET application programming interface (Microsoft Corp./USA). An expanded version of an air pressure system, which provided solution exchange and perfusion, as well as oocyte immobilization was used as described earlier. [6].

Solutions and Reagents

For storage of oocytes, modified Barth's solution contained (in mM): 88 NaCl, 1 KCl, 0.41 $CaCl_2$, 0.82 $MgSO_4$, 2.5 $NaHCO_3$, 2 $Ca(NO_3)_2$, 7.5 HEPES, pH was adjusted to 7.5 with Tris and supplemented with 5 mg/l doxycycline and 5 mg/l gentamicine. Standard buffered saline solutions (100 Na) contained (in mM): 100 NaCl, 2 KCl, 1 $MgCl_2$, 1.8 $CaCl_2$, 10 HEPES, adjusted to pH 7.5, pH 7.4 or pH 6.5 with TRIS. For test solutions containing activating or inhibiting substances the following stock solutions were used: 1 M (in H_2O) inorganic phosphate (P_i) at pH 7.4, 100 mM (in DMSO) amiloride, 100 mM (in H_2O) L-Proline, 100 mM (in H_2O) γ-Aminobutyric acid (GABA) and 100 mM (in H_2O) sodium phosphonoformate tribasic hexahydrate (PFA). After addition of the reagents, all solutions were filtered using a 0.22 µm filter, prior to filling the solution vials. All standard reagents were purchased from either Sigma-Aldrich or Fluka.

Oocyte Preparation

Female *Xenopus laevis* frogs were purchased from Xenopus Express (France) or African Xenopus Facility (R. South Africa). The frogs were anesthetized in MS222 (tricaine methanesulphonate) after which portions of ovaries were surgically removed and cut in small pieces. Collagenase treatment on oocytes was done for 45 min with 1 mg/ml of crude type 1A in 100 Na solution

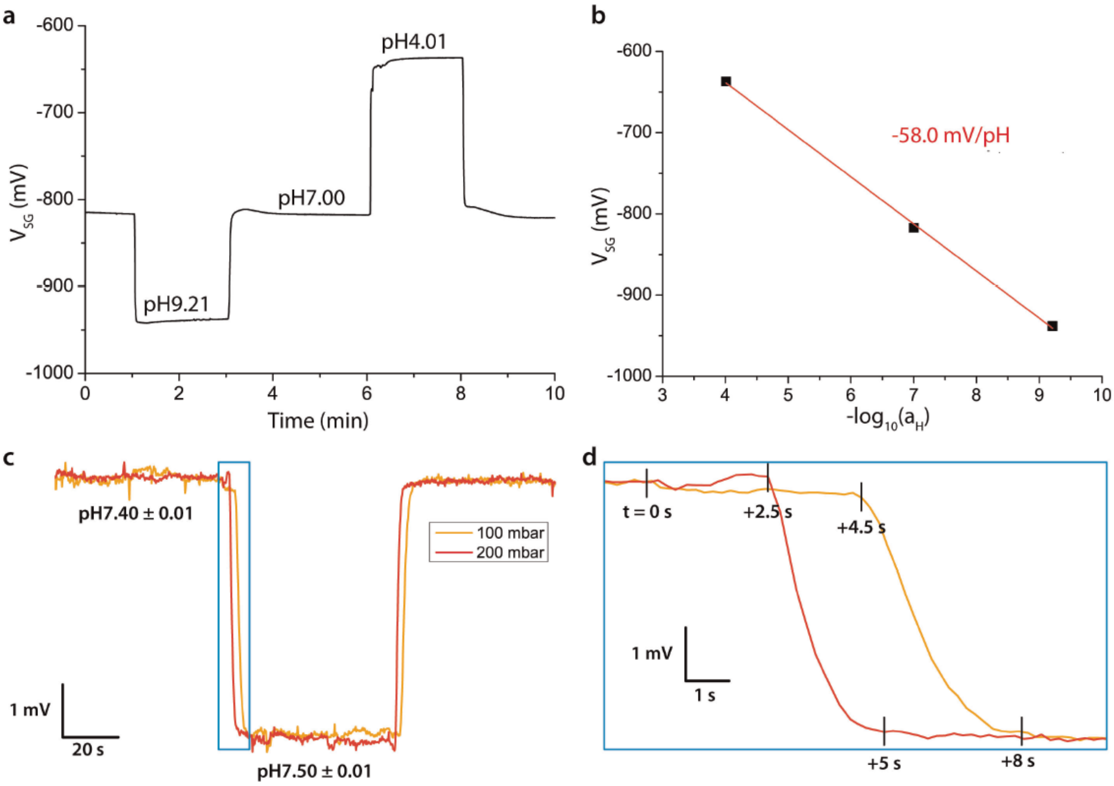

Figure 3. pH reference measurements. a) Time-dependent measurement of phosphate reference buffers at pH 4.01, pH 7.00 and pH 9.21 and b) linear fit of the data points obtained from the baselines of each buffer. Slope and standard error of the linear fit are shown. c) Time-dependent measurement of 100 Na solutions buffered at pH 7.40 and pH 7.50 for two different perfusion pressures (100 mbar and 200 mbar). d) Expanded view of data in panel c during the exchange of solutions from pH 7.40 to pH 7.50. Valves were switched at t = 0 s.
doi:10.1371/journal.pone.0039238.g003

(without Ca^{2+}) in presence of 0.1 mg/ml trypsin inhibitor type III-O. Healthy stage V-VI oocytes were selected, maintained in modified Barth's solution at 16°C and injected with typically 5 ng total of cRNA of the α,β,γ sub-units of the *Xenopus* isoform of ENaC, [25] GAT1, [26] flounder NaPi-IIb, [27] mouse NaPi-IIc, [28] mouse PAT1 [29] or human PiT-2 [18] according to procedures previously conducted in our laboratory. After injection, the oocytes were incubated for 3 days at 16°C in Barth's solution. Non-injected oocytes of the same batch were used as negative controls. All animal handling procedures were approved by Swiss Cantonal and Federal veterinary authorities.

Procedure for Oocyte Experiments

Before the experiment, the oocytes were thoroughly washed in 100 Na solution at pH 7.4 to prevent the diffusion of protons between the oocyte chamber and the microperfusion channel. After priming of the system with 100 Na pH 7.4 solution, the cell was pipetted into the oocyte chamber. The air port plug was then inserted into the oocyte chamber and a constant air pressure of 5 mbar was applied. The perfusion system was then pressurized at 100 mbar which, in combination with the inlet capillaries (30 cm length, 200 µm inner diameter), resulted in a flow rate of approx. 1 µl/s when one of the solenoid valves was open. The oocyte was perfused with 100 Na solution at pH 6.5 (for PAT1) or pH 7.4 (all others) for 5 min to create stable steady-state conditions before initiating a transport activation protocol. The perfusion sequence was programmed beforehand using a built-in macro feature of the GUI. This feature provided high timing accuracy of the solution switching and guaranteed the repeatability of the perfusion sequence.

Results and Discussion

pH-sensing Characterization of the ISFET

To determine the response of the sensor to changes in bulk proton concentration and correlate the changes in output voltage to the pH change, the sensor was superfused with buffered solutions at varying pH. In a representative measurement, a slope of −58.0 with a linearity error of 1.5 mV/pH ($R_{adj}^2 = 0.99862$) was found using a three-point extrapolation with standard phosphate buffer solutions at pH 4.01, pH 7.00 and pH 9.21 (Fig. 3a,b). This value was close to the prediction from the Nernstian equation (−59 mV/pH), which demonstrated the excellent proton buffering capacity of Ta_2O_5. The detection limit of ΔpH was determined to be approx. 0.005 units (signal-to-noise ratio of 3). The drift slope depended on a number of factors, such as ambient light intensity, but was typically less than 0.1 mV/min. The sensor-to-sensor variation was insignificant, which resulted from the large sensor structure and precise CMOS manufacturing processes. In a second experiment, the sensor was superfused with 100 Na solutions at pH 7.50 and pH 7.40 (Fig. 3c). The experiment showed an expected decrease of 5.4 mV (i.e. $\Delta pH = -0.1$) with a rapid transition from the first steady-state signal to the next one. Even though the flow inside the microperfusion channel was laminar, the signal response was not perfect due to cross-diffusion at the junction where the inlet channels meet. Also, there was some dead time between the switching of the valves and the signal response onset due to the relatively large solution exchange volume (approx. 4 µl) in relation to the flow rate (1 or 2 µl/s). In total, it took approx. 8 s at 100 mbar and approx. 5 s at 200 mbar to reach steady-state conditions after valve actuation, demonstrating that the sensor response was predominantly limited by the flow rate (Fig. 3d). Nevertheless, for the uptake experiments on oocytes these values are fully acceptable due to the comparatively slow proton diffusion between the membrane surface and the sensor surface (see below). With regards to selectivity, the sensitivity of the Ta_2O_5-based sensor towards Na^+ and K^+ is less than 1 mV/M, as has been described previously. [30].

Transport Experiments on Oocytes Heterologously Expressing Various Membrane Transport Proteins

Proline transport mediated by PAT1. Assays conducted on oocytes heterologously expressing the proton-driven amino acid transporter (PAT1) showed a significant decrease of V_{SG} upon exposure of the cell to a 1 mM proline solution (Fig. 4a). The signal reached a steady state after 5 min and returned to the initial baseline after washout of proline. PAT1 is known to reversibly bind amino acids and cotransport them stoichiometrically with one proton/amino acid per cycle. [31] Under our experimental conditions, we attribute the downward deflection of V_{SG}, upon exposure of the cell to proline, to reflect a lateral movement of protons away from the sensor region due to the depletion of protons at the extracellular membrane surface during the H^+/proline coupled transport. Moreover, given the large volume of the oocyte and low transport turnover rate of PAT1, we would expect neither the intracellular proline concentration nor intracellular pH to change sufficiently during the experiment such that reverse mode behavior (proton and proline efflux) might occur in the region of oocyte membrane exposed to the sensor. Thus, even though PAT1 works bidirectionally, the exposure time of 5 minutes was apparently insufficient to significantly change the proton gradient across the cell membrane.

Phosphate transport mediated by NaPi-IIb and PiT-2. In contrast to PAT1, for oocytes heterologously expressing the electrogenic sodium-coupled phosphate cotransporter (NaPi-IIb) the signal deflection was reversed, which indicated that a decrease in surface pH occurred (Fig. 4b). This can be understood when we consider that P_i is present at the membrane surface as both divalent (HPO_4^{2-}) and monovalent ($H_2PO_4^-$) phosphate species with an assumed $pK_a = 6.8$ under physiological conditions and distributed according to the following equilibrium,

$$HPO_4^{2-} + H^+ \rightleftharpoons H_2PO_4^- \qquad (1.1)$$

The electrogenic NaPi-IIb translocates 3 Na^+ together with one divalent P_i per transport cycle, [32] which results in the increase of $[H^+]_S$ due to the depletion of the divalent species.

For the electroneutral isoform NaPi-IIc, a detectable pH decrease at the membrane surface is also induced upon exposure to P_i (Fig. 4c). This was expected given that NaPi-IIc also prefers divalent P_i, [33] and translocates two Na^+ per cycle with no net charge movement. [34] This result also establishes that the sensor (i) is capable of sensing electroneutral transport processes and (ii) does not simply respond to a change in the cell membrane potential as might be predicted for the electrogenic transporters that mediate net charge translocation.

In contrast to the SLC34 family of sodium coupled P_i cotransporters, members of the SLC20 family prefer monovalent P_i ($H_2PO_4^-$), and translocate two Na^+ per transport cycle together with one positive net charge. The resulting shift of the equilibrium to the right (see equation above) would therefore result in a decrease in $[H^+]_S$, which explains the downward deflection (increase in pH) of V_{SG} in PiT-2 upon exposure to P_i (Fig. 4d). The amplitude of the change in V_{SG} at steady state was significantly lower compared to NaPi-IIb and NaPi-IIc and most likely resulted from the lower surface expression of protein compared to NaPi-IIb,c. The changes in surface pH registered by the ISFET sensor for NaPi-IIb and PiT-2 were in qualitative agreement with TEVC measurements conducted in combination with surface pH measurements using a pH-sensitive glass microelectrode. [18].

Control experiments confirm the specificity of the sensor for detecting local ΔpH. Control experiments on non-injected oocytes showed minimal deflections of V_{SG}, both for P_i and proline (Fig. 4e,f). These may be due to endogenous membrane proteins that could interact with proline and P_i. In particular, the presence of amino acid-modulated membrane activity has been determined in uptake studies. [35] Nonetheless, considering that relatively high concentrations of proline and P_i were used in our experiments, the contribution of the endogenous activity can be neglected when the level of exogenous expression is sufficiently high. To further demonstrate that modulation of proton-independent transport proteins did not induce a potential change at the sensor surface, we conducted experiments on oocytes overexpressing the γ-aminobutyric acid (GABA) transporter (GAT1) (Fig. 4g) and the epithelial sodium channel (ENaC) (Fig. 4h). GAT1 is a sodium-chloride-dependent cotransporter highly specific for GABA. [36] ENaC is a sodium channel whose conductance can be blocked using amiloride ($K_i < 1$ µM). [37,38] For oocytes expressing either of these membrane proteins, we were unable to resolve a significant change in V_{SG}. This finding allowed us to exclude the presence of detection artifacts at the sensor surface and confirmed the specificity of the sensor to changes in local proton concentration.

Correlating the ISFET response to transport activity. We used oocytes overexpressing PAT1 to correlate the change in membrane surface pH with PAT1 activity. For the oocyte on the ISFET sensor, application of proline will result in a net intracellular translocation of protons into the oocyte, and a concomitant membrane depolarization. A new steady-state membrane potential will be reached that is a function of both the PAT1 protein expression level and transport rate, as well as the endogenous leak conductance of the oocyte. The latter effectively shunts the secondary active transport process mediated by PAT1. As the endogenous leak may vary from cell to cell, for a given expression level, the change in membrane potential will also vary and is therefore not a good quantitative measure of transport activity. Moreover, the proline transport rate will itself be a function of membrane potential due to voltage-dependent partial reactions in the transport cycle. [29] Therefore, to correlate transport activity with ΔpH detected by the sensor for individual oocytes (Fig. 5a), we first determined the steady-state membrane potential reached during transport under the same conditions as for the ISFET assay (inset, Fig. 5b). For that case, the net membrane current is zero and comprises the inward transporter-related flux that is balanced by an equal, but opposite current

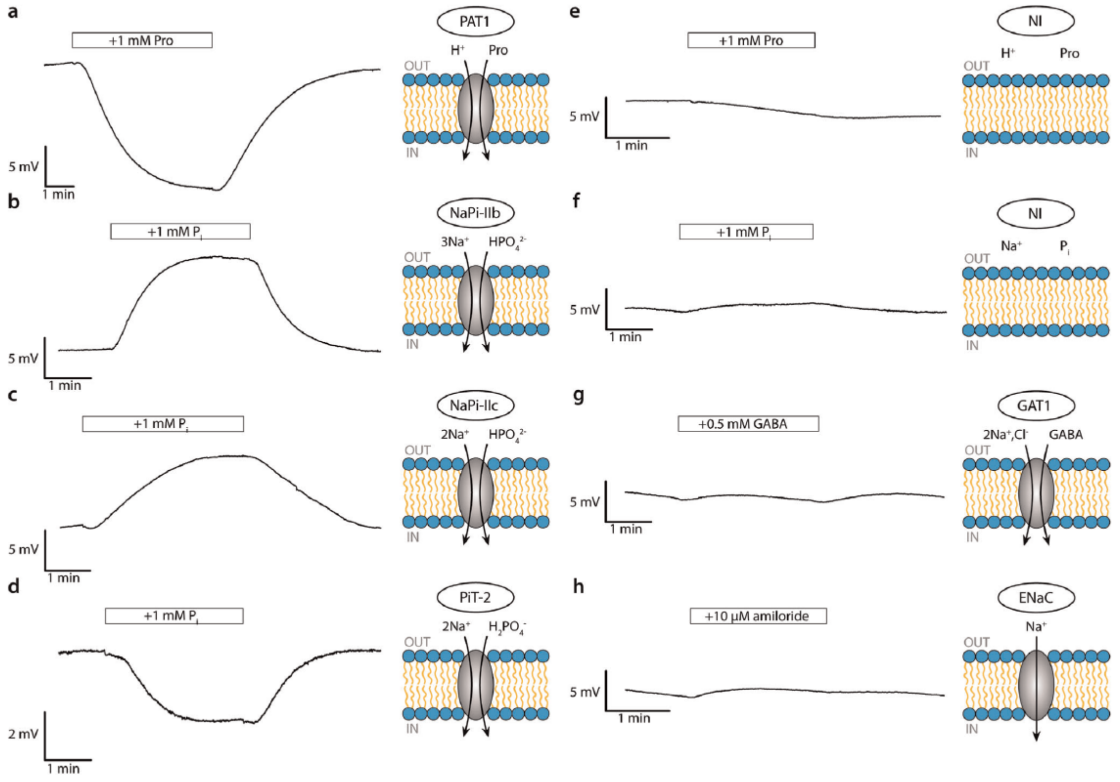

Figure 4. Membrane transport experiments. Experiments conducted on oocytes heterologously expressing various membrane transport proteins indicated with their respective controls on non-injected (NI) oocytes showing sensor readout (V_{SG}) as a function of time. Only part of the initial stabilizing baseline region that preceded substrate application is shown (see Materials and Methods): a) PAT1, b) NaPi IIb, c) NaPi-IIc, d) PiT-2, e) Proline control, f) P_i control, g) GAT1, h) ENaC. In each case either the same or representative oocytes from the same batch were pretested using a two-electrode voltage clamp to confirm functional expression. The bars indicate the duration of application of the respective activating and blocking agents. Arrows indicate flux direction of substrate according to the assumed driving force conditions.
doi:10.1371/journal.pone.0039238.g004

mediated by endogenous channels and pumps. We then voltage clamped the oocyte to determine the transporter-related current by subtracting the current in the absence of proline from that obtained with proline to eliminate proline-independent endogenous currents. From this I-V data we could estimate the transport flux corresponding to the steady-state potential for the ISFET assay (Fig. 5b). To ensure minimal substrate accumulation, we first tested the response using the TEVC to avoid long substrate exposure incurred with the ISFET system.

We observed a reasonable correlation between changes in V_{SG} and the substrate-dependent current for six oocytes expressing PAT1 (Fig. 5c). This finding supports the assumption that the change in surface proton concentration is directly proportional to the total substrate current, which for a given turnover rate and driving force, is a measure of the number of active transporters in the membrane. Indeed, this is to be expected if the dependence of protons on the translocation of a substrate-specific substance is stoichiometric. The substrate turnover rate is then proportional to $[H^+]_S$, which allows quantitative substrate activation and inhibition studies. This implies that a high coupling strength between $[H^+]_S$ and $[H^+]_D$ is maintained to minimize secondary effects compromising the linearity of concentration change. We assume that optimizing the geometry of the structures involved in the immobilization of oocytes (hole diameter, sensor-to-hole distance) will lead to improved coupling strength between the membrane transport proteins and the sensor surface, without compromising the effectiveness of the proton-selective diffusion barrier. This may also be the reason for the deviation of data points in Fig. 5c.

Conclusion

We present an integrated microdevice based on ISFET technology for monitoring proton-dependent membrane transport. Based on the ability of protons to migrate along the cell surface without diffusing back into the bulk solution, our method can sense surface pH free from detection artifacts stemming from other solutes. To verify the hypothesis, we conducted experiments on *Xenopus laevis* oocytes heterologously expressing various membrane transport proteins. Only transport systems that resulted directly (e.g. PAT1) and indirectly (e.g. NaPi-IIb,c, PiT-2) in a change in local pH gave significant responses. The results show that surface pH can be monitored with high precision and reliability. Moreover, control experiments demonstrate that solutes involved in the transport cycle do not diffuse along the cell

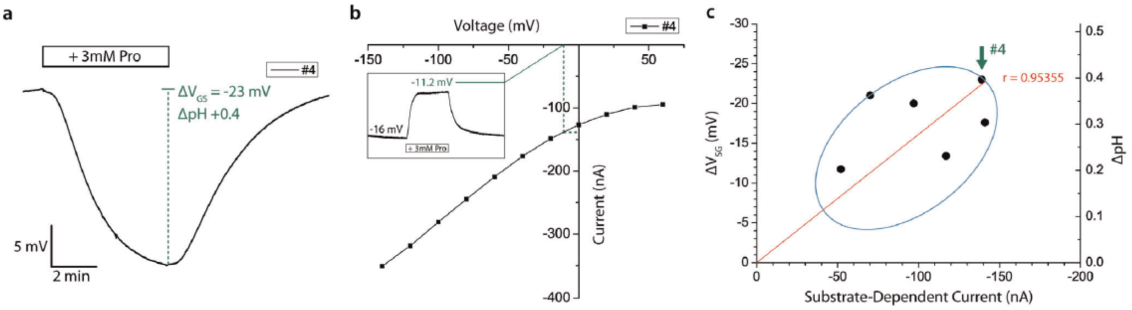

Figure 5. Correlation of pH response with protein expression level. Correlating sensor response with transport activity. a) Sensor response to proline superfusion of a representative oocyte (designated #4 in c) heterologously expressing PAT1. b) TEVC I-V data of the proline-dependent current of oocyte #4 in response to the addition of 3 mM proline solution to the 100 Na buffer. Inset shows the change in membrane potential induced by proline application for the same oocyte as in a. c) Correlation of ΔV_{SG} and the substrate-dependent current. Each point represents data from a single oocyte. Arrow marks the data point of oocyte #4 (−23 mV, −140 nA).
doi:10.1371/journal.pone.0039238.g005

membrane with sufficient efficiency to be detected by the sensor. Furthermore, studies correlating the change in surface pH with the population density of the amino acid cotransporter PAT1 have been done, revealing the feasibility of quantitative experiments, such as dose-response screenings. Optimization of the coupling between the transporter surface and the detection site will then lead to devices suitable for large-scale integration with potential for efficient and cost-effective high-throughput screenings. Furthermore, application to other cell types may be feasible by further miniaturization and modification of the cell immobilization site.

Acknowledgments

We gratefully acknowledge Christoph Bärtschi for CNC-machining of parts (Laboratory of Organic Chemistry, ETH), Dr. Andreas Werner (Institute of Physiology, UZH) for injecting oocytes, Drs. Simone Carmago and Anne-Kristine Meinild (Institute of Physiology, UZH) for generously providing PAT1 and GAT-1 cRNA, respectively, Eva Hänsenberger (Institute of Physiology, UZH) for expert preparation of oocytes; Prof. Ken-Ichi Miyamoto for provision of oocytes in Japan (Dept of Health Biosciences, University of Tokushima, JPN).

Author Contributions

Conceived and designed the experiments: DFS TG YM ICF PSD. Performed the experiments: DFS MP TG. Analyzed the data: DFS ICF PSD. Contributed reagents/materials/analysis tools: YM ICF PSD. Wrote the paper: DSF ICF PSD.

References

1. Hodgkin AL, Huxley AF (1952) A quantitative description of membrane current and its application to conduction and excitation in nerve. J Physiol 117: 500–544.
2. Schnizler K, Kuster M, Methfessel C, Fejtl M (2003) The roboocyte: automated cDNA/mRNA injection and subsequent TEVC recording on Xenopus oocytes in 96-well microtiter plates. Receptors Channels 9: 41–48.
3. Papke RL, Stokes C (2010) Working with OpusXpress: methods for high volume oocyte experiments. Methods 51: 121–133.
4. Hamill OP, Marty A, Neher E, Sakmann B, Sigworth FJ (1981) Improved patch-clamp techniques for high-resolution current recording from cells and cell-free membrane patches. Pflugers Arch 391: 85–100.
5. Cucu D, Simaels J, Jans D, Van Driessche W (2004) The transoocyte voltage clamp: a non-invasive technique for electrophysiological experiments with Xenopus laevis oocytes. Pflugers Arch 447: 934–942.
6. Schaffhauser DF, Andrini O, Ghezzi C, Forster IC, Franco-Obregon A, et al. (2011) Microfluidic platform for electrophysiological studies on Xenopus laevis oocytes under varying gravity levels. Lab Chip 11: 3471–3478.
7. Dahan E, Bize V, Lehnert T, Horisberger JD, Gijs MA (2007) Integrated microsystem for non-invasive electrophysiological measurements on Xenopus oocytes. Biosens Bioelectron 22: 3196–3202.
8. Strickholm A (1961) Impedance of a Small Electrically Isolated Area of Muscle Cell Surface. J Gen Physiol 44: 1073–1088.
9. Hille B (2001) Ion Channels of Excitable Membranes: Sinauer Associates.
10. Olivares W, McQuarrie DA (1975) On the theory of ionic solutions. Biophys J 15: 143–162.
11. Bergveld P (1970) Development of an Ion-Sensitive Solid-State Device for Neurophysiological Measurements. Ieee T Bio-Med Eng Bm17: 70-&.
12. Baumann WH, Lehmann M, Schwinde A, Ehret R, Brischwein M, et al. (1999) Microelectronic sensor system for microphysiological application on living cells. Sensor Actuat B-Chem 55: 77–89.
13. Lehmann M, Baumann W, Brischwein M, Ehret R, Kraus M, et al. (2000) Non-invasive measurement of cell membrane associated proton gradients by ion-sensitive field effect transistor arrays for microphysiological and bioelectronical applications. Biosens Bioelectron 15: 117–124.
14. Sakata T, Miyahara Y (2008) Noninvasive Monitoring of Transporter−Substrate Interaction at Cell Membrane. Anal Chem 80: 1493–1496.
15. Burckhardt BC, Kroll B, Fromter E (1992) Proton transport mechanism in the cell membrane of Xenopus laevis oocytes. Pflugers Arch 420: 78–82.
16. Aronson PS, Nee J, Suhm MA (1982) Modifier role of internal H+ in activating the Na+-H+ exchanger in renal microvillus membrane vesicles. Nature 299: 161–163.
17. Blanchard MG, Longpre JP, Wallendorff B, Lapointe JY (2008) Measuring ion transport activities in Xenopus oocytes using the ion-trap technique. Am J Physiol Cell Physiol 295: C1464–1472.
18. Ravera S, Virkki LV, Murer H, Forster IC (2007) Deciphering PiT transport kinetics and substrate specificity using electrophysiology and flux measurements. Am J Physiol Cell Physiol 293: C606–620.
19. Marx D, Tuckerman ME, Hutter J, Parrinello M (1999) The nature of the hydrated excess proton in water. Nature 397: 601–604.
20. Agmon N (1995) The Grotthuss Mechanism. Chem Phys Lett 244: 456–462.
21. Medvedev ES, Stuchebrukhov AA (2011) Proton diffusion along biological membranes. J Phys Condens Matter 23: 234103.
22. Antonenko YN, Pohl P (1998) Coupling of proton source and sink via H+-migration along the membrane surface as revealed by double patch-clamp experiments. FEBS Lett 429: 197–200.
23. Vanhal REG, Eijkel JCT, Bergveld P (1995) A Novel Description of Isfet Sensitivity with the Buffer Capacity and Double-Layer Capacitance as Key Parameters. Sensor Actuat B-Chem 24: 201–205.
24. Casans S, Ramirez D, Navarro AE (2000) Circuit provides constant current for ISFETs/MEMFETs. Edn 45: 164–+.
25. Fakitsas P, Adam G, Daidie D, van Bemmelen MX, Fouladkou F, et al. (2007) Early aldosterone-induced gene product regulates the epithelial sodium channel by deubiquitylation. J Am Soc Nephrol 18: 1084–1092.
26. MacAulay N, Bendahan A, Loland CJ, Zeuthen T, Kanner BI, et al. (2001) Engineered Zn(2+) switches in the gamma-aminobutyric acid (GABA) transporter-1. Differential effects on GABA uptake and currents. J Biol Chem 276: 40476–40485.
27. Werner A, Murer H, Kinne RK (1994) Cloning and expression of a renal Na-Pi cotransport system from flounder. Am J Physiol 267: F311–317.

28. Segawa H, Kaneko I, Takahashi A, Kuwahata M, Ito M, et al. (2002) Growth-related renal type II Na/Pi cotransporter. J Biol Chem 277: 19665–19672.
29. Boll M, Foltz M, Rubio-Aliaga I, Kottra G, Daniel H (2002) Functional characterization of two novel mammalian electrogenic proton-dependent amino acid cotransporters. J Biol Chem 277: 22966–22973.
30. Gundersen CB, Katz B, Miledi R (1982) The Antagonism between Botulinum Toxin and Calcium in Motor-Nerve Terminals. P Roy Soc Lond B Bio 216: 369–376.
31. Foltz M, Mertl M, Dietz V, Boll M, Kottra G, et al. (2005) Kinetics of bidirectional H+ and substrate transport by the proton-dependent amino acid symporter PAT1. Biochem J 386: 607–616.
32. Forster IC, Loo DD, Eskandari S (1999) Stoichiometry and Na+ binding cooperativity of rat and flounder renal type II Na+-Pi cotransporters. Am J Physiol 276: F644–649.
33. Bacconi A, Virkki LV, Biber J, Murer H, Forster IC (2005) Renouncing electroneutrality is not free of charge: switching on electrogenicity in a Na+-coupled phosphate cotransporter. Proc Natl Acad Sci U S A 102: 12606–12611.
34. Murer H, Forster I, Biber J (2004) The sodium phosphate cotransporter family SLC34. Pflugers Arch 447: 763–767.
35. Taylor PM, Kaur S, Mackenzie B, Peter GJ (1996) Amino-acid-dependent modulation of amino acid transport in Xenopus laevis oocytes. J Exp Biol 199: 923–931.
36. Mager S, Naeve J, Quick M, Labarca C, Davidson N, et al. (1993) Steady states, charge movements, and rates for a cloned GABA transporter expressed in Xenopus oocytes. Neuron 10: 177–188.
37. George AL, Jr., Staub O, Geering K, Rossier BC, Kleyman TR, et al. (1989) Functional expression of the amiloride-sensitive sodium channel in Xenopus oocytes. Proc Natl Acad Sci U S A 86: 7295–7298.
38. Kellenberger S, Schild L (2002) Epithelial sodium channel/degenerin family of ion channels: a variety of functions for a shared structure. Physiol Rev 82: 735–767.
39. Dumont JN, Brummett AR (1978) Oogenesis in Xenopus laevis (Daudin). V. Relationships between developing oocytes and their investing follicular tissues. J Morphol 155: 73–97.

BRIEF COMMUNICATIONS

nature genetics

Mutations in *SLC20A2* link familial idiopathic basal ganglia calcification with phosphate homeostasis

Cheng Wang[1,11], Yulei Li[1,11], Lei Shi[2,11], Jie Ren[1], Monica Patti[3], Tao Wang[4], João R M de Oliveira[5], María-Jesús Sobrido[6,7], Beatriz Quintáns[6,7], Miguel Baquero[8], Xiaoniu Cui[1], Xiang-Yang Zhang[1], Lianqing Wang[2], Haibo Xu[9], Junhan Wang[10], Jing Yao[1], Xiaohua Dai[1], Juan Liu[1], Lu Zhang[1], Hongying Ma[1], Yong Gao[1], Xixiang Ma[1], Shenglei Feng[1], Mugen Liu[1], Qing K Wang[1], Ian C Forster[3], Xue Zhang[2] & Jing-Yu Liu[1]

Familial idiopathic basal ganglia calcification (IBGC) is a genetic condition with a wide spectrum of neuropsychiatric symptoms, including parkinsonism and dementia. Here, we identified mutations in *SLC20A2*, encoding the type III sodium-dependent phosphate transporter 2 (PiT2), in IBGC-affected families of varied ancestry, and we observed significantly impaired phosphate transport activity for all assayed PiT2 mutants in *Xenopus laevis* oocytes. Our results implicate altered phosphate homeostasis in the etiology of IBGC.

Basal ganglia calcification was first noted in the 1850s and is now a frequent finding in clinical neuroimaging. Familial IBGC (MIM 213600), also known as Fahr disease, is a rare genetic condition characterized by symmetric calcification in the basal ganglia and other brain regions, a wide spectrum of neuropsychiatric symptoms, including parkinsonism, dystonia, tremor, ataxia, dementia, psychosis, seizures and chronic headache, and normal serum levels of calcium, phosphate, alkaline phosphatase and parathyroid hormone[1]. The typical age at clinical onset is between 30 and 50 years, and most individuals affected with IBGC are asymptomatic during childhood and young adulthood. The neuropathological hallmark of IBGC is vascular and pericapillary calcification, mainly of calcium phosphate, in the affected brain areas[2,3]. IBGC is frequently inherited in an autosomal dominant manner. We and others have shown that IBGC is genetically heterogeneous[4,5]. However, the causative genes and the underlying pathophysiology have remained elusive.

We have previously mapped a locus showing linkage with IBGC to the 8p21.1–8q11.23 chromosomal region in a large Chinese family[5]. To further refine the linked region, we genotyped ten polymorphic markers in the 8p21.1–8q11.23 interval in a different four-generation Chinese family with IBGC (SD-IBGC) (**Fig. 1a–d**, **Supplementary Fig. 1**, **Supplementary Table 1**, **Supplementary Methods** and **Supplementary Note**). Our two-point linkage analysis generated a maximum logarithm-of-odds (LOD) score of >3 at five markers, D8S524, D8S531, D8S532, D8S587 and D8S1831, confirming genetic mapping to the same chromosomal region (**Supplementary Table 2**). Additional haplotype data, together with our previously reported linkage analysis in a Chinese family with IBGC (HN-IBGC)[5], narrowed the linked region to an 18.7-Mb interval between the D8S505 and D8S1833 markers (**Supplementary Fig. 2**) that contains 77 genes in the RefSeq database. We sequenced 41 candidate genes within the interval in the index subject of the previously reported HN-IBGC family and identified a missense mutation (c.1492G>A) in *SLC20A2* (NM_006749) that leads to a substitution of arginine for glycine at codon 498 (p.Gly498Arg) in the PiT2 protein (**Fig. 1e**, **Table 1**, **Supplementary Fig. 3** and **Supplementary Table 3**). In the index subject of the SD-IBGC family, we found a different missense mutation (c.1802C>G) in the same gene, resulting in a serine-to-tryptophan substitution at codon 601 (p.Ser601Trp) (**Fig. 1e**, **Table 1** and **Supplementary Fig. 3**). Examination of all available members of the HN-IBGC and SD-IBGC families using restriction analysis showed that the two missense mutations fully segregate with the brain calcification phenotype in each of the families (**Table 1**, **Supplementary Fig. 4** and **Supplementary Table 4**). In five additional IBGC-affected families of varied ancestry (one Chinese, one Brazilian of European descent and three Spanish), we identified independent *SLC20A2* mutations (**Fig. 1e**, **Table 1** and **Supplementary Fig. 3**). Using restriction analysis, we screened 508 unrelated Chinese controls for the c.1492G>A, c.1802C>G and c.1802C>T mutations, 288 unrelated Spanish controls for the c.124_126delGTG, c.1723G>A and c.1784C>T mutations, and 101 unrelated Brazilian controls (mostly of European ancestry) for the c.1409delC mutation. None of these mutations was found in the corresponding control individuals. In addition, none of our identified mutations is present in the 1000 Genomes Project database or the ESP2500 data set of the National Heart, Lung, and Blood Institute (NHLBI) Exome Sequencing Project, which consists of 2,439 exomes (1,351 from European and 1,088 from African-American individuals). In an additional 11 individuals with IBGC, including 7 subjects with familial disease (3 Chinese, 3 Brazilian and 1 Spanish) and 4 subjects with sporadic disease (Chinese), we did not find any pathogenic mutation in *SLC20A2*.

---

[1] Key Laboratory of Molecular Biophysics of the Ministry of Education, College of Life Science and Technology and Center for Human Genome Research, Huazhong University of Science and Technology (HUST), Wuhan, China. [2] McKusick-Zhang Center for Genetic Medicine, State Key Laboratory of Medical Molecular Biology, Institute of Basic Medical Sciences, Chinese Academy of Medical Sciences and Peking Union Medical College, Beijing, China. [3] Institute of Physiology, Zurich Center for Integrated Human Physiology, University of Zurich, Zurich, Switzerland. [4] Department of Neurology, Union Hospital of HUST, Wuhan, China. [5] Department of Neuropsychiatry, Keizo Asami Laboratory, Federal University of Pernambuco, Recife, Brazil. [6] Fundación Pública Galega de Medicina Xenómica, Clinical Hospital of Santiago de Compostela, Servicio Galego de Saúde (SERGAS), Santiago de Compostela, Spain. [7] Center for Network Research on Rare Diseases (CIBERER), Institute of Health Carlos III, Barcelona, Spain. [8] Department of Medicine, University of València, Servei de Neurologia, Hospital Universitari i Politècnic La Fe, València, Spain. [9] Department of Radiology, Union Hospital of HUST, Wuhan, China. [10] Department of Clinical Laboratory, Hospital of HUST, Wuhan, China. [11] These authors contributed equally to this work. Correspondence should be addressed to J.-Y.L. (liujy@mail.hust.edu.cn) or X.Z. (xuezhang@pumc.edu.cn).

Received 8 September 2011; accepted 14 December 2011; published online 12 February 2012; doi:10.1038/ng.1077

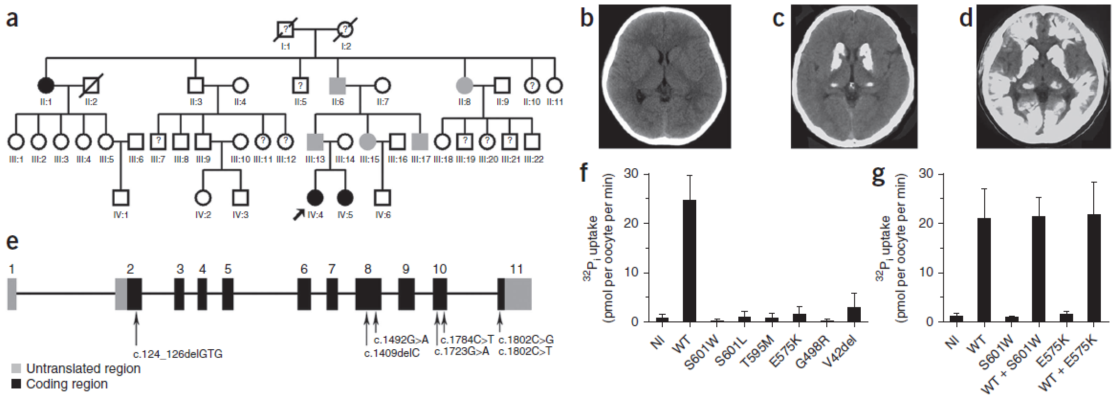

Figure 1 Mutations of *SLC20A2* in IBGC. (**a**) Pedigree of the SD-IBGC family. Filled symbols represent individuals affected with brain calcification, including both symptomatic (black) and asymptomatic (gray) individuals. The arrow indicates the index subject. The question marks indicate individuals from whom samples were not available. (**b–d**) Brain computed tomography (CT) scans showing no abnormal calcification (IV:1 of SD-IBGC) (**b**), symmetric calcification in the basal ganglia and thalamus (III:17 of SD-IBGC) (**c**) and severe and extensive calcification in the basal ganglia and other brain regions (IV:4 of SD-IBGC) (**d**). Calcification appears as bright areas on CT scans. The locations of brain calcification in all available affected members of SD-IBGC are presented in **Supplementary Figure 1**. (**e**) Schematic representation of the *SLC20A2* gene with IBGC-associated mutations indicated. (**f**,**g**) Assays of the P_i transport function of PiT2. Injection of *Xenopus* oocytes with RNA complementary to *SLC20A2* encoding the six PiT2 mutants resulted in an obvious decrease in $^{32}P_i$ uptake relative to oocytes expressing wild-type PiT2 (**f**). Coinjection of oocytes with RNA complementary to *SLC20A2* encoding wild-type and mutant (S601W or E575K) PiT2 did not have an obvious effect on $^{32}P_i$ uptake relative to oocytes expressing only wild-type protein (**g**). NI, non injected; WT, wild type. Error bars, s.d.

The highly conserved glutamate residue at position 575 (**Supplementary Fig. 5**) is critical for the inorganic phosphate (P_i) transport activity of PiT2 (ref. 6). Using $^{32}P_i$ transport assays in *Xenopus* oocytes, it was shown that a glutamic acid–to-lysine substitution at this residue (p.Glu575Lys) eliminates P_i transport function[6]. To determine whether the identified *SLC20A2* mutations impair the P_i transport function of PiT2, we individually expressed wild-type human *SLC20A2* and the six mutants (encoding S601W, S601L, T595M, E575K, G498R and V42del PiT2 variants) in *Xenopus* oocytes and carried out $^{32}P_i$ transport assays (**Supplementary Table 5** and **Supplementary Methods**)[7]. The c.1409delC frameshift mutation (encoding a p.Pro470Leufs*37 alteration) was not included in the assays because it would most likely lead to a complete loss of PiT2 function. We found that all the assayed mutations resulted in substantially impaired P_i transport (**Fig. 1f**). We also carried out $^{32}P_i$ transport assays in which wild-type SLC20A2 was coexpressed with the S601W or E575K mutants at a 1:1 ratio. In these experiments, expression of the mutant did not have an obvious effect on the P_i transport activity of the wild-type PiT2 protein (**Fig. 1g**).

P_i is indispensable for many biological processes in all kingdoms of life. In humans, physiological maintenance of total-body P_i levels and of the balanced distribution of P_i (85% in bones, 14% in cells and 1% in serum and extracellular fluids of soft tissues) is achieved by a tightly regulated process in which sodium-dependent phosphate (Na/P_i) transporters have a central role[8]. Three types of Na/P_i transporters with different regulatory functions in P_i homeostasis have been identified. The type II Na/P_i transporters are the major mediators of intestinal P_i absorption and renal P_i reabsorption, and mutations in the corresponding genes have been associated with genetic disorders with abnormal calcium phosphate deposition (kidney stone formation or lung calcification)[8]. The type III Na/P_i transporters, including PiT1, encoded by *SLC20A1*, and PiT2, encoded by *SLC20A2*, are broadly expressed with widely varied expression levels in different tissues, indicating that they may have a housekeeping role in the uptake of P_i into cells[9,10]. Increased serum P_i concentration could induce vascular calcification and abnormal calcium phosphate deposition in the walls of blood vessels and has been found to be associated with cardiovascular events and death in individuals with chronic kidney diseases, as well as in the general population[11]. It has been shown that PiT1 on vascular smooth muscle cells (VSMCs) is likely to be the key mediator in P_i-induced vascular calcification[12]. Until now, no mutation in the *SLC20A1* and *SLC20A2* genes had been found in human genetic disorders with vascular calcification. In the present study, we have identified IBGC-associated mutations in *SLC20A2*. Our functional data suggest that these *SLC20A2* mutations most likely have an effect through haploinsufficiency rather than by encoding dominant-negative activities.

IBGC shows marked intra- and interfamilial variability in clinical expression[1]. We did not observe obvious genotype-phenotype correlation in our study families with *SLC20A2* mutations. More extensive mutation analysis in additional families might provide insight into the molecular basis of the clinical heterogeneity in IBGC.

Table 1 ***SLC20A2* mutations identified in seven families with IBGC**

IBGC family	Mutation type	DNA change	Amino-acid change	Ancestry	Members screened
HN-IBGC	Missense	c.1492G>A	p.Gly498Arg	Chinese	9[a], 21[b] and 1[c]
SD-IBGC	Missense	c.1802C>G	p.Ser601Gln	Chinese	8[a] and 16[b]
BJ-IBGC	Missense	c.1802C>T	p.Ser601Leu	Chinese	2[a]
FSP 2	Frameshift	c.1409delC	p.Pro470Leufs*37	Brazilian	3[a] and 1[b]
IBGC-II	Missense	c.1723G>A	p.Glu575Lys	Spanish	2[a]
839	Missense	c.1784C>T	p.Thr595Met	Spanish	1[a]
1B334	Deletion	c.124_126delGTG	p.Val42del	Spanish	2[a]

[a]Affected family members. IBGC was defined by the presence of brain calcification on CT scans. [b]Unaffected family members. [c]The boy (3 years) for whom no brain CT scan was available.

Although *SLC20A2* expression has a broad tissue distribution, it is expressed at higher levels in brain regions affected in IBGC, as revealed in the Allen Institute Human Brain Atlas and by PiT2 ligand staining in the mouse brain[13]. Thus, it would not be unreasonable to postulate that the brain regions affected in IBGC are more sensitive to an imbalance in P_i homeostasis, with a functional loss of *SLC20A2* resulting in regional P_i accumulation in the extracellular matrix, thereby causing calcium phosphate deposition. This tissue-specific expression profile of *SLC20A2* might explain regional vulnerability to the pathologic changes in IBGC, a disorder in which no calcification is encountered outside of the brain. Histopathological examination of individuals with IBGC have revealed that calcium deposits are predominantly located within the walls of small arteries and veins and along capillaries[2,3]. Notably, the major Na/P_i transporter gene expressed in VSMCs is *SLC20A1* and not *SLC20A2* (ref. 12). Therefore, elevated local P_i concentration, resulting from IBGC-associated mutations in *SLC20A2*, might alternatively induce VSMC osteochondrogenic differentiation and calcification mediated by the PiT1-encoding *SLC20A1* gene[12]. Clearly, further studies are still needed to elucidate the molecular mechanisms of IBGC.

The identification of pathogenic mutations in *ENPP1* (encoding ectonucleotide pyrophosphatase/phosphodiesterase 1, which converts ATP to AMP and pyrophosphate) and *NT5E* (encoding the ecto-5′-nucleotidase CD73, which converts AMP to adenosine and P_i) in autosomal recessive forms of human arterial calcification highlights the important roles of extracellular adenosine and inorganic pyrophosphate in the development of vascular calcification[14,15]. These results, together with our findings, advance the general understanding of the functional pathways involved in different forms of vascular calcification.

Overall, our results establish loss-of-function mutations in *SLC20A2* as the molecular basis for a large subset of IBGC cases and identify disturbed regional P_i homeostasis as a primary pathophysiological mechanism. To our knowledge, this is the first gene linked to this condition, and we herein show that mutations in this gene are distributed worldwide. These findings lay the groundwork for the future development of new therapeutic drugs for IBGC and other conditions associated with brain calcification.

URLs. 1000 Genomes Project, http://www.1000genomes.org/; NHLBI Exome Sequencing Project (ESP) Exome Variant Server, http://evs.gs.washington.edu/EVS/; Allen Institute Human Brain Atlas, http://human.brain-map.org/.

Note: Supplementary information is available on the Nature Genetics website.

ACKNOWLEDGMENTS

We would like to thank all the family members for their enthusiastic participation in the study. X.Z. would like to thank K. Hong, Q. Liu, Z. Wu, W. Xia, C. Zhang and L. Zou for clinical support. J.R.M.d.O. would like to thank R. Lemos and D. Oliveira for technical support. This study was mainly supported by the National Natural Science Foundation of China (30670736 and 30972655 to J.-Y.L. and 30730097 and 31021091 to X.Z.) and by the Program for Changjiang Scholars and Innovative Research Team in University (PCSIRT; IRT1006 to X.Z.). I.C.F. is supported by the Swiss National Science Foundation. M.L. is supported by the National Natural Science Foundation of China (30871386). J.R.M.d.O. is supported by the John Simon Guggenheim Memorial Foundation and by Conselho Nacional de Desenvolvimento Científico e Tecnológico M.-J.S. and B.Q. are supported by research contracts from the Institute of Health Carlos III and by FEDER funds. The study was approved by the ethics committees of HUST and Peking Union Medical College. Written informed consent was obtained from all participants or their legal guardians.

AUTHOR CONTRIBUTIONS

J.-Y.L. conceived the study. J.-Y.L. and X.Z. designed the experiments, obtained financial support and wrote the paper. The group of J.-Y.L. discovered the first *SLC20A2* mutation. X.Z. coordinated the subsequent international collaboration. C.W., Y.L., L.S. and J.R. carried out the linkage analysis and *SLC20A2* mutation screening. L.S., L.W., C.W. and X.-Y.Z. were responsible for molecular cloning. M.P. and I.C.F. conducted $^{32}P_i$ transport assays. Y.L. performed the bioinformatics analysis. T.W., J.R.M.d.O., M.-J.S., B.Q., M.B., H.X. and J.W. were responsible for clinical evaluation and sample collection. X.C., X.D., J.Y., J.L., L.Z., H.M., Y.G., X.M. and S.F. carried out mutation screening for other candidate genes. M.L. and Q.K.W. supported the genetic analyses.

COMPETING FINANCIAL INTERESTS

The authors declare competing financial interests: details accompany the full-text HTML version of the paper at http://www.nature.com/naturegenetics/.

1. Manyam, B.V. *Parkinsonism Relat. Disord.* **11**, 73–80 (2005).
2. Miklossy, J. *et al. Acta Neuropathol.* **109**, 643–653 (2005).
3. Wider, C., Dickson, D.W., Schweitzer, K.J., Broderick, D.F. & Wszolek, Z.K. *J. Neurol.* **256**, 839–842 (2009).
4. Oliveira, J.R. *et al. Neurology* **63**, 2165–2167 (2004).
5. Dai, X. *et al. Am. J. Med. Genet. B Neuropsychiatr. Genet.* **153B**, 1305–1310 (2010).
6. Bottger, P. & Pedersen, L. *J. Biol. Chem.* **277**, 42741–42747 (2002).
7. Ravera, S., Virkki, L.V., Murer, H. & Forster, I.C. *Am. J. Physiol. Cell Physiol.* **293**, C606–C620 (2007).
8. Prié, D. & Friedlander, G. *N. Engl. J. Med.* **362**, 2399–2409 (2010).
9. Villa-Bellosta, R. *et al. Am. J. Physiol. Renal Physiol.* **296**, F691–F699 (2009).
10. Kavanaugh, M.P. & Kabat, D. *Kidney Int.* **49**, 959–963 (1996).
11. Kendrick, J., Kestenbaum, B. & Chonchol, M. *Adv. Chronic Kidney Dis.* **18**, 113–119 (2011).
12. Giachelli, C.M. *Kidney Int.* **75**, 890–897 (2009).
13. Lagrue, E. *et al. J. Biomed. Sci.* **17**, 91 (2010).
14. Rutsch, F. *et al. Nat. Genet.* **34**, 379–381 (2003).
15. St. Hilaire, C. *et al. N. Engl. J. Med.* **364**, 432–442 (2011).

REFERENCES

Adams, S.V., and DeFelice, L.J. (2003). Ionic currents in the human serotonin transporter reveal inconsistencies in the alternating access hypothesis. Biophys. J. *85*, 1548-1559.

Akyuz, N., Altman, R.B., Blanchard, S.C., and Boudker, O. (2013). Transport dynamics in a glutamate transporter homologue. Nature.

Andrini, O., Ghezzi, C., Murer, H., and Forster, I.C. (2008). The leak mode of type II Na(+)-P(i) cotransporters. Channels (Austin) *2*, 346-357.

Andrini, O., Meinild, A.-K., Ghezzi, C., Murer, H., and Forster, I.C. (2012). Lithium interactions with Na+-coupled inorganic phosphate cotransporters: insights into the mechanism of sequential cation binding. AJP: Cell Physiology *302*, C539.

Bacconi, A., Virkki, L.V., Biber, J., Murer, H., and Forster, I.C. (2005). Renouncing electroneutrality is not free of charge: switching on electrogenicity in a Na+-coupled phosphate cotransporter. Proc. Natl. Acad. Sci. U.S.A. *102*, 12606-12611.

Bergwitz, C., Roslin, N.M., Tieder, M., Loredo-Osti, J.C., Bastepe, M., Abu-Zahra, H., Frappier, D., Burkett, K., Carpenter, T.O., and Anderson, D., et al. (2006). SLC34A3 mutations in patients with hereditary hypophosphatemic rickets with hypercalciuria predict a key role for the sodium-phosphate cotransporter NaPi-IIc in maintaining phosphate homeostasis. Am. J. Hum. Genet. *78*, 179-192.

Berner, W., Kinne, R., and Murer, H. (1976). Phosphate transport into brush-border membrane vesicles isolated from rat small intestine. Biochem. J. *160*, 467-474.

Bezanilla, F. (2005). Voltage-gated ion channels. IEEE Trans Nanobioscience *4*, 34-48.

Biber, J., Hernando, N., and Forster, I. (2013). Phosphate transporters and their function. Annu. Rev. Physiol. *75*, 535-550.

Biber, J., Stieger, B., Stange, G., and Murer, H. (2007). Isolation of renal proximal tubular brush-border membranes. Nat Protoc *2*, 1356-1359.

Boron, W.F., and Boulpaep, E.L. (2012). Medical physiology (Philadelphia, Pa, London: Saunders).

Bossi, E., Fabbrini, M.S., and Ceriotti, A. (2007). Exogenous protein expression in Xenopus oocytes: basic procedures. Methods Mol. Biol. *375*, 107-131.

Brunger, A.T., Strop, P., Vrljic, M., Chu, S., and Weninger, K.R. (2011). Three-dimensional molecular modeling with single molecule FRET. J. Struct. Biol. *173*, 497-505.

Busch, A., Waldegger, S., Herzer, T., Biber, J., Markovich, D., Hayes, G., Murer, H., and Lang, F. (1994). Electrophysiological analysis of Na+/Pi cotransport mediated by a transporter cloned from rat kidney and expressed in Xenopus oocytes. Proc. Natl. Acad. Sci. U.S.A. *91*, 8205-8208.

Busch, W., and Saier, M.H. (2002). The transporter classification (TC) system, 2002. Crit. Rev. Biochem. Mol. Biol. *37*, 287-337.

Cha, A., and Bezanilla, F. (1998). Structural implications of fluorescence quenching in the Shaker K+ channel. J. Gen. Physiol. *112*, 391-408.

Chambers, R.W., Kajiwara, T., and Kearns, D.R. (1974). Effect of dimer formation on the electronic absorption and emission spectra of ionic dyes. Rhodamines and other common dyes. J. Phys. Chem. *78*, 380-387.

Chen, J.G., Liu-Chen, S., and Rudnick, G. (1997). External cysteine residues in the serotonin transporter. Biochemistry *36*, 1479-1486.

Cherubino, F., Bertram, S., Bossi, E., and Peres, A. (2012). Pre-steady-state and reverse transport currents in the GABA transporter GAT1. Am. J. Physiol., Cell Physiol. *302*, C1096-108.

Claxton, D.P., Quick, M., Shi, L., de Carvalho, Fernanda Delmondes, Weinstein, H., Javitch, J.A., and McHaourab, H.S. (2010). Ion/substrate-dependent conformational dynamics of a bacterial homolog of neurotransmitter:sodium symporters. Nat. Struct. Mol. Biol. *17*, 822-829.

Crisman, T.J., Qu, S., Kanner, B.I., and Forrest, L.R. (2009). Inward-facing conformation of glutamate transporters as revealed by their inverted-topology structural repeats. Proc. Natl. Acad. Sci. U.S.A. *106*, 20752-20757.

Deisenhofer, J., Epp, O., Miki, K., Huber, R., and Michel, H. (1985). Structure of the protein subunits in the photosynthetic reaction centre of Rhodopseudomonas viridis at 3Å resolution. Nature *318*, 618-624.

Dutzler, R. (2006). The ClC family of chloride channels and transporters. Curr. Opin. Struct. Biol. *16*, 439-446.

Ehnes, C., Forster, I.C., Bacconi, A., Kohler, K., Biber, J., and Murer, H. (2004a). Structure-function relations of the first and fourth extracellular linkers of the type IIa Na+/Pi cotransporter: II. Substrate interaction and voltage dependency of two functionally important sites. J. Gen. Physiol. *124*, 489-503.

Ehnes, C., Forster, I.C., Kohler, K., Bacconi, A., Stange, G., Biber, J., and Murer, H. (2004b). Structure-function relations of the first and fourth predicted extracellular linkers of the type IIa Na+/Pi cotransporter: I. Cysteine scanning mutagenesis. J. Gen. Physiol. *124*, 475-488.

Eskandari, S., Wright, E.M., and Loo, D D F (2005). Kinetics of the reverse mode of the Na+/glucose cotransporter. J. Membr. Biol. *204*, 23-32.

Eto, N., Tomita, M., and Hayashi, M. (2006). NaPi-mediated transcellular permeation is the dominant route in intestinal inorganic phosphate absorption in rats. Drug Metab. Pharmacokinet. *21*, 217-221.

Faham, S., Watanabe, A., Besserer, G.M., Cascio, D., Specht, A., Hirayama, B.A., Wright, E.M., and Abramson, J. (2008). The crystal structure of a sodium galactose transporter reveals mechanistic insights into Na+/sugar symport. Science *321*, 810-814.

Forrest, L.R. (2013). (Pseudo-)Symmetrical Transport. Science *339*, 399-401.

Forrest, L.R., Krämer, R., and Ziegler, C. (2011). The structural basis of secondary active transport mechanisms. Biochim. Biophys. Acta *1807*, 167-188.

Forrest, L.R., and Rudnick, G. (2009). The rocking bundle: a mechanism for ion-coupled solute flux by symmetrical transporters. Physiology (Bethesda) *24*, 377-386.

Forrest, L.R., Zhang, Y.-W., Jacobs, M.T., Gesmonde, J., Xie, L., Honig, B.H., and Rudnick, G. (2008). Mechanism for alternating access in neurotransmitter transporters. Proc. Natl. Acad. Sci. U.S.A. *105*, 10338-10343.

Forster, I., Hernando, N., Biber, J., and Murer, H. (1998). The voltage dependence of a cloned mammalian renal type II Na+/Pi cotransporter (NaPi-2). J. Gen. Physiol. *112*, 1-18.

Forster, I.C., Hernando, N., Biber, J., and Murer, H. (2012). Phosphate transport kinetics and structure-function relationships of SLC34 and SLC20 proteins. Curr Top Membr *70*, 313-356.

Forster, I.C., Hernando, N., Biber, J., and Murer, H. (2013). Phosphate transporters of the SLC20 and SLC34 families. Mol. Aspects Med. *34*, 386-395.

Forster, I.C., Loo, D.D., and Eskandari, S. (1999). Stoichiometry and Na+ binding cooperativity of rat and flounder renal type II Na+-Pi cotransporters. Am. J. Physiol. *276*, F644-9.

Gadsby, D.C. (2009). Ion channels versus ion pumps: the principal difference, in principle. Nat. Rev. Mol. Cell Biol. *10*, 344-352.

Garcia, M.L., Viitanen, P., Foster, D.L., and Kaback, H.R. (1983). Mechanism of lactose translocation in proteoliposomes reconstituted with lac carrier protein purified from Escherichia coli. 1. Effect of pH and imposed membrane potential on efflux, exchange, and counterflow. Biochemistry *22*, 2524-2531.

Ghezzi, C., Meinild, A.-K., Murer, H., and Forster, I.C. (2011). Voltage- and substrate-dependent interactions between sites in putative re-entrant domains of a Na(+)-coupled phosphate cotransporter. Pflugers Arch. *461*, 645-663.

Ghezzi, C., Murer, H., and Forster, I.C. (2009). Substrate interactions of the electroneutral Na+-coupled inorganic phosphate cotransporter (NaPi-IIc). J. Physiol. (Lond.) *587*, 4293-4307.

Greer, J., Erickson, J.W., Baldwin, J.J., and Varney, M.D. (1994). Application of the three-dimensional structures of protein target molecules in structure-based drug design. J. Med. Chem. *37*, 1035-1054.

Gu, J., and Bourne, P.E. (2009). Structural bioinformatics (Hoboken, N.J: Wiley-Blackwell).

Hille, B. (2001). Ion channels of excitable membranes (Sunderland, Mass: Sinauer Associates).

Hoffmann, N., Thees, M., and Kinne, R. (1976). Phosphate transport by isolated renal brush border vesicles. Pflugers Arch. *362*, 147-156.

Hunte, C., Screpanti, E., Venturi, M., Rimon, A., Padan, E., and Michel, H. (2005). Structure of a Na+/H+ antiporter and insights into mechanism of action and regulation by pH. Nature *435*, 1197-1202.

Jardetzky, O. (1966). Simple allosteric model for membrane pumps. Nature *211*, 969-970.

Karlin, A., and Akabas, M.H. (1998). Substituted-cysteine accessibility method. Meth. Enzymol. *293*, 123-145.

Kashyap, S., and Mohapatra, P.R. (2013). Pulmonary alveolar microlithiasis. Lung India *30*, 143-147.

Klare, J.P. (2013). Site-directed spin labeling EPR spectroscopy in protein research. Biol. Chem. *394*, 1281-1300.

Köhler, K., Forster, I.C., Stange, G., Biber, J., and Murer, H. (2002a). Identification of functionally important sites in the first intracellular loop of the NaPi-IIa cotransporter. Am. J. Physiol. Renal Physiol. *282*, F687-96.

Köhler, K., Forster, I.C., Stange, G., Biber, J., and Murer, H. (2002b). Transport function of the renal type IIa Na+/P(i) cotransporter is codetermined by residues in two opposing linker regions. J. Gen. Physiol. *120*, 693-705.

Köhler, K., Forster, I.C., Stange, G., Biber, J., and Murer, H. (2003). Essential cysteine residues of the type IIa Na+/Pi cotransporter. Pflugers Arch. *446*, 203-210.

Krishnamurthy, H., and Gouaux, E. (2012). X-ray structures of LeuT in substrate-free outward-open and apo inward-open states. Nature *481*, 469-474.

Kuntz, D., Marie, P., Berhel, M., and Caulin, F. (1986). Treatment of post-menopausal osteoporosis with phosphate and intermittent calcitonin. Int J Clin Pharmacol Res *6*, 157-162.

Kvist, T., Hansen, K.B., and Bräuner-Osborne, H. (2011). The use of Xenopus oocytes in drug screening. Expert Opin Drug Discov *6*, 141-153.

Lakowicz, J.R. (op. 2006). Principles of fluorescence spectroscopy (New York, N.Y: Springer).

Lambert, G., Forster, I.C., Stange, G., Köhler, K., Biber, J., and Murer, H. (2001). Cysteine mutagenesis reveals novel structure-function features within the predicted third extracellular loop of the type IIa Na(+)/P(i) cotransporter. J. Gen. Physiol. *117*, 533-546.

Lambert, G., Traebert, M., Biber, J., and Murer, H. (2000). Cleavage of disulfide bonds leads to inactivation and degradation of the type IIa, but not type IIb sodium phosphate cotransporter expressed in Xenopus laevis oocytes. J. Membr. Biol. *176*, 143-149.

Lambert, G., Traebert, M., Hernando, N., Biber, J., and Murer, H. (1999). Studies on the topology of the renal type II NaPi-cotransporter. Pflugers Arch. *437*, 972-978.

Landau, E.M., and Rosenbusch, J.P. (1996). Lipidic cubic phases: a novel concept for the crystallization of membrane proteins. Proc. Natl. Acad. Sci. U.S.A. *93*, 14532-14535.

Larsson, H.P. (2004). Fluorometric measurements of conformational changes in glutamate transporters. Proceedings of the National Academy of Sciences *101*, 3951-3956.

Lederer, E., and Miyamoto, K.-i. (2012). Clinical consequences of mutations in sodium phosphate cotransporters. Clin J Am Soc Nephrol *7*, 1179-1187.

Leighton, B.H., Seal, R.P., Shimamoto, K., and Amara, S.G. (2002). A hydrophobic domain in glutamate transporters forms an extracellular helix associated with the permeation pathway for substrates. J. Biol. Chem. *277*, 29847-29855.

Levshin, L.V., and Nizamov, N. (1966). Concentration quenching of the luminescence of rhodamine dyes in binary solvents. J Appl Spectrosc *5*, 531-534.

Lolkema, J.S., and Slotboom, D.J. (2003). Classification of 29 families of secondary transport proteins into a single structural class using hydropathy profile analysis. J. Mol. Biol. *327*, 901-909.

Loo, D.D., Hazama, A., Supplisson, S., Turk, E., and Wright, E.M. (1993). Relaxation kinetics of the Na+/glucose cotransporter. Proc. Natl. Acad. Sci. U.S.A. *90*, 5767-5771.

Loo, D.D., Hirayama, B.A., Karakossian, M.H., Meinild, A.-K., and Wright, E.M. (2006). Conformational Dynamics of hSGLT1 during Na+/Glucose Cotransport. The Journal of General Physiology *128*, 701-720.

Magagnin, S., Werner, A., Markovich, D., Sorribas, V., Stange, G., Biber, J., and Murer, H. (1993). Expression cloning of human and rat renal cortex Na/Pi cotransport. Proc. Natl. Acad. Sci. U.S.A. *90*, 5979-5983.

Magen, D., Berger, L., Coady, M.J., Ilivitzki, A., Militianu, D., Tieder, M., Selig, S., Lapointe, J.Y., Zelikovic, I., and Skorecki, K. (2010). A loss-of-function mutation in NaPi-IIa and renal Fanconi's syndrome. N. Engl. J. Med. *362*, 1102-1109.

Mager, S., Naeve, J., Quick, M., Labarca, C., Davidson, N., and Lester, H.A. (1993). Steady states, charge movements, and rates for a cloned GABA transporter expressed in Xenopus oocytes. Neuron *10*, 177-188.

Mancusso, R., Gregorio, G.G., Liu, Q., and Wang, D.-N. (2012). Structure and mechanism of a bacterial sodium-dependent dicarboxylate transporter. Nature *491*, 622-626.

Mannuzzu, L.M., Moronne, M.M., and Isacoff, E.Y. (1996). Direct physical measure of conformational rearrangement underlying potassium channel gating. Science *271*, 213-216.

Meinild, A.-K., and Forster, I.C. (2012). Using lithium to probe sequential cation interactions with GAT1. Am. J. Physiol., Cell Physiol. *302*, C1661-75.

Okoh, M.P., Hunter, J.L., Corrie, J.E.T., and Webb, M.R. (2006). A Biosensor for Inorganic Phosphate Using a Rhodamine-Labeled Phosphate Binding Protein †. Biochemistry *45*, 14764-14771.

Pajor, A.M., Hirayama, B.A., and Loo, D.D. (1998). Sodium and lithium interactions with the Na+/Dicarboxylate cotransporter. J. Biol. Chem. *273*, 18923-18929.

Parent, L., Supplisson, S., Loo, D.D., and Wright, E.M. (1992). Electrogenic properties of the cloned Na+/glucose cotransporter: II. A transport model under nonrapid equilibrium conditions. J. Membr. Biol. *125*, 63-79.

Patti, M., Ghezzi, C., and Forster, I.C. (2013). Conferring electrogenicity to the electroneutral phosphate cotransporter NaPi-IIc (SLC34A3) reveals an internal cation release step. Pflugers Arch.

Penido, Maria Goretti M G, and Alon, U.S. (2012). Phosphate homeostasis and its role in bone health. Pediatr. Nephrol. *27*, 2039-2048.

Perez, C., and Ziegler, C. (2013). Mechanistic aspects of sodium-binding sites in LeuT-like fold symporters. Biol. Chem. *394*, 641-648.

Prié, D., Huart, V., Bakouh, N., Planelles, G., Dellis, O., Gérard, B., Hulin, P., Benqué-Blanchet, F., Silve, C., and Grandchamp, B., et al. (2002). Nephrolithiasis and osteoporosis associated with hypophosphatemia caused by mutations in the type 2a sodium-phosphate cotransporter. N. Engl. J. Med. *347*, 983-991.

Radanovic, T., Gisler, S.M., Biber, J., and Murer, H. (2006). Topology of the type IIa Na+/P(i) cotransporter. J. Membr. Biol. *212*, 41-49.

Radestock, S., and Forrest, L.R. (2011). The alternating-access mechanism of MFS transporters arises from inverted-topology repeats. J. Mol. Biol. *407*, 698-715.

Ressl, S., Terwisscha van Scheltinga, Anke C, Vonrhein, C., Ott, V., and Ziegler, C. (2009). Molecular basis of transport and regulation in the Na(+)/betaine symporter BetP. Nature *458*, 47-52.

Rudnick, G. (2006). Serotonin transporters--structure and function. J. Membr. Biol. *213*, 101-110.

Saier, M.H., Yen, M.R., Noto, K., Tamang, D.G., and Elkan, C. (2009). The Transporter Classification Database: recent advances. Nucleic Acids Res. *37*, D274-8.

Sauer, G.A., Nagel, G., Koepsell, H., Bamberg, E., and Hartung, K. (2000). Voltage and substrate dependence of the inverse transport mode of the rabbit Na(+)/glucose cotransporter (SGLT1). FEBS Lett. *469*, 98-100.

Schaffhauser, D.F., Patti, M., Goda, T., Miyahara, Y., Forster, I.C., and Dittrich, P.S. (2012). An integrated field-effect microdevice for monitoring membrane transport in Xenopus laevis oocytes via lateral proton diffusion. PLoS ONE *7*, e39238.

Segawa, H., Kaneko, I., Takahashi, A., Kuwahata, M., Ito, M., Ohkido, I., Tatsumi, S., and Miyamoto, K.-i. (2002). Growth-related renal type II Na/Pi cotransporter. J. Biol. Chem. *277*, 19665-19672.

Segawa, H., Onitsuka, A., Kuwahata, M., Hanabusa, E., Furutani, J., Kaneko, I., Tomoe, Y., Aranami, F., Matsumoto, N., and Ito, M., et al. (2009). Type IIc sodium-dependent phosphate transporter regulates calcium metabolism. J. Am. Soc. Nephrol. *20*, 104-113.

Stefani, E., and Bezanilla, F. (1998). Cut-open oocyte voltage-clamp technique. Meth. Enzymol. *293*, 300-318.

Ullrich, K.J., and Murer, H. (1982). Sulphate and phosphate transport in the renal proximal tubule. Philos. Trans. R. Soc. Lond., B, Biol. Sci. *299*, 549-558.

Vinothkumar, K.R., and Henderson, R. (2010). Structures of membrane proteins. Q. Rev. Biophys. *43*, 65-158.

Virkki, L.V., Forster, I.C., Bacconi, A., Biber, J., and Murer, H. (2005). Functionally important residues in the predicted 3(rd) transmembrane domain of the type IIa sodium-phosphate co-transporter (NaPi-IIa). J. Membr. Biol. *206*, 227-238.

Virkki, L.V., Murer, H., and Forster, I.C. (2006a). Mapping conformational changes of a type IIb Na+/Pi cotransporter by voltage clamp fluorometry. J. Biol. Chem. *281*, 28837-28849.

Virkki, L.V., Murer, H., and Forster, I.C. (2006b). Voltage clamp fluorometric measurements on a type II Na+-coupled Pi cotransporter: shedding light on substrate binding order. J. Gen. Physiol. *127*, 539-555.

Wadiche, J.I., Arriza, J.L., Amara, S.G., and Kavanaugh, M.P. (1995). Kinetics of a human glutamate transporter. Neuron *14*, 1019-1027.

Wagner, C.A., Friedrich, B., Setiawan, I., Lang, F., and Bröer, S. (2000). The use of Xenopus laevis oocytes for the functional characterization of heterologously expressed membrane proteins. Cell. Physiol. Biochem. *10*, 1-12.

Wang, C., Li, Y., Shi, L., Ren, J., Patti, M., Wang, T., de Oliveira, João R M, Sobrido, M.-J., Quintáns, B., and Baquero, M., et al. (2012). Mutations in SLC20A2 link familial idiopathic basal ganglia calcification with phosphate homeostasis. Nat. Genet. *44*, 254-256.

Werner, A., and Kinne, R.K. (2001). Evolution of the Na-P(i) cotransport systems. Am. J. Physiol. Regul. Integr. Comp. Physiol. *280*, R301-12.

Wright, E.M., Loo, Donald D F, and Hirayama, B.A. (2011). Biology of human sodium glucose transporters. Physiol. Rev. *91*, 733-794.

Yamashita, A., Singh, S.K., Kawate, T., Jin, Y., and Gouaux, E. (2005). Crystal structure of a bacterial homologue of Na+/Cl--dependent neurotransmitter transporters. Nature *437*, 215-223.

Yernool, D., Boudker, O., Jin, Y., and Gouaux, E. (2004). Structure of a glutamate transporter homologue from Pyrococcus horikoshii. Nature *431*, 811-818.

Yoon, B.-J. (2009). Hidden Markov Models and their Applications in Biological Sequence Analysis. CG *10*, 402-415.

Zhao, Y., Terry, D., Shi, L., Weinstein, H., Blanchard, S.C., and Javitch, J.A. (2010). Single-molecule dynamics of gating in a neurotransmitter transporter homologue. Nature *465*, 188-193.

Zhao, Y., Terry, D.S., Shi, L., Quick, M., Weinstein, H., Blanchard, S.C., and Javitch, J.A. (2011). Substrate-modulated gating dynamics in a Na+-coupled neurotransmitter transporter homologue. Nature *474*, 109-113.

Zhou, R., Kunzelmann, S., Webb, M.R., and Ha, T. (2011). Detecting intramolecular conformational dynamics of single molecules in short distance range with subnanometer sensitivity. Nano Lett. *11*, 5482-5488.

CURRICULUM VITAE

Personal information

Surname: PATTI

First name: Monica

Date of birth: March 14th, 1984

Nationality: Italian

Languages: Italian (mother tongue), English (fluent)

Gender: Female

Address: Bergstrasse 57, 8032 Zurich

Mobile: +41 0765349460

E-mail: monica.patti@uzh.ch
monica.patti@gmail.com

Education

June 2010 – October 2013	**University of Zurich, Switzerland** **PhD Studies in Physiology** PhD thesis: *“Structure-function studies on a sodium-coupled phosphate cotransporter”* Advisor: PD Ian Forster
October 2007 – July 2009	**Università di Trieste, Italy** **M.S. in Neuroscience** Master thesis: *"Identification of new markers of resistance to the antiangiogenic therapy in the gliomas"* Advisors: Prof. Dr. Carlo Sala, Dr Chiara Verpelli
October 2003 – December 2007	**Università degli Studi dell'Insubria, Varese, Italy** **B.S. in Biotechnology** Bachelor thesis: *“Point mutations responsible for interaction with substrates in KAAT1, a Na+/Cl-dependent membrane transport protein”* Advisors: Prof. Dr. Enrico Peres, Dr. Elena Bossi
September 1998 – July 2003	**Liceo “Alessandro Manzoni”, Italy** Sociology and Psychology

Work experiences

June 2010 – October 2013	**University of Zurich, Switzerland** PhD Student in the group of PD. Ian Forster. Teaching assist in practical workshops for Medical Student (first and second years)
January 2010 – May 2010	**Università degli studi di Milano, Italy** Trainee post-degree in neuroscience in the group of Prof. Dr. Carlo Sala
October 2008 – July 2009	**Università degli studi di Milano, Italy** Undergraduate student in the group of Prof. Dr. Carlo Sala
April 2007 – September 2007	**Universita dell'insubria, Italy** Bachelor student in the group of Dr. Elena Bossi

Publications

“Structural model of the human renal Na+-phosphate cotransporter NaPi.” Patti M., Fenollar-Ferrer C., Knöpfel T., Werner A., Forster I. C., Forrest L. R. *Manuscript submitted.*

“Using time-resolved fluorometry to study the transport cycle dynamics of a Na+-coupled phosphate cotransporter.” Patti M. and Forster IC. *Manuscript in preparation*.

“Conferring electrogenicity to the electroneutral phosphate cotransporter NaPi-IIc (SLC34A3) reveals an internal cation release step.” Patti M, Ghezzi C, Forster IC. *Pflugers Arch.* (2013)

“An integrated field-effect microdevice for monitoring membrane transport in Xenopus laevis oocytes via lateral proton diffusion.” Schaffhauser DF, Patti M, Goda T, Miyahara Y, Forster IC, Dittrich PS. *PLoS One*. 7(7):e39238. (2012)

“Mutations in SLC20A2 link familial idiopathic basal ganglia calcification withphosphate homeostasis”, Wang C, Li Y, Shi L, Ren J, Patti M, Wang T, de Oliveira JR, Sobrido MJ, Quintáns B, Baquero M, Cui X, Zhang XY, Wang L, Xu H, Wang J, Yao J, Dai X, Liu J, Zhang L, Ma H, Gao Y, Ma X, Feng S, Liu M, Wang QK, Forster IC, Zhang X, Liu JY. *Nature Genetics*. 44, 254–256 (2012)

"Anti-angiogenic therapy induces integrin-linked kinase 1 up-regulation in a mouse model of glioblastoma", Verpelli C, Bertani G, Cea V, Patti M, Bikfalvi A, Bello L, Sala C. *PLoS One.* 5(10):e13710. (2010)

References

PD Dr. Ian Forster, senior scientist in Physiology at Institute of Physiology in the University of Zurich, Zurich – Switzerland (IForster@access.uzh.ch)

Dr. Andreas Werner, principal investigator at the Institute for Cell and Molecular Biosciences Medical School at University of Newcastle upon Tyne, Newcastle – United Kingdom (andreas.werner@ncl.ac.uk)

Prof. Dr. François Verrey, head of the Institute of Physiology in Zurich University, Zurich – Switzerland (verrey@access.uzh.ch)

Dr. Elena Bossi, principal investigator at Department of Biotechnology and Molecular Science at Università dell'Insubria, Varese – Italy (elena.bossi@uninsubria.it).

Dr. Chiara Verpelli, associate researcher CNR Institute of Neuroscience, Department of Pharmacology, Universita di Milano, Milan – Italy (c.verpelli@in.cnr.it)

ACKNOWLEDGEMENTS

Prof. Dr. François Verrey for giving me the possibility to work in his lab.
PD Dr. Ian Forster for guidance, the support and especially the patience during all these years. I could not have imagined having a better advisor and mentor for my PhD study.

The other members of my thesis committee, Prof. Dr. Carsten Wagner and PD Dr. Stephan Kellenberger for the interesting discussions and advises.

All present and former members of Verrey and Wagner groups for the nice work environment. In particular Dr. Soline Bourgeois, Dr. Stine Meinild Lundby, Dr. Daniel Schaffhauser, Eva Hänsenberger, Gerti Stieger and Carlos Munoz for the fun time spent in the office.

All our collaborators in particular Dr. Lucy Forrest, Dr. Cristina Fenollar-Ferrer C, Dr. Andreas Werner, Dr. Elena Bossi.

Special thanks to the other fantastic persons I met during these years: Dr. Maria Daniela Renna, Alessandra Vollero, Diego Mariani, Yu Wang, Justyna Ruminska.

Finally, I would like to thank my old and new family; they were always supporting me and encouraging me.